Imperial College of Science, Technology and Medicine
Department of Bioengineering

Mathematical Model of the Cerebral Circulation and Distribution of Cerebrospinal Fluid

Karla Elena Sanchez Cazares

Submitted in part fulfilment of the requirements for the degree of
Doctor of Philosophy, Imperial College London, 2018.

Declaration of originality

I, Karla Elena Sanchez Cazares confirm that the work presented in this thesis is my own. Where information has been derived from other sources, I acknowledge and indicate it as such in the thesis.

Copyright declaration

Abstract

Shifts in cerebral fluid are known to be important in a number of diseases, and in conditions of microgravity such as space travel. In this work we develop a fluid mechanical model from first-principles incorporating key features of the flow of both blood and cerebrospinal fluid (CSF) in the intracranial and spinal spaces.

For the cerebral blood vessels, we model the arteries and veins as symmetric bifurcating trees with constant geometrical scaling factors between generations, assume one-dimensional flow in each vessel and account for elastic effects via a pressure-area relationship, and we assume the capillaries have a constant resistance. We treat the vessel walls as porous media to find the transmural flux of plasma. We assume flow between the other compartments to be proportional to the pressure difference; additionally, the flow to the outer-dural space is assumed to be one-way. The set of ordinary differential equations for the evolution of the fluid pressures and volumes of each compartment can be solved numerically. Additional features include autoregulation, which we model by ensuring constant pressure at the microcirculation, meaning the resulting model must be solved iteratively. Also, we can model the effect of postural changes by including hydrostatic effects in the spinal column.

The results are in accordance with physiological measurements and indicate that the pressure in the vasculature is highly sensitive to changes in vessel geometry, which also affects the transmural flux, whilst ventricular and spinal subarachnoid spaces are sensitive to compliances. We investigate transitions from supine to standing and upside down positions and also the effect of the external pressure surrounding the outer-dural spinal compartment. The model is computationally inexpensive and can be used as a platform for further analysis of cerebrovascular behaviour.

Acknowledgements

I would like to express my gratitude to several people that have made this work possible.

I want to thank my supervisor Dr Jennifer Tweedy for her guidance and support, without which this would not have been possible. Her rigorous and methodical approach to solving problems allowed me to enhance my understanding of the theoretical foundations of engineering. She was also a very kind and supportive mentor, and a role model.

I want to thank my co-supervisor Prof Kim Parker for his kindness and generosity with his time as well as his teaching. His insights about the complexities of vascular mechanics enlightened me throughout this PhD. An admirable source of knowledge and wisdom and a privilege to work with. I thank him for going above and beyond duty, and for teaching me by example what a good scientist (and person) should be.

I would also like to thank my master supervisors Prof Clive Beggs and Prof Simon Shepherd for giving me the opportunity to work on my first cerebrovascular project sparking my interest on the subject, and for their encouragement on pursuing a PhD.

A very special thanks goes to Vassia, Alejandra and Maryam for sharing this incredible journey and for their outstanding support. I would like to thank members of the Tweedy group past and present, staff at the Bioengineering department and lecturers who allowed me to teach their students. Special mention also goes to Tom and Luke for their kind support.

Above all, the pursuit of this project would not have been possible without the care and support of Nick and my family. I would like to thank my mum, for being my first academic mentor and for feeding my interest in science from an early age. I would like to thank Carlos and Patty for their kindness and support. I would like to thank Gill, Tony and Joanna who were always very kind, supportive and encouraging. Finally, I would like to give the biggest thanks to Nick, for his incredible support and patience over the years, and for being my source of strength and inspiration, this achievement is for both of us.

Dedication

To my mother, my lifelong mentor

"Everything should be made as simple as possible, but not simpler."

Albert Einstein

Contents

List of Tables

List of Figures

Nomenclature

Acronyms / Abbreviations

BBB	Blood-brain barrier
CBF	Cerebral blood flow
CoW	Circle of Willis
CSA	Cross-sectional Area
CSF	Cerebrospinal fluid
ICA	Internal carotid artery
ICP	Intracranial pressure
MRI	Magnetic resonance imaging
ODE	Ordinary differential equation
PVI	Pressure volume index
SAS	Subarachnoid space
SSS	Superior sagittal sinus
TBI	Traumatic brain injury
VA	Vertebral artery

Greek symbols

α Choroid plexus constant of proportionality

β Term describing elastic term of vessel

ϵ Wall strain

η Number of vessels

γ Scaling factor for vessel cross-sectional area

λ Eigenvalue (Chapter 3)

λ Scaling factor for vessel length (Chapter 2)

μ Viscosity

ν Arterovenous diameter ratio

Ω Annular resistance term

ϕ Transmural pressure to elastic modulus ratio

ρ Density

σ Poisson's ratio

τ Time constant (Chapter 3)

τ Wall tensile stress (Chapter 2)

ϱ Root vessel ratio

ξ Scaling factor of resistance

Other Symbols

$\widehat{\ }$ Net within a generation, e.g. $\widehat{V}$ net volume

Roman symbols

$\mathscr{A}$ Compliant area

$\mathscr{P}$ Compliant pressure

$\mathscr{R}$ Compliant resistance

$\mathscr{S}$ Compliant transmural flux

$\mathscr{V}$ Compliant volume

A Area

C Compliance

C_5 Compliance of the central canal

C_6 Compliance of the spinal cavity

d Diameter

E Elastic modulus

H Rate of change in dural pressure

h Thickness

I_{42} Intracranial arachnoid villi indicator term

I_{6e} Spinal arachnoid villi indicator term

k Permeability to fluid movement

k_1 Cerebral vascular permeability

k_{13} Permeability between cerebral vasculature and ventricles

k_{14} Permeability between cerebral vasculature and subarachnoid space

k_{34} Ventricular permeability to subarachnoid space

k_{35} Permeability between the ventricles and central canal

k_{42} Intracranial arachnoid villi permeability

k_{46} Permeability between the intracranial and spinal subarachnoid space

k_{c5} Permeability between the spinal circulation and the central canal

l Length

N Total number of generations, size of vascular tree

n Generation number

p Pressure

p_1^* Effective pressure in the cerebral vasculature

p_2 Pressure in the dural sinuses

p_3 Pressure in the cerebral ventricles

p_4 Pressure in the intracranial subarachnoid space

p_5 Pressure in the central canal

p_6 Pressure in the spinal subarachnoid space

p_e Spinal external pressure

p_{20} Initial pressure in the dural sinuses

p_{60} Initial pressure in the spinal subarachnoid space

p_{h35} Hydrostatic pressure between the ventricles and central canal

p_{h46} Hydrostatic pressure between the intracranial and spinal subarachnoid space

p_c Pressure in the spinal circulation (Chapter 4)

Q Volumetric flux

R Resistance

R_{35} Resistance between the ventricles and central canal

R_{46} Resistance between the intracranial subarachnoid space an the spinal subarachnoid space

S Volumetric flux

S_1 Transmural volumetric flux from the cerebral vasculature

S_{10} Initial cerebral vascular flux

S_{13} Flux from the cerebral vasculature to the ventricles

S_{14} Flux from the cerebral vasculature to the intracranial subarachnoid space

S_{34} Flux from the ventricles to the intracranial subarachnoid space

S_{35} Flux from the ventricles to the central canal

S_{42} Flux from the intracranial subarachnoid space to the dural sinuses

S_{46} Flux from the intracranial subarachnoid space to the spinal subarachnoid space

S_{6e} Flux from the spinal subarachnoid space to the external epidural space

S_{c5} Flux from the spinal vasculature to the central canal

t Time

V Volume

V_1 Volume in the cerebral vasculature

V_2 Volume in the dural sinuses

V_3 Ventricular volume

V_4 Volume in the intracranial subarachnoid space

V_5 Volume in the central canal

V_6 Volume in the spinal subarachnoid space

V_{30} Initial volume in the ventricles

V_{40} Initial volume in the intracranial subarachnoid space

V_{50} Initial volume in the central canal

V_{60} Initial volume in the spinal subarachnoid space

V_{c} Volume in spinal vasculature

$\mathbf{A}$ Coefficient matrix of compliant arteries (Chapter 2)

$\mathbf{A}$ Permeability matrix (Chapter 4)

$\mathbf{a}$ Vector of constants of compliant arteries

$\mathbf{b}$ Spinal constants vector

$\mathbf{I}$ Identity matrix (Chapter 3 and 4)

$\mathbf{M}$ Matrix of constants (Chapter 3 and 4)

$\mathbf{p}_a$ Pressure vector of compliant arteries

$\mathbf{p}_v$ Pressure vector of compliant veins

$\mathbf{p}$ Pressures vector (Chapter 3 and 4)

$\mathbf{q}$ Vector of constants (Chapter 3 and 4)

$\mathbf{V}$ Coefficient matrix of compliant veins

$\mathbf{v}$ Constant vector of compliant veins

$\mathbf{v}$ Eigenvector (Chapter 3 and 4)

Superscripts

s Surface, e.g. A^s surface area

x Cross section, e.g. A^x cross-sectional area

ave Average, e.g. p^{ave} average pressure

in	Input, e.g. p^{in} input pressure
out	Output, e.g. p^{out} output pressure
tot	Total
trans	Transmural

Subscripts

a	Arterial
n	Generation number
0	Generation zero
b	Brain
c	Capillaries (Chapter 2)
c	Spinal circulation (Chapter 4)
csf	Cerebrospinal fluid
h	Hydrostatic
s	Spine
v	Venous

Chapter 1

Introduction

In this chapter we provide the foundations of the research undertaken by giving an introduction, the motivation and objectives, an overview of the anatomical and physiological features relevant to the cerebral circulation and cerebrospinal fluid, and the background on existing modelling approaches.

1.1 Overview

Lack of blood flow to the brain at normal body temperature causes a person to lose consciousness within 4 to 5 seconds, followed by permanent tissue damage in 5 to 8 minutes, typically resulting in some form of physical or mental impairment, and if prolonged death[1] (Guyton, 2006). The human brain receives 13–14% of the total cardiac output and 18% of the total oxygen consumption at rest, a substantial amount considering that for an average body weight and height, an adult brain typically weighs around 1.3 kg (Hartmann et al., 1994; Levick, 2010; Guyton, 2006). The brain has a high metabolic demand, however, as seen in the kidney, this is not necessarily representative of blood flow uptake[2]. Blood flow to the brain in the healthy

[1]The brain tissue can survive without blood supply for up to 30 minutes under careful surgical procedure involving cooling the body to temperatures below 20°C to restrict the blood supply (Yan et al., 2013).

[2]The kidneys are approximately one tenth the size of the brain, and yet they have an uptake on a per gram basis up to twice the oxygen consumption of the brain with seven times as much blood flow, thus far exceeding their metabolic demand (Boron and Boulpaep, 2016; Levick, 2010).

adult is approximately 750 ml of blood per minute (Linninger et al., 2016). The microcirculation in the brain has specialised tight junctions between the endothelial cells that allow only very small molecules to pass through i.e. water, oxygen and carbon dioxide, effectively forming a barrier between the blood and the brain tissue (Fitzgerald, 1998). Local blood flow control in the brain is not only due to tissue oxygen concentration but also due to concentrations of carbon dioxide and hydrogen ions. A rise or fall in concentrations of either of these can dilate or constrict the vessels to reestablish concentration balance and with it tissue homeostasis (Guyton, 2006).

The brain is surrounded by a fluid composed of mostly water and proteins, the cerebrospinal fluid (CSF). The CSF provides buoyancy and protection to the brain, and it is also involved in compensating for hydrostatic effects. In healthy conditions arterial pulsatility causes CSF to shift outward resulting in brain and spinal cord movement. Arterial pulsatility is also thought to be involved with CSF movement for aiding venous return (Linninger et al., 2009). The cerebral circulation has different baseline conditions for subjects living in high altitude and can adapt for a short period of time to a microgravity environment[3]. The brain also has its own immune system aided by glial cells. These glial cells are involved in a number of processes in the brain predominantly of neurological nature, however, they are also involved in regulation of local blood flow (Abbott, 2013).

Abnormalities in cerebral physiological features, physical assaults to the brain or an abnormal interaction between the cerebral circulation and CSF has been associated with pathological conditions such as hydrocephalus, chiari malformation, and multiple sclerosis (Sweeney et al., 2018; Czosnyka et al., 2012; Milhorat et al., 1999; Caplan et al., 1990; Alsop et al., 2000; Weller and Carare, 2018; Elliott et al., 2013; Zamboni et al., 2009). Chronic conditions acquired with age, e.g. blood vessels stiffening and even lack of sleep, have also been associated with the development of pathological conditions such as Alzheimer's disease and other forms of vascular dementia (Iliff et al., 2012).

Although understanding of the cerebral fluids (blood and CSF) has advanced over the last

[3]In this context a short period of time refers to a year on average. The longest single stay in space by a human, 437 days, was achieved by Valeri Polyakov in 1995 (Schwirtz, 2009)

decades with the introduction of tools such as different imagining techniques[4], a concrete knowledge about the interaction of these fluids and their detrimental effects is still lacking.

The intricate interaction between the cerebral circulation and CSF and its effect on the brain and spinal cord makes the cerebral circulation a very complex and delicate system to study. In fact, all of the briefly described processes above could deserve a research project in their own right. Our focus here however, is purely a fluid mechanical one.

In this research we explore the relationship between the cerebral circulation and the CSF in the cranial and spinal compartments starting from first principles. We do this by constructing a set of mathematical models that obey fundamental laws of physics to functionally describe how the two fluids, blood and CSF, interact. The aim is to construct a relatively simple cerebrovascular model that is functionally accurate and use this to evaluate the effects of CSF spaces in the cranium and spinal cavity. We also study the effects that some key parameters have on the rest of the model in order to understand their physiological relevance and potential involvement in pathology.

1.2 Motivation and objectives

This project is motivated by evidence suggesting that abnormal cerebrovascular and cerebrospinal fluid dynamics can precede several pathological conditions leading to debilitating and often permanently impaired outcomes. Anomalous interactions between cerebral blood flow and CSF distribution have been linked to hydrocephalus, blood brain barrier rupture, syrinxes due to high CSF pressure in the spinal cavity, visual impairment due to high intracranial pressure in microgravity environments, and even multiple sclerosis (§1.1). Other conditions that involve chronic behaviour are also being investigated for their potential link to neurodegenerative conditions such as Alzheimer's disease. These chronic behaviours include high blood pressure and its effects on cerebral blood flow and autoregulation, effects of stiffening of the

[4]The first brain ultrasound was taken in 1942 by the Austrian neurologist brothers Karl and Friedrich Dussik, followed by computer tomography in 1972, and magnetic resonance imaging in 1977 (Woo, 2002; Wijdicks, 2018; Damadian et al., 1976).

blood vessels with ageing in the brain, changes in CSF clearance and the accumulation of amyloid beta, and overall reduction of CSF volume with ageing.

Furthermore, it is generally accepted that the majority of CSF is drained through the arachnoid villi, however, little has been done to fully understand their role in CSF regulation and the effects of one or several becoming occluded. This is even more the case with regards on the spinal arachnoid villi which is consistently neglected in modelling efforts.

A mathematical model of the distribution and flow of fluid in the cranium could help us understand the normal regulatory mechanisms of the hydrodynamic behaviour of the brain, and also become a tool that can enhance our understanding of the perfusion of the brain and aid in the diagnosis of cerebrovascular pathophysiology.

A number of authors have attempted to model cerebral blood flow and CSF movement over the years (§1.5). The models, however, are often based on overly simplified approaches and lack key mechanistic features such as the influence of gravity, rectification at the point of the arachnoid granulations or unrealistic modelling of the ventricles.

Our aim is to construct a model that can address the main mechanistic features of the cerebrovascular system overcoming, where possible, existing limitations of current modelling efforts. The primary aim of this research is to develop a mathematical model capable of capturing the key physiological hydrodynamics of the brain. The focus of this research is to investigate the effects of pressure and volume fluctuations in the cranium and spinal cavity, assessing CSF exit routes and effects of hydrostatic pressure with gravitational changes.

1.3 Cerebrovascular anatomy and physiology

1.3.1 The brain and cerebral meninges

At a macroscopic level, the human brain is comprised of the cerebrum, the brain stem and the cerebellum. Each of these regions (Figure 1.1) is concerned with different activities in the

human body such as motor control and language processing (cerebellum), nerve connections to the spinal cord (brain stem) or memory consolidation, vision and hearing (cerebrum).

The cerebrum, the largest part of the brain, can be physically distinguished by its arrangement of white and grey matter. The grey matter is visible in the cortex, whilst the white matter is found deep within the brain (the distinction in colour is due to the lining of myelin sheaths of the neurons which is predominantly lipid tissue). This is where the majority of intracranial neuronal and non-neuronal cells are found.

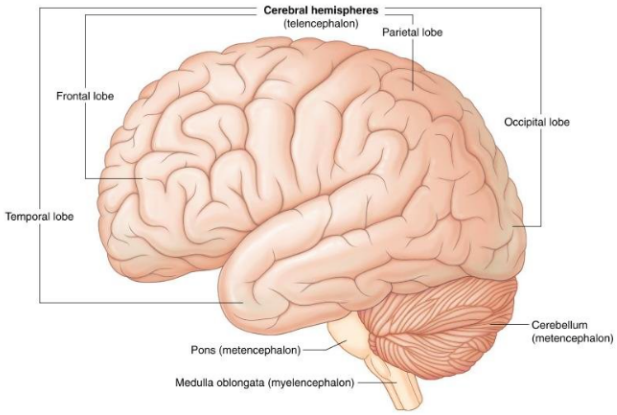

Figure 1.1: Gross anatomy of the brain, main regions (Drake et al., 2009)

The brain is protected by a series of layers or meninges (Figure 1.2): the pia mater, the arachnoid mater and the dura mater. The pia mater is a thin fibrous mesh containing relatively few cells[5], requiring capillary blood supply, that envelops the brain and spinal cord. It is permeable to CSF, and it forms a continuous space around the vessels entering the brain sulci and fissures, called the paravascular space (Hladky and Barrand, 2014; Fitzgerald, 1998). The narrow space formed between the nervous tissue and the pia mater is called the subpial space. The pia mater is *attached* to the arachnoid mater via the arachnoid trabeculi, which are elongated sheets of arachnoid mater. This space between the pia and arachnoid mater is called the subarachnoid space (SAS) and it is where the majority of CSF is contained[6](Gupta et al., 2010; Brinker et al., 2014).

The arachnoid mater has a similar composition to that of the pia mater. It differs from the pia in that its location is mostly towards the skull and not around the sulci and fissures, except

[5]Mainly loose connective tissue composed of collagen, elastin and reticulum fibres.
[6]The other main site being the cerebral ventricles.

for the longitudinal fissure separating both hemispheres. The arachnoid mater is considered avascular. The superior part of the arachnoid mater is attached to the dura mater, though often a space between the two is cited (Vandenabeele et al., 1996; Schachenmayr and Friede, 1978; Reina et al., 2002). The arachnoid mater extends continuously towards the spine widening around the thoracic region and narrowing at the cauda esquina, ending at the level of the second sacral vertebra (Figure 1.2).

The dura mater, shown in Figure 1.2, is a thick fibrous layer composed of predominantly collagen fibres with some elastic fibres. The dura mater is considered inelastic (Gray, 1989). The cerebral dura mater is composed of two layers, the innermeningeal (facing the arachnoid mater) and the endosteal (facing the bone of the skull). The formation of the space between the two layers is important as it gives rise to the venous dural sinuses, apart from these the two dura mater layers are fused together. The inner meningeal dura mater is considered avascular while the endosteal dura mater receives blood from the cranial fossa arteries (Hacking, 2018b).

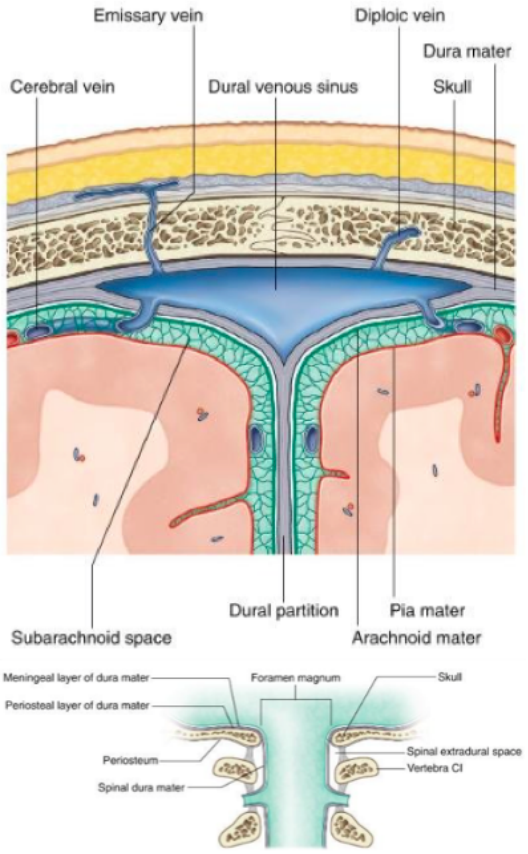

Figure 1.2: Meninges of the brain and spinal cord (Drake et al., 2009).

Deep within the brain we find other structures that are not part of the nervous tissue but are closely interconnected to the vasculature, these are the ventricular system and overall the CSF circulation. We review this in more detail in the following sections.

1.3.2 Cerebral vasculature

Blood supply to the brain is normally through the paired internal carotid arteries (ICA) and the paired vertebral arteries (VA). Each ICA branches from the common carotid artery (Figure

1.3a) and enters the cranial cavity traversing the dura mater and arachnoid mater by the carotid canal before dividing into the middle cerebral artery, the anterior cerebral artery, the posterior communicating artery and the anterior choroid artery[7](Gray, 1989). The VA directed to the brain rises from the subclavian arteries entering the cranium through the foramen magnum piercing the dura and arachnoid mater in the region of the medula oblongata where it joins to form the basilar artery giving rise to the posterior aspect of the Circle of Willis (CoW), as seen in Figure 1.3a.

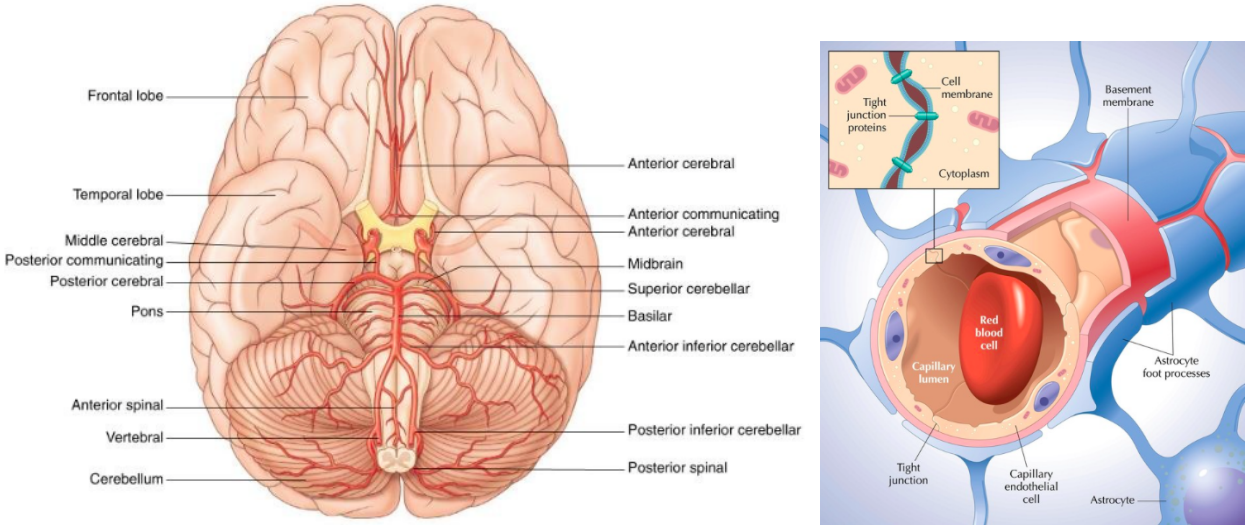

(a) **(b)**

Figure 1.3: Schematic of (a) blood supply to the brain (Drake et al., 2009), and (b) blood-brain barrier (Davis, 2014).

The CoW is a prominent anastomosis at the base of the skull predominantly supplied by the ICAs and the basilar artery. This polygon shaped structure with significant anatomical variations has the main purpose of ensuring uninterrupted blood supply to the brain if one of the main delivery arteries becomes obstructed. Several smaller arteries branch from the CoW to cover the brain surface before entering the deep brain to reach the grey matter (Gray, 1989). Variations account for 60% of the CoW, these include: cerebral and communicating arteries, anterior and posterior, which may all be absent or repeated. Often the absence of one or more of these arteries is accompanied by reciprocal enlargement of the other arteries. Cerebral arteries are typically thinner than in the rest of the body (Cipolla, 2009).

[7]Variations of the ICA include longitudinal differences depending on the length of the neck and the level of the carotid bifurcation.

Capillaries in the brain have endothelial cells with very tight junctions forming a continuous layer with a reduced permeability of bloodbourne particles to the brain other than water, lipid-soluble molecules and other actively transported substances. This selective membrane, shown in Figure 1.3b, called the blood-brain barrier (BBB), has influences from glial cells to regulate flow and transport across the membrane. It is estimated 85% of the BBB is covered by glial cell processes (Fitzgerald, 1998). The BBB is absent from the circumventricular organs, including the posterior lobe of the pituitary gland and the pineal body[8] facilitating chemical exchange and hormonal delivery (thought to be important for the hypothalamus sampling the chemical composition of blood). Capillaries surrounding the choroid plexuses are also fenestrated, however, here the ependymal cells in the ventricles have tight junctions forming a blood-CSF barrier. This is in order to protect the brain tissue from bloodbourne substances that could be transferred through the CSF (Fitzgerald, 1998). The capillaries in the brain are surrounded by astrocytic endfeet and pericytes, both thought to be involved in metabolic vasodilation and vasoconstriction. The space between the astrocytic endfeet and the endothelial membrane of the BBB form a paravascular space that has long been thought to be involved in the lymphatic processes in the brain due to its ability to facilitate flow throughout the vasculature, and thus any excess flow, that can ultimately be drained by the CSF and thorugh the venous dural sinuses. Although it is well accepted that CSF and interstitial fluid interact to remove metabolic waste, this aspect of the brain has gathered more attention in recent years due to the work of Nedergaard and colleagues linking these paravascular pathways to their potential role in Alzheimer's disease as a result of accumulation of amiloid beta (Xie et al., 2013; Iliff et al., 2012). In their research, a connection is also made (in mice) with sleep and an efficient metabolic clearance. These pathways, which have also been reported by Boulton et al. (1999) and Guyton (2006), are currently under research with other teams (Abbott et al., 2018; Taoka et al., 2018; Weller and Carare, 2018). The flow and spaces of CSF have been considered as *The third circulation* as early as 1926 (by Cushing) due to their lymphatic-like role in the brain (Welch and Friedman, 1960).

There is an extensive network of veins inside the cranium, which can be subdivided into three

[8]The rest of the circumventricular organs are the area postrema, the subfornical organ, the organum vasculosum of the lamina terminalis, the median eminence and the subcommissural organ.

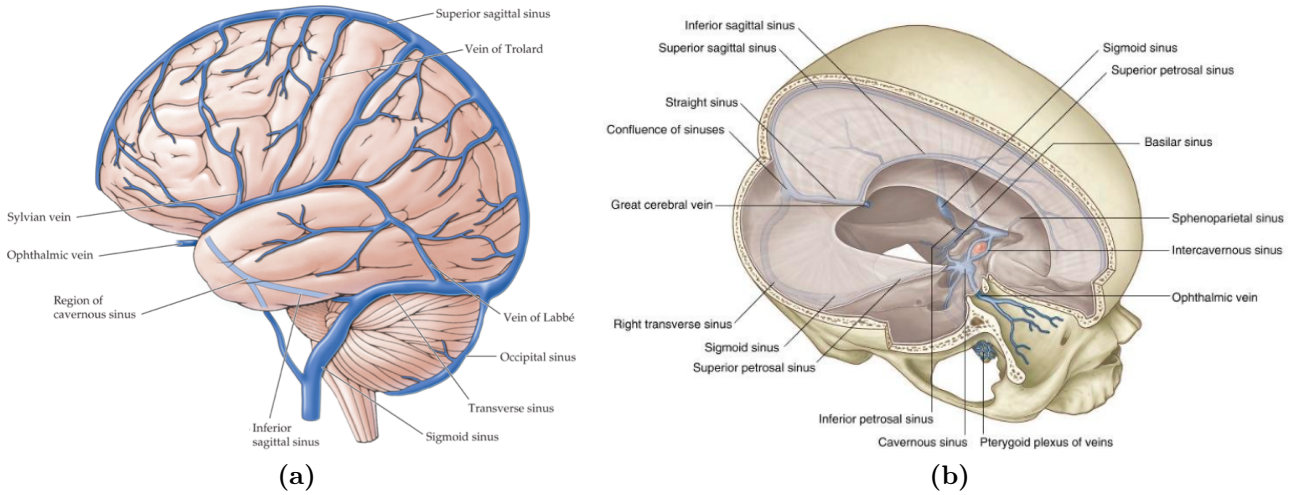

Figure 1.4: Schematic of the cerebral veins and dural sinuses (a) relative to the brain tissues, and (b) to the skull and dura mater Drake et al. (2009).

main regions: cerebral veins, cerebellar veins and veins of the brain stem; and it has unique features such as the lack of valves to prevent retrograde flow, this is thought to be compensated for by the skull enclosure and the movement of CSF with the arterial pulse (Linninger et al., 2016). The cerebral veins are thinner than in the rest of the body, much like the intracranial arteries. Apart from the veins of the brain stem, in specific those around the medulla oblongata, that can drain towards the radicular veins, all the other intracranial veins drain to the venous dural sinuses[9]. Figure 1.4a shows the main cerebral veins and dural sinuses, whilst Figure 1.4b shows the dural sinuses in relation to the dura mater and cranium. The dural sinuses are channels in the meninges of the cranium (i.e. between the two layers of the dura mater) that drain intracranial deoxygenated blood and cerebrospinal fluid[10]. Their walls are lined by endothelium with no muscular tissue, and they form a network of flow that ultimately drains into the prominent extracranial veins, such as the paired internal jugular veins and the paired vertebral veins. The dural sinuses can be divided into posterosuperior and anteroinferior, with the most prominent sinus being the superior sagittal sinus (SSS) which sits on the sagittal line throughout the skull in the middle of both brain hemispheres. Blood is collected either through the veins connecting directly to them or through the venous lacunae, which are small *pools* of blood from one or several veins that directly feed into the dural sinuses. These lacunae are

[9]We refer to them as simply dural sinuses in further text for simplicity.

[10]They also drain intermeningeal blood from the diploic veins, and a small portion of extracranial blood via the emissary veins.

typically observed in the SSS.

The dural sinuses also collect CSF from the subarachnoid space, this is done through small granulations or *villi* located on the arachnoid mater. We review these villi in more detail and CSF flow in the next section.

1.3.3 Cerebrospinal fluid

The CSF surrounds the brain and spinal cord, it is found in bigger quantities in the cranial and spinal SAS, but also within the cerebral ventricles and the central canal (depicted simply in Figure 1.6). CSF has been quantified to have an average volume of 150 ml with approximately 500-600 ml produced every 24 hours (Damkier et al., 2013). CSF is composed of mostly water (97%) and proteins, similar to blood plasma. Differences with blood plasma include a higher concentration of sodium, chloride and hydrogen ions, and a smaller concentration of calcium and potassium (Marieb, 2010). CSF serves several functions including regulation of intracranial pressure, regulation of the chemical environment of the central nervous system and aids intracerebral transport (Di Terlizzi and Platt, 2006). CSF also provides mechanical protection of the nervous tissue during physical trauma, and it plays a role in preventing backflow of the intracranial veins due to the pressure balance effect it has with the arterial pulse and the enclosed nature of the cranial vault (Gupta et al., 2010; Linninger et al., 2016; El Sankari et al., 2011).

Disturbed CSF dynamics and the accumulation of metabolites has been thought to be associated with Alzheimer's disease (Nedergaard, 2013; El Sankari et al., 2011; Weller and Nicoll, 2003). Other CSF-related conditions include hydrocephalus (high intracranial pressure which if left untreated can lead to severe permanent impairment or death) and syringomyelia (highly pressurised CSF sacs located along the spinal cord, central canal and epidural spaces) (Milhorat et al., 1994; Czosnyka et al., 2004; Marmarou et al., 1994).

The circulation of CSF is assumed to move from the choroid plexuses to the ventricles to the SAS, via the lateral aperture, and from there to the spinal cavity and outside the dura through

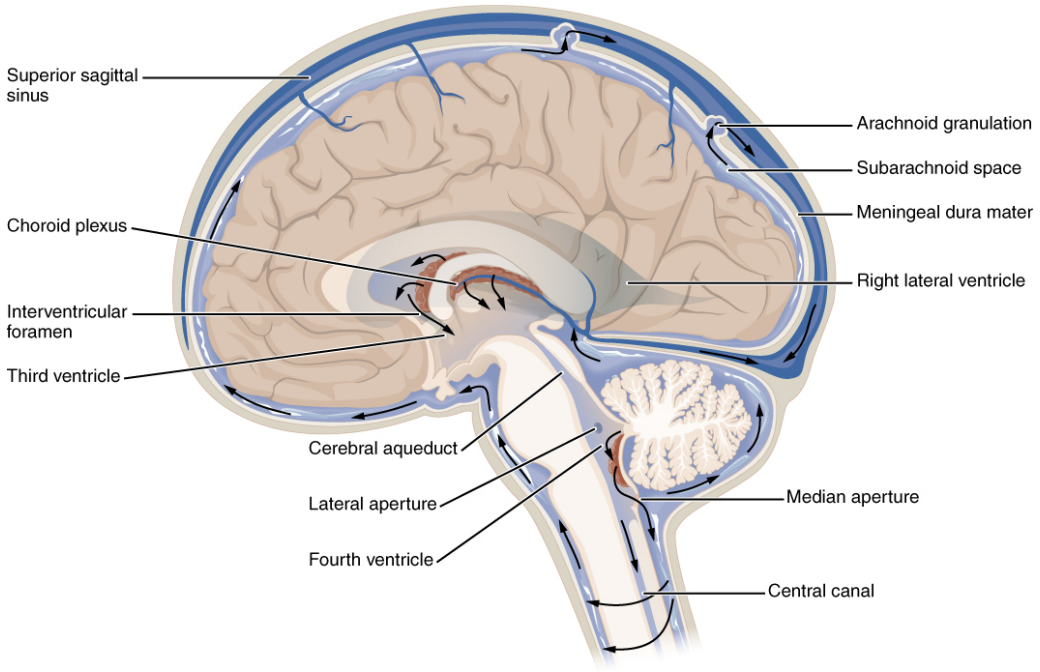

Figure 1.5: Depiction of the cerebrospinal fluid circulation (OpenStax, 2016).

the cranial arachnoid villi, specially that of the SSS. This simplified view of the CSF circulation, however, does not normally consider spinal exit routes which as we shall see are numerous along the spinal arachnoid mater.

The choroid plexus is formed of a single layer of cuboidal epithelial cells, and it is cited as the main source of CSF production, this dates back to experiments done by Dandy (1918). However, as it was quickly learned, after removing choroid plexuses from infants to stop progression of hydrocephalus, that these were not the only source of CSF production. It is now accepted that extrachoroidal CSF production sites and their contribution could be significant, however, the mechanisms and quantification remains largely underexplored (Hammock and Milhorat, 1976).

The cerebral ventricles are structures of irregular shape formed of ependymal cells. There are four ventricles, each connected by an aqueduct or canal forming an interconnected network of distinct CSF spaces, each with its own CSF supply (i.e. choroid plexus). The lateral ventricles, located one in each hemisphere, are the most prominent ones. They communicate with the third ventricle via the foramen of Monroe, which in turn communicates with the fourth ventricle via the interventricular foramen or aqueduct of Sylvious. The fourth ventricle communicates with the SAS and the spinal cord, as well as the central canal. The ventricles communicate with the

cranial SAS by the foramen of Magendie or median aperture located on the fourth ventricle.

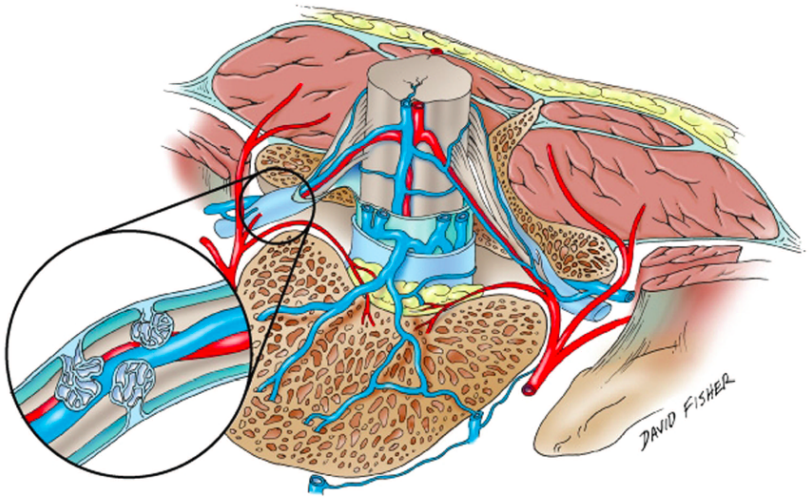

Figure 1.6: Spinal arachnoid villi at the spinal dural sheath (Tubbs et al., 2007). As in the cranium, spinal arachnoid villi drain CSF to veins adjacent to the dura mater. Spinal arachnoid villi are found throughout the spinal cavity (in the spinal dural sheath) in different amounts depending on the regions i.e. cervical, thoracic and lumbar.

The arachnoid villi are small protrusions communicating the CSF in the SAS to the venous dural sinuses in the cranium, and in the spinal cavity to in the epidural space (Figure 1.6). The arachnoid villi are found in the arachnoid mater (intracranial and spinal). They are numerous in the SSS and in the thoracic and lumbar regions of the spine. Intracranially, the arachnoid villi act as CSF rectifiers as they balance the pressure between the SAS and the dural sinuses. It is generally accepted that one, and perhaps the main, route of CSF drainage is through the arachnoid villi. The exact process of transport, however, has had incompatible views in the past, in particular when it comes to active or passive transport. Although Cushing, who was first to discover the arachnoid villi and its role in CSF flow, concluded they must have a valvular nature due to the ease of passage of flow from the SAS into the sinuses but not the other way around. This was challenged by Weed who proposed it to be the result of a diverticulum from which osmosis and pinocytosis were involved. In 1960, Welch and Friedman, following work from Davson (1956), provided evidence of the arachnoid villi working effectively as a valve. Welch and Friedman, in a detailed experiment of macaque arachnoid villi, observed that these arachnoid villi were structurally a series of delicate tubes close together that change in shape with changes in pressure. The villi arrangement was seen to flatten when the pressure in the sinuses was greater than the SAS (since the fluid in the dural sinuses would exert pressure on

the villi), and then relax (i.e. expand) when the pressure in the dural sinuses was reduced, thus allowing passage from the SAS to the dural sinuses (Figure 1.7). They highlighted the effects hydrostatic pressure changes and the importance of these valves for keeping an enclosed environment from which the intracranial fluids are protected against negative pressure[11], and suggested that this communication between the dural sinuses and CSF space was unidirectional and nonlinear (Welch and Friedman, 1960; Welch and Pollay, 1961).

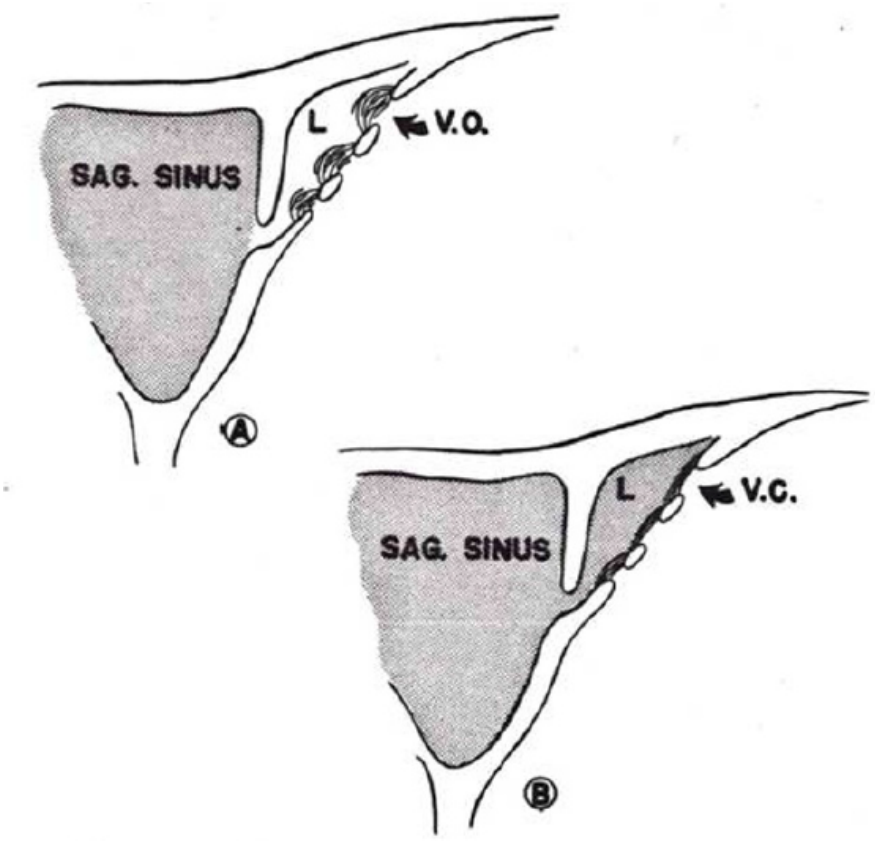

Figure 1.7: Schematic of macaque arachnoid villi when superior sagittal sinus pressure is high (A) and low (B), where V.O and V.C. stand for villi open and villi closed, respectively (Welch and Friedman, 1960).

CSF drainage is not exclusive to the arachnoid villi; other sites specially those surrounding the cranial and spinal nerves i.e. ocular, cochlear, spinal ganglions, have been reported to drain CSF and mix with extracranial (and extraspinal) lymphatics (Cserr, 1971; Nedergaard, 2013). However, it is thought that the contribution of CSF drainage through other pathways must be small in comparison to the numerous arachnoid villi. CSF is also contained in the central canal, we discuss this and other anatomical features of the spine in the next section.

[11]The dural sinuses do experience negative pressure in the standing position, as we shall see in §1.4.

1.4 The spinal cord and spinal cavity

1.4.1 Gross anatomy and spinal fluids

The spinal cord is the nervous tissue extending extracranially along the vertebral column, from the medulla oblongata to the lumbar region of the spine. It weights on average 30 grams and has a length[12] of approximately 45 cm. Protected by the vertebrae and vertebral discs, it sits below the brain and provides innervation to different parts of the body. As in the brain, the spinal cord is formed of grey and white matter, and is protected by the pia, arachnoid and dura mater[13], with the exception of the dura mater which in the spine is single layered. Between the vertebrae and the spinal dura mater there is an epidural space containing fatty padding, a network of veins and lymphatic fluid.

The spinal cavity[14] is divided into five main regions: cervical, thoracic, lumbar, sacral and coccyx (Figure 1.8), each with its own vertebrae. In each of these sections the spinal cord has differences in its cross sections, both in area, ratio between grey and white matter, and size of the central canal. The central canal is sometimes quoted as becoming obliterated after the age of 40 years old, however, this has been challenged by Millorat and colleagues in the study of several older post-morten specimens with a noticeable central canal (Milhorat et al., 1999). Furthermore, the cen-

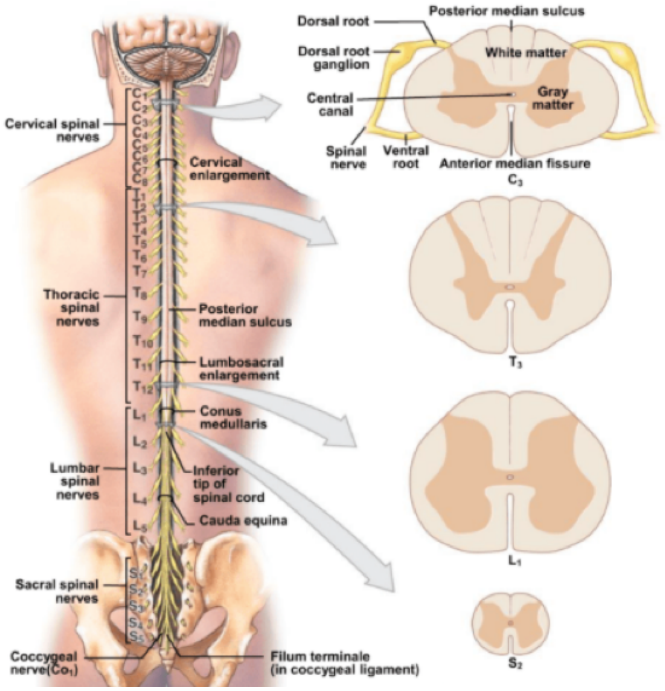

Figure 1.8: Gross anatomy of the spinal cord (Drake et al., 2009).

[12] Average for European males, data from Barson and Sands (1977).

[13] We denote *spinal* to distinguish from intracranial meninges where applicable, e.g. spinal SAS and spinal dura mater.

[14] It is common in the literature to denote the spinal cavity as the spinal canal, we use the term cavity here to avoid confusion with the central canal.

tral canal has been associated in chiari malformation and abnormal pressure resulting from syringes. The central canal is filled with CSF and is wider in the superior cervical region as well as the thoracic region, and extends to the conus medullaris.

The blood supply to the spinal cord is through two major routes that could be described as longitudinal and transversal from a superior cross-section view: the VA (described in §1.3.2), and the radicular arteries. The VA supply to the anterior spinal artery and the posterior spinal arteries (left and right), these spinal arteries run along the spinal cord, however the blood supply is only sufficient for the cervical region. Therefore, from the lower cervical and thoracic region, additional arteries (radicular) provide additional blood supply through the intervertebral foramina[15]. These spinal branches (segmental and radicular), are ramifications from the dorsal thoracic aorta. The radicular arteries (anterior and posterior) supply the spinal cord by passing through the dura mater where they branch further into smaller arteries. A prominent anterior radicular artery, in terms of calibre, is known as the great anterior radicular artery or the artery of Adamkiewicz (Figure 1.9a). The posterior radicular artery bifurcates into two posterior spinal arteries. Drainage from the spinal cord is through the anterior and posterior spinal veins which then anastomose and drain to the internal and external vertebral plexuses (Figure 1.9b).

The venous drainage is almost a mirror image of the arterial supply, with the exception of having only one posterior spinal vein (i.e. unpaired) running along the medial side of the cord. The medullary capilaries drain to the internal venous plexus and the coronal venous plexus, enter the sulcal veins and to the anterior and posterior spinal veins. From the spinal veins, blood passes through the anterior and radicular veins and out through the intervertebral veins (in the foramina) into the bigger veins and ultimately into the inferior vena cava.

Although there are no dural sinuses in the spine, there are dural sacs in the intervertebral foramina, which are sheaths of dura mater surrounding the vertebral nerves where arachnoid villi drains CSF (Figure 1.6). These sacs are different from the epidural space in the sense that they lie in between the vertebral discs rather than running along the spinal cavity.

[15]The intervertebral foramina is a transversal section that allows passage of nerves and blood vessels through the membranes of the spinal canal.

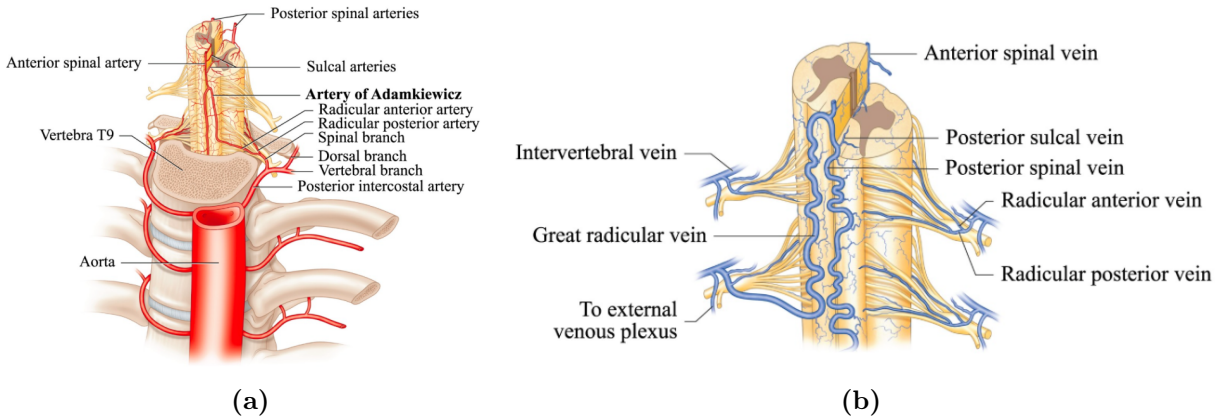

Figure 1.9: Blood supply and drainage of the spinal cord (Campos, 2015).

The central canal is essentially a continuation of the cerebral ventricles, it is structurally similar with the exception of having a choroid plexus (i.e. only ependymal lining), and it communicates with the ventricles as it does with the regional capillaries. It is thought that CSF production in the spine occurs mainly via the ependymal cells of the central canal and from the fourth ventricle. CSF drainage is through the arachnoid villi and other routes through the cauda esquina (end of the spinal cord). While there are arachnoid granulations in each region of the spine (cervical, thoracic and lumbar), it has been found that the lumbar region has a higher concentration of these granulations. Perhaps suggesting that a gravity factor is involved. The spinal cavity accounts for a significant proportion of the total subarachnoid CSF (approximately 60%), meaning that CSF in the brain is substantially influenced by the spine (Alperin et al., 2006).

1.4.2 Postural hydrostatics

We have discussed so far aspects concerning supine healthy adults. In an upright position, the brain sits above the heart level creating a hydrostatic pressure gradient with respect to the heart. The distensibility of the veins makes them very susceptible to changes in pressure, and this is also true in the cerebral veins. As mentioned earlier in the chapter, the intracranial veins are protected against changes in hydrostatic pressure by the enclosure provided by the skull and more specifically the pressure balance of the CSF and arachnoid villi. Extracranially, the cerebral veins are not protected and thus the prominent veins such as the internal jugular veins

partially collapse in the upright position. In the upright position most of the venous drainage takes place in the vertebral veins (Guyton, 2006).

The venous dural sinuses are not susceptible to collapse (due to their properties already described), however, they do experience negative pressure. In the standing position (Figure 1.10), the pressure relative to the cranium can be negative or positive depending on posture (Guyton, 2006). When passing from supine to standing position, as gravitational pressure effects become noticeable, the dural sinuses decrease in pressure. This is critical during brain surgery since the position of the head can allow for air to become trapped resulting in vascular air embolism. Similarly, following decompression craniectomy complications can result in the sinking of the skin flap of the removed skull to relieve intracranial pressure, with potentially fatal outcomes (Han et al., 2008). Furthermore, this is a key problem during space flight since the lack of gravity causes the CSF to flow upwardly leading to long term complications like visual impairment. In a recent study, it was reported that astronauts, who experience high intracranial pressure during missions, had an upward shift in the brain and spinal cord which caused blockage of the arachnoid villi at the superior sagittal sinus (Roberts et al., 2017).

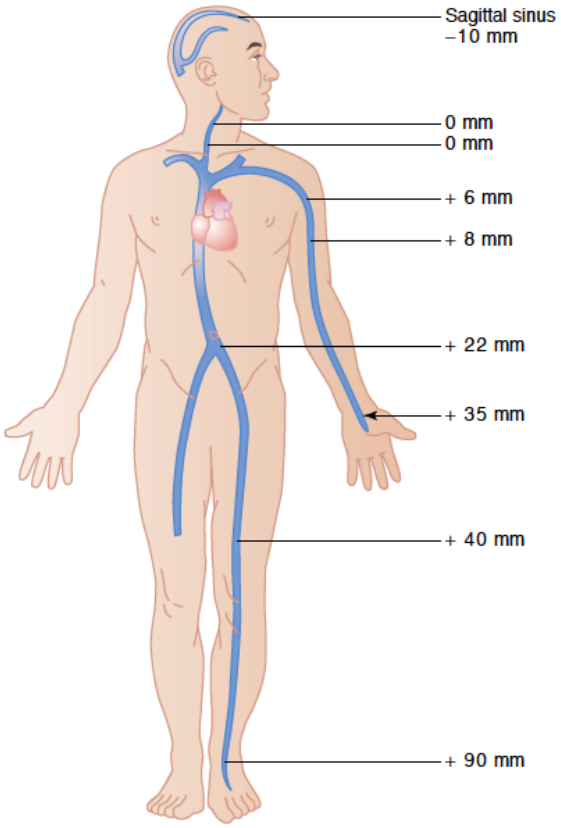

Figure 1.10: Gravitational effects on veins and dural sinuses (Guyton, 2006). In the standing position veins above the heart level can collapse due to negative hydrostatic pressure created by the distance relative to the heart (as shown by mm).

In a sitting position, CSF oscillations between the cranium and spinal canals have also been observed to decrease by 48% (Alperin et al., 2006). Pressure in the dural sinuses decreases to zero at a 25 degree angle, and can reach -10 mmHg in the upright position (Iwabuchi et al., 1983). Intracranial pressure is normally around 11 mmHg in the supine position. When

a person is in an upside-down position, the opposite occurs, pressure in the dural sinuses increases. Gravity also affects arteries and capillaries, however, since their pressure is not as close to atmospheric pressure as the veins are, the effects are less pronounced.

1.5 Current modelling approaches

Modelling of cerebral blood flow and CSF has been done for several decades and has gathered momentum over the last few years. From black box models derived without considering the physical relationships of the system, to complex 3D models that analyse, often patient-specific, sections of the brain (e.g. tumour or an arterial bifurcation) rather than the system as a whole. Compartmental models have been the preferred approach when studying cerebral fluids due to their simplicity, as it enables information to be elicited without expanding to complex details. In this context, the compartment represents a particular region, often spatially averaged, and the variables represent the amounts of certain quantities within the compartment. These 0D compartmental models are usually represented as lumped electrical analogues, where a vessel or an entire compartment is expressed in terms of voltage, current and resistance (Ohm's law), without detailing spatial features. Although their advantages include less computational effort and faster information acquisition for analysing the global components of the system, the main limitation of 0D models is the assumption of spatial uniformity, even when considering unsteady states. This assumption can limit the ability of the model to evolve into more in-depth approximations, not to mention higher risk of estimation error in parameter scaling. The linearity of these models, although easier to compute, can typically describe the system only in very general terms. One-dimensional (1D) modelling of the cerebrovascular system approaches apply the Navier-Stokes equations for describing the fluid and vessels in a simplified manner, making several assumptions (e.g. axisymmetry) to reduce the equations to one dimension. These models are often a good compromise in that they provide a closer approximation than 0D model to the nature of the cerebrovasculature without demanding high computational efforts of 2D or 3D models and still providing valuable information upon which higher complexity can be built. A summary of the main research teams in cerebrovascular and spinal modelling is

provided next.

Important historical discoveries of intracranial and spinal fluids have led to the progression into modern day modelling. A selection of these discoveries (prior to the first modelling attempt in 1975) is summarised in Table 1.1.

The doctoral thesis and related publications by Marmarou et al. (1975) is typically regarded as the first model of intracranial hydrodynamics. Marmarou analysed the CSF distribution in the cranium and spinal cavity, with focus on the compliance of the compartments and the outflow resistance. Firstly analysed in cats by a bolus injection method, the compliance was measured against the volume change over time, which he refers as CSF absorption rate. He confirmed a nonlinear relationship exists between intracranial pressure and volume, from its logarithmic form he derived a pressure-volume index (PVI) related to the slope of pressure vs volume. Since this index is directly related to compliance, he suggested PVI could be used as an indicator of compliance when intracranial pressure rises. He proposed that disturbances in volume from a stable intracranial reference pressure can be quantified and assessed for pathology. Further iterations of the model provide an electrical analogue for CSF formation and absorption (Czosnyka et al., 2012). Marmarou's legacy remains as PVI is used (along with other methods) to assess hydrocephalous (Marmarou et al., 1978, 1987, 1994; Czosnyka et al., 2012; Shapiro et al., 1980; Relkin et al., 2005).

A decade later Zagzoule and Marc-Vergnes published the first model of the cerebral vasculature using 34 segments representing the main arteries and veins, with the capillaries lumped into single compartment (Zagzoule and Marc-Vergnes, 1986), through reduced Navier-Stokes equations and a pressure-area relationship which is a function of the vessel elastic modulus. By using a set of estimates of cross-sectional area, length, and elastic modulus relevant to each of the segments, the differential equations are solved numerically. Results show agreement for blood flow and pressure for humans at rest. Although a good first approximation, the model does not take CSF into consideration as it is described to be 'negligible' to the cerebral circulation. Other more recent work by Zagzoule and colleagues involves stenosis, the analysis of pulsatile flow in the spinal cord and compliance of the dura mater (Najeme et al., 1992; Cassot et al.,

1664	**Willis T.** *Cerebri Anatome.* First accurate anatomical description of blood supply to the brain (Rengachary et al., 2008).
1783	**Monro A.** *Observations on the structure and function of the nervous system.* Analytic description of intracranial volumes of brain, CSF and blood as a constant relationship (Wilson, 2016).
1824	**Kellie G.** Experimental evaluation of Monro's observations leading to the Monro-Kellie hypothesis (Wilson, 2016).
1842	**Magendie F.** *Recherches anatomique et physiologique sur le liquide cephalo-rachidien ou cerebro-spinal.* First detailed description and naming of cerebrospinal fluid (Magendie, 1842).
1891	**Quincke H. and Winter W.** Developed independently the lumbar puncture method for relieving CSF pressure in the spine (Gray, 1921).
1901	**Cushing H.** Developed further on the Monro-Kellie hypothesis, and performed experiments showing the existence of openings between the dural sinuses and subdural space (i.e. SAS) with resemblance of 'valvular action' (Madsen et al., 2006).
1914	**Weed L.** Interpretation of arachnoid villi using a filtration method (Weed, 1914).
1918	**Dandy W.** Extirpation of choroid plexus in an attempt to cure hydrocephalus (Dandy, 1918).
1925	**Cushing H.** Lecture on "The Third Circulation" proposing a lymphatic-like role of CSF for cerebral drainage pathways (Madsen et al., 2006).
1952	**Bering E.** Studied role of choroid plexus in production of CSF, transmission of arterial pulsatility to CSF, and ventricular size in hydrocephalus (Bering, 1952).
1960	**Welch K. and Friedman V.** Experimental demonstration of arachnoid villi functioning as valves (Welch and Friedman, 1960).
1962	**Pappenheimer J.** Dye dillution techniques for estimation of steady-state CSF production and absorption (Madsen et al., 2006).
1970	**Davson H.** Consolidated view of arachnoid villi as important CSF drainage points (Davson et al., 1970).

TABLE 1.1 Timeline of key cerebrovascular and CSF discoveries prior 1975.

2000; Cathalifaud et al., 2016).

Sorek et al. (1988) presented a seven-lumped compartmental model with resistances (defined as fluidity) and compliances to represent the main vascular segments of the brian as well as the choroid plexus and ventricles. The equations are linearised for solution of the unsteady state. Monroe-Kellie was enforced through input-output volume flux. Results showed agreement with literature values. Limitations of the model include globalised parameters and bi-directional flow betwen the dural sinuses and SAS CSF.

Between 1988 and 2003, Ursino and colleagues presented a set of detailed mathematical models of intracranial hydrodynamics with the use of electrical analogues, including low-pass filters for changes from bigger to smaller vessels and diodes to account for the arachnoid villi. Ursino and colleagues provides the first blood-CSF integrated model. The team incorporates the ICA pulse wave as input to the model and assumes a parallel arrangement of vessels giving a total resistance which is computed with the rest of the parameters. The model also attempts to model autoregulation by means of a feedback loop that changes the cerebrovscular resistance. The model is further improved providing good evidence of modelling capabilities using compartmental models for cerebral hydrodynamics. Limitations include assumption of uniformity and vessel arrangement thus disregarding the complexity of the CoW and capillary network, as well as neglecting a source of CSF production dependent of blood flow. The models, however, have provided insight for other modelling efforts and are regarded as key due to the ease of study of intracranial interactions (Ursino and Lodi, 1997; Ursino, 1988a; Ursino et al., 2000; Ursino and Lodi, 1998; Ursino and Di Giammarco, 1991; Loth et al., 2001).

Compartmental modelling has also been adopted by Czosnyka and colleagues, where they apply clinical information readily available on the bigger arteries entering the cranium as input and use a compartmental model of two main vascular compartments (arteries and capillary-veins) with a compartment of the CSF with formation and absorption points. Here the model assumes CSF is formed in the arterial compartment, thus providing a more realistic representation of the physiology. Limitations include the joint compartment of capillaries and veins and the potential reversible flow at the dural sinuses (Piechnik et al., 2001; Czosnyka et al., 2012).

Detailed work by Linninger and colleagues provides a foundation for one-dimensional cerebrovascular models, as well as a precedent for 3D models of the cranial and spinal cavities for fluid-structure interaction. With focus on hydrocephalus, Linninger and colleagues analysed CSF flow using a reconstructed pulsatile arterial input and adding 1D compartments for each vascular and CSF segment, including a spinal component of CSF. Further models include the use of patient-specific microvasculature reconstruction with a separate mesh representing the CSF space. As with other models of higher complexity, these type of models pose their own limitations when it comes to computational expense (Linninger et al., 2005, 2007, 2009, 2016; Gould et al., 2017).

Other higher order models include those presented by Muller and colleagues where they detail the cerebral vasculature with special focus on the venous output for both intracranial and extracranial veins in order to asses a potential role of venous abnormalities in multiple sclerosis (Müller et al., 2013; Müller and Toro, 2014; Toro, 2016; Toro et al., 2019). Other teams have focused on the brain tissue, modelling it as a poroelastic medium (Tully and Ventikos, 2011), or in specific 3D features of tumours or other pathological conditions (Radaelli et al., 2008), or whole body models with special focus on the cerebrovasculature (Blanco et al., 2015). Emerging research indicates a potential increase in models mimicing the role of paravascular space in CSF movement (Aldea, 2017).

Regarding the spinal cord, models have been more limited. Current modelling techniques typically treat the spinal cavity as a concentric cylinder closed on one end and open on the other with input and output on the open-ended end, using either 1D fluid mechanical models or finite element approaches to analyse stresses in pathology (e.g. syringomyelia) and postural changes (Bertram et al., 2005; Bertram, 2009). Postural changes have been studied in detail by several teams (Alperin et al., 2006; Blomqvist and Stone, 2011; Michael and Marshall-Bowman, 2015; Lawley et al., 2017), some of which have involved data collected from NASA missions. However, models on postural changes remain scarce.

A good example of modelling postural changes is presented by Olufsen et al. (2004) where a model of eleven compartments is tested from sitting to standing position and compared to

physiological data obtained from a subject using an index finger probe. The model incorporates autoregulation by means of a piece-wise linear function and dynamical features through Kirchoff's law. It provides agreement with measured data and shows the decrease in venous pressure when transitioned to the standing position. Limitations include no information about the dural sinuses.

Lakin et al. (2007) present a model on microgravity also accounting for averaged values in a compartmental arrangement. The model, resembling closely that of Sorek et al., incorporates features like BBB permeability changes and osmotic pressure gradients. However, it ignores important gravitational aspects such as those involved with the intracranial veins and dural sinuses. It is also unclear how the gravitational terms are included in the model, although the hydrostatic effect mentioned can be interpreted as having adapted hydrostatic terms to the governing equations.

A recent model by Sánchez et al. (2018) provides a detailed analysis of idealised flow in a concentric spinal cord and its movement with arterial pulsations. It solves numerically a large set of two-dimensional differential equations to estimate upward and downward flow of a vertical spine and the effects of bolus injection in the CSF dynamics. Limitations include the lack of compliance for the spinal region and a spinal cord of same diameter throughout the spinal cavity.

Linninger et al. (2016) also gives detail of a spinal cavity dynamics, highlighting the effects of the arachnoid trabercula mesh in the spinal SAS on the CSF dynamics (Linninger et al., 2007).

These last two studies are examples of distributed fluid dynamics models of the spine. Other teams have also started to explore the spinal cord using computational fluid dynamics (Cheng et al., 2014). However, further work is required if postural changes are to be included. The pursuit of understanding the nature of craniospinal fluid mechanics requires a more holistic approach.

1.6 Thesis outline

This thesis is organised in a series of self-contained but linked chapters each pertaining to a different model, with an introductory chapter (Chapter 1), and a discussion and future work chapter (Chapter 5). Chapter 2 presents a vascular model of the cerebral circulation which can be used as a standalone or in combination with the models developed in Chapters 3 and 4. Chapter 3 presents a model of the intracranial spaces including the vasculature (model from Chapter 2), the venous dural sinuses, the cerebral ventricles and the subarachnoid space. Chapter 4 builds on the intracranial model (Chapter 3) by incorporating spinal compartments, the central canal and spinal subarachnoid space, to account for hydrostatic effects and the changes in CSF when interacting with intracranial and arachnoid villi.

Chapter 2

Vascular model

In this chapter we develop a detailed model of the cerebral vasculature as a set of two symmetric, self-similar, bifurcating trees describing the arteries and veins. This model is intended to be self-contained as well as to play an important part in our model of the cerebrospinal fluid circulation which will be developed in later chapters. We explore in this model: (1) scaling factors and the number of generations; (2) pressures along the vasculature; (2) volumetric fluxes between generations in bifurcating trees; (3) cerebral autoregulation; and (5) sensitivity to a selection of parameters.

2.1 Introduction to the model

The cerebral circulation is large and complex. The number of vessels, their distribution, and the presence of at least one key loop (i.e. Circle of Willis) makes it difficult to model. Attempts to model the cerebrovasculature typically focus on anatomical accuracy, and whilst this can be achieved to an acceptable level for the larger vessels, the opposite is true for the microcirculation and in particular the smaller vessels connecting the two (§1.5). One of the reasons for this is the limited knowledge of the smaller vessels in the brain. We know the name, location, and to some extent the anatomical variation of the big arteries and veins in the brain, however, we know much less about the smaller vessels. We accept that arterioles can be identified region-

ally, e.g. periventricular arterioles, but we do not know their number and density estimates vary depending the region and local demand (Cavaglia et al., 2001; Kuschinsky and Paulson, 1992). We also do not know to how many capillaries a single high resistance artery[1] or venule connects to, which makes anatomical modelling difficult. However, our focus on this model is not anatomical accuracy but rather functionality.

As seen in Chapter 1, the blood supply to the brain is achieved through the internal carotid arteries (ICA) and the vertebral arteries (VA). The VAs join to form the basilar artery which connects to the Circle of Willis as do the two ICAs. Circulation after the Circle of Willis (CoW) branches out through several conduit arteries (e.g. middle cerebral artery, posterior and anterior cerebral arteries) reaching the arteries that sit on the surface of the brain before branching further into smaller arteries (e.g. pial arteries).

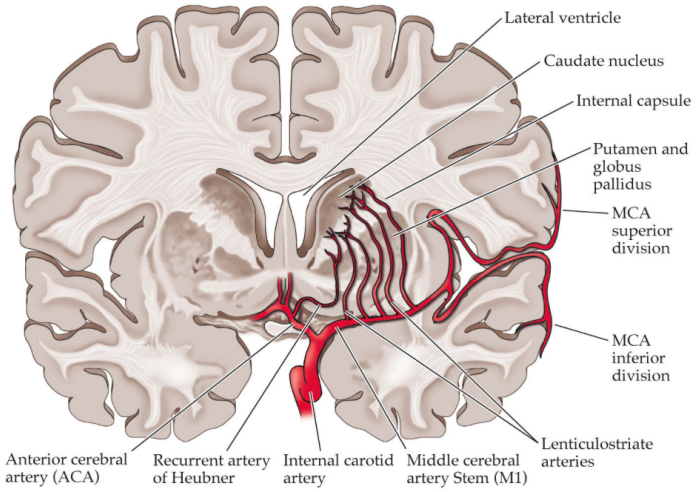

Figure 2.1: Example of small cerebral arteries supplying blood to the region of the brain adjacent to the lateral wall of the lateral ventricle (Queens University at Kingston, 2005).

It is often convenient to model the cerebral circulation from the ICA, the VA or both, since it is possible to obtain experimental data (i.e. velocity, cross-sectional area) that can feed into the model. The interaction of this arterial input with the CoW however would require another level of complexity to support the multiple inputs and outputs, curvature and possibly non-laminar flow. This could be overcome by assuming the CoW as a lumped parameter, or by integrating good examples of existing models dedicated to the CoW (Alastruey et al., 2007; Hillen et al., 1986). There are fewer examples of distributed models post CoW. Interestingly,

[1]We use the term of high resistance arteries to avoid confusion regarding arterioles.

it is in the smaller vessels where the effects of vascular resistance are most important and complications such as blood clots, hypoxia or breakdown of the blood-brain barrier (BBB) can have a significant impact on the brain (Obermeier et al., 2013). Figure 2.1 shows one of the structural patterns that conduit arteries and smaller vessels form after the CoW. The neglect in cerebral modelling of the smaller vessels is unsurprising when considering limited clarity on the quantification of smaller vessels and their plasticity over time (Maguire et al., 2006; Johansson, 2000).

Modelling the veins in the brain is also challenging and it is only recently that there have been firm efforts to explore this (Müller and Toro, 2014). As seen in Chapter 1, the cerebral veins lack valves and forward flow in the veins is probably augmented by the changes in arterial volume due to the arterial pulse which, in the constant volume cranium, must interact with the venous volume. The cerebral veins drain to several epimeningeal compartments that ultimately drain to the confluence of sinuses before exiting to the internal jugular veins or the vertebral veins. Modelling attempts on the small veins and venules are to our knowledge nonexistent.

In this model we focus on the cerebral circulation of the smaller vessels including high resistance arteries and venules, and how they interact with the capillaries (§2.2.2) and surrounding CSF. The interaction of the vasculature with the cerebral ventricles, subarachnoid space and venous dural sinuses is explored in Chapter 3. The interaction of the intracranial system with the spinal CSF compartments is explored in Chapter 4.

2.1.1 Model description and assumptions

The complexity of the cerebral vasculature can be reduced by modelling blood flow in each vessel as one dimensional (1D). We simplify the analysis further by assuming self-similarity in the smaller vessels governing the relationships between generations.

The model is formed of two symmetrical bifurcating trees, one for the arteries and one for the veins, where all the vessels within a generation are geometrically identical. Both trees bifurcate, so the n^{th} generation has 2^n vessels and up to a maximum number of generations

$N-1$, as seen in Figure 2.2. We assume that both the arterial and venous tree has the same number of generations. The root vessel of the arterial tree, generation 0, is represented as the effective arterial input feeding the bifurcating tree. The arterial input is assumed as a single starting point for all superficial and penetrating arteries, that is the arteries surrounding the brain tissue before entering the deeper brain to become smaller arteries and high resistance arteries. The arterial root vessel should be seen as an effective root vessel that incorporates the major arteries entering the cranium and the CoW. Similarly, the root vessel of the venous tree represents the effective venous output that exits the bifurcating tree to connect to the bigger veins and subsequently to the venous dural sinuses which will be covered in Chapter 3. We again emphasise the model is not an attempt of anatomical accuracy, but one of functionality.

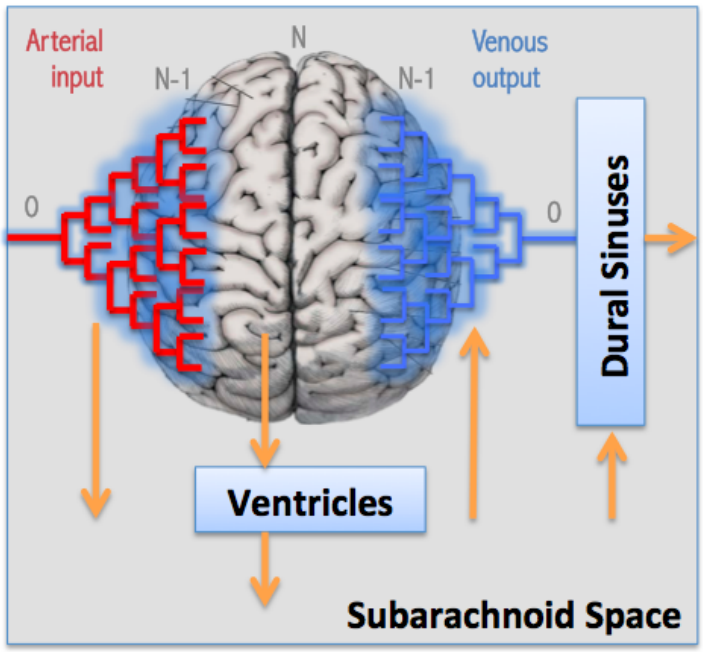

Figure 2.2: Schematic of the cerebral vascular model and its interaction with cerebrospinal fluid spaces and dural sinuses. Subarachnoid space, cerebral ventricles and venous dural sinuses are introduced as part of the intracranial model (Chapter 3).

The last arterial generation of the tree, $N-1$, becomes the input to the capillary generation N. We do not attempt to model the capillaries as a bifurcating tree as they have a wider structural variation, we instead assume the capillary bed results in an arrangement of effective parameters (e.g. resistance, pressure) which we then use to connect both the arterial and venous trees. The output of generation N becomes the input of the venous tree, generation $N-1$, which then follows a binary convergence until reaching the output of the entire vascular tree in the

venous generation 0.

Blood flow is pulsatile in nature due to the contraction and relaxation of the heart muscle with each cardiac cycle. Pressure fluctuations from systolic to diastolic cause the vessel to distend and contract creating a quasi-periodic wave of blood with specific velocity characteristics throughout the arteries. Vascular wave propagation analysis is complex and in the brain is further complicated by the interaction with surrounding CSF, and the confined spaced of the skull and spinal cord. This presents a level of complexity beyond that intended for this initial simple model. As we aim to model the main parameters in the smaller vasculature, a simpler yet rigorous option is to assume the flow in the model can be first approximated as steady state flow. This means the parameters derived from the model will describe a mean value over several cardiac cycles. This is an acceptable approach in cerebrovascular modelling and one that has been taken in modelling efforts over time (Czosnyka et al., 2012; Linninger et al., 2009; Ursino, 1988a).

The compliance of the blood vessels can also introduce considerable complexity into the model. However, in this model we deal with this by first analysing a reference, rigid case (§2.2), where we construct the cerebral vasculature assuming no changes in cross-sectional area (CSA) due to pressure. The behaviour of the compliant case is then analysed using the rigid case as a reference, and introducing a pressure-area relationship to allow for distensibility and compliance in the vasculature (§2.4).

In the brain, the fluid interacting outside the vasculature is crucial to cerebral blood flow. In this chapter we account for this interaction by means of transmural flux from the blood towards extravascular tissue. We assume this fluid is transferred transmurally throughout the smaller vasculature and effectively becomes part of the CSF feeding into the CSF spaces (i.e. cerebral ventricles and the subarachnoid space). We investigate in the following chapter the effect of this interaction with the rest of the intracranial space.

The pressure external to the vasculature and the global cerebral blood flow is assumed to be constant in this model. We set the external pressure, input arterial pressure, and cerebral blood flow as boundary conditions in the model. We describe the full list of parameters used in this

model in §2.3.

The following sections describe the reference and compliant cases of this vascular model and the governing equations.

2.2 Rigid reference case

We first describe the mathematical relationship of the model parameters when changes in CSA are accounted for by means of a scaling law and self-similarity only, meaning the changes in pressure do not cause the vessels to distend or contract, i.e. rigid vessels. We describe the formation for the arterial tree, the capillaries, and the venous tree.

2.2.1 Arteries

Bifurcation and self-similarity

The arterial tree is self-similar with respect to CSA and length, meaning the characteristics related to CSA and length of a vessel in a given generation n will be a scaled version of the preceding generation $n-1$.

We introduce the scaling factors γ for vessel CSA A^x, and λ for vessel length l. The rest of the parameters in the model are derived from these two fundamental parameters, values which we discuss in §2.3.2.

Given $l_n = \lambda\, l_{n-1}$ and the length of the 0^{th} generation l_0, it can be shown by induction that $l_n = \lambda^n l_0$. Similarly, it can be shown that $A^x_n = \gamma^n A^x_0$.

We use the notation in Table 2.1 to describe the parameters of the model[2]. For example, $\widehat{A}^s_{an}$ denotes the net arterial surface area in generation n, whereas A^s_{an} denotes the arterial surface area in a single vessel in generation n. The arterial tree has generations $n = 0, 1, 2, \cdots, N-1$

[2]The full nomenclature list can be found at the beginning of the thesis.

	Parameter		Subscript		Superscript		Other
A	area	a	arterial	ave	average	$\widehat{\ }$	net in a generation
d	diameter	c	capillaries	in	input		
h	thickness	e	external	out	output		
η	no. of vessels	n	generation n	s	surface		
k	permeability	v	venous	tot	total		
l	length	0	generation 0 (root)	trans	transmural		
p	pressure			x	cross section		
Q	volumetric flux						
R	resistance						
S	transmural flux						
V	volume						

Table 2.1: Notation conventions.

where generation 0 is the root vessel and generation $N-1$ connects to the the capillaries, which we denote as generation N noting that we do not assume it to be a binary generation.

Based on the above scaling and notation conventions, the parameters for the arterial tree are:

$$\eta = 2^n, \tag{2.1}$$

$$A^x_{an} = \gamma^n A^x_{\mathrm{a}0}, \tag{2.2}$$

$$\widehat{A}^x_{an} = (2\gamma)^n A^x_{\mathrm{a}0}, \tag{2.3}$$

$$l_{an} = \lambda^n l_{\mathrm{a}0}, \tag{2.4}$$

$$d_{an} = \gamma^{n/2} d_{\mathrm{a}0}, \tag{2.5}$$

$$A^s_{an} = (\gamma^{1/2}\lambda)^n A^s_{\mathrm{a}0}, \tag{2.6}$$

$$\widehat{A}^s_{an} = (2\gamma^{1/2}\lambda)^n A^s_{\mathrm{a}0}, \tag{2.7}$$

$$V_{an} = (\gamma\lambda)^n V_{\mathrm{a}0}, \tag{2.8}$$

$$\widehat{V}_{an} = (2\gamma\lambda)^n V_{\mathrm{a}0}, \tag{2.9}$$

where,

$$A^x_{\mathrm{a}0} = \pi d^2_{\mathrm{a}0}/4, \tag{2.10}$$

$$A^s_{\mathrm{a}0} = \pi d_{\mathrm{a}0} l_{\mathrm{a}0}, \tag{2.11}$$

$$V_{\mathrm{a}0} = A^x_{\mathrm{a}0} l_{\mathrm{a}0}. \tag{2.12}$$

We assume the vessel wall thickness scales in proportion to the diameter, so that $h_{\mathrm{a}n} = \gamma^{n/2} h_{\mathrm{a}0}$.

Mass and momentum conservation

For a given generation, treated as a control volume, mass cannot be created or destroyed, so the rate of change of mass in the control volume equals the net mass flux entering that generation. Assuming blood is incompressible (a very good approximation), conservation of mass for the arterial tree of N generations is governed by

$$\frac{d\widehat{V}_{\mathrm{a}n}}{dt} = \widehat{Q}_{\mathrm{a}n} - \widehat{S}_{\mathrm{a}n}. \tag{2.13}$$

We assume quasi-steady flow of blood ignoring the effects of the arterial pulse. That is, the cerebral blood flow Q is the time averaged flow rate over a time that is long compared to the period of the cardiac cycle. We also assume that $S << Q$, so that, to first order $Q^{\mathrm{in}} = Q^{\mathrm{out}}$. For a single vessel in generation n we have $Q_{\mathrm{a}n} = Q_{\mathrm{a}n-1}/2$, then

$$Q_{\mathrm{a}n} = 2^{-n} Q_{\mathrm{a}0}, \tag{2.14}$$

$$\widehat{Q}_{\mathrm{a}n} = Q_{\mathrm{a}0}, \tag{2.15}$$

where $Q_{\mathrm{a}0} = Q$, and $Q_{\mathrm{v}0} = Q - \sum \widehat{S}_{\mathrm{v}n}$, where $\widehat{S}_{\mathrm{v}n} << Q$.

We assume each vessel is approximated as an axisymmetrical cylindrical tube with a cross-sectional area perpendicular to its centreline and uniform thin walls. We assume flow inside the vessels is laminar, incompressible and Newtonian. As seen in Chapter 1, this first approximation

is acceptable for modelling one-dimensional flow in the vasculature. Furthermore, Reynolds number in the smaller vessels is very small and well below transitional or turbulent flow (Fung and Zweifach, 1971; Lew and Fung, 1969).

Given the assumptions above and neglecting gravity effects[3], we can apply the steady Navier–Stokes equations to describe the fluid motion inside a vessel,

$$\rho(\mathbf{u}.\boldsymbol{\nabla})\mathbf{u} = -\boldsymbol{\nabla}p + \mu\boldsymbol{\nabla}^2\mathbf{u}, \tag{2.16}$$

where $\mathbf{u}$ is the displacement of the fluid, p the pressure, and μ the viscosity. We know from the continuity equation (and our incompressibility assumption) that $\boldsymbol{\nabla}.\mathbf{u} = 0$. Assuming steady, unidirectional and fully-developed flow, we can reduce Equation (2.16) to

$$0 = -\frac{\Delta p}{l} + \frac{\mu}{r}\frac{\partial}{\partial r}\left(r\frac{\partial w}{\partial r}\right), \tag{2.17}$$

where r is the radial coordinate, w the axial velocity component, and Δp the pressure difference along the cylinder. Solving Equation (2.17) gives

$$w = -\frac{\Delta p r^2}{4\mu l} + c_1 \ln r + c_2, \tag{2.18}$$

where c_1 and c_2 are constants to be defined by the boundary conditions. At $r = 0$, we require w to be finite, which implies $c_1 = 0$. We apply a no-slip boundary condition at the walls of the cylinder, $w = 0$ at $r = \mathrm{d}/2$ which sets $c_2 = \Delta p \mathrm{d}^2/16\mu l$, thus, $w = \Delta p((d/2)^2 - r^2)/4\mu l$. Integrating the axial velocity over the cross-sectional area to obtain the volumetric flux, gives the classic Hagen–Poiseuille equation,

$$\Delta p = \frac{128\mu l}{\pi \mathrm{d}^4} Q. \tag{2.19}$$

We find the resistance across a vessel in terms of cross-sectional area as $R = 8\pi\mu l/(A^x)^2$.

[3]Gravity effects are addressed in Chapter 4.

Substituting Equations (2.2) and (2.4) into the resistance equation to incorporate the scaling factors, we obtain the arterial resistance of a single vessel in generation n, as

$$R_{an} = \left(\frac{\lambda}{\gamma^2}\right)^n R_{\mathrm{a}0}, \tag{2.20}$$

where $R_{\mathrm{a}0} = 8\pi\mu l_{\mathrm{a}0}/(A^x_{\mathrm{a}0})^2$ is the arterial resistance of the root vessel. We assume the vessels are connected in parallel, hence the net resistance of generation n is $\widehat{R}_{an} = 2^{-n}R_{an}$, thus

$$\widehat{R}_{an} = \xi^n R_{\mathrm{a}0}, \tag{2.21}$$

where $\xi = \lambda/2\gamma^2$ is the resistance scaling.

Substitution of Equation (2.21) into (2.19) gives the pressure difference across generation n

$$p^{\mathrm{in}}_{an} - p^{\mathrm{out}}_{an} = \xi^n Q R_{\mathrm{a}0}. \tag{2.22}$$

The nature of the vascular tree implies the output pressure in one generation is the input pressure in the successive generation, that is for $p^{\mathrm{out}}_{an} = p^{\mathrm{in}}_{an+1}$, as visualised in Figure 2.3.

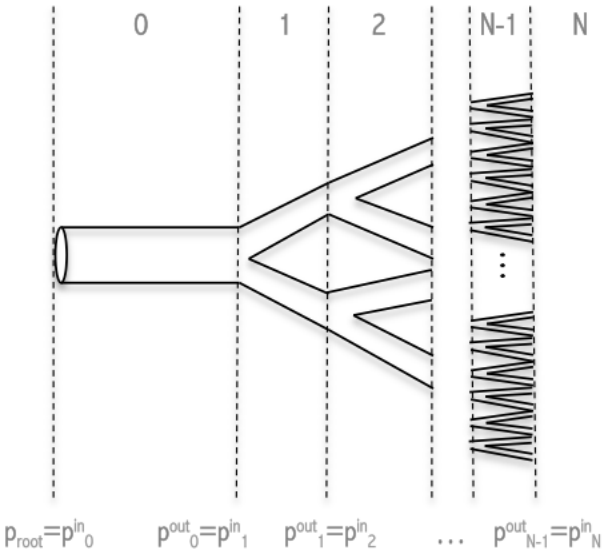

Figure 2.3: Schematic of arterial branching. Interconnection between blood vessels and related pressures.

Letting the root pressure be the input pressure of the arterial tree ($p^{\mathrm{in}}_{\mathrm{a}0} = p_{\mathrm{root}}$) and consid-

ering the generations are in series whilst neglecting energy losses at bifurcations, we obtain the pressure difference across the arterial tree as the sum of the pressure differences in each generation,

$$p_{an}^{\text{out}} = p_{\text{root}} - R_{\text{a}0} Q \sum_{i=0}^{n} \xi^i, \tag{2.23}$$

$$= p_{\text{root}} - R_{\text{a}0} Q \left(\frac{\xi^{n+1} - 1}{\xi - 1} \right), \tag{2.24}$$

where $\xi \neq 1$, and for the entire arterial tree $n = 0, 1, 2, \cdots, N-1$.

Similarly, we find the input pressure for generation n,

$$p_{an}^{\text{in}} = p_{an}^{\text{out}} + R_{an} Q$$

$$= p_{\text{root}} - R_{\text{a}0} Q \sum_{i=0}^{n-1} \xi^i \tag{2.25}$$

$$= p_{\text{root}} - R_{\text{a}0} Q \left(\frac{\xi^n - 1}{\xi - 1} \right). \tag{2.26}$$

We assume the average arterial pressure in generation n, p_{an}^{ave}, is given by the arithmetic mean of the input and output pressures, which substituting with Equations (2.24) and (2.26) gives,

$$p_{an}^{\text{ave}} = p_{\text{root}} - R_{\text{a}0} Q \left(\frac{\xi^n - 1}{\xi - 1} + \frac{\xi^n}{2} \right). \tag{2.27}$$

From Equation (2.24) we can obtain the pressure at the outlet of the arterial tree, by setting $n = N - 1$,

$$p_{\text{a}N-1}^{\text{out}} = p_{\text{root}} - R_{\text{a}0} Q \frac{\xi^N - 1}{\xi - 1}. \tag{2.28}$$

Transmural flux

The fluid transferred from the circulation to outside the vasculature is composed generally of plasma, water-soluble molecules, and metabolites excluding the formed elements of blood and

large proteins (Guyton, 2006), and we assume it ultimately forms part of the CSF. To model the transmural flux throughout the circulation, we treat the blood vessel wall as a porous medium. We assume this porous medium to be homogeneous and isotropic, and the vessel wall large compared to a single pore. The flow in the porous medium can be described by the Darcy equation,

$$\mathbf{u} = -\frac{k}{\mu_{\text{csf}}}\boldsymbol{\nabla} p, \tag{2.29}$$

where $\mathbf{u}$ is the volumetric flux per unit area in the medium, k is the permeability of the medium, μ_{csf} the shear viscosity of the CSF ($\mu_{\text{csf}} \neq \mu_{\text{blood}}$), and $\boldsymbol{\nabla} p$ the fluid pressure difference across the wall. We are interested in the flux across the vessel, $\mathbf{u} \cdot \mathbf{n} A$, and we assume this area to be the surface area of the vessel A^s. This implies the pressure difference Δp through the wall thickness h, is that between the lumen and the outside the vessel,

$$S = -\frac{k A^s \Delta p}{\mu h}, \tag{2.30}$$

where S is the transmural flux, k is the permeability of the vessel, and h the vessel thickness.

Rewriting Equation (2.30) in the adopted arterial notation we obtain

$$S_{an} = \frac{k_{\text{a}} A^s_{an}}{\mu_{\text{csf}} h_{an}} (p^{\text{ave}}_{an} - p_e), \tag{2.31}$$

where we assume the vessel thickness h_{an} scales in proportion to the diameter, that is $h_{an} = \gamma^{n/2} h_{\text{a}0}$ as denoted in Equation (2.5).

We find the net transmural flux from generation n by substituting Equations (2.7) and (2.27) into (2.31),

$$\begin{aligned} \widehat{S}_{\text{an}} &= \frac{k_{\text{a}} \widehat{A}^s_{an}}{\mu_{\text{csf}} h_{\text{an}}} (p^{\text{ave}}_{an} - p_e) \\ &= \frac{(2\lambda)^n k_{\text{a}} A^s_{\text{a}0}}{\mu_{\text{csf}} h_{\text{a}0}} (p_{\text{root}} - R_{\text{a}0} Q \left(\frac{\xi^n - 1}{\xi - 1} + \frac{\xi^n}{2} \right) - p_e), \end{aligned} \tag{2.32}$$

Notice that whilst we assume a constant wall permeability for this model, the scaling factor

allows for the transmural flux to change as a function of the surface area, wall thickness, and change in transmural pressure. In other words, although we assume constant permeability throughout the tree the transmural flux varies from generation to generation due to the scaled nature of the tree.

To find the transmural flux in the entire arterial tree we solve for the cumulative transmural flux,

$$\begin{aligned}\widehat{S}_{an}^{\text{tot}} &= \frac{k_{\text{a}} A_{\text{a0}}^{s}}{\mu_{\text{csf}} h_{\text{a0}}} \sum_{n=0}^{N-1} (2\lambda)^n \left(p_{\text{root}} - R_{\text{a0}} Q \left(\frac{\xi^n - 1}{\xi - 1} + \frac{\xi^n}{2} \right) - p_e \right) \\ &= \frac{k_{\text{a}} A_{\text{a0}}^{s}}{\mu_{\text{csf}} h_{\text{a0}}} \left[\left(\frac{(2\lambda)^N - 1}{2\lambda - 1} \right) \left(p_{\text{root}} - p_e + \frac{R_{\text{a0}} Q}{(\xi - 1)} \right) - \left(\frac{(2\lambda\xi)^N - 1}{2\lambda\xi - 1} \right) \frac{R_{\text{a0}} Q (\xi + 1)}{2(\xi - 1)} \right]. \end{aligned} \tag{2.33}$$

2.2.2 Capillaries

The capillaries form a complex network of vessels sufficiently challenging that previous attempts to model it have limited accuracy (Peyrounette et al., 2018). In the capillaries, several common modelling assumptions break down and complications include (but are not limited to): (1) idealisation of blood as a homogeneous fluid is difficult to sustain due to the packed arrangements of erythrocytes inside each capillary, (2) physical arrangement varies between regions of an organ, e.g. capillary density around the hippocampus, (3) the BBB forms a protective layer in the capillaries that does not expand to every part of the microcirculation, as it is the case on the circumventricular organs (Gray, 1989), and (4) metabolic effects, aquaporin channels, glial cells and overall osmotic pressure differences can have a significant effect (Papadopoulos et al., 2004).

Modelling the capillaries is further complicated by the defining properties of a capillary itself and the boundaries that separate them from high resistance arteries and venules. Visualising every capillary in the brain is difficult and current methods to quantify them rely on density approximations and scaling[4] (Duvernoy et al., 1981). Furthermore, the capillary density changes change over time, and what is considered average for a healthy range of individuals might not

[4]We explore this further in §2.3.

be applicable to the rest of the population even within a similar age group (Zatorre et al., 2012; Maguire et al., 2006). An increase in size of an organ demands delivery of more oxygen and nutrients and with it the proximity to a blood vessel. One can hypothesise about angiogenesis in growth of brain regions with high plasticity. It is now established that the human brain keeps growing new neurons throughout our lifetime (Eriksson et al., 1998). It could be argued that the indirect effect of this would have to be supported by physical characteristics such as the proliferation of blood vessels (Greenberg and Jin, 2005).

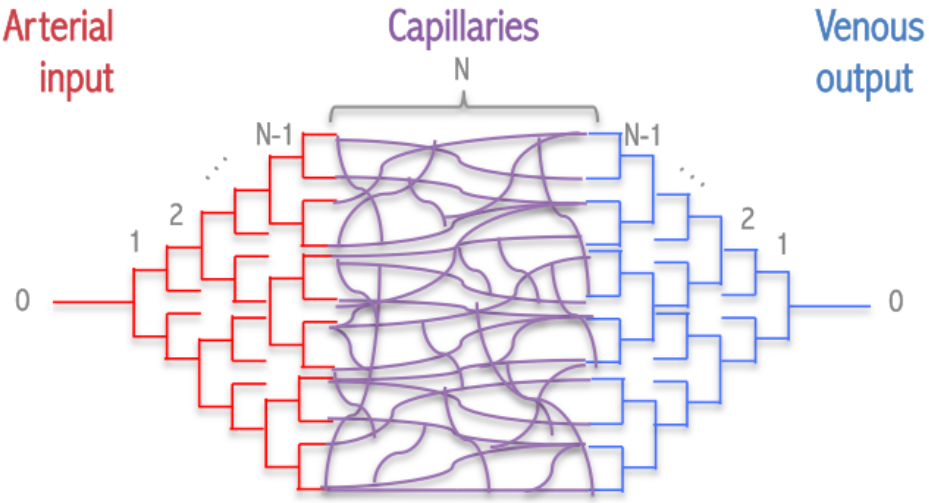

Figure 2.4: Representation of the capillaries connecting the arterial and venous trees.

These are only a few of the challenges of modelling the capillaries. Exploring each of these and by extension all of them, represents a level of complexity beyond the scope of this work. We therefore do not attempt to model the capillaries, but rather assume its mesh-like structure will result in an overall resistance that combined with the output pressure of the last generation of the arterial tree will give rise to an output pressure where the venous tree can begin its converging branching.

We could make assumptions regarding the number of high resistance arteries connecting to a capillary and therefore obtain CSA and other important parameters from the number of high resistance arteries in generation $N-1$. However, doing so would imply that we assume a parallel arrangement of capillaries which, as pointed out before, would be difficult to sustain due to their complex network. For the purposes of simplicity we assume only the pressure and

transmural flux in the capillaries can be estimated.

In our model the arterial and venous trees are connected through a lumped capillary segment that we treat as a set of vessels with fixed net resistance R_{c} (Figure 2.4). We assume laminar flux and thus the pressure drop across the capillaries is described by

$$p_{\mathrm{c}}^{\mathrm{in}} - p_{\mathrm{c}}^{\mathrm{out}} = R_{\mathrm{c}} Q, \tag{2.34}$$

where we assume $p_{\mathrm{c}}^{\mathrm{in}} = p_{\mathrm{a}N-1}^{\mathrm{out}}$ and $p_{\mathrm{c}}^{\mathrm{out}} = p_{\mathrm{v}N-1}^{\mathrm{in}}$.

The transmural flux is described by

$$\widehat{S}_{\mathrm{c}} = k_{\mathrm{c}}(p_{\mathrm{c}}^{\mathrm{ave}} - p_e), \tag{2.35}$$

where k_{c} is the global capillary permeability, and $p_{\mathrm{c}}^{\mathrm{ave}} = (p_{\mathrm{c}}^{\mathrm{in}} + p_{\mathrm{c}}^{\mathrm{out}})/2$.

2.2.3 Veins

Binary convergence and self-similarity

Mirroring the arterial vessel tree, the blood vessels in the venous circulation converge pairwise in successive generations, meaning each successive generation in the venous forward direction ($N-1$ to 0, as per Figure 2.4) has half the number of vessels, i.e. 2^{-n}.

We assume the same scaling factors γ and λ apply to the venous vessel tree. The self-similar

parameters for the venous tree are,

$$A^x_{vn} = \gamma^n A^x_{v0}, \tag{2.36}$$

$$\widehat{A}^x_{vn} = (2\gamma)^n A^x_{v0}, \tag{2.37}$$

$$l_{vn} = \lambda^n l_{v0}, \tag{2.38}$$

$$d_{vn} = \gamma^{n/2} d_{v0}, \tag{2.39}$$

$$A^s_{vn} = (\gamma^{1/2}\lambda)^n A^s_{v0}, \tag{2.40}$$

$$\widehat{A}^s_{vn} = (2\gamma^{1/2}\lambda)^n A^s_{v0}, \tag{2.41}$$

$$V_{vn} = (\gamma\lambda)^n V_{v0}, \tag{2.42}$$

$$\widehat{V}_{vn} = (2\gamma\lambda)^n V_{v0}, \tag{2.43}$$

where

$$A^x_{v0} = \pi d^2_{v0}/4, \tag{2.44}$$

$$A^s_{v0} = \pi d_{v0} l_{v0}, \tag{2.45}$$

$$V_{v0} = A^x_{v0} l_{v0}. \tag{2.46}$$

As in the arteries, we assume the vessel wall thickness scales in proportion to the diameter, then $h_{vn} = \gamma^{n/2} h_{v0}$.

Mass and momentum conservation

Analysing the venous tree from generation 0 to generation $N-1$, we can apply the same considerations from the arterial tree regarding mass and momentum conservation. We thus have

$$\frac{d\widehat{V}_{vn}}{dt} = \widehat{Q}_{vn} - \widehat{S}_{vn}, \tag{2.47}$$

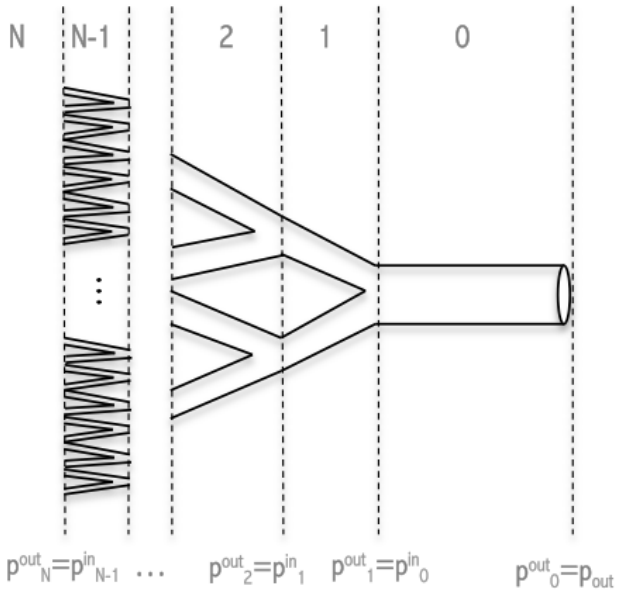

Figure 2.5: Schematic of venous branching. Interconnection between blood vessels and related pressures.

where

$$Q_{\mathrm{v}n} = 2^{-n} Q_{\mathrm{v}0}, \tag{2.48}$$

$$\widehat{Q}_{\mathrm{v}n} = Q_{\mathrm{v}0}, \tag{2.49}$$

and $Q_{\mathrm{v}0} = Q - \sum \widehat{S}_{\mathrm{v}n}$, where $\widehat{S}_{\mathrm{v}n} << Q$.

The momentum conservation equation gives the resistance $R_{\mathrm{v}n}$ of a single venous vessel and the venous net resistance $\widehat{R}_{\mathrm{v}n}$ of all the vessels in generation n,

$$R_{\mathrm{v}n} = \left(\frac{\lambda}{\gamma^2}\right)^n R_{\mathrm{v}0}, \tag{2.50}$$

$$\widehat{R}_{\mathrm{v}n} = \xi^n R_{\mathrm{v}0}, \tag{2.51}$$

where $R_{\mathrm{v}0} = 8\pi\mu l_{\mathrm{v}0}/(A^x_{\mathrm{v}0})^2$ is the venous resistance in the root vessel. The pressure difference across generation n is then

$$p^{\mathrm{in}}_{\mathrm{v}n} - p^{\mathrm{out}}_{\mathrm{v}n} = \widehat{R}_{\mathrm{v}n} Q. \tag{2.52}$$

Working out the pressure difference from the capillaries to the venous root vessel (Figure 2.5), that is from generation $N-1$ to 0, we sum the pressure drop across previous generations to obtain the output venous pressure[5]

$$\begin{aligned} p_{\mathrm{v}n}^{\mathrm{out}} &= p_{\mathrm{c}}^{\mathrm{out}} - R_{\mathrm{v}0} Q \xi^{N-1} \sum_{i=0}^{N-1-n} \xi^{-i} \\ &= p_{\mathrm{c}}^{\mathrm{out}} - R_{\mathrm{v}0} Q \xi^{N-1} \left(\frac{1-\xi^{-(N-n)}}{1-\xi^{-1}} \right), \end{aligned} \tag{2.53}$$

the input pressure,

$$\begin{aligned} p_{\mathrm{v}n}^{\mathrm{in}} &= p_{\mathrm{c}}^{\mathrm{out}} - R_{\mathrm{v}0} Q \xi^{N-1} \sum_{i=0}^{N-n-2} \xi^{-i}, \\ &= p_{\mathrm{c}}^{\mathrm{out}} - R_{\mathrm{v}0} Q \xi^{N-1} \left(\frac{1-\xi^{-(N-n-1)}}{1-\xi^{-1}} \right), \end{aligned} \tag{2.54}$$

and the average pressure, which as in the arteries, is defined as the arithmetic mean between input and output pressures,

$$p_{\mathrm{v}n}^{\mathrm{ave}} = p_{\mathrm{c}}^{\mathrm{out}} - R_{\mathrm{v}0} Q \xi^{N-1} \left(\frac{1-\xi^{-(N-n)}}{1-\xi^{-1}} + \frac{\xi^{-1}}{2} \right). \tag{2.55}$$

Relationship of scaling factor ξ with vasculature

We can obtain the venous output pressure from the input pressure p_{root} by expanding the capillary pressure in terms of the arterial input, which gives

$$p_{\mathrm{v}0}^{\mathrm{out}} = p_{\mathrm{root}} - Q \left(R_{\mathrm{c}} + (R_{\mathrm{a}0} + R_{\mathrm{v}0}) \left(\frac{\xi^N - 1}{\xi - 1} \right) \right). \tag{2.56}$$

Multiplying Equation (2.56) by $(\xi-1)/Q(R_{\mathrm{a}0}+R_{\mathrm{v}0})$, gives,

$$\xi^N - \left(\frac{p_{\mathrm{root}} - p_{\mathrm{v}0}^{\mathrm{out}}}{Q} - R_{\mathrm{c}} \right) \frac{\xi}{R_{\mathrm{a}0}+R_{\mathrm{v}0}} + \left(\frac{p_{\mathrm{root}} - p_{\mathrm{v}0}^{\mathrm{out}}}{Q(R_{\mathrm{a}0}+R_{\mathrm{v}0})} - \frac{R_{\mathrm{c}}}{R_{\mathrm{a}0}+R_{\mathrm{v}0}} - 1 \right) = 0. \tag{2.57}$$

[5] A more detailed working of this derivation can be found in Appendix A.1.

Letting

$$\kappa = \left(\frac{p_{\text{root}} - p_{\text{v0}}^{\text{out}}}{Q} - R_{\text{c}} \right) \frac{1}{R_{\text{a0}} + R_{\text{v0}}},$$

we can rewrite Equation (2.56) as the polynomial

$$\xi^N - \kappa\xi + \kappa - 1 = 0, \tag{2.58}$$

which emphasises the importance of ξ in our calculations. When $\xi = 1$ the factored form of the finite partial sum cannot be used to find a solution. The value of ξ is reviewed and determined in §2.3.

Transmural flux across the vasculature

Similar to the arteries, we use the simplified Darcy Equation (2.30) to model the transmural flux across to the venous circulation. The venous transmural flux $\widehat{S}_{\text{v}n}$ in generation n is then

$$\widehat{S}_{\text{v}n} = \frac{k_{\text{v}} A_{\text{v0}}^s (2\lambda)^n}{\mu_{\text{csf}} h_{\text{v0}}} (p_{\text{v}n}^{\text{ave}} - p_e). \tag{2.59}$$

where k_{v} is the venous vessel permeability, A_{v0}^s the venous surface area in generation 0, and $h_{\text{v}n}$ the venous vessel thickness. The total transmural flux in the venous tree is,

$$\begin{aligned}
\widehat{S}_{\text{v}n}^{\text{tot}} &= \frac{k_{\text{v}} A_{\text{v0}}^s}{\mu_{\text{csf}} h_{\text{v0}}} (2\lambda)^{N-1} \sum_{n=0}^{N-1} (2\lambda)^{-n} \left(p_{\text{c}}^{\text{out}} - R_{\text{v0}} Q \xi^{N-1} \left(\frac{1 - \xi^{-(N-n)}}{1 - \xi^{-1}} + \frac{\xi^{-1}}{2} \right) - p_e \right) \\
&= \frac{k_{\text{v}} A_{\text{v0}}^s}{\mu_{\text{csf}} h_{\text{v0}}} (2\lambda)^{N-1} \left[\left(\frac{1 - (2\lambda)^{-N}}{1 - (2\lambda)^{-1}} \right) \left(p_{\text{c}}^{\text{out}} - p_e - R_{\text{v0}} Q \xi^{N-1} \frac{3\xi - 1}{2\xi - 2} \right) - \frac{R_{\text{v0}} Q}{\xi - 1} \left(\frac{(\frac{\xi}{(2\lambda)})^N - 1}{(\frac{\xi}{(2\lambda)}) - 1} \right) \right].
\end{aligned} \tag{2.60}$$

We can now find the transmural flux in the entire cerebrovascular network from the sum of the arterial and venous vascular trees plus the capillary transmural flux,

$$\widehat{S}_{\text{vasculature}}^{\text{tot}} = \widehat{S}_{an}^{\text{tot}} + \widehat{S}_{\text{c}} + \widehat{S}_{\text{v}n}^{\text{tot}}. \tag{2.61}$$

We expand on the interaction of Equation (2.61) with the CSF spaces in Chapter 3.

2.3 Determination of parameters

We determine the parameters to use in the model by describing their connectivity with other parameters as well as their estimates from experimental data where available. We first determine the diameter of the arteries and veins in generation 0. Equation (2.5) gives the following relationship for the arterial diameter of the root vessel

$$d_{\mathrm{a}0} = \gamma^{-n/2}\, d_{an}. \tag{2.62}$$

Since the arterial tree reaches the capillaries at generation N, as a first approximation we can assume that

$$d_{\mathrm{a}0} = \gamma^{-N/2}\, d_{\mathrm{c}}, \tag{2.63}$$

where d_{c} is the capillary diameter. We choose a value of $d_{\mathrm{c}} = 6 \times 10^{-6}$ m as it is the approximate diameter of an erythrocyte (Guyton, 2006). By knowing the number of generations in the tree N and the scaling factor of CSA γ, we can thus obtain a value for the diameter of the root vessel. We formulate the number of generations in §2.3.1 and give the value for this diameter in §2.3.3.

Generally veins have a larger diameter than their equivalent arteries, so we assume that

$$d_{\mathrm{v}0} = \nu\, d_{\mathrm{a}0}, \tag{2.64}$$

where ν is the arterovenous diameter ratio. We assume this value is in the range of $1 < \nu < 3$ based on the averaged value of the diameter between the ICA and IJV and that of smaller arteries and veins (Levick, 2010; Caro et al., 2012). We analyse ν in combination with the scaling factors in §2.3.3 to establish its value.

To determine a value for the arterial wall thickness in generation 0, h_{a0}, we assume this is 10% of the diameter as per Caro et al. (2012), then $h_{a0} = 0.1d_{a0}$. For the venous wall thickness in generation 0, h_{v0}, we assume this can be approximated by half that of the arterial vessel wall, $h_{v0} = h_{a0}/2$. This is an estimation based on the smaller thickness of bigger veins with respect to arteries (Levick, 2010; Caro et al., 2012).

For the vessel length, we assume the length of the root vessel for the arterial and venous tree is the same. We assign a value of $l_{a0} = l_{v0} = 0.085$ m based on half the value of the common carotid artery (Levick, 2010).

In our model we assume that the larger arteries and veins are almost impermeable. Due to the lack of experimental data, we assign a very small permeability value as a proof of concept for the arterial permeability in generation 0, $k_{a0} = 1 \times 10^{-21}$, and we assume its venous counterpart has a smaller permeability, $k_{v0} = k_{a0}/2$.

To estimate the capillary resistance, we assume the pressure drop in our model does not exceed 15 mmHg, which when factored by the cerebral blood flow we obtain a capillary resistance of 0.02 mmHg.min/ml. Table 2.2 shows a summary of the estimated parameters, excluding N, ν, γ which we define in §2.3.3. We adopt the following convention for significant figures: up to two significant figures for values less than 10, up to one decimal place for values above 10. For values smaller than two decimal places, scientific notation is adopted with up to two significant figures.

	Value	Units
l_{a0}	8.5×10^{-2}	m
l_{v0}	8.5×10^{-2}	m
k_{a0}	1×10^{-21}	m^2
k_{v0}	0.5×10^{-21}	m^2
R_c	0.02	mmHg.min/ml

Table 2.2: Estimated parameter values.

The Fahraeus-Lindqvist effect is important when studying flow in small blood vessels due to the greater concentration of erythrocytes as the diameter changes from bigger to smaller diameter (Barbee and Cokelet, 1971). However, for simplicity we assume this change in viscosity is

minimal and allow for a constant viscosity throughout the vasculature.

We take the following values from the literature (Table 2.3): viscosity of blood μ_{blood}, viscosity of CSF μ_{csf}, arterial Young's modulus E_{a}, venous Young's modulus E_{v}, and capillary permeability k_{c}. We use the arterial input pressure p_{root}, external pressure p_e and the cerebral blood flow Q as our boundary conditions which we also take from the literature.

	Value	Units	Reference
E_{a}	9×10^5	N/m^2	(Caro et al., 2012).
E_{v}	7×10^4	N/m^2	(Caro et al., 2012).
μ_{blood}	3.5×10^3	Pa.s	(Guyton, 2006).
μ_{csf}	7.3×10^3	Pa.s	(Gupta et al., 2010).
p_e	11	mmHg	(Steiner and Andrews, 2006).
p_{root}	90	mmHg	(Guyton, 2006).
Q	750	ml/min	(Linninger et al., 2009).
d_{c}	6×10^{-6}	m	(Guyton, 2006).
k_{c}	1.9×10^{-11}	ml/mmHg.min	(Guyton, 2006).

Table 2.3: Parameter values from literature.

2.3.1 Number of generations

To determine the number of generations N, we need to estimate the number of capillaries in the brain.

The number of capillaries in the entire human body are estimated as 10 billion (Guyton, 2006). If we assume variation in the number of capillaries in the entire body is negligible compared to their absolute number, and that the number of capillaries in an individual organ is proportional to the fraction of the cardiac output that perfuses the organ, we can estimate the number of capillaries in the brain based on this estimate. The brain obtains approximately 13% of the total cardiac output, which means the cerebral capillaries are in the region of 130 million capillaries or approximately 2^{27}, thus giving 27 generations.

We can also estimate the number of vessels by capillary density. Literature reports an average capillary density in the human brain of 1500 vessels per mm^3 (Gray, 1989). Assuming a brain volume of 1.5×10^{-3}m^3, we obtain 2^{31} capillaries, resulting in $N = 31$.

If we assume a volume fraction of capillaries in the brain, we can relate the CSA of a capillary to the area occupied in the cross-section, that is $\pi d_c^2/4D^2$, where d_c^2 is the capillary diameter and D the distance between capillaries. If we now relate this proportionality to the volume ratio between the brain and that of the capillaries, we can obtain the number of vessels,

$$\begin{aligned} \frac{\pi d_c^2}{4D_c^2} &= \frac{\eta_c \pi d_c^2 l_c}{2V_b} \\ \implies \eta_c &= \frac{V_b}{l_c d_c^2}, \end{aligned} \tag{2.65}$$

where η_c is the number of capillaries in the brain, and V_b the brain volume. For a capillary length of 0.6 mm, a brain volume as before, and a distance between capillaries of approximately the diameter of a capillary (6×10^{-6} m), we obtain a approximate value of 2^{33} number of vessels, resulting in $N = 33$.

We can start seeing a pattern emerging about the number of generations, even when the number of capillaries varies substantially from one approach to another. The approach we select however, is based on functionality. This is a simpler yet a reasonable approximation since measurement for flow velocity through a capillary u_c and total cerebral blood flow Q are widely reported (Levick, 2010). Relating the ratio between the total cerebral blood flow and the volumetric flux through a single capillary with velocity u_c, we obtain

$$\eta_c = \frac{4Q}{u_c \pi d_c^2}. \tag{2.66}$$

Assuming $u_c = 1 \times 10^{-3}$ m/s and $Q = 750$ ml/min, we obtain an estimate of 2^{28} capillaries and therefore $N = 28$ generations.

In Equation (2.5) we defined the diameter of the arterial root vessel as a function of the number of generations. From the value chosen for the capillary diameter, we can see how our first approximation for this diameter is an overestimation. If we now consider that the number of generations above is representative of the root vessel upon entry to the cranium as it is to the smaller vasculature, we can see how an effective root vessel for the bigger vasculature could emerge. However, the branching will start with the root vessel, therefore, our effective

root vessel for the smaller vasculature must be a fraction of this estimation. We can solve this by assuming this initial estimation of effective root vessel diameter is applicable to the larger arteries such as those upon first entry to the cranium. If we take the ratio between a large cerebral artery and a small one, we can approximate the value of this ratio. We denote this root vessel ratio as ϱ and we assume it is in the range of 0.6-0.8 as based on the average value of an internal carotid artery and a small artery (Levick, 2010; Caro et al., 2012).

To test our choice on the number of generations, in §2.3.3 we investigate its interaction with the scaling factors γ and λ, the arterovenous ratio ν, and the ratio of the root vessel ϱ. In the next section we determine the bounds for the scaling factors γ and λ.

2.3.2 Scaling factors

To determine the values of the CSA scaling factor γ, and the length scaling factor λ, we analyse the bifurcating tree behaviour within the physical constraints of a finite volume.

Minimum and maximum bounds

Physically both scaling parameters have to be greater than zero and less than one. Less than one since the vessel length and CSA decrease with increasing generations. This gives the minimum and maximum boundaries

$$0 < \gamma, \lambda < 1. \tag{2.67}$$

The CSA of an individual vessel is limited by

$$2\gamma > 1, \tag{2.68}$$

since the velocity in generation n is observed to decrease as n increases which means that the net CSA in generation n must increase with every generation. This gives $\gamma > 1/2$ a new

minimum constraint.

Similarly, if the total surface area of the vasculature, defined as $\widehat{A}_n^s = (2\gamma^{1/2}\lambda)^n A_0^s$ in Equations (2.7) and (2.41), increases as the individual vessel surface area decreases, then the surface area scaling relationship must be greater than one,

$$2\gamma^{1/2}\lambda > 1, \tag{2.69}$$

which implies $\lambda > 1/(2\gamma^{1/2})$.

The total resistance of the vasculature, defined as $\widehat{R}_n^s = \xi^n R_0^s$ in Equations (2.21) and (2.51), increases as the vessel diameter decreases, meaning the resistance scaling relationship must be greater than one

$$\xi > 1, \tag{2.70}$$

which is consistent with Equations (2.24)–(2.28), (2.53)–(2.58).

The volume scaling between generations is defined as $\widehat{V}_n^s = (2\gamma\lambda)^n V_0$ as per Equations (2.9) and (2.43). It seems intuitive to assume the total volume grows with increasing generations since the total CSA grows. However the cerebral vasculature is within the boundaries of a finite volume, the skull. We could think of this cranial space as an ultimate constraint, however a better approach is to consider that the small vasculature must be close enough to the brain tissue for adequate perfusion. As a result, the space for the vasculature must become more and more restrictive as the vessels bifurcate. This makes sense since the smaller the vessels the closer they need to be to the tissue in order to facilitate diffusion and metabolic transport. This also makes sense from the perspective of the bounds already established. If the volume scaling were greater than one and we were to substitute the scaling in Equation (2.68) to this volume boundary, we would obtain that $\lambda > 1$ which would invalidate our assumption that length must decrease with increasing generations, i.e. Equation (2.67).

Therefore we assume the model obeys a volume scaling less than one,

$$2\gamma\lambda < 1, \tag{2.71}$$

resulting in $\lambda < 1/(2\gamma)$, which along with Equation (2.68) implies $1/2 < \gamma, \lambda < 1$.

Cohn's volume filling model

There is an additional volume consideration, this is described by Cohn in his volume filling theory (Cohn, 1954). Cohn states that in geometric bifurcations of blood vessels, these must occupy a given volume by filling the space efficiently. Assuming the volume of a cube, the cube can be split in half on each of its axes resulting in eight distinct cubes (Figure 2.6a). If we bisect the cube again, we would obtain eight cubes for every initial cube, i.e. 8^i where i is the number of splits. If we now assume a blood vessel located at the centre of the cube bifurcates with every split, we can deduce $l_{\text{vessel}} = 1/2^i$. To determine the scaling of this bifurcation to the root vessel l_0, Cohn estimates the length would halve in size every three splits, and so $l_{\text{vessel}} = l_0/2^{i/3}$.

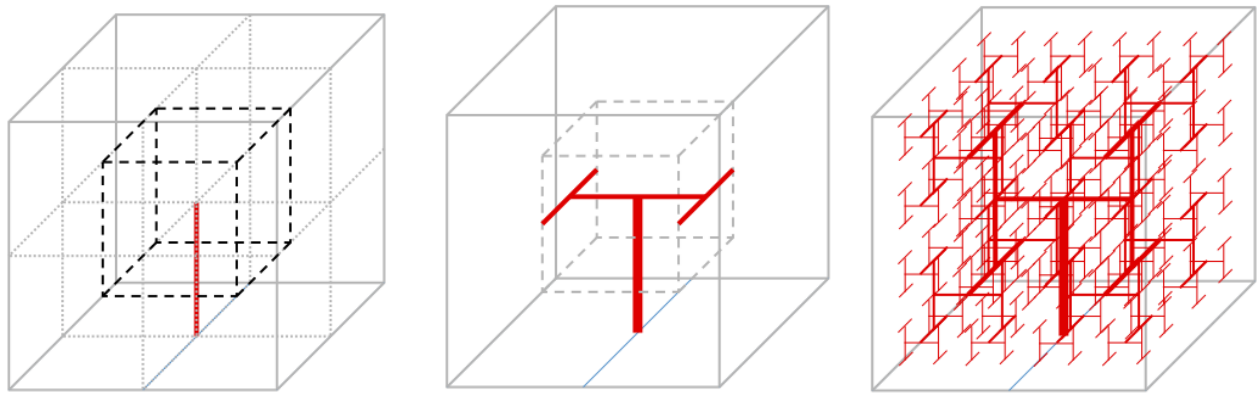

(a) **(b)** **(c)**

Figure 2.6: Cohn's model of space filling. (a) cube split in half on each plane forming eight symmetrical cubes with root vessel in centre of the main cube, (b) illustration of vessel bifurcating within a cube, (b) further bifurcations following centred bifurcations filling available space. Source: reproduced with permission from Prof Kim H Parker.

If we take this approach and assume Cohn's scaling for length as a minimum boundary in our

model, we obtain that

$$\lambda \geq \frac{1}{2^{1/3}}. \tag{2.72}$$

In the next subsection we assess the constraints for γ and λ together to form a region of acceptable values.

Region of acceptable values

The defined bounds for the scaling factors result in a reduced region where a suitable combination of values for γ and λ can be found. This region is shown in Figure 2.7 where we set λ as an independent variable of γ.

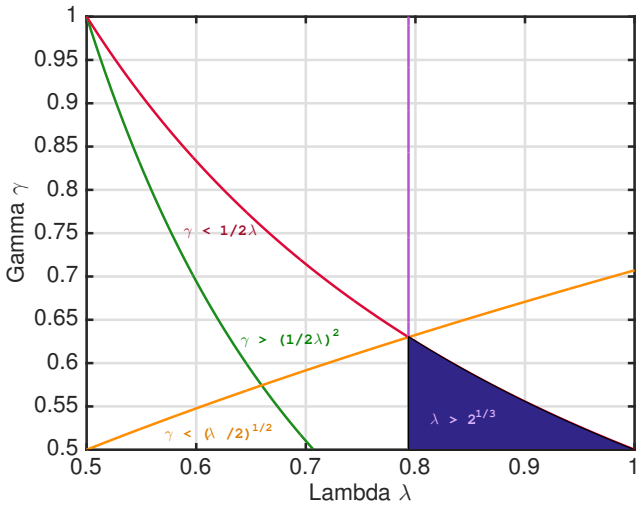

Figure 2.7: Region of acceptable values for γ and λ delimited within 0.5 and 1. Colour code: constraint for surface area ($2\gamma^{1/2}\lambda > 1$) is marked in green, the constraint for resistance ($\lambda/2\gamma^2 > 1$) in orange, the volume constraint ($\lambda/2\gamma^2 > 1$) in red, and Cohn's space filling constraint in magenta, which results in the shaded area in blue where combinations of γ and λ can be determined.

Delimited within 0.5 and 1, in this figure we see the constraint for surface area ($2\gamma^{1/2}\lambda > 1$) in green, the constraint for resistance ($\lambda/2\gamma^2 > 1$) in orange, the volume constraint ($\lambda/2\gamma^2 > 1$) in red, and Cohn's space filling constraint in magenta, which results in the shaded area in blue where combinations of γ and λ can be determined.

The choice of values for γ and λ is interconnected with the number of generations N, the

root vessel ratio ϱ, and the arterovenous ratio ν, meaning the change in one will affect the others. In the next section we analyse these parameters in combination and determine the set of acceptable values to use in our vascular model.

2.3.3 Interaction between ratios and scaling factors

To investigate the interaction between ratios and scaling factors and thus select an acceptable combination of values, we perform a numerical analysis between the ranges of these parameters as defined in the previous sections. A recap of the range of values for each parameter is given in Table 2.4.

	Value range
N	20 - 36
γ	0.5 - 0.64
λ	0.79 - 1
ν	1 - 3
ϱ	0.6 - 0.8

Table 2.4: Value range for ratios and scaling factors.

This results in a five-dimensional set of parameters. To estimate an appropriate set of combinations we set an acceptance criteria based on pressure values, since these are well documented in the literature. We select a pressure range of the smaller arteries between 20-40 mmHg, and a venous pressure range between 0-20 mmHg for a healthy recumbent subject.

We use Matlab 2015a with a series of nested loops and the equations described in sections §2.1-§2.2 with the parameter values in Table 2.2 and Table 2.3. We tested a total of 41,923 combinations using a step size of 1×10^{-3} and an accuracy of four significant figures.

Given the acceptable values, we select the combination of parameters in Table 2.5. We make an exception for the notation convention of significant figures since the model is highly sensitive to the scaling factors and ratios below, in particular regarding the CSA scaling factor γ.

We can now calculate the properties of the arterial and venous root vessels d_{a0}, d_{v0}, h_{a0}, h_{v0}, these are included in Table 2.6 together with the rest of the model parameters.

	Value
N	28
γ	0.5547
λ	0.805
ν	1.85
ϱ	0.75

Table 2.5: Ratios and scaling factors for the vascular model.

	Value	Units	Reference
d_{a0}	1.7×10^{-2}	m	§2.3.3.
d_{c}	6×10^{-6}	m	(Guyton, 2006).
d_{v0}	3.2×10^{-2}	m	§2.3.3.
E_{a}	9×10^{5}	$\mathrm{N/m^2}$	(Caro et al., 2012).
E_{v}	7×10^{4}	$\mathrm{N/m^2}$	(Caro et al., 2012).
γ	0.5547	–	§2.3.3
h_{a0}	1.7×10^{-3}	m	§2.3.3.
h_{v0}	8.6×10^{-4}	m	§2.3.3.
k_{a0}	1×10^{-21}	$\mathrm{m^2}$	§2.3.3.
k_{c}	1.9×10^{-11}	$\mathrm{Pa.s/m^3}$	§2.3.3.
k_{v0}	0.5×10^{-21}	$\mathrm{m^2}$	§2.3.3.
λ	0.805	–	§2.3.3.
l_{a0}	8.5×10^{-2}	m	§2.3.
l_{v0}	8.5×10^{-2}	m	§2.3.
μ_{blood}	3.5×10^{-3}	Pa.s	(Guyton, 2006).
μ_{csf}	7.3×10^{-4}	Pa.s	(Gupta et al., 2010).
N	28	–	§2.3.3
ν	1.85	–	§2.3.3
p_{root}	90	mmHg	(Guyton, 2006).
p_e	11	mmHg	(Steiner and Andrews, 2006).
Q	750	ml/min	(Linninger et al., 2009).
R_{c}	0.02	mmHg.min/ml	§2.3.
ϱ	0.75	–	§2.3.3

Table 2.6: Parameter values for vascular model.

2.4 Compliant case

In the previous section we considered rigid cylindrical vessels. We know this to be physiologically unrealistic since the blood vessels dilate and constrict with changes in pressure. In this section we address this issue by including a constitutive relation (§2.4.1) to describe the vessel distensibility to pressure changes relative to the rigid case (§2.4.2). We analyse the impact of this pressure-area relationship in the results section (§2.6) by comparing the stress-free state

(i.e. rigid case) and the complaint case.

The composition of blood vessels (in dry mass) consists of fibres and cells that have different degrees of elastic behaviour, these are: elastin, collagen, and smooth muscle. Elastin and smooth muscle are relatively compliant when compared to collagen, but the elasticity of smooth muscle depends upon its tone which is determined by many neural and hormonal factors and is difficult to control or to quantitate (Matsumoto and Nagayama, 2012). The small arteries are composed of 60% smooth muscle and the rest by roughly equal amounts of elastin and collagen. Typically the more peripheral the vessel the more smooth muscle is contained. The small veins have a similar composition with respect to elastin and collagen but to a smaller extent (0.3), they also contain less smooth muscle and are thinner than the arteries. Vessels in the brain are typically thinner than arteries of similar diameter in the rest of the body (Cipolla, 2009), as mentioned in Chapter 1.

The blood vessel walls exhibit a viscoelastic behaviour. This is important specially in larger arteries where they need to withstand relatively high pressures and the vessel wall needs to accommodate for the peaks and recoils that high and low pressures can cause with each cardiac cycle.

For simplicity, and given the fact that this model only considers the small vessels in the brain which fall within a physiological pressure range where viscoelastic effects are small (Tardy et al., 1991), we assume the blood vessel walls are linearly elastic. Also, although the vessels are unlikely to be homogeneous or isotropic, we make this assumption as a first approximation and assume incompressibility of a very thin vessel wall ($h_n = 0.1d_n$) where we relate the effects of stress and strain with an effective elastic modulus relative to an equilibrium state. This effective elastic modulus we assume remains constant within the boundaries of the smaller vasculature.

The pressure-area relationship presented here assumes there is no collapse of the cerebral vessels as it is applicable only to non-collapsible tubes. This is appropriate in our model since we work under the assumption that vessels in the brain do not tend to collapse. Under healthy conditions the cerebral blood vessels are in constant interaction with surrounding CSF which is

likely to prevent collapse. Any excess of CSF typically drains into the venous dural sinuses thus preventing vessel collapse from excessive CSF pressure on the vasculature, and any low pressure driving lower cerebral blood flow which could also lead to vessel collapse is compensated for by the cerebral autoregulation[6]. Furthermore, hydrostatic changes can induce negative pressure in the dural sinuses but not in the blood vessels due to the effect of the arachnoid villi and the cranium enclosure (Guyton, 2006), thus CSF (along with the ararchnoid villi) effectively function as safeguards for preventing intracranial vessel collapse[7].

2.4.1 Pressure-area relationship

For small deformations, of a stress-free state (i.e. reference case), where the stress-strain curve of a radially tensioned vessel can be considered linear, we find that Hooke's law can be applied (Fung, 2013)

$$\tau = E\epsilon \tag{2.73}$$

where τ is the wall tensile stress, E the elastic modulus, and ϵ the wall strain. We assume the blood vessels are axisymmetric and cylindrical (as mentioned in §2.2). We also assume the blood vessel wall is thin, homogeneous and isotropic with linearly elastic behaviour. We are interested in the circumferential stress departing from a reference state, we can apply Laplace's law relating transmural pressure to circumferential wall stress to Equation (2.73) to obtain

$$\frac{(p_i - p_e)d}{2h} = \frac{E}{1-\sigma^2}\frac{d-d_0}{d_0}, \tag{2.74}$$

where $p_i - p_e$ is the transmural pressure, p_i the pressure inside the vessel (luminal presure), p_e the pressure outside the vessel (external pressure), d the luminal diameter of the vessel, d_0 the luminal diameter of the vessel of the stress-free state (i.e. $p_i = p_e$), h the vessel wall thickness, and σ the Poisson's ratio. The term (1-σ^2) is included to account for the Poisson effect on the wall as it is strained. Assuming the vessel wall is incompressible, i.e. $\sigma = 0.5$, and that $1/d$ can

[6]We address autoregulation for this model in §2.5.

[7]We assess effect of the arachnoid villi and hydrostatic changes in Chapters 3 and 4, respectively.

be approximated by $1/d_0$ (Alastruey et al., 2011), we solve Equation (2.74) for the transmural pressure

$$\begin{aligned} p_i - p_e &= \frac{4\sqrt{\pi}Eh}{3A_0}\left(\sqrt{A} - \sqrt{A_0}\right), \\ &= \frac{\beta}{A_0}\left(\sqrt{A} - \sqrt{A_0}\right), \end{aligned} \tag{2.75}$$

where $\beta = 4\sqrt{\pi}Eh/3$ is a term describing the elastic behaviour of the vessel, $A = \pi d^2/4$ the deformed CSA, and $A_0 = \pi d_0^2/4$ the CSA of the stress-free state.

2.4.2 Changes due to wall compliance

Arteries

We introduce calligraphic letters to distinguish compliant from rigid parameters, i.e. $\mathscr{A}$, $\mathscr{V}$, $\mathscr{S}$, $\mathscr{P}$ denote compliant area, volume, transmural flux and pressure, respectively. Rewriting Equation (2.75) in this notation,

$$\mathscr{P}_{\mathrm{an}}^{\mathrm{trans}} = \frac{\beta_{an}}{A_{\mathrm{an}}^{x}}\left(\sqrt{\mathscr{A}_{\mathrm{an}}^{x}} - \sqrt{A_{\mathrm{an}}^{x}}\right), \tag{2.76}$$

where $\beta_{an} = 4/3\sqrt{\pi}E_{\mathrm{a}}h_{an}$ is a constant term describing the elastic behaviour of the arterial wall, $\mathscr{P}_{an}^{\mathrm{trans}} = \mathscr{P}_{\mathrm{an}}^{\mathrm{ave}} - \mathscr{P}_e$ is the compliant transmural pressure in the n^{th} arterial generation, and $\mathscr{P}_{An}^{\mathrm{ave}} = (\mathscr{P}_{An}^{\mathrm{in}} + \mathscr{P}_{An}^{\mathrm{out}})/2$ is the compliant average pressure in the n^{th} arterial generation.

Solving for the compliant arterial CSA we obtain,

$$\mathscr{A}_{\mathrm{an}}^{x} = A_{\mathrm{an}}^{x}\left(1 + \frac{\mathscr{P}_{an}^{\mathrm{trans}}\sqrt{A_{\mathrm{an}}^{x}}}{\beta_{an}}\right)^2. \tag{2.77}$$

Expanding β_{an}, $\sqrt{A^x_{an}}$, and substituting of $h_{\mathrm{a}0} = 0.1\ d_{\mathrm{a}0}$ reduces Equation (2.77) to

$$\begin{aligned}\mathscr{A}^x_{an} &= A^x_{an}\left(1 + \frac{15\mathscr{P}^{\mathrm{trans}}_{an}}{4E_{\mathrm{a}}}\right)^2 \\ &= A^x_{an}\left(1+\phi_{an}\right)^2, \end{aligned} \tag{2.78}$$

where $\phi_{an} = 15\mathscr{P}^{\mathrm{trans}}_{an}/4E_{\mathrm{a}}$ is the transmural pressure to elastic modulus ratio. Equation (2.78) implies that changes in CSA from the reference[8] are only dependent on the changes in transmural pressure and elastic modulus.

One of the assumptions in deriving the pressure-area relationship included the vessel tethering in the axial direction with changes in cross-section large compared to longitudinal ones, meaning the compliant length is assumed to be constant. We also assume the parameters of the root vessel are the same for both rigid and compliant case.

We can now derive the rest of the parameters,

$$\widehat{\mathscr{A}^x_{an}} = \widehat{A}^x_{an}(1+\phi_{an})^2, \tag{2.79}$$

$$\mathscr{A}^s_{an} = A^s_{an}(1+\phi_{an}), \tag{2.80}$$

$$\widehat{\mathscr{A}^s_{an}} = \widehat{A}^s_{an}(1+\phi_{an}), \tag{2.81}$$

$$\mathscr{V}_{an} = V_{an}(1+\phi_{an})^2, \tag{2.82}$$

$$\widehat{\mathscr{V}}_{an} = \widehat{V}_{an}(1+\phi_{an})^2, \tag{2.83}$$

$$\mathscr{S}_{an} = \frac{k_{\mathrm{a}}A^s_{an}}{\mu_{\mathrm{csf}}h_{an}}\mathscr{P}^{\mathrm{trans}}_{an}(1+\phi_{an}), \tag{2.84}$$

$$\widehat{\mathscr{S}}_{an} = \frac{k_{\mathrm{a}}\widehat{A}^s_{an}}{\mu_{\mathrm{csf}}h_{an}}\mathscr{P}^{\mathrm{trans}}_{an}(1+\phi_{an}). \tag{2.85}$$

The compliant resistance is given by $\widehat{\mathscr{R}}_{an} = 8\pi\mu_b l_{an}/(\widehat{\mathscr{A}^x_{an}})^2$, which when linearised (to reduce the fourth power relation for the compliant CSA) reduces to

$$\widehat{\mathscr{R}}_{an} = \widehat{R}_{an}\left(1 - 4\phi_{an}\right), \tag{2.86}$$

[8]N.B. The calculations for the rigid case are done to provide a reference for what would be observed if we constrained the model to its unstressed reference values.

with error of order $\mathscr{O}(15\Delta p_{\mathrm{a}}^{\mathrm{trans}}/4E_{\mathrm{a}})$.

The compliant pressure difference in the n^{th} arterial generation of the compliant case is

$$\mathscr{P}_{an}^{\mathrm{in}} - \mathscr{P}_{an}^{\mathrm{out}} = \widehat{R}_{an} Q \left(1 - 4\phi_{an}\right). \tag{2.87}$$

We assume $\mathscr{P}_{\mathrm{a}0}^{\mathrm{in}} = p_{\mathrm{a}0}^{\mathrm{in}} = p_{\mathrm{root}}$, and that the compliant pressure for a given generation follows $\mathscr{P}_{an+1}^{\mathrm{out}} = \mathscr{P}_{an}^{\mathrm{in}}$. Expanding ϕ_{an} in Equation (2.87) and letting $\psi_{an} = 15R_{an}Q$ we find that for $n = 0, 1, 2, \cdots, N-1$,

$$\begin{aligned}
-\mathscr{P}_{\mathrm{a}0}^{\mathrm{out}} + \psi_{\mathrm{a}0}\mathscr{P}_{\mathrm{a}0}^{\mathrm{ave}} &= -p_{\mathrm{root}} + \widehat{R}_{\mathrm{a}0} Q \left(1 - 15\mathscr{P}_e\right), \\
\mathscr{P}_{\mathrm{a}1}^{\mathrm{in}} - \mathscr{P}_{\mathrm{a}1}^{\mathrm{out}} + \psi_{\mathrm{a}1}\mathscr{P}_{\mathrm{a}1}^{\mathrm{ave}} &= \widehat{R}_{\mathrm{a}1} Q \left(1 - 15\mathscr{P}_e\right), \\
&\vdots \\
\mathscr{P}_{\mathrm{a}N-1}^{\mathrm{in}} - \mathscr{P}_{\mathrm{a}N-1}^{\mathrm{out}} + \psi_{\mathrm{a}N-1}\mathscr{P}_{\mathrm{a}N-1}^{\mathrm{ave}} &= \widehat{R}_{\mathrm{a}N-1} Q \left(1 - 15\mathscr{P}_e\right).
\end{aligned} \tag{2.88}$$

We can then find the compliant pressures on each generation by solving Equation (2.104), which in matrix form can be written as

$$\mathbf{A}\mathbf{p}_{\mathrm{a}} = \mathbf{a}, \tag{2.89}$$

where $\mathbf{A}$ is the coefficient matrix of the compliant arteries, $\mathbf{p}_{\mathrm{a}}$ the vector of pressures, and $\mathbf{a}$ is a vector of constants resulting from the rigid case and the compliant external pressure. Full matrix details can be found in Appendix A.2.

Capillaries

The capillary pressures in the compliant case are defined by

$$\mathscr{P}_{\mathrm{c}}^{\mathrm{in}} = \mathscr{P}_{\mathrm{a}N-1}^{\mathrm{out}}, \tag{2.90}$$

$$\mathscr{P}_{\mathrm{c}}^{\mathrm{in}} - \mathscr{P}_{\mathrm{c}}^{\mathrm{out}} = R_{\mathrm{c}} Q, \tag{2.91}$$

$$\mathscr{P}_{\mathrm{c}}^{\mathrm{out}} = \mathscr{P}_{\mathrm{v}N-1}^{\mathrm{in}}, \tag{2.92}$$

$$\widehat{\mathscr{S}_{\mathrm{c}}} = k_{\mathrm{c}} \left(\mathscr{P}_{\mathrm{c}}^{\mathrm{ave}} - \mathscr{P}_{e} \right), \tag{2.93}$$

where the capillary resistance and the capillary permeability are the same as in the rigid case.

Veins

We apply the same considerations to the veins as we do for the arteries, and obtain the following relationships,

$$\mathscr{A}_{\mathrm{v}n}^{x} = \widehat{A}_{\mathrm{v}n}^{x}(1+\phi_{\mathrm{v}n})^2, \tag{2.94}$$

$$\widehat{\mathscr{A}_{\mathrm{v}n}^{x}} = \widehat{A}_{\mathrm{v}n}^{x}(1+\phi_{\mathrm{v}n})^2, \tag{2.95}$$

$$\mathscr{A}_{\mathrm{v}n}^{s} = A_{\mathrm{v}n}^{s}(1+\phi_{\mathrm{v}n}), \tag{2.96}$$

$$\widehat{\mathscr{A}_{\mathrm{v}n}^{s}} = \widehat{A}_{\mathrm{v}n}^{s}(1+\phi_{\mathrm{v}n}), \tag{2.97}$$

$$\mathscr{V}_{\mathrm{v}n} = V_{\mathrm{v}n}(1+\phi_{\mathrm{v}n})^2, \tag{2.98}$$

$$\widehat{\mathscr{V}}_{\mathrm{v}n} = \widehat{V}_{\mathrm{v}n}(1+\phi_{\mathrm{v}n})^2, \tag{2.99}$$

$$\mathscr{S}_{\mathrm{v}n} = \frac{k_{\mathrm{v}} A_{\mathrm{v}n}^{s}}{\mu_{\mathrm{csf}} h_{\mathrm{v}n}} \mathscr{P}_{\mathrm{v}n}^{\mathrm{trans}}(1+\phi_{\mathrm{v}n}), \tag{2.100}$$

$$\widehat{\mathscr{S}_{\mathrm{v}n}} = \frac{k_{\mathrm{v}} \widehat{A}_{\mathrm{v}n}^{s}}{\mu_{\mathrm{csf}} h_{\mathrm{v}n}} \mathscr{P}_{\mathrm{v}n}^{\mathrm{trans}}(1+\phi_{\mathrm{v}n}), \tag{2.101}$$

$$\widehat{\mathscr{R}}_{\mathrm{v}n} = \widehat{R}_{\mathrm{v}n} \left(1 - 4\phi_{\mathrm{v}n}\right), \tag{2.102}$$

$$\mathscr{P}_{\mathrm{v}n}^{\mathrm{in}} - \mathscr{P}_{\mathrm{v}n}^{\mathrm{out}} = \widehat{R}_{\mathrm{v}n} Q \left(1 - 4\phi_{\mathrm{v}n}\right). \tag{2.103}$$

where $\phi_{\mathrm{v}n} = (15\mathscr{P}_{\mathrm{v}}^{\mathrm{trans}}/4E_{\mathrm{v}})^2$.

We assume $\mathscr{P}_{\mathrm{v}N-1}^{\mathrm{in}} = \mathscr{P}_{\mathrm{c}}^{\mathrm{out}}$, and that the compliant pressure for a given generation follows $\mathscr{P}_{\mathrm{v}n}^{\mathrm{out}} = \mathscr{P}_{\mathrm{v}n-1}^{\mathrm{in}}$. Expanding $\phi_{\mathrm{v}n}$ in Equation (2.103) and letting $\psi_{\mathrm{v}n} = 15R_{\mathrm{v}n}Q$ we construct the converging venous tree by setting $n = N - i$ where $i = 1, 2, \cdots, N$.

$$\begin{aligned}
-\mathscr{P}_{\mathrm{v}N-1}^{\mathrm{out}} + \psi_{\mathrm{v}N-1}\mathscr{P}_{\mathrm{v}N-1}^{\mathrm{ave}} &= -\mathscr{P}_{\mathrm{c}}^{\mathrm{out}} + \widehat{R}_{\mathrm{v}N-1}Q\left(1 - 15\mathscr{P}_e\right), \\
\mathscr{P}_{\mathrm{v}N-2}^{\mathrm{in}} - \mathscr{P}_{\mathrm{v}N-2}^{\mathrm{out}} + \psi_{\mathrm{v}N-2}\mathscr{P}_{\mathrm{v}N-2}^{\mathrm{ave}} &= \widehat{R}_{\mathrm{v}N-2}Q\left(1 - 15\mathscr{P}_e\right), \\
&\vdots \\
\mathscr{P}_{\mathrm{v}0}^{\mathrm{in}} - \mathscr{P}_{\mathrm{v}0}^{\mathrm{out}} + \psi_{\mathrm{v}0}\mathscr{P}_{\mathrm{v}0}^{\mathrm{ave}} &= R_{\mathrm{v}0}Q\left(1 - 15\mathscr{P}_e\right).
\end{aligned} \tag{2.104}$$

We solve for the compliant pressures vector $\mathbf{p}_{\mathrm{v}}$,

$$\mathbf{V}\mathbf{p}_{\mathrm{v}} = \mathbf{v}, \tag{2.105}$$

where $\mathbf{V}$ is the venous coefficient matrix, and $\mathbf{v}$ is the venous vector of constants resulted from the reference case and the compliant external pressure. Full matrix details can be found in Appendix A.3.

2.5 Cerebral autoregulation

The brain is very sensitive to a shortage of oxygen and nutrients and must therefore maintain uninterrupted blood supply in a regular and uniform manner. Acute changes in arterial blood pressure, low or high concentrations of oxygen, carbon dioxide, nitric oxide, sudden changes in temperature and muscle activation can all cause vessel dilation or constriction (Panerai, 2008). The cerebral circulation has developed anatomical and physiological adaptations to ensure uninterrupted blood delivery to the brain. Anatomically, examples include the circle of Willis which allows for collateral flow in the case of one connecting vessel becoming obstructed, and the large surface area of the microcirculation[9] that ensures oxygen and nutrients are delivered

[9] Approximately 100 cm2/g of tissue (Pardridge, 2012).

within a relative short distance to the brain tissue. Physiologically, the vessels dilate and constrict to changes in pressure and metabolic demand.

Autoregulatory mechanisms maintain relatively constant blood flow despite pressure changes, typically in the range of 60-160mmHg (Levick, 2010). In addition to metabolic and myogenic factors, the cerebral circulation is also controlled by the sympathetic nervous system. The latter can constrict large and medium size arteries during heavy exercise to prevent high pressure reaching the microcirculation, although to a lesser extent as this can be overruled by the autoregulatory mechanisms (Guyton, 2006). These mechanisms are triggered within 4 seconds or less of increased arterial pressure (Aaslid et al., 1989). In cases where changes in pressure are prolonged (chronic), long-term regulation adapts to a wider range of pressure (e.g. 50-250mmHg) without significantly impacting blood flow. An effect of this includes increased or decreased vascularity relative to tissue demand.

Cerebral autoregulation in humans was first described by Lassen (1959) in a review of studies conducted on cerebral blood flow[10] (Lassen, 1959, 1964). In his review, Lassen found that extreme levels of cerebral hypotension, such as less than half the baseline mean arterial blood pressure would cause critically low cerebral blood flow (CBF) which could lead to hypoxia (Figure 2.8a). Hypertension on the other hand, did not cause a further increase in CBF in the studies. He concluded that CBF was independent of changes in mean arterial blood pressure and that only at very low pressure levels would CBF be compromised. Subsequent studies found that an increase in pressure over 150 mmHg (above the limit studied by Lassen) was indeed detrimental for CBF where it could increase to twice its baseline (Figure 2.8b).

Current cerebral autoregulation curves deviate from Lassen's constant cerebral blood flow at high pressures. In Figure 2.8b, Guyton presents an updated version of Lassen's curve where it can be seen that in acute autoregulation CBF increases mildly between 50 mmHg and approximately 180 mmHg after which CBF becomes critically high, in long-term autoregulation CBF does not significantly exceed these values.

Modelling efforts in autoregulation typically involve changes in cerebral blood flow to induced

[10] Autoregulation in animals had been studied by Fog two decades earlier (Fog, 1938).

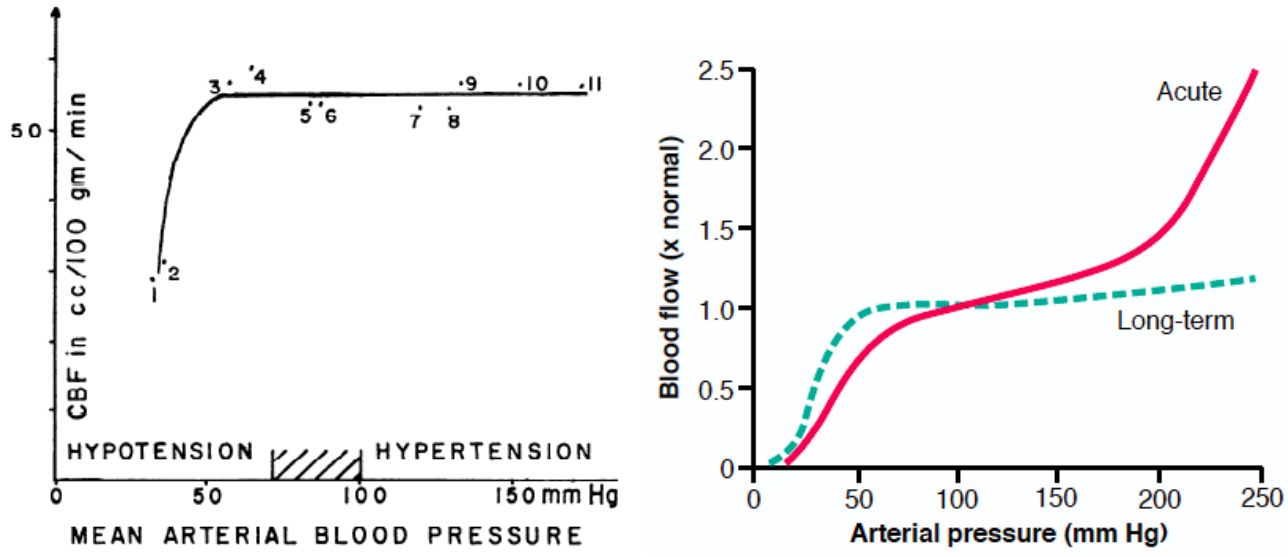

Figure 2.8: Cerebral autoregulation curves. (a) Lassen autoregulation curve on the review of 11 studies on cerebral blood flow and changes with mean arterial pressure, source: Cerebral blood flow and oxygen consumption (Lassen, 1959). (b) Guyton autoregulation curve, updated version of Lassen curve (Guyton, 2006).

metabolic conditions e.g. arterial reactivity to CO_2 where the vascular resistance is calculated and analysed in conjunction with what is known as static and dynamic autoregulation where several key patterns have emerged (i.e. autoregulation index) for assessing the level of autoregulation in a given subject.

The exact mechanism of cerebral autoregulation is complex and we do not attempt to investigate it as part of this work. Instead, we focus on the effects autoregulation has on the vessels directly and what this means for the rest of the cerebrovasculature.

2.5.1 Autoregulation function

Irrespective of the specific mechanisms driving autoregulation, it seems clear that from the fluid mechanical point of view that the resulting effect is the expansion and contraction of the blood vessels to promptly accommodate abrupt changes in pressure, to avoid disruption of the smaller vessels and microcirculation.

If the vascular resistance is the key parameter in autoregulation, it seems appropriate to analyse

further the effect of the resistance scaling ξ to changes in pressure. In §2.2 we defined $\xi^n = (\lambda/2\gamma^2)^n$ as this is the resistance scaling of the n^{th} generation. However we assumed in §2.4 that changes in the length of a vessel are negligible compared to changes in its diameter, we can then deduce that the changes due to autoregulation in our model must be solely expressed by changes in γ.

To define the autoregulation function, we analyse the behaviour of γ at different input pressures, $d\gamma/dp_{\text{root}}$. By setting the acceptance criteria based on the output pressure of the small high resistance arteries, capillaries and venules, it is possible to find the acceptable values of γ and thus we can analyse the behaviour γ has when changing p_{root}.

We use the same acceptance criteria set for the combination matrix in §2.3.3 with the following differences: we keep all other scaling and factor parameters fixed (i.e. we use the values for λ, ν and ϱ as in Table 2.6); and we now extend this criteria to the compliant case as well. We run the code with input pressure p_{root} equal to 40 to 200 mmHg in steps of 5 mmHg and record the values of suitable γ for which the pressures are within the acceptance criteria. Where more than one value of γ is found, an average is taken for that inlet pressure. The results are shown in Figure 2.9, where we observe the acceptable value of γ decreases as the input pressure increases. This is reasonable since the CSA will be more restrictive at greater pressures.

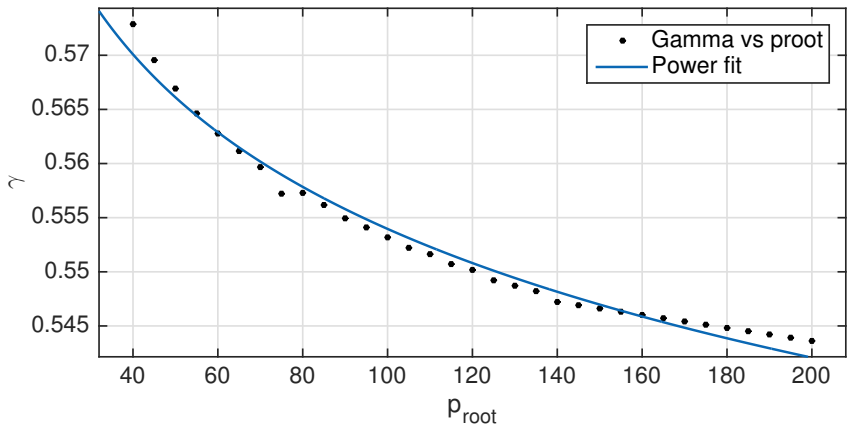

Figure 2.9: Changes in cross-sectional area scaling factor γ with respect to input pressure p_{root}.

Suitable values for γ beyond 145 mmHg were not found directly and an extrapolation had to be performed from the previous pressures. It can be seen in Figure 2.9 that even without

those points the behaviour of γ with respect of p_{root} closely resembles a power fit. We therefore approximate the behaviour of γ with a power function,

$$\gamma = a p_{\text{root}}^{b}, \tag{2.106}$$

where the coefficients are $a = 0.6399$ mmHg^{-1} and $b = -0.03131$. The model is highly sensitive to changes in γ and the use of large number of significant figures is preferable.

In Figure 2.10 we observe the behaviour of the pressures throughout the vasculature with this autoregulation function when run for a range of input pressures (Figure 2.10a), and the behaviour of the CSA in (Figure 2.10b). Whilst this is a first approximation, we can observe the effect of the autoregulation function for a range of input pressures in Figure 2.10a and the effect in cross-sectional area in Figure 2.10b.

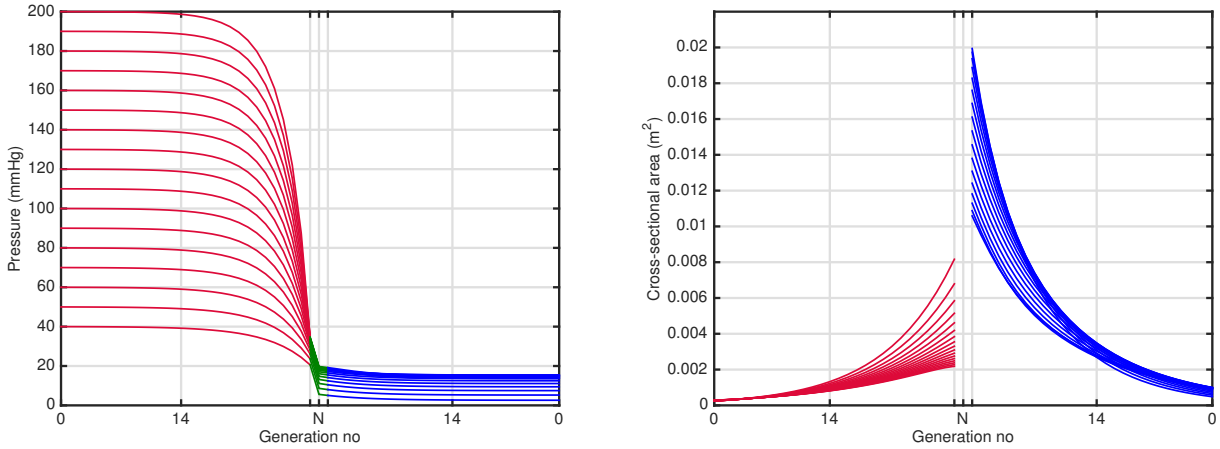

(a) **(b)**

Figure 2.10: Autoregulation function on, (a) pressure across the cerebral vasculature (b) CSA across the vasculature. Here we see the arterial tree represented in red from generation 0 to generation $N-1$, the capillaries in green (for the pressures only) in generation N, and the venous tree in blue from generation $N-1$ to generation 0.

We see that the functional consequences of the highly complex mechanism of cerebral autoregulation can be modelled reasonably well in our model by assuming that the area scaling parameter γ is a function of p_{root}.

In the next section (§2.6) we see the full set of results of the model for both rigid and compliant cases, and we test the changes in different parameters on the model in §2.7. We discuss the

significance of these results §2.8.

2.6 Results

We present the results for the rigid and compliant case for CSA, surface area, volume, resistance, pressure through the small vasculature, transmural pressure, and transmural flux. The figures describe the rigid case on the left and the compliant case on the right. The net value for each generation is presented from the arterial generation 0 to generation $N-1$, and for the venous generation $N-1$ to generation 0. In the case of resistance and pressure, we also add a data point for the capillaries in generation N. This is consistant with the equations introduced in §2.3–§2.4.

We use the boundary conditions for cerebral blood flow $Q = 750$ ml/min, arterial input pressure $p_{\text{root}} = 90$ mmHg, and external pressure $p_e = 11$ mmHg. We use these and the rest of the parameter values in Table 2.6. We give a brief description of the results in this section and discuss them further in §2.8.

Cross-sectional area and transmural pressure

In Figure 2.11 we observe the net CSA increases with increasing generations, as we expect due to the scaling boundaries introduced in §2.3.3. We notice that the net CSA for each generation does not change significantly for the arteries, whilst in the veins it does, particularly for the innermost generation $(N-1)$, i.e. smallest venules. Here we are assuming that the input pressure is constant, we explore the effect of changing the input pressure in the next section (§2.7).

The pronounced changes on the venous side (21% larger for the compliant terminal venule than for the rigid case) is due to the smaller transmural pressure to elasticity ratio, $\phi_{\text{v}n}$, which we introduced in §2.4. From Equation (2.95) we can deduce that even if the veins have a smaller transmural pressure than the arteries, the elastic modulus is one order of magnitude smaller

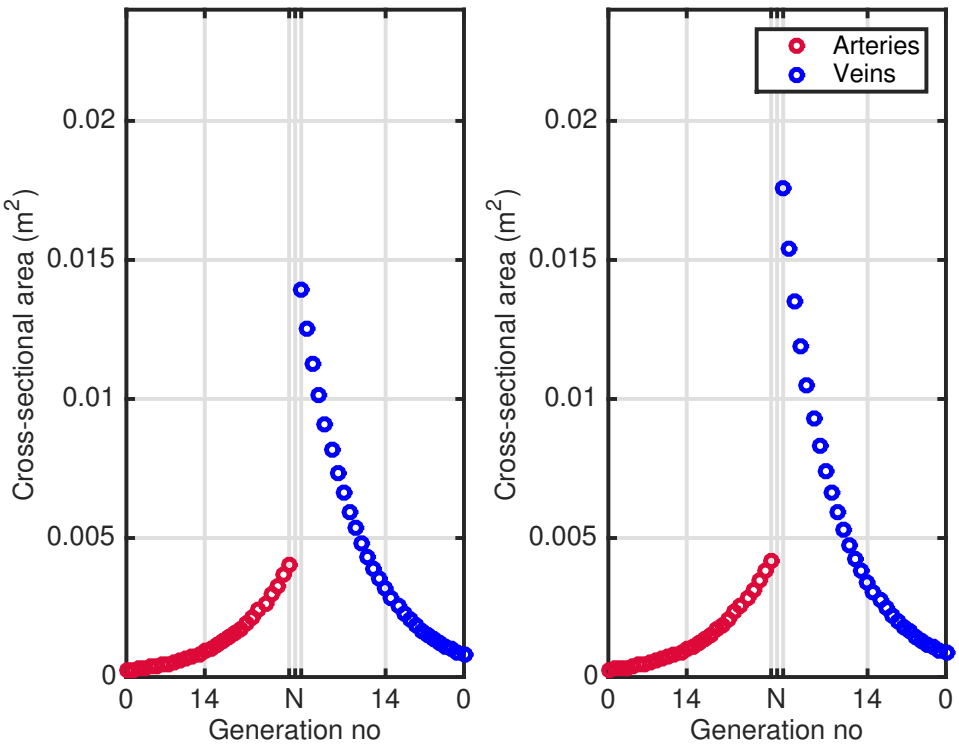

Figure 2.11: Total cross-sectional area per generation for the rigid case (left), and the compliant case (right).

than the arterial one, thus ϕ_{vn} will be sufficiently big thus allowing the veins with the smallest transmural pressure to increase the most.

In Figure 2.12 we observe that the venous transmural pressure is smaller than 10 mmHg for all generations, whilst that of the arteries is $\approx$ 60 mmHg in total. Between generations the arterial transmural pressure can be up to a maximum of 15 mmHg (in the case of generation $N-1$), however, the arterial elastic modulus is still greater which results in $\phi_{\text{vn}} > \phi_{an}$. Taking generation $N-1$ for the arterial and venous case, we find that $\mathscr{P}_{vn}^{\text{trans}}/E_{\text{v}} \approx 10^{-1}\mathscr{P}_{an}^{\text{trans}}/E_{\text{a}}$.

The fact that the transmural pressure is negative in the rigid case makes no difference in the rigid CSA since this is solely defined by the scaling law.

Assuming the high resistance arteries are found between generation 14 and generation $N-1$, we find that their CSAs are between 1×10^{-3} and 4×10^{-3} m^2 for both rigid and compliant cases. This is in agreement with values reported in literature where a range of 7×10^{-3} to 1.3×10^{-3} m^2 has been reported (Levick, 2010; Guyton, 2006; Caro et al., 2012).

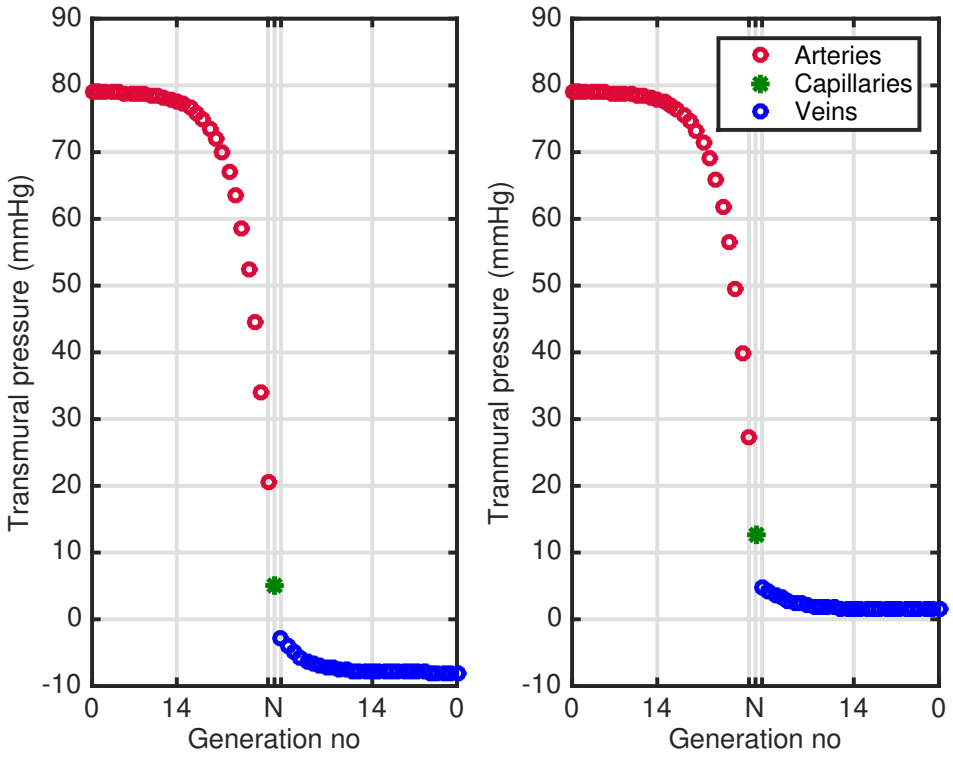

Figure 2.12: Net transmural pressure per generation for the rigid case (left), and the compliant case (right).

Taking the same approach on the venous tree and assuming the venules are found between generation $N-1$ and generation 14, we find that their CSAs are between 3.5×10^{-3} and 1.4×10^{-3} m^2 for the rigid case, and between 1.8×10^{-2} and 3.8×10^{-3} m^2 for the compliant case. This is also in agreement with values reported in the literature where a range of 1.2×10^{-3} to 5.7×10^{-2} m^2 has been reported (Levick, 2010; Guyton, 2006; Caro et al., 2012).

Regarding the transmural pressure, as we keep a constant external pressure, the transmural pressure curve is simply the vascular pressure minus the external pressure. We evaluate the vascular pressure in detail later on this section.

Surface area

In Figure 2.13 we observe an increase in total surface area from generation 0 to generation $N-1$ for both arteries and veins, also as expected from the scaling law. Since the surface area is related to the CSA, we see a similar behaviour between arteries and veins. We again

see a more pronounced change in the small venules for the compliant case (an increase of 0.148 m^2 in generation $N-1$) due to the implications of the pressure-area relationship previously mentioned.

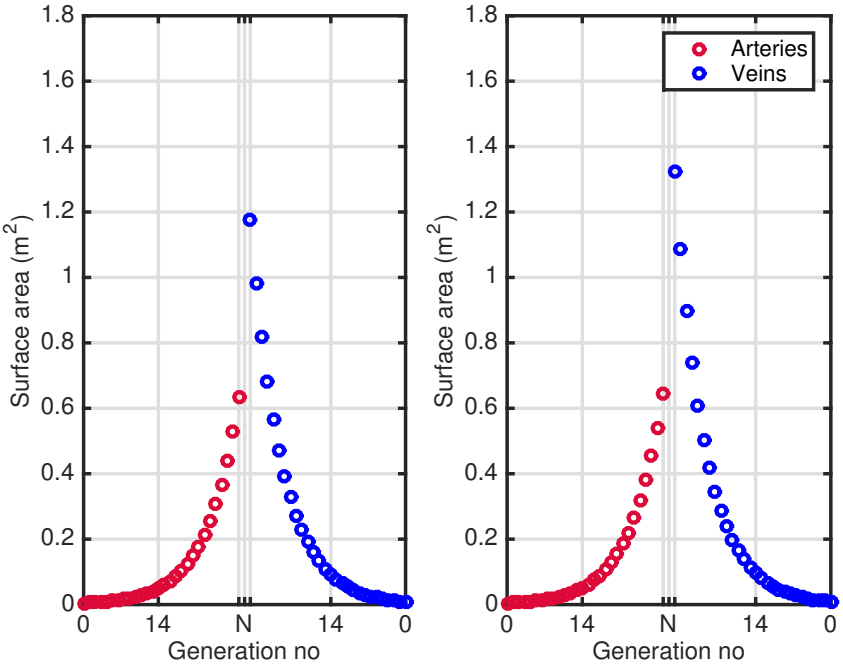

Figure 2.13: Total surface area per generation for the rigid case (left), and the compliant case (right).

Vascular surface area is typically measured in the microvascular region and when reacting to certain metabolic agents (Pardridge, 2012; Rosen et al., 1991). Limitations of these measurements include the extrapolation of a given area (typically in grey or white matter) to the entire brain, the consideration of blood vessels only within the brain tissue when blood vessels are found elsewhere in the cranium, or when measurements are made under certain pathological conditions e.g. vascular surface area of a brain tumour.

To compare our results, we calculate first the estimated surface area of an individual small artery and vein, and then scale to the total surface area with an approximate number of vessels in the small vasculature. According to Levick (2010)[11], the estimated number of blood vessels in the small arteries and high resistance arteries is around 1,380,000 whilst that in the small veins and venules is between 180,000-2,100,000 (Levick, 2010; Guyton, 2006). This gives a value

[11] Although this is an estimate taken from an animal model (dog mesentary), we take this data as a rough estimate until more accurate measurements emerge.

of 0.16–0.69 m^2 for the total surface area of the small arteries and high resistance arteries, and 0.04–2.2 m^2 for the total surface area of the small veins and venules. We observe that in both cases our results are within this range.

Volume

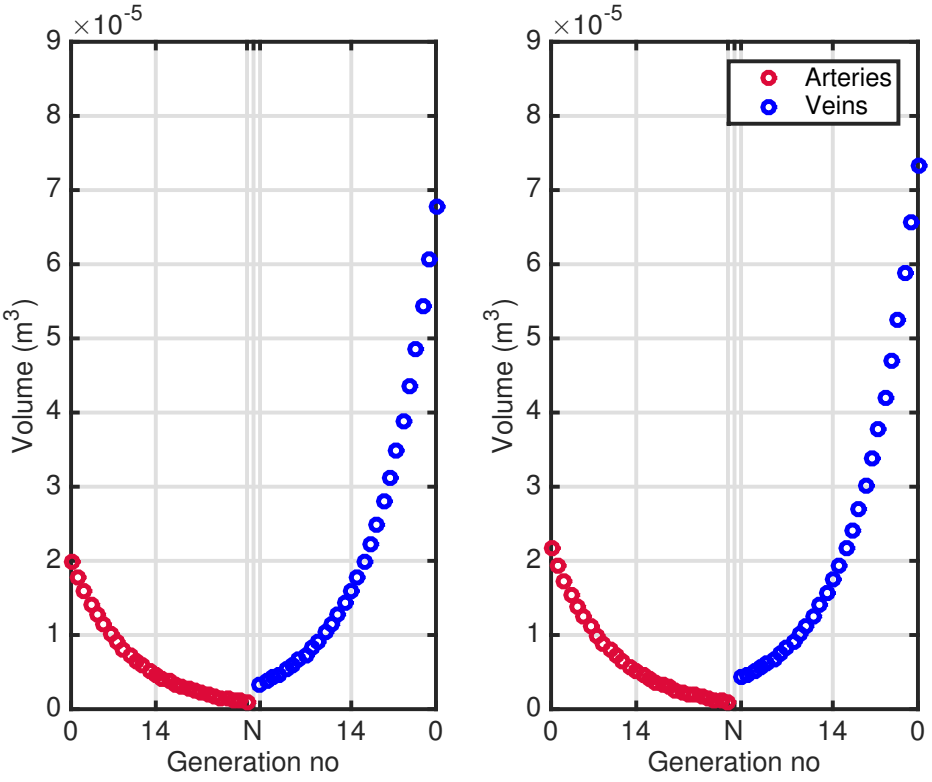

Figure 2.14: Net volume per generation for the rigid case (left), and the compliant case (right).

In Figure 2.14 we observe that the generational volume decreases with increasing generation number, again as expected given the set of bounds we see the decrease in volume with increasing generations. In the compliant case we also notice a mild increase in both arteries and veins from the rigid case, with a more pronounced increase on the veins ($0.54 \times 10^{-5} m^3$) than the arteries ($0.18 \times 10^{-5} m^3$). This is a milder response than in the CSA which can only be attributed to the normalising effect the length has on the volume.

To compare our results we take the same approach as in the surface area to obtain a range of 1.1×10^{-7}–$1.4 \times 10^{-5} m^3$ for the smallest arteries and high resistance arteries, and a range of

1.7×10^{-7}–1.6×10^{-4}m^3. We see the venous tree results are well within this range, and so are the arterial tree with a mildly larger volume for the arterial root vessel ($+0.77 \times 10^{-5}$m^3).

Resistance

In Figure 2.15 we see the generational resistance in the arteries is significantly greater than their venous counterpart (over one order of magnitude) in both the rigid and compliant cases. The compliant arterial resistance is mildly reduced from the rigid case (0.09×10^8 Pa.s/m^3), while in the veins the decrease in resistance is more pronounced (0.53×10^7 Pa.s/m^3). We also observe that the introduced constant capillary resistance is very close to the last arterial generation ($N-1$). This is physiologically desirable since it is commonly accepted that the majority of the vascular resistance occurs on the small high resistance arteries and capillaries.

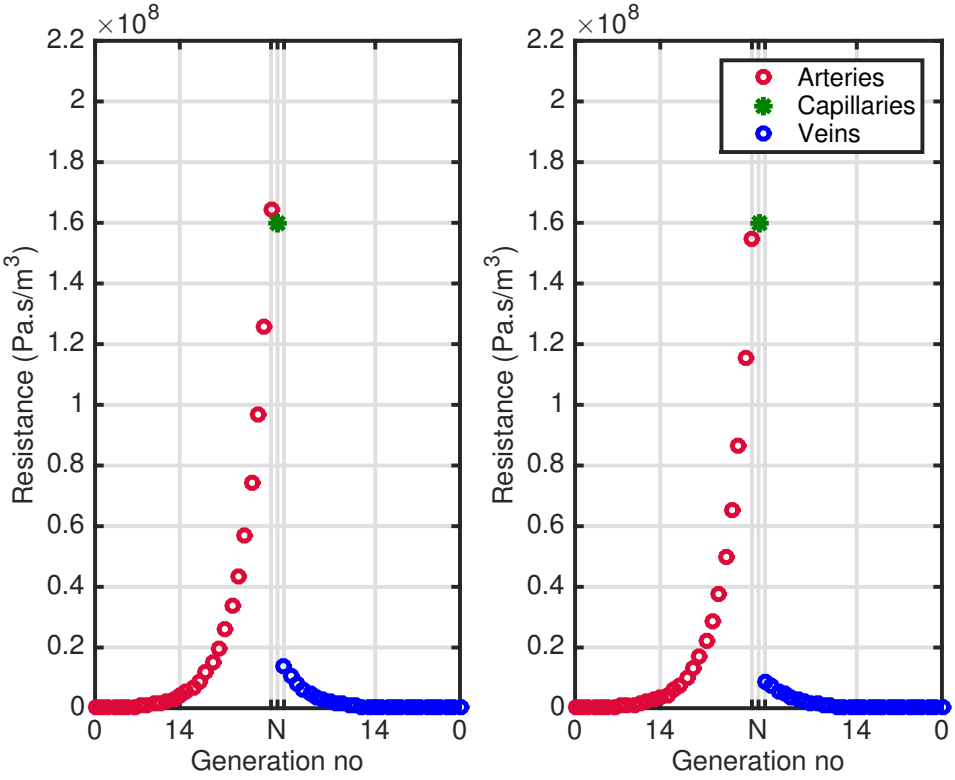

Figure 2.15: Total resistance per generation for the rigid case (left), and the compliant case (right).

Values for vascular resistance in the brain are reported with respect to the resistance to outflow (Czosnyka et al., 2012). This is not comparable to this vascular model as the outflow in the

brain relates to that on the venous dural sinuses, which we introduce in the intracranial model (Chapter 3). In this vascular model we are interested in the smaller vasculature.

Pressure in the vasculature has a pronounced drop across the small arteries and high resistance arteries. In the brain, in addition to the smooth muscle activation there are metabolic influences that guide the arterial wall to dilate or contract according to local tissue demand. Since vascular resistance is related to the fourth power of the radius (in laminar flow by Hagen–Poiseuille), we can expect that a decrease in radius will result in a significantly increased resistance.

Given the pressure drop between arteries and high resistance arteries in the rest of the body, which is comparable to that in the brain, and knowing the cerebral blood flow, we can estimate that for the last arterial generation $N-1$, this would be in the range of 1.3×10^{-2} to 2.7×10^{-2} mmHg.min/ml (1.1×10^{8}–2.1×10^{8} Pa.s/m^3), which is what we find. For the veins the pressure drop is very small and thus we find the resistance in generation $N-1$ very small (1×10^{-3} to 2×10^{-3} mmHg.min/ml) and that of generation 0 close to zero ($\approx 1.2 \times 10^{-6}$ Pa.s/m^3).

Pressure

The characteristic pressure curves can be seen in Figure 2.16. We observe how the high resistance arteries cause the majority of the pressure drop, confirming what we saw in the resistance results (Figure 2.15). We also see that the pressure drop between the the arterial generation $N-1$ and the capillaries is smaller in the compliant case than in the rigid case, this is reasonable since the resistance in the arterial generation $N-1$ decreased for the compliant case thus allowing for a smaller pressure drop.

We also notice that the venous pressure drop is small in both cases but even more so in the compliant case. This is expected since the veins have thinner walls (introduced as 0.1 d_{vn}), thus the changes in resistance will be very small which is also linked to the compliant CSA being less pronounced (as we saw in Figure 2.15). In the rigid case the small pressure drop is due to scaling of the vessel radius (and the small pressure feeding to it from the capillaries). The values of these pressures are also within those reported in literature (Guyton, 2006).

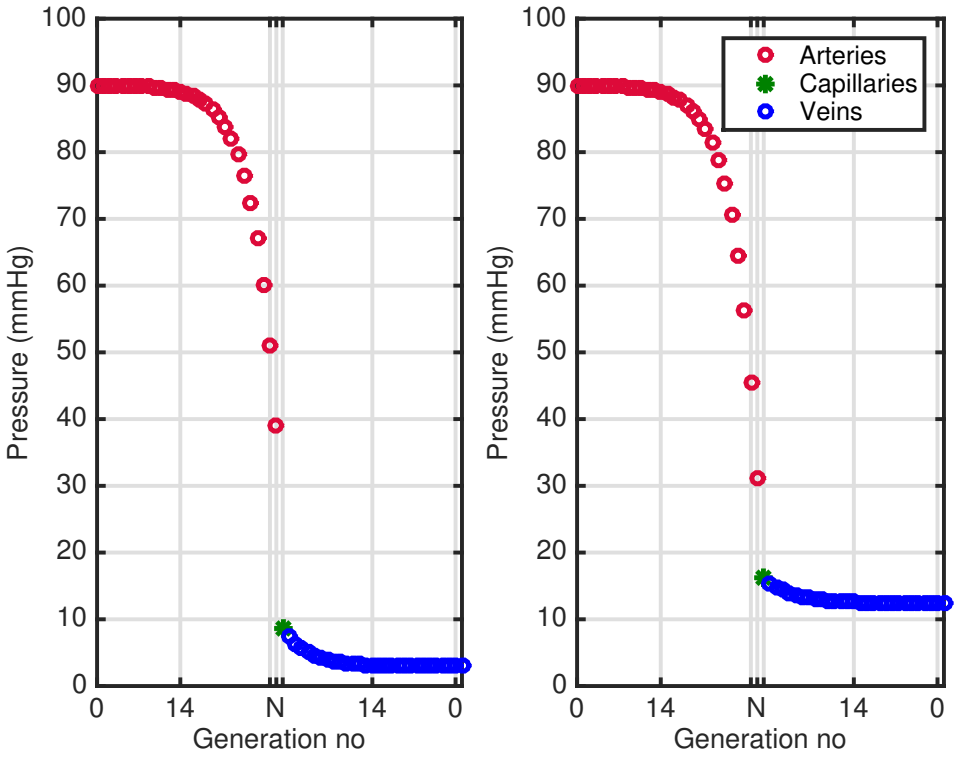

Figure 2.16: Net pressure per generation for the rigid case (left), and the compliant case (right).

Transmural flux

The transmural flux, which is the fluid transferred to the space outside the vasculature, can be seen in Figure 2.17. Here we observe a noticeable difference between the rigid and compliant cases, specially with respect to the capillaries. The absolute values for the arteries remain relatively constant, however, in the veins flux is going into the vasculature (negative transmural flux). The reason for this is due to the negative transmural pressure seen in Figure 2.12. Negative transmural flux is also possible in the compliant case, but this is relatively small compared to the changes in the rigid transmural flux.

We see the higher values for transmural flux in the vascular tree occurs in the smaller arterial vessels which is expected due to the smaller vessel thickness. This arterial transmural flux, however, is only a small proportion of that in the capillaries, the arterial transmural flux in generation $N-1$ for example, is one fourth that of the capillaries. We also notice that for the rigid case the capillaries transmural flux is less than half that of the compliant case. The reason for this is due to a smaller transmural pressure than in the compliant case (Figure 2.12).

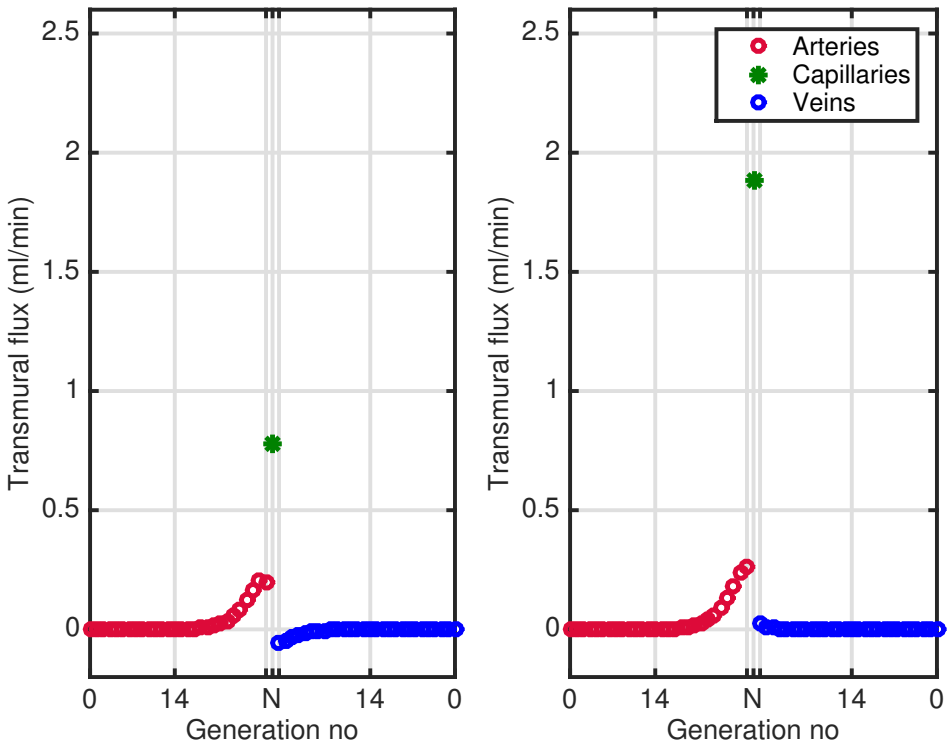

Figure 2.17: Net transmural flux per generation for the rigid case (left), and the compliant case (right).

If we assume the flux in the arteries is the flux going into the ventricles via the choroid plexuses, we find a good agreement with the measured CSF production rate of 0.25–0.47 ml/min (Czosnyka et al., 2004; Damkier et al., 2013). However neither does a single generation feeds into the ventricles nor it is exclusively done by the arteries as the capillaries also contribute. We review this and other details as part of the intracranial model in Chapter 3 where we add the CSF spaces and analyse them along with the vasculature.

2.7 Parameter sensitivity analysis

We investigate the sensitivity of the model against all the parameters introduced with the exception of the scaling factors and ratios as these were reviewed in detail as part of §2.3–§2.5. From here onward we use only the compliant case for our model. We also analyse the sensitivity of the model to the boundary conditions, that is, to cerebral blood flow Q, input pressure p_{root}, and external pressure p_e.

The parameters with arterial and venous counterparts, i.e. vessel permeability, elastic modulus and vessel length, are changed by means of a ratio that is applicable to both arteries and veins as indicated in their respective sections.

We present the variables most affected by each of these parameters. We use a one-at-a-time sensitivity analysis method and analyse the effect each of the parameters has on the model whilst keeping the rest of the parameters fixed. In the case of transmural flux, we show the results for the arterial and venous trees as we deduce the changes in the capillaries are directly proportional to the transmural pressure, we thus show only the change in capillary pressure and discuss if significant changes in capillary transmural flux occur. We discuss here and in the next section the impact on the model and its physiological relevance.

Permeability

We change the permeability of the root vessel of the arterial and venous trees by a factor of $\pm 50\%$ with respect to their baseline value, represented here as k_{b}. As per Table 2.6, the baseline permeability for the arteries is 1×10^{-21} mm^2, and for the veins 0.5×10^{-21} mm^2. Changes in permeability affect only the transmural flux on the model, we thus show the arterial and venous transmural flux only since the lumped transmural flux in the capillaries changes linearly, i.e. the capillary baseline value of 1.9 ml/min changes by $\pm$ 0.94 ml/min.

We observe in Figure 2.18 that the larger the permeability the larger the transmural flux. We recall the parameters in Equations (2.85) and (2.101) where we see that all, except for viscosity and elastic modulus, are directly related to the transmural flux. Since pressure remains unaffected by the change in baseline permeability, and we keep a constant external pressure, we can deduce that the changes in transmural flux from the baseline will be solely due to the change in permeability, which is what we find. If we observe the values for generation $N-1$ of the arterial and venous trees, their values are exactly $\pm$ 50% from the baseline. Further scenarios tested showed this was the case for all.

We conclude that the vessel permeability affects the transmural flux only, and this change is

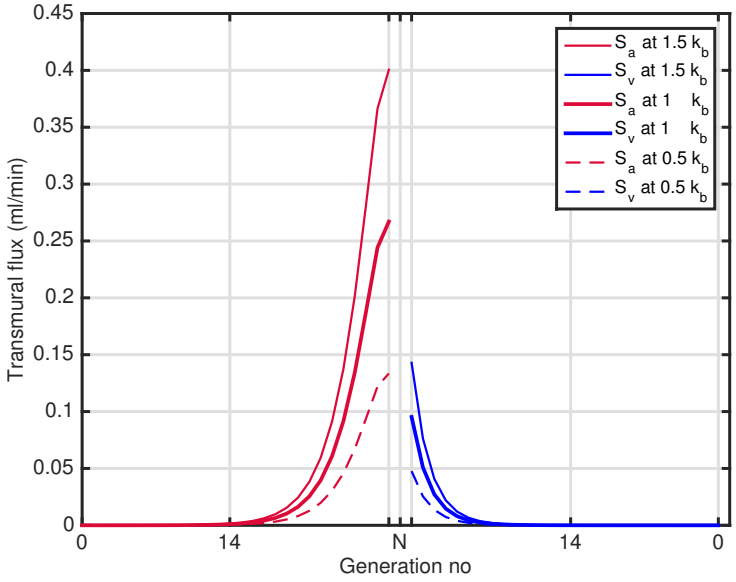

Figure 2.18: Transmural flux sensitivity to vascular permeability, where k_b is the baseline permeability.

proportional to the introduced change in permeability, as expected. As mentioned in §2.2.1 and §2.2.3, we assume that $S << Q$, so the effect of S on the vasculature is negligible.

Elasticity

The model is highly sensitive to changes in the elastic modulus of the root vessel of the arterial and venous tree. We present here changes of $\pm 15\%$ from their baseline value, denoted as E_b. As per Table 2.6, the baseline elastic modulus for the arteries is 9×10^5 Pa, and for the veins 7×10^4 Pa. Changes in elastic modulus affect most significantly the pressure, CSA, volume, and transmural flux. The changes in pressure are directly proportional to all the variables (as per the equations in §2.4), thus it is unsurprising to see an increase in the rest of the figures as pressure increases.

We observe in Figure 2.19 that the effects are mostly on the venous side, with consistently higher pressure the lower the elastic modulus. This is consistent with Equations (2.87) and (2.103), where we can observe that the transmural pressure to elastic modulus ratio ϕ_n would increase the smaller the elastic modulus.

In Figure 2.12 for the compliant case we observed there is a positive transmural pressure for the

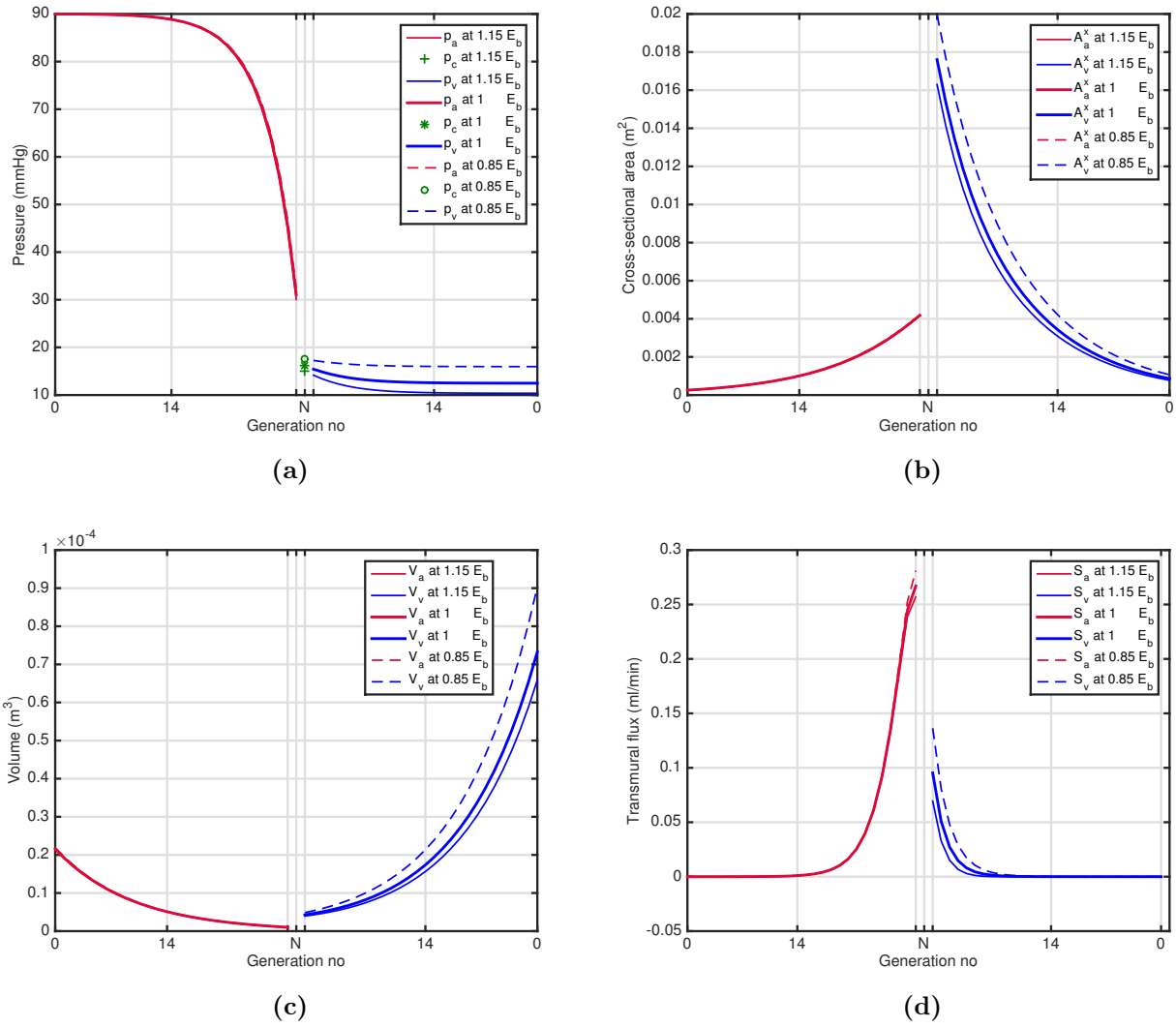

Figure 2.19: Sensitivity to elastic modulus, where E_b is the baseline elastic modulus. (a) Pressure across vasculature, (b) cross-sectional area, (c) volume, (d) transmural flux.

baseline case, by reducing the elastic modulus whilst keeping a constant external pressure we can see how we would obtain an increase in pressure. This can also be appreciated in Equation (2.104) where the pressure terms on the left hand side which are higher than the external pressure on the right hand side due to the positive transmural pressure, would indeed increase. If the transmural pressure were negative (i.e. the constant external pressure was higher than the baseline), the opposite would occur.

In Figure 2.19b we see the CSA has a nonlinear decrease between generation $N-1$ and generation 0 of the venous side, when the elastic modulus is 15% less than the baseline. For a higher elastic modulus the changes are smaller and closer to the baseline.

In the case of the volumes (Figure 2.19c), we also see a greater effect when the elastic modulus is smaller, however, here the effect is more pronounced towards generation 0 rather than towards the smaller venules (generation $N-1$). The reason for this is the balancing effect of the increasing length towards the bigger veins, which is greater than the change in elastic modulus as per the scaling factor λ.

In Figure 2.19d we observe the changes in transmural flux are slightly more pronounced in the case of the smaller elastic modulus but not significantly so. We also see there is small effect on the high resistance arteries, in particular arterial generation $N-1$. This is expected since the compliant surface area is no longer a quadratic expression with respect to the transmural pressure to elastic modulus ratio but rather a linear one, as seen in Equations (2.81) and (2.97). This results in milder effects for the transmural flux. If pressure were more significantly different to changes in elastic modulus, we would see a greater effect on transmural flux as the latter is directly affected by them.

We conclude that the model is highly sensitive to changes in the vessel elastic modulus, particularly on the venous side. The changes are more pronounced when the elastic modulus is smaller, where we see an increase in all variables.

Length

Due to the scaling relationships, the model is very sensitive to changes in vessel length, even though we neglect changes in vessel length with changes in pressure. The effects are accentuated on the venous side due to the pressure-area relationship introduced in §2.4 where the elastic modulus is smaller than its arterial counterpart. We present here changes of $\pm 10\%$ from their baseline value, denoted as l_{b}. As per Table 2.6, the baseline length for the arterial and venous root vessel is 8.5×10^{-2} m.

In Figure 2.20a we observe the venous pressure increases as we reduce the length. This makes sense since we assume Hagen–Poiseuille flow, however, the pressure drop is not changed by the same factor as the length is being changed.

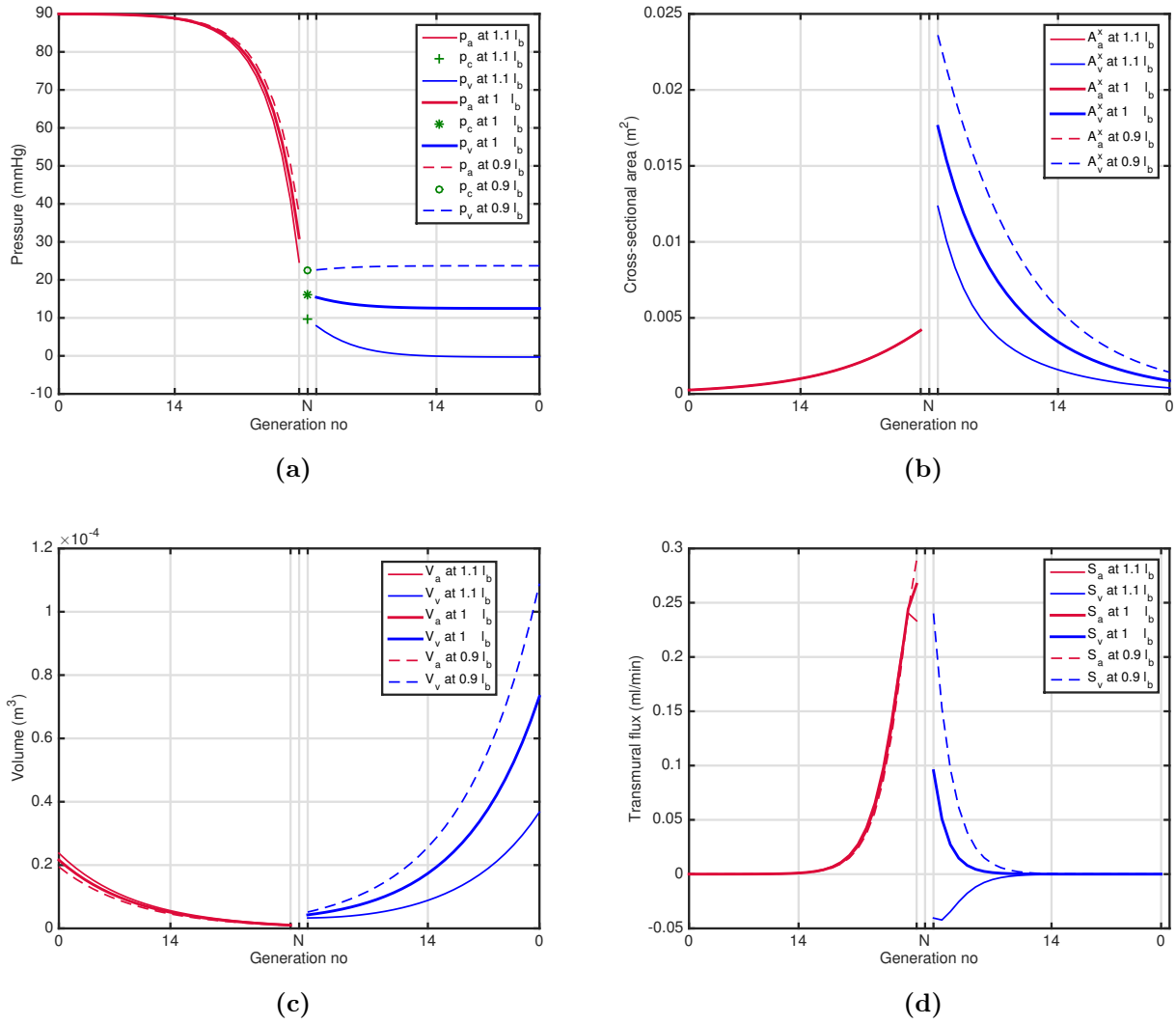

Figure 2.20: Sensitivity to length of root vessel, where l_{b} is the baseline length. (a) Pressure across vasculature, (b) cross-sectional area, (c) volume, (d) transmural flux.

If we re-arrange Equation (2.104) so that all the terms of pressure, except for external pressure, are on the left hand side, and expand $\psi_{\mathrm{v}n}$ we obtain

$$\mathscr{P}_{\mathrm{v}n}^{\mathrm{in}} - \mathscr{P}_{\mathrm{v}n}^{\mathrm{out}} = \frac{\xi^n R_{\mathrm{v}0} Q \left(E_{\mathrm{v}} - 15\mathscr{P}_e\right)}{1 + 7.5\xi^n R_{\mathrm{v}0} Q}. \tag{2.107}$$

Hence we can see that a change in the length of the root vessel, which is in $R_{\mathrm{v}0}$, will have a nonlinear behaviour on the pressure drop, which is what we observe. The pressure difference for the larger length is greater than that of the small length. This behaviour of the pressure difference causes the average pressure to change which ultimately affects the transmural pressure and the rest of the variables.

In Figure 2.20b we see the effects on the CSA. As we saw in §2.4, the compliant CSA has a quadratic relationship with respect to the rigid case. This relationship is driven by the transmural pressure to elastic modulus ratio ϕ, which as we know, it is greater in the smaller venules, which is why the effects are more pronounced on this region.

In Figure 2.20c we see that as in the previous case (elastic modulus sensitivity), the volume is affected more in the bigger veins due to the direct relationship length has with volume, which is more significant than the transmural pressure to elastic modulus ratio.

We can observe transmural flux in Figure 2.20d, where we appreciate that in the case of an increase in length, the pressure decreases to below the external pressure causing a negative transmural flux in the smaller venules. In other words, as we increase the length, the transmural pressure becomes negative, and flux is transferred into the venules.

We conclude that the model is highly sensitive to length, where we see a nonlinear effect on pressure which causes the rest of the variables to become significantly affected. As the length is increased, pressure can fall below the external pressure value allowing flux to enter the venules transmurally.

Capillary resistance

We present changes of $\pm 25\%$ from the baseline capillary resistance, denoted as R_{c}. As per Table 2.6, the baseline capillary resistance is 0.02 mmHg.min/ml. Changes in capillary resistance are more significant in the pressure, which in turn affects CSA, volume, and transmural flux. As in the previous cases, the changes are noticeable on the venous side for reasons already mentioned. As we increase the capillary resistance, the capillary pressure drop increases resulting in a smaller input venous pressure, as expected.

In Figure 2.21a we observe the pressures in generation $N-1$ change by 4 mmHg from the baseline, approximately 25% for each 25% of capillary resistance. This is consistent with Equation (2.91) where we assume a linear relationship between capillary resistance and capillary output pressure which then becomes the venous input pressure of generation $N-1$. There is a

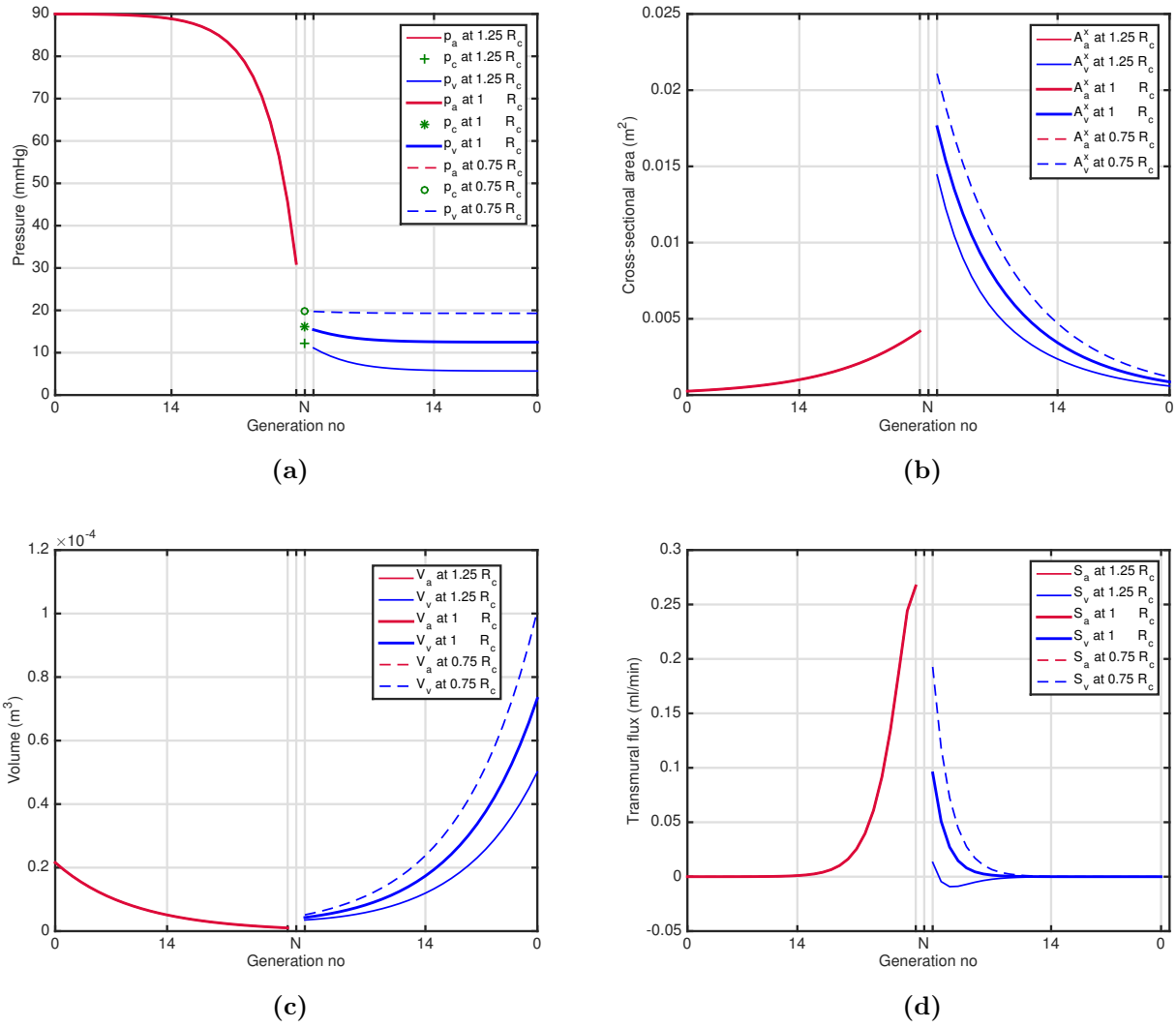

Figure 2.21: Sensitivity to capillary resistance, where R_{d} is the baseline capillary resistance. (a) Pressure across vasculature, (b) cross-sectional area, (c) volume, (d) transmural flux.

mild pressure drop for the higher capillary resistance between generation $N-1$ and generation 14. The pressures however, change linearly between generation 14 and generation 0.

The change in pressure causes the CSA to have changes of approximately ± 5 mm^2 on the venous generation $N-1$ (Figure 2.21b), that is a change of 28% for each 25% change in capillary resistance. On volume (Figure 2.21c) the effect is more pronounced in generation 0 (as in previous cases), and we see a change of approximately ± 20 cm^3, representing the same percentage change as in the CSA.

Regarding transmural flux, we see that as the capillary resistance increases the pressure decreases to below the external pressure, and thus the negative transmural flux forces flux into

the smaller venules (Figure 2.21d). The changes in transmural flux are approximately $\pm$ 0.09 ml/min in the venous generation $N-1$. The baseline transmural pressure at the venous generation $N-1$ is approximately 3.4 mmHg; if this transmural pressure increases by 1 mmHg this translates into a change of 30% in transmural flux, thus a change in over 3 mmHg causes the transmural flux to change by a factor of 2, as is the case here.

We conclude that changes in capillary resistance have a linearly proportional effect on the venous pressure, CSA and volume. Transmural flux is very sensitive to changes in transmural pressure, therefore any change in pressure from the baseline transmural pressure has a significant effect on the transmural flux. As in previous cases, when the transmural pressure is negative, the transmural flux is also negative.

External pressure

We present changes of ± 5 mmHg from the baseline external pressure, denoted as p_{e}. As per Table 2.6, the baseline external pressure is 11 mmHg. We observe in Figure 2.22 that changes in external pressure have a significant effect on the venous pressure drop, and thus the rest of the variables.

In Figure 2.22a we observe that at lower external pressure, there is an increase in venous pressure, and an increase in transmural pressure. This is expected as per Equation (2.104), where we also see that increasing external pressure decreases the transmural pressure. For high external pressure we see that the transmural flux (Figure 2.22d) becomes negative which means the transmural pressure has also become negative and therefore the venous pressure is smaller than the external pressure, which is what we see in Figure 2.22a. A significant increase in transmural flux is seen when the external pressure decreases, as expected.

In Figures 2.22b and 2.22c we observe the changes in CSA and volume are slightly more pronounced, which is expected since they are both dependent on changes in transmural pressure. As the external pressure decreases the transmural pressure increases and the CSA increases from its baseline case. We see a similar behaviour in the volume Figure 2.22c, although with changes

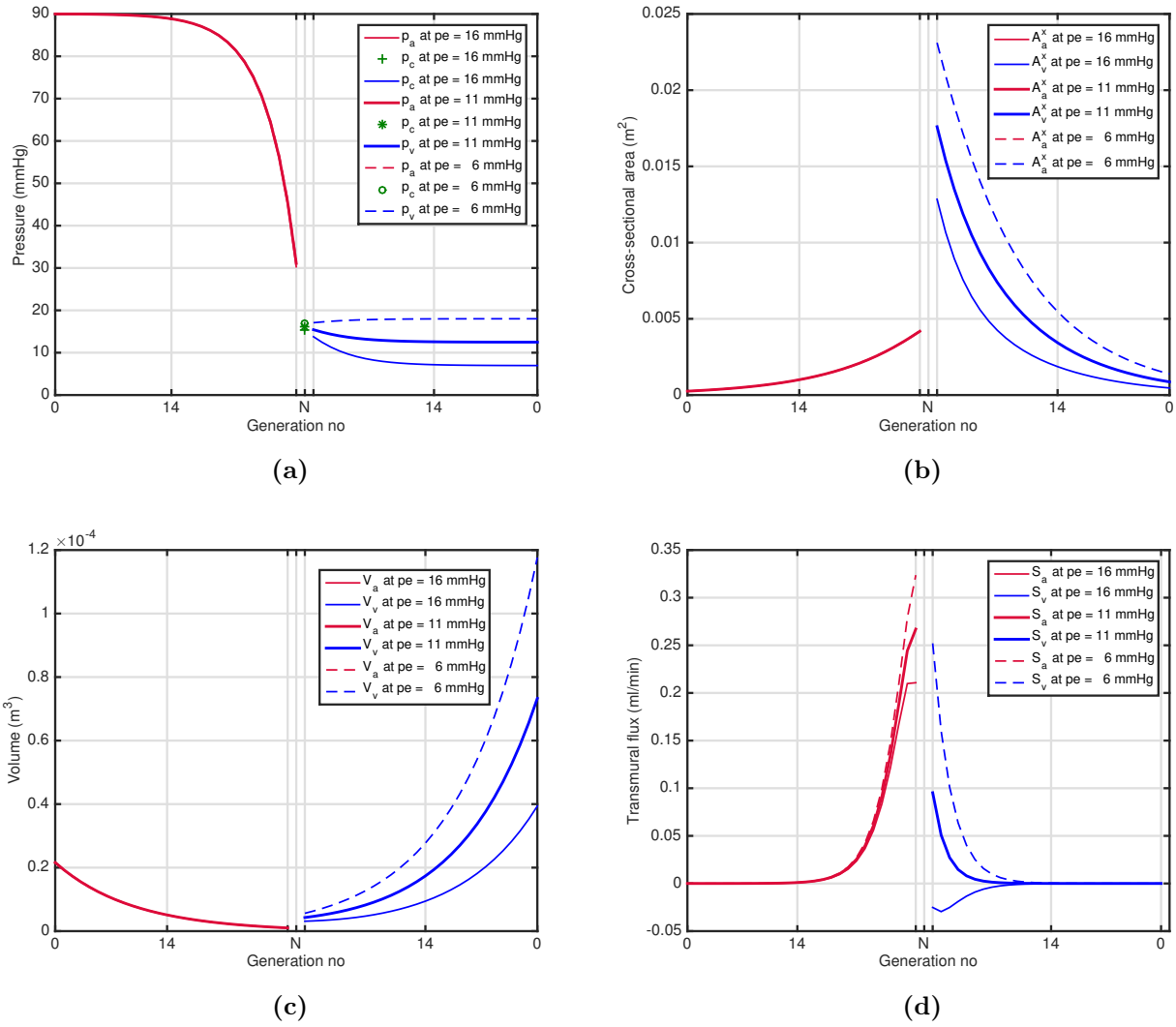

Figure 2.22: Sensitivity to external pressure, where p_e is the baseline external pressure. (a) Pressure across vasculature, (b) cross-sectional area, (c) volume, (d) transmural flux.

more pronounced towards the venous root vessel, for reasons already explained.

We conclude that the external pressure has a moderate effect on the model, with particular emphasis on the venous side due to its small transmural pressure and smaller elastic modulus. The change in external pressure was over $\pm$ 50% the baseline value, however, since the value of the external pressure is smaller than the arterial, we see there is no effect on the arterial side. In the case of the venous side, the change represents a noticeable increase and decrease for the already small transmural pressure which translates into smaller and larger values from the baseline. We see that the smaller the external pressure, the larger the transmural pressure which allows the rest of the variables (i.e. venous pressure, transmural flux, CSA, and volume)

to increase.

Cerebral blood flow

We present the effect of changes in cerebral blood flow, Q, of ± 50 ml/min from the baseline. As per Table 2.6, the baseline value is 750 ml/min. We can observe in Figure 2.23 that the model is very sensitive to changes in cerebral blood flow, specially on the venous side.

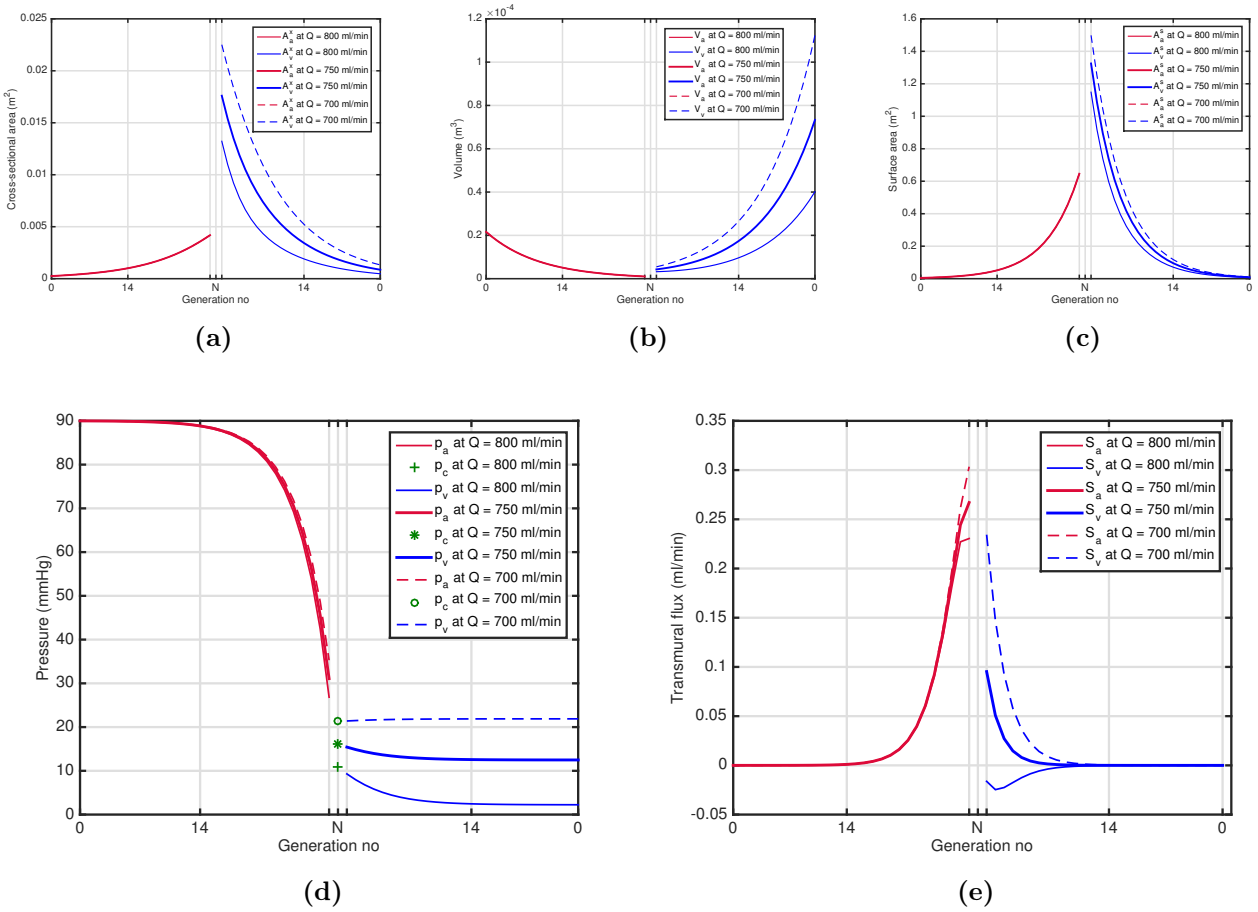

Figure 2.23: Sensitivity to cerebral blood flow, where Q is the baseline cerebral blood flow. (a) Cross-sectional area, (b) volume, (c) surface area, (d) pressure, (e) transmural flux.

Changes in cerebral blood flow have a similar effect on the variables as changes in length. The reason for this can be appreciated in the re-arranged Equation (2.107). There we can see the qualitative behaviour of cerebral blood flow with changes from the baseline. Quantitatively however, we see that cerebral blood flow requires only 6% of change from the baseline to have a significant effect (as opposed to 10% in length changes). This is because by changing Q, which

is a boundary condition, the pressure changes as per Hagen–Poiseuille equation in the reference case. In other words, we are setting new boundary conditions in the model and the pressure needs to accommodate for this.

In this analysis we also present changes in surface area (Figure 2.23c), which, unlike previous cases, is now affected. As we do not change the resistance but rather the cerebral blood flow directly, the vascular resistance remains unaffected apart from mild changes on the smallest venule due to the change in transmural pressure.

We conclude the model is highly sensitive to changes in cerebral blood flow, with the venous pressure being most affected which in turn affects the rest of the variables.

Input pressure

Here we see the effects that changes in input pressure have on the model. We vary the input pressure by ±30 mmHg from the baseline, denoted as p_{root}. As per Table 2.6, the baseline input pressure is 90 mmHg. We observe in Figure 2.24 that changes in input pressure have a more significant effect on the arterial side than on the venous one, this is expected since $p_{\text{root}} = \mathscr{P}^{\text{in}}_{\text{a0}}$.

In Figure 2.24a we observe that irrespective of the input pressure, the pressure in the capillaries and on the venous side remains relatively similar to the baseline (within ≈3–5 mmHg), which is what the autoregulation function is intended to do. In §2.5 we introduced an autoregulation function based on scaling factor γ to accommodate for changes in pressure. The changing γ allows the CSA to change (Figure 2.24b) which in turn changes the arterial resistance (Figure 2.24c) and thus the arterial pressure, which is what we see here.

We distinguish the behaviour from the previous cases (where the majority of the changes were due to the pressure-area relationship) by noticing that the changes in CSA are not directly proportional to the change in the pressure. In Figure 2.24b we observe that the arterial CSA has an opposite effect from the pressure. Since we see that the changes in resistance due to changes in the input pressure occur almost entirely in the smaller arteries, we observe in Figure 2.24c that the higher arterial CSA results in a lower arterial resistance. This is a nice feature of

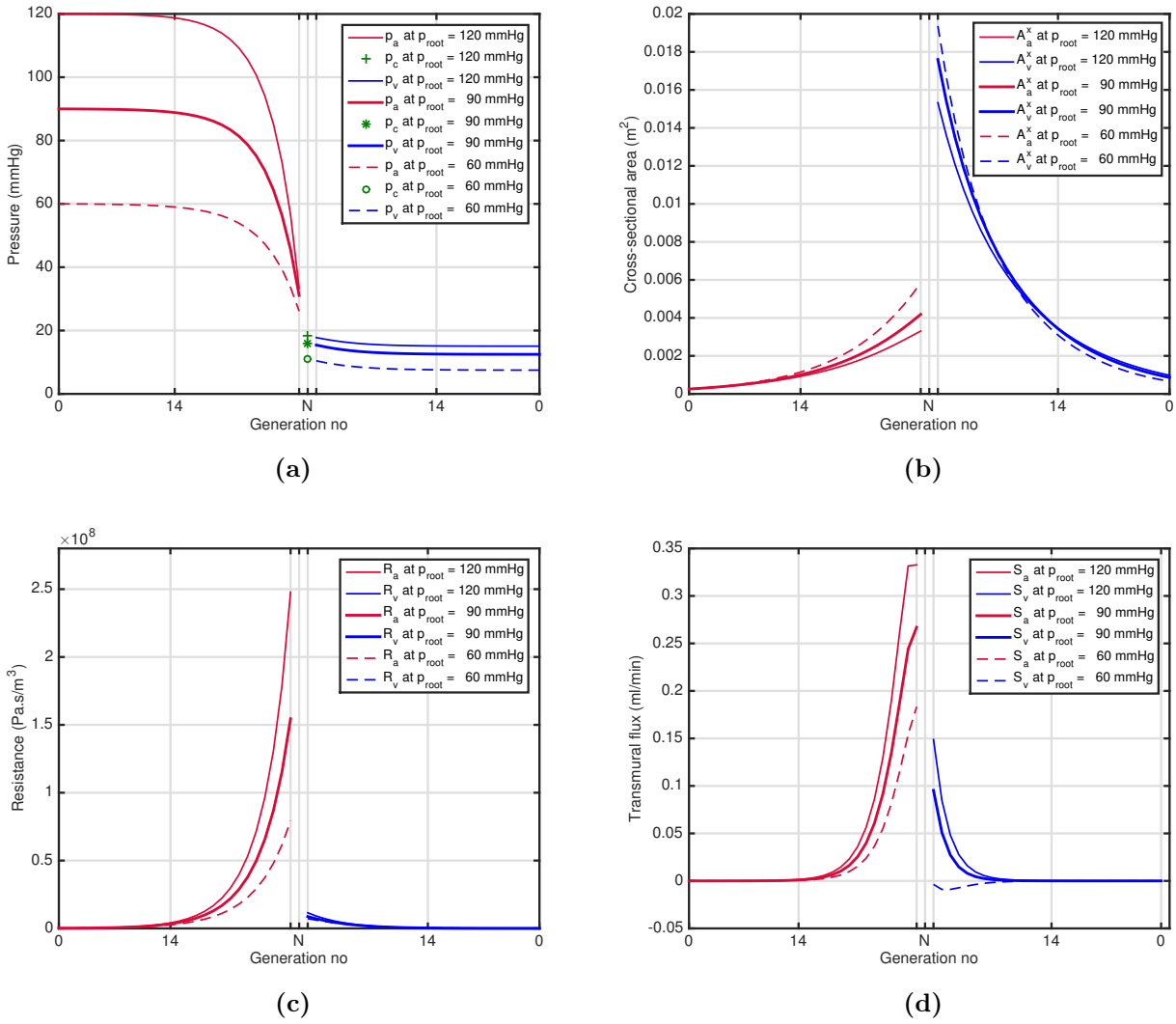

Figure 2.24: Sensitivity to input pressure, where p_{root} is the baseline input pressure. (a) Pressure across vasculature, (b) cross-sectional area, (c) resistance, (d) transmural flux.

the model since we see the changes in resistance due to changes in input pressure occur almost entirely in the smaller arteries, as reported physiologically (Guyton, 2006; Levick, 2010).

We also see in Figure 2.24b that autoregulation is taking place in the venous CSA where γ is allowing the venous CSA to remain relatively close to the baseline, thus having minimal impact on the resistance and ultimately the pressures.

Lastly, we observe in Figure 2.24d that since the lower input pressure results in a venous pressure that is below the external pressure value, negative transmural flux occurs in the smaller venules. For the arterial transmural flux, the changes can be seen to be consistent with changes in pressures which thus affect the transmural pressure and gives the directly proportional results

on the arterial transmural flux that we observe.

We conclude that changes in input pressure result in a change in γ, as introduced by the autoregulation function in §2.5, which results in a change in CSA and vascular resistance that allows the pressure in the capillaries and venous side to remain very similar to the baseline values. The changes from input pressure on the transmural flux are directly proportional to those of the arterial and venous pressure.

2.8 Summary and discussion

In this chapter we developed a one-dimensional steady flow vascular model of the cerebral circulation, with specific focus of the smaller vessels. From first principles we constructed symmetrical bifurcating trees for the cerebral arteries and veins connecting to a lumped-parameter compartment representing the capillaries. The model assumes mass is conserved within the vasculature, and simplification of the Navier–Stokes equations leads to the Hagen–Poiseuille equation to describe flow through the cylindrical vessels. These governing equations work alongside a set of scaling laws derived from the cross-sectional area scaling factor γ and the length scaling factor λ for the construction of the vascular trees with N generations. The geometrical series starts from an effective root vessel that incorporates the major arteries entering the cranium and the circle of Willis, giving rise to the bifurcation of the smaller vessels in the brain (§2.1–§2.2).

The selection of parameters combines values taken from the literature, along with relationships between arteries and veins described in the form of the arterovenous diameter ratio ν and the root vessel ratio ϱ. We select a range of acceptability for ν between 1–3 based on the larger veins compared to arteries, and for ϱ a range of 0.6–0.8 based on the comparison of an internal carotid artery diameter and that of a smaller artery.

The size of the trees is defined by the number of generations, which is in turn associated with the number of capillaries in the brain. Through a volumetric flux argument we select a first

estimate of 28 generations which we later test, within the limits of ± 8 generations, along with the scaling factors and ratios (§2.3.3).

The scaling factors follow tight inequalities from physiological assumptions that result in an acceptable region resembling that of a right angle triangle between a range of values for γ (0.5–0.635) and those of λ (0.794–1) from which physiologically acceptable combinations of the two scaling factors can be derived. We use this region in combination with the number of generations, arterovenous diameter ratio and the root vessel ratio to create a feasible set of combinations for the model (§2.3).

Once the reference case is constructed, we account for compliance by introducing a constitutive relation between stress and strain to allow distensibility of the vessel wall with changes in pressure. This pressure-area relationship uses the reference case from which changes in the vessel occur. We found that through simplifications of previous assumptions, the cross-sectional area is directly proportional to the quadratic of the transmural pressure to elastic modulus ratio, ϕ. This changes with every generation and it is one order of magnitude greater on the venous side due to the smaller elastic modulus. From this relationship we find the rest of the parameters including the compliant pressures, which as mentioned, are relative to the reference case (§2.4).

The simplicity of the vascular trees constructed along the physiological arguments around their scaling laws offers the detail and robustness of a distributed model at a low computational expense. This is key when attempting to understand the behaviour of the cerebral circulation, since important parameters such as the elastic modulus of the vessels or changes in the mean arterial blood pressure can be analysed easily to study their effects on the rest of the vasculature.

Another key feature in our model is the introduction of autoregulation. The brain uses a complex set of interactions to regulate blood flow. As we focus on the fluid mechanical features in this model, we can see that the effects of autoregulation has on the vasculature are in vascular resistance, primarily in the high resistance arteries. Since in our model the vascular resistance is a function of γ and λ, and since changes in length are negligible to those of cross-sectional area, we concluded that we can capture the effects of autoregulation in our model by changes in γ. We therefore introduced an autoregulation function that allows for changes in cross-sectional

area regulated by changes in pressure.

This change in γ results in sustained constant cerebral blood flow with minimal or no affect on the capillaries and veins. The result not only describes the crucial effects of autoregulation in the cerebral circulation, as seen by the pressure and cross-secitonal area plots, but it highlights in our model that the complex mechanisms driving autoregulation can be accounted for in this scaling factor γ. Having a single parameter, γ in this case, that describes a series of processes is one of the driving features of modelling. By understanding the simple, we can explore the complex, as is in this case for the processes involved in autoregulation. To our knowledge, this approach to autoregulation is novel in cerebral modelling before (§2.5).

We present the results for the rigid and compliant case in §2.6 for the baseline boundary conditions previously defined. The model finds the cross-sectional area, length, volume, surface area, resistance, pressure and transmural flux throughout the vasculature, with detail for individual vessels and between generations (although we only showed net values). Here it was possible to see the subtle and yet very important differences the pressure-area relationship makes on the model. We observed how the total cross-sectional area and surface area of the smallest venules grows from the rigid case as compliance is introduced, due to the smaller ratio between transmural pressure and elastic modulus. The compliant volume changed mildly from the rigid case, and it is only noticeable in the larger veins where a small increase ($\approx 5 \times 10^{-6}$ m^3) is seen due to the small transmural pressure and larger cross-sectional area from the rigid case. With respect to resistances, we notice a small decrease in the compliant case and how the veins have close to zero resistance. We also note that the resistance of the last arterial generation is approximately equal to the capillary resistance, confirming this is a good first approximation.

The characteristic pressure curve from arteries to veins is seen to be more physiologically reasonable for the compliant case where we observe a greater pressure drop in the high resistance arteries. We also notice the venous pressure remains higher than the external pressure which ensures a positive transmural pressure for the compliant case. The transmural flux can be seen to take place predominantly in the smaller vessels as expected, and that this is significantly greater on the arterial side than the venous side. In the rigid case the venous transmural pressure

is negative for the smaller vessels which causes a negative transmural flux. In the compliant case the transmural pressure is positive and small, which directly translates to the transmural flux. We also saw the significant difference the compliant case made with the capillary flux where a value twice that of the rigid case is observed. We find the values produced by the model are within a physiologically reasonable range.

The model was also tested within a range of parameters finding that the model is highly sensitive to changes in elastic modulus, length and cerebral blood flow, and moderately sensitive to changes in capillary resistance, external pressure and input pressure (§2.7). Changes in vascular permeability only affected transmural flux, and in a relatively proportional manner. This is rather expected since we have assumed that the transmural flux is much less than the convective flux of blood through the vasculature and have neglected its effect on the hemodynamics. We saw early in the chapter how the model was highly sensitive to changes in γ and λ, it is therefore unsurprising to see the model being significantly affected by changes in the root vessel length, where we see that an increase in 10% the baseline value is enough to reduce the venous pressure to values close to zero which then causes the transmural pressure to become negative as this is below the external pressure value, and thus predicts negative transmural flux.

The elastic modulus is important in describing the compliant behaviour of the model, and given that the veins have a transmural pressure to elastic modulus ratio one order of bigger than the arterial one, it is expected that a change in the elastic modulus has a bigger impact on the veins than the arteries. The sensitivity tests reveal that changes in elastic modulus by $\pm$ 15% are significant on the venous side. The changes appear more significant when the elastic modulus is decreased than when it is increased, this makes the ratio even smaller which causes the venous pressure to rise and thereby affects all the other variables as they are directly dependent of the transmural pressure.

This influence of the elastic modulus is interesting from a physiological point of view since the blood vessels are thought to get stiffer with age, and blood pressure is also relatively higher in the older population (Greenwald, 2007). According to our model, blood pressure in the brain could increase as a result of the vessels becoming stiffer. Interestingly, according to our

model, the cerebral circulation would accommodate for a change in elastic modulus as long as the increase is not greater than 15%. As with many things in physiology, this is not the full picture since the stiffening of the blood vessels would also have an impact on the surrounding cerebrospinal fluid which would ultimately affect the cerebral veins (we explore this in the next chapter). However, as far as the vasculature alone is concerned, our model is able to account for this physiologically relevant behaviour in the brain.

Changes in cerebral blood flow can be compensated for in the cerebral circulation, according to our model, as long as these are within $\pm$ 50 ml/min. This seems like a very tight limit, and it is possible that this would be the case if no other factors were involved to compensate the changes, however, as we shall see in Chapter 3, this is also dependent on the interaction with cerebrospinal fluid.

The model was mildly sensitive to changes in capillary resistance, where it was able to accommodate changes up to $\pm$ 25% from the baseline. The effect was only noticeable on the venous side since the capillary resistance affects the capillary output pressure that feeds into the veins. Here it was observed that the higher the capillary resistance the lower the input pressure, and thus all the rest of the variables. This is reasonable due to the Hagen–Poiseuille relationship we established.

The model is, perhaps unsurprisingly, sensitive to external pressure for the compliant veins. The changes introduced were in the region of $\pm$ 50% its baseline which proved to be significant. However, since this is a boundary condition not involved with any of the scaling laws introduced (as opposed to the cerebral blood flow and input pressure) and it only relates to the transmural pressure, the changes are relative to the transmural pressure to elastic modulus ratio.

We analysed further the effects of autoregulation by observing the changes in the rest of the parameters to different input pressures. We were able to see that unlike the other parameter tests, changes in input pressure affected both arteries and veins but to a greater extent on the arterial side. We could see that as the input pressure increases so does the arterial resistance due to the inverse fourth-power law of the cross-sectional area and associated regulatory γ. This is a nice depiction of the effects of autoregulation and one that is often reported in the

literature (Panerai, 2008; Guyton, 2006).

2.9 Concluding remarks

- We constructed a set of bifurcating trees representing the small cerebral arteries and veins, connected through a lumped-parameter capillary compartment, with the use of two main scaling factors (γ for cross-sectional area and λ for length).
- The resulted cerebrovascular model is compliant as per a pressure-area relationship based on a reference (rigid) case.
- Autoregulation is incorporated to the model by means of changes in γ.
- Results show the compliant case adequately models changes in the cerebral vasculature.
- The sensitivity results show the changes in the cerebral circulation when different parameters (e.g. pressure, blood flow, elastic modulus, permeability) vary.
- The model neatly captures the main features of the cerebral circulation by means of simple scaling relationships, from first principles, and at a low computational expense.

Chapter 3

Intracranial model

In this chapter we enhance the vascular model developed in Chapter 2 by introducing the cerebrospinal fluid spaces and investigating their interaction with the cerebral vasculature. We explore: (1) dynamics of pressures and fluxes of the cerebrospinal fluid compartments for a range of parameters; (2) effects of opening and closing the arachnoid villi valve on the intracranial pressures and fluxes; (3) stability of the solution to perturbations; and (4) effects of changes in cerebral blood flow and vascular input pressure, on the cerebrospinal fluid.

3.1 Introduction to the model

The primary intracranial fluid compartments outside the vasculature are the cerebral ventricles and the subarachnoid space (SAS), where most of the cerebrospinal fluid (CSF) resides. The SAS was introduced in Chapter 1 and defined as the space delimited by the arachnoid mater at its outermost part, and the pia mater at its inner part (Figure 3.1). Thus the CSF in the SAS surrounds the brain, cerebral ventricles, and vasculature. This CSF can influence the vasculature, and the vasculature can also influence the pressure in the SAS, in particular by the expansion and contraction of the vessels during each cardiac cycle (Wagshul et al., 2011; Terem et al., 2018). The other major site of localised CSF are the cerebral ventricles. Here, the choroid plexuses are thought to produce the majority of CSF (Sakka et al., 2011), however

the sources and volume of the CSF production remain under debate (Brinker et al., 2014). Extrachoroidal CSF production is difficult to quantify; however, studies suggest that the total CSF turnover from other sources (presumably vascular) could be substantial (Bering Jr and Sato, 1963; Koh et al., 2005). Globally, CSF production has been estimated between 0.25–0.47 ml/min (mean 0.35 ml/min), with variability dependent on metabolic rate (Czosnyka et al., 2004).

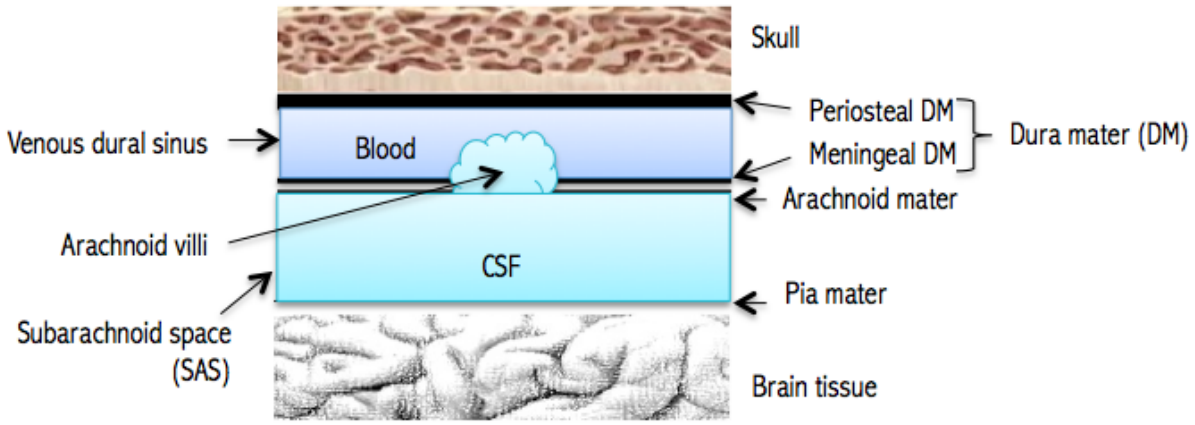

Figure 3.1: Cerebral meninges. Interaction between blood and CSF, and localisation of arachnoid villi.

Ventricular CSF communicates with the subarachnoid CSF through the foramen of Magendie and the foramen of Lushka[1], the pressures in the ventricles and SAS are thus related. Similarly, ventricular and vascular pressures interact with one another via the choroid plexuses. Due to restrictions on volume expansion of the SAS, and the ability of CSF to flow in response to pressure gradients, it is likely that CSF pressure in the SAS has a significant influence in the CSF pressure in the ventricles, more so perhaps than the vascular pressure. Early experiments on hydrocephalus led surgeons to the removal of the choroid plexuses in order to stop progression of the condition (Dandy, 1918), as it was believed all CSF was produced in the choroid plexuses, and hydrocephalus might be the result of overproduction. Not only was the procedure unsuccessful, but it led to the reassessment of the choroid plexus as a single source of CSF production and its specific involvement in hydrocephalus.

It has been observed in animal experiments that enlargement of the ventricles can occur when a blockage is imposed in one of the ventricular pathways e.g. aqueduct of Sylvius (Klarica et al.,

[1]Also known as the median and lateral apertures, respectively. See Chapter 1 for further anatomical detail.

2009). In non-stenotic conditions ventricular enlargement can also occur when intracranial pressure is kept at a constant high pressure (> 15 mmHg), irrespective of CSF production rate (Børgesen and Gjerris, 1987). This also suggests pressure in the SAS is highly influential on the ventricles.

Despite the importance of this pressure interaction between ventricles and SAS, in modelling of the intracranial dynamics it is often assumed that the pressure difference between the two is negligible (Ursino and Lodi, 1997). In our model we treat them as distinct pressures, and study them alongside the vasculature.

The venous dural sinuses[2] are major sites of drainage for both CSF from the SAS, and de-oxygenated blood from the cerebral vasculature. The dural sinuses have the characteristic of being surrounded by a rigid structure, the skull. They are, as it name suggests, enclosed by the dura mater membranes, where the periosteal dura mater lines the skull, and the meningeal dura mater is adjacent to the arachnoid mater (Figure 3.1).

The arachnoid mater has small granulations, or villi, and connects the SAS with the venous dural sinuses. These arachnoid villi essentially act as one-way valves allowing fluid in the SAS to exit when pressure in the SAS is greater than that in the dural sinuses. It has been shown experimentally that there cannot be flow from the dural sinuses to the SAS (Welch and Friedman, 1960). This is important since it allows maintaining a balanced pressure gradient between the SAS and the cerebral circulation. Furthermore, these valves might also help overcome the effects of subatmospheric pressure in the venous circulation.

In the standing position, pressure in the head and neck becomes subatmospheric, leading to the partial collapse of the internal jugular veins (Guyton, 2006). The valve function of the arachnoid villi prevents blood flowing into the SAS when the hydrostatic pressure difference between the cranium and the heart is other than zero[3]. In the supine position, the valve function of the arachnoid villi also prevents blood flowing into the SAS when the pressure difference between the SAS and the dural sinuses is positive.

[2]For simplicity, we refer to the venous dural sinuses as dural sinuses in this document, and to the cerebral ventricles as ventricles.

[3]We explore the effects of hydrostatic pressure in the intracranial fluids in Chapter 4.

We introduce the effects of the arachnoid villi as a one-way valve in our model and study its effect on the interaction between pressures and fluxes. We assume a supine position in this model.

In Chapter 2 we covered the cerebral vasculature in detail. We now expand this model by including the ventricles, dural sinuses, and SAS. Modelling these three new spaces in one-dimensional form, can present significant difficulties. For example, the ventricles are not geometrically congruent with simplifications for axisymmetric one-dimensional flow (e.g. not cylindrical, thus Hagen-Poiseuille flow cannot be assumed), neither is the SAS, although it can be argued the latter could be represented spherically, however by doing so, we would be scaling up the complexity of the model even further, thus departing from the simplicity we set off to achieve. In compartmental analysis (a 0D model), we can overcome these challenges. Here the pressures are assumed to be uniform throughout the compartment but not constant in time, facilitating the analysis without assuming a particular geometry. We can couple the one-dimensional vascular model with a compartmental intracranial model of the CSF spaces by taking the averaged effective pressure of the vasculature interacting with an external CSF pressure (and related fluxes), whilst retaining the set of parameters affecting the vasculature and assessing the interaction of the new compartments with the vascular model.

We present a zero-dimensional (0D) intracranial model comprising of four compartments: the cerebral vasculature (compartment 1), the venous dural sinuses (compartment 2), the cerebral ventricles (compartment 3), and the intracranial SAS (compartment 4). The model is depicted in Figure 3.2, where the arterial input is denoted by red arrows, the venous output by blue arrows, and the CSF flux between compartments by purple arrows.

We define p_1^* as the effective pressure of the vascular model (compartment 1). It can be thought of as the pressure that if it were the same as in compartments 3 and 4 that would result in there being no net flux out of the vasculature. We define it mathematically in greater detail in the following sections.

Pressures in compartments 2, 3, and 4 are denoted p_2, p_3, and p_4 respectively. S_{13} denotes the net transmural flux from the vasculature to the ventricles, S_{14} the net transmural flux from the

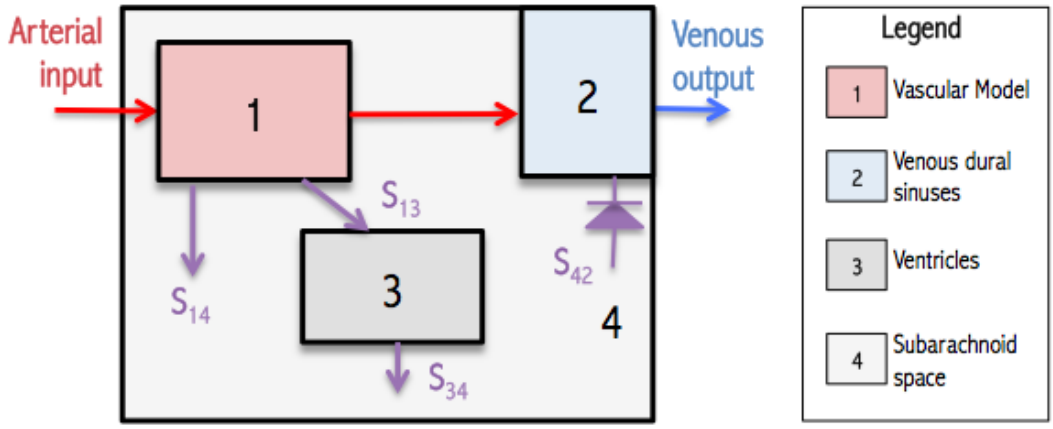

Figure 3.2: Schematic diagram of the intracranial compartmental model.

vasculature to the subarachnoid space, S_{34} the volumetric flux from the ventricles to the SAS, and S_{42} the volumetric flux through the arachnoid villi. We refer to the collective activity of these microvascular villi as the arachnoid villi valve between the CSF and the venous blood.

In Figure 3.2, compartment 4 can be seen surrounding compartments 1 and 3, and interacting with compartment 2 via the arachnoid villi valve. This type of interconnectivity in compartmental modelling (one compartment inside another) is innovative and appropriate in cerebrovascular modelling.

3.2 Derivation of governing equations

3.2.1 Mass conservation

Let each compartment be defined as a control volume i. Conservation of mass requires that the sum of the rate of change of mass within the control volume and the net mass flux out of the control volume is zero. Assuming that CSF is incompressible, mass conservation in compartments 3 and 4 implies

$$\frac{dV_i}{dt} = \sum_{j \neq i} (S_{ji} - S_{ij}) \,, \tag{3.1}$$

where V_i is the volume of compartment i, S_{ij} the volumetric flux from compartment i to compartment j, and S_{ji} the volumetric flux from compartment j to compartment i. We assume CSF flow can be in either direction, with the positive direction defined by the order of the subscripts, except between compartments 4 and 2 where only flow from 4 to 2 can occur due to the presence of the valve.

We assume volume changes in compartment 1 are the result of the volume flux in the vascular model when interacting with an external pressure which we now define as the pressure in the SAS, p_4. Compartment 2 represents the venous dural sinuses, and we assume it is rigid, i.e. $dV_2/dt = 0$.

3.2.2 Fluxes

In order to calculate the flux between compartments, we assume the volumetric flux S_{ij} is proportional to the pressure drop,

$$S_{ij} = k_{ij}(p_i - p_j), \tag{3.2}$$

for $i = 1, 2, 3, 4$, where p_i is the fluid pressure in compartment i, p_j is the fluid pressure in compartment j, and k_{ij} is the permeability to fluid movement between compartments i and j. We define pressure in compartment 1, p_1^*, as the effective pressure from the vascular model (as mentioned in §3.1). We assume the output pressure of the vascular model is the pressure of compartment 2, p_2.

3.2.3 Volume-pressure relationship

We describe the time variation of the compartmental pressure with respect to volume by introducing a compliance $C = dV/dp$, and assume a linear constitutive relationship between intracranial volumes and pressures in compartments 3 and 4, which leads to

$$V_i = V_{i0} + C_i(p_i - p_{ei}), \tag{3.3}$$

for $i = 3,\ 4$, where V_i is the volume of compartment i, C_i is compliance of compartment i, p_i is the internal pressure of compartment i, p_{ei} the external pressure of compartment i, and V_{i0} is the compartmental volume at zero transmural pressure i.e. $p_i = p_{ei}$. As mentioned in §3.1, pressure in the ventricles is influenced by pressure in the SAS, and so we assume volume changes in compartment 3 are governed by pressure in compartment 4. In other words, the external pressure of compartment 3 is the pressure in compartment 4.

The vasculature interacts with the compartmental model in different ways: through the effective pressure p_1^*, the transmural flux S_1, the volume change V_1 and by determining pressure in the dural sinuses p_2.

3.2.4 Monro-Kellie hypothesis

The Monro–Kellie hypothesis, first postulated by Alexander Monro in 1783 and later supported experimentally by George Kellie (Mokri, 2013), states that the volume inside the cranium can be divided into three main components: brain tissue volume (V_{brain}), blood volume (V_{blood}), and CSF volume (V_{CSF}), whose sum is conserved, due to the confinement of the skull, thus

$$V_{\text{brain}} + V_{\text{blood}} + V_{\text{CSF}} = \text{constant}. \tag{3.4}$$

Due to the near incompressibility of the nervous tissue under healthy conditions (Miller et al., 2000), we assume V_{brain} is constant, thus $V_{\text{blood}} + V_{\text{CSF}} = \text{constant}$, and hence $V_1 + V_2 + V_3 + V_4 = \text{constant}$. As mentioned earlier, we also assume the venous dural sinuses volume, V_2, is constant. Thus the changing volumes satisfying the Monro-Kellie hypothesis are those involving the cerebral circulation (V_1), the cerebral ventricles (V_3), and the SAS (V_4).

3.2.5 Summary

From §3.2.1–§3.2.4 and the fluxes defined in Figure 3.2, we summarise the governing equations for the intracranial model as

$$\frac{dV_3}{dt} = S_{13} - S_{34}, \tag{3.5}$$

$$\frac{dV_4}{dt} = S_{14} + S_{34} - S_{42}, \tag{3.6}$$

$$V_3 = V_{30} + C_3(p_3 - p_4), \tag{3.7}$$

$$V_4 = V_{40} + C_4(p_4 - p_{\text{skull}}), \tag{3.8}$$

$$V_1 + V_3 + V_4 = \text{constant}, \tag{3.9}$$

where p_{skull} is the pressure[4] outside the arachnoid mater (e.g. epimeningeal).

The intracranial fluxes are defined by,

$$S_{13} = k_{13}(p_1^* - p_3), \tag{3.10}$$

$$S_{14} = k_{14}(p_1^* - p_4), \tag{3.11}$$

$$S_{34} = k_{34}(p_3 - p_4), \tag{3.12}$$

$$S_{42} = k_{42}I_{42}(p_4 - p_2), \tag{3.13}$$

where I_{42} is an indicator function of the status of the valve, defined as

$$I_{42} = \begin{cases} 1 & \text{if} \quad p_4 \geq p_2 \\ 0 & \text{if} \quad p_4 < p_2, \end{cases} \tag{3.14}$$

implying the valve is only open when the pressure in the subarachnoid space, p_4, exceeds that of the dural sinuses, p_2, resulting in positive volumetric flux S_{42}.

We can simplify the governing equations to obtain the pressures in compartments 3 and 4, and

[4]It should be possible to derive a p_{skull} with further assumptions on pressure differences between meninges of the skull, however, as we shall see in the following derivations this is not essential in our model as we can find a solution with a simpler approach.

the related fluxes. We recall from the vascular vascular model, that its volume, here denoted as V_1, is a function of the cerebral blood flow Q and its external pressure, here assumed to be p_4 as mentioned earlier (as well as other parameters). In the vascular model we assumed quasi-steady flow of blood, ignoring the effects of the arterial pulse. That is, Q is the time averaged flow rate over long period of time compared to the cardiac cycle. We also assume that $S_1 << Q$, thus $Q^{\text{in}} = Q^{\text{out}}$. This means that changes in V_1 are only due to changes in p_1^* and p_4 through the vascular compliance of compartment 1. Taking this into consideration we can differentiate equation (3.9) leading to

$$\frac{dV_1}{dt} + \frac{dV_3}{dt} + \frac{dV_4}{dt} = 0, \tag{3.15}$$

$$\frac{dp_4}{dt} = \frac{-\frac{dV_3}{dt} - \frac{dV_4}{dt}}{\partial V_1/\partial p_4}. \tag{3.16}$$

Substitution of volume terms from equations (3.5) – (3.8) into equation (3.16), gives the ordinary differential equations for the pressures for compartments 3 and 4,

$$\frac{dp_3}{dt} = \frac{S_{13} - S_{34}}{C_3} + \frac{-S_{13} - S_{14} + S_{42}}{\partial V_1/\partial p_4}, \tag{3.17}$$

$$\frac{dp_4}{dt} = \frac{-S_{13} - S_{14} + S_{42}}{\partial V_1/\partial p_4}. \tag{3.18}$$

3.3 Estimation of model parameters

We start by estimating parameters k_{13} and k_{14}. In the vascular model we obtained the transmural flux from the microcirculation to the space outside the vasculature S_1 from Equation (2.61), we have

$$S_1 = \widehat{S}^{\text{tot}}_{\text{vasculature}} = \widehat{S}^{\text{tot}}_{an} + \widehat{S}^{\text{tot}}_{\text{c}} + \widehat{S}^{\text{tot}}_{\text{v}n}. \tag{3.19}$$

We can assume this flux is divided between the ventricles (compartment 3) and the SAS (compartment 4), by means of S_{13} and S_{14} respectively, thus

$$S_1 = S_{13} + S_{14}, \tag{3.20}$$

where S_{13} and S_{14} are defined in equations (3.10) and (3.11), respectively.

As we saw in the previous chapter, external pressure has a significant effect on the total transmural flux S_1. We thus investigate the behaviour of dS_1/dp_4 for a given range of pressures.

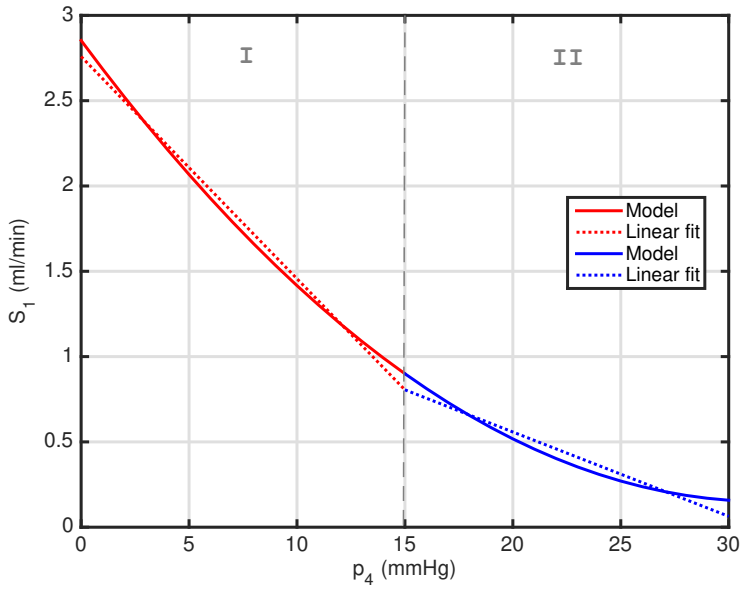

Figure 3.3: Changes in S_1 with respect to p_4 (solid line), piecewise linear approximation (dotted line) in two pressure intervals 0-15 mmHg (red), 15-30 mmHg (blue).

We observe in Figure 3.3 that S_1 behaves nonlinearly with respect to p_4 primarily because of the nonlinear axial pressure drop in the blood vessels. However, we can approximate S_1 as a piecewise linear function of p_4, which we define over the following pressure intervals,

$$S_1(p_4) = \begin{cases} \text{Region I}: \quad S_{1_{\text{I}}}(p_4) \quad \text{for} \quad 0 \geq p_4 \geq 15 \\ \text{Region II}: \quad S_{1_{\text{II}}}(p_4) \quad \text{for} \quad 15 \geq p_4 \geq 30 \end{cases} \tag{3.21}$$

where $S_{1_{\text{I}}}, S_{1_{\text{II}}}$ are linear functions of S_1 at each pressure interval. The healthy physiological range for intracranial pressure lies between 5–15 mmHg, and so S_1 will likely be in region I.

We add a wider pressure range for robustness.

Based on conditions in Equation (3.21), we can thus find the vascular volumetric flux for region I as

$$S_{1_{\mathrm{I}}} = S_{10_{\mathrm{I}}} - k_{1_{\mathrm{I}}} \Delta p_{4_{\mathrm{I}}}, \tag{3.22}$$

where $S_{10_{\mathrm{I}}}$ is the volumetric flux at zero transmural pressure in region I, and $k_{1_{\mathrm{I}}}$ is the vascular permeability in region I. We do the same for region II. If we now assume that permeabilities between compartments 1 & 3, and 1 & 4, are proportional to the vascular permeability $k_{1_{\mathrm{I}}}$, then

$$k_{13_{\mathrm{I}}} = \alpha k_{1_{\mathrm{I}}}, \tag{3.23}$$

$$k_{14_{\mathrm{I}}} = (1 - \alpha) k_{1_{\mathrm{I}}}, \tag{3.24}$$

where α is is the fraction of the vascular flux that goes to compartment 3, which is assumed to be constant. To estimate the value of α, we assume the permeability of the vascular compartment k_1, is proportional to the volume of the CSF between the ventricles and the subarachnoid space. Therefore by finding the volume ratio, we can find a permeability ratio. We thus define

$$\alpha = \frac{V_3}{V_{\mathrm{csf}}}, \tag{3.25}$$

where V_{csf} is the total intracranial CSF volume, that is $V_{\mathrm{csf}} = V_3 + V_4$. Values for total CSF volume have been reported between 90–258 ml (Alperin et al., 2006; Brinker et al., 2014), of which between 16–25 ml correspond to the ventricles and the rest to the cranial and spinal SAS (Alperin et al., 2006; Sakka et al., 2011). Spinal SAS has been reported between 77-81 ml (Alperin et al., 2006; Edsbagge et al., 2011). Taking an averaged value of 20.6 ml for the ventricles and 104.9 for the intracranial CSF, thus giving a total intracranial CSF of 125.5, we obtain a rounded value of $\alpha = 0.16$. Given the wide range of reported volumes, this value of α must be taken with caution.

We also calculate the effective pressure in compartment 1, p_1^*. Based on the above analysis for S_1, we can assume a transmural flux proportional to the pressures in compartments 1 and 4, thus

$$S_1 = k_1(p_1^* - p_4). \tag{3.26}$$

Substitution of Equation (3.22) into (3.26) gives,

$$p_1^* = \frac{S_{10}}{k_1}, \tag{3.27}$$

where p_1^* is independent of p_4 for the calculated initial flux S_{10}.

We now focus on the value for p_2, which is the output pressure of the vascular model. We evaluate dp_2/dp_4 in the vascular model for a range of p_4.

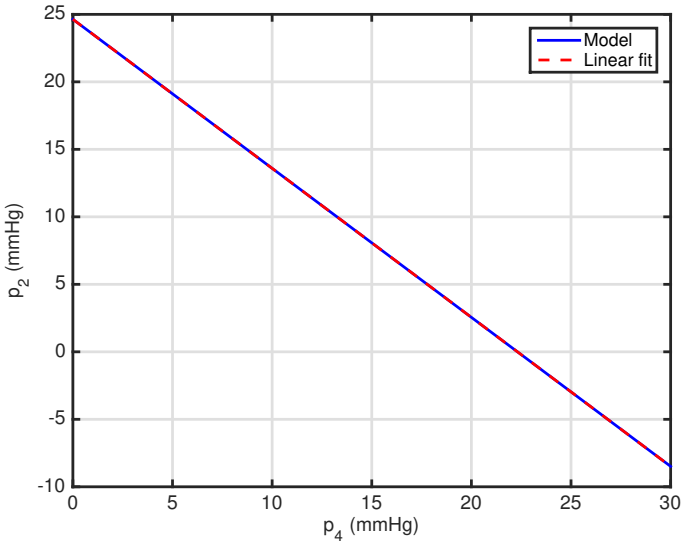

Figure 3.4: Changes in p_2 with respect to p_4 (solid blue line), and a linear fit (dashed red line).

We observe in figure 3.4 that p_2 changes linearly with respect to p_4, then,

$$p_2 = p_{20} - Hp_4, \tag{3.28}$$

where p_{20} is the initial pressure in compartment 2, and H the rate of change of p_2 with respect to p_4. The calculated values give $p_{20} = 22.3$ mmHg and $H = 0.87$. Note this value will change for a different range of p_4, while the range selected for the intracranial model (0 to 30 mmHg) is slightly wider than the average of a healthy person in the supine position (Czosnyka et al., 2004), this is likely to change during postural[5] changes where intracranial pressures can become negative (Michael and Marshall-Bowman, 2015)

Another unknown parameter in our model is the change in V_1 with respect to external pressure p_4, i.e. $\partial V_1/\partial p_4$. We know from the analysis in the vascular model that volume in the vasculature changes nonlinearly with respect to external pressure.

As $\partial V_1/\partial p_4$ is dependent on p_4, we must defer to numerical methods, where we iterate the value of p_4 from our set of ordinary differential equations (3.17) and (3.18), with a range of pressure values (in this case 0 to 30 mmHg for consistency). Its value is therefore found during the unsteady state analysis (§3.6).

To estimate the value of the valve permeability k_{42}, we investigate the resistance to CSF outflow in the literature, and assess its appropriateness for use in our model. Studies by Ekstedt (1978) and Albeck et al. (1991), suggest this resistance must be in the range of 6–10 mmHg/ml/min. However, measured values are readings taken from the lumbar puncture outflow of healthy subjects when saline is infused at a constant rate in the supine position. It is unknown whether the arachnoid villi opens at any point and if the measured value is representative of this flow, or a complement of it, or neither. We therefore do not make a direct comparison of the two flows, but rather assume that the permeability of the arachnoid villi must be similar or greater than other permeabilities in order to ensure an intracranial pressure balance. For the purposes of a proof-of-concept of this model, we assume the resistance to CSF outflow in the arachnoid villi is 0.5 mmHg/ml/min, thus the permeability of the valve is $k_{42} = 2.5 \times 10^{-10}$ m^3/s/Pa.

Values for the flow in the foramen of Magendie and the foramen of Luschka, that is S_{34} in our model, are inconclusive; some estimates suggest this can be up to 18 ml/min, which is 50 times greater than the CSF production rate (Gupta et al., 2009). The aqueduct of Sylvius however,

[5]Postural changes will be covered in detail in Chapter 4.

which is a distinct channel proximal to the fourth ventricle, has been measured routinely, perhaps because it can be measured using magnetic resonance imaging (MRI). The value for this flow is approximately 3.44 ml/min, one order of magnitude greater than the production rate. If we assume the flow in the aqueduct of Magendie is of a similar scale, we can approximate k_{34} by taking the ratio between the production flow and the flow at the aqueduct of Sylvius and apply it to the ratio between permeabilities k_{13} (permeability of production rate) and k_{34}. Since flow in the aqueduct of Sylvius is one order of magnitude greater than the production rate, we estimate $k_{34} \approx 10 \times k_{13}$.

To estimate V_{30} and V_{40}, we assume that these volumes are related to the cerebral blood volume V_1 in the same ratio as S_{13} and S_{14} are related to the cerebral blood flow Q

$$V_{30} = V_1 \left(1 : 100 = S_{13} : Q\right) \tag{3.29}$$

$$V_{40} = V_1 \left(1 : 100 = S_{14} : Q\right), \tag{3.30}$$

where V_1 is the total volume of the cerebral vasculature.

To estimate the volume in the dural sinuses V_2, we need to account for the volume of blood as well as the volume of CSF going into the dural sinuses. We then have

$$V_2 = \frac{V_{\mathrm{v0}}}{\varrho} + \upsilon V_4, \tag{3.31}$$

where $1/\varrho$ is the increase in volume from the small veins to the dural sinuses, ϱ is as defined in Chapter 2 (i.e. radii ratio between the lumped entry vessel and the model root vessel), V_{v0} the volume in the last venous generation (generation 0), and υ is the fraction of volume in the SAS that goes into the dural sinuses. If we assume as a first approximation that a fifth of the volume in the SAS is at any one time in the dural sinuses, we obtain $\upsilon = 1/5$.

Lastly, we expect the compliance of the ventricles to be related to the compliance of the ependyma, since the ventricles are essentially sacs formed from ependymal cells. This however, is difficult to measure, and to our knowledge no measurements have been attempted. Cranial and ventricular compliance is routinely tested in intensive care units following trau-

matic brain injury (TBI), subarachnoid haemorrhage or in hydrocephalous or tumour patients. Sites for monitoring intracranial pressure (ICP) via a pressure probe include the parenchyma, the subarachnoid, and the ventricles. Recording of changes in volume vs changes in pressure to calculate the compliance consists in either manual CSF bolus injection to the ventricles (gold standard) or through the Spiegelberg compliance device (Yau et al., 2002, 2000). The latter method quantifies the ventricular compliance by measuring the change in intraventricular volume (via a double lumen balloon as a pressure probe) and the cerebral perfusion pressure[6] when automatically increasing the volume to a zero reference ICP. One of the issues with measurements of intracranial compliance and in particular ventricular compliance is the fact that the studies conducted typically involve pathological conditions. In these cases the ICP is typically already elevated and thus the reading of volume changes, and by extension the calculation of compliance, is based on potentially already stretched ventricles. A way to address this problem is by accounting for the difference in the measured pressure (gauge pressure) and the initial ICP to obtain an absolute pressure, that is $p_{\text{absolute}} = p_{\text{gauge}} + p_0$, where p_{gauge} is the measured pressure and p_0 the initial ICP. In Yau et al. (2002), if we take an averaged value between the sampled TBI and tumour patients groups we obtain 0.865 ml/mmHg within the 0-10 mmHg range, if we assume this is valid for p_{gauge} =5 mmHg, and the initial ICP p_0 =20 mmHg, then we can estimate a compliance of 4.3 ml/mmHg, that is if we assume compliance is linearly related to the ICP for a healthy case. In both studies a linear relationship can be seen between compliance and ICP for a range of 0-10 mmHg of gauge ICP, after this range it is very clearly nonlinear but we can assume that for a lower gauge pressure a linear approximation is reasonable. We take a rounded value of 4 ml/mmHg as a first estimate in our model and assess further a different value of ventricular compliance (i.e. $\pm$ one order of magnitude) as part of the sensitivity analysis.

The values to use in the intracranial model are summarised in Tables 3.1 and 3.2. We specify the values for S_1 for region I only in Table 3.2, however values for region II are similar though not shown.

[6]Cerebral perfusion pressure is defined in clinical literature as the difference between mean arterial pressure and intracranial pressure.

	Value	Units
α	0.16	–
C_3	3.01×10^{-9}	m^3/Pa
H	1.10	–
k_{42}	2.51×10^{-10}	$m^3/Pa.s$
p_{20}	24.63	mmHg

Table 3.1: Parameter values for the intracranial model.

	Value	Units
k_1	3.8×10^{-11}	$m^3/Pa.s$
k_{13}	6.1×10^{-12}	$m^3/Pa.s$
k_{14}	3.2×10^{-11}	$m^3/Pa.s$
k_{34}	6.1×10^{-11}	$m^3/Pa.s$
p_1^*	21.6	mmHg
S_{10}	6.6	ml/min

Table 3.2: Estimated parameter values for pressure region I.

As in Chapter 2, we adopted the following convention for significant figures: up to two significant figures for values less than 10, up to one decimal place for values above 10. For values smaller than two decimal places, scientific notation is adopted with up to two significant figures.

3.4 The steady state solution

In steady state, equations (3.5) and (3.6), imply that

$$0 = S_{13} - S_{34}, \tag{3.32}$$

$$0 = -S_{13} - S_{14} + S_{42}. \tag{3.33}$$

Expanding terms, using equations (3.10)–(3.13),

$$0 = k_{13}(p_1^* - p_3) - k_{34}(p_3 - p_4), \tag{3.34}$$

$$0 = -k_{13}(p_1^* - p_3) - k_{14}(p_1^* - p_4) + k_{42}I_{42}(p_4 - (p_{20} - Hp_4)), \tag{3.35}$$

which can be rewritten as a matrix equation,

$$\begin{pmatrix} -(k_{13}+k_{34}) & k_{34} \\ k_{13} & k_{14}+k_{42}I_{42}(1+H) \end{pmatrix} \begin{pmatrix} p_3 \\ p_4 \end{pmatrix} = \begin{pmatrix} -k_{13}p_1^* \\ k_{13}p_1^* + k_{14}p_1^* + k_{42}I_{42}p_{20} \end{pmatrix}, \tag{3.36}$$

where we find,

$$p_3 = \frac{p_1^*(k_{13}(k_{14}+k_{34}+k_{42}I_{42}(1+H))+k_{14}k_{34})+k_{34}k_{42}I_{42}p_{20}}{k_{13}(k_{14}+k_{34}+k_{42}I_{42}(1+H))+k_{34}(k_{14}+k_{42}I_{42}(1+H))}, \tag{3.37}$$

$$p_4 = \frac{p_1^*(k_{13}(k_{14}+k_{34})+k_{14}k_{34})-k_{42}I_{42}p_{20}}{k_{13}(k_{14}+k_{34}+k_{42}I_{42}(1+H))+k_{34}(k_{14}+k_{42}I_{42}(1+H))}. \tag{3.38}$$

For the valve in a closed position, $I_{42}=0$, equations (3.37) and (3.38) reduce to,

$$p_3 = p_1^*, \tag{3.39}$$

$$p_4 = p_1^*, \tag{3.40}$$

which results in no flux as all the pressures balance to the value of p_1^*. This means the equilibrium pressures for the ventricles and SAS is that of the vasculature, and no net CSF flux is expected intracranially.

When the valve is open there will be a steady state solution which depends on the interaction of all of the boundary conditions and parameters. This solution is interesting in itself but it also provides a basis for the solution of the dynamic problem which will be discussed in detail in the next section.

Using the values in Table 3.1, Table 3.2 for the appropriate pressure range (as mentioned in §3.3), the baseline values of the vascular model, and boundary conditions $Q = 750$ ml/min (cerebral blood flow) and $p_{\text{root}} = 90$ mmHg (input vascular pressure), we solve equations (3.37) and (3.38) for the valve in an open position, i.e. $I_{42}=1$. The results are summarised in Tables 3.3–3.5, where p_1^* and V_1 are included for completeness.

	Steady state value (mmHg)
p_1^*	21.6
p_2	10.9
p_3	13.2
p_4	12.4

Table 3.3: Pressures.

	Steady state value (ml/min)
S_{13}	0.41
S_{14}	2.4
S_{34}	0.41
S_{42}	2.4

Table 3.4: Fluxes.

	Steady state value (ml)
V_1	614.9
V_2	145.8
V_3	30.8
V_4	144.1

Table 3.5: Volumes.

We can observe the pressures and CSF volumes are consistent with those found in the literature, as well as the volumetric flux S_{13} which we relate to the CSF production rate in the choroid plexuses (Czosnyka and Pickard, 2004; Piechnik et al., 2001).

We do not have experimental values for extrachoroidal CSF production, S_{14}, however part of our assumptions included the volume proportionality ratio α. Since the pressures in the ventricles and SAS are similar but not equal, we see that S_{14} is close to six times the flow in S_{13}. Similarly, we do not have values for the overall flow between the ventricles and SAS, S_{34}, but we know that in equilibrium this must be equal to S_{13} as per equations (3.32) and (3.33), which is what we find.

Vascular volume V_1 represents the volume of blood in the vasculature prior to entering the venous dural sinuses. Literature values for cerebral blood volume usually describe the relative blood volume to white and grey matter (Hacking, 2018a; Krieger et al., 2012). Since our model also accounts for the vasculature outside the brain tissue (i.e. superficial pial arteries and veins),

we can expect to have a greater volume, especially since the vessels immediately outside the brain tissue are bigger than the ones inside.

Literature giving quantitative data for the venous dural sinuses is limited. Poor imaging visibility of the dural sinuses makes it difficult to assess them regarding volume and volumetric flux. As a result, our model values V_2 and S_{42} remain without a literature comparison. However, we know the volumetric flux through the arachnoid villi in equilibrium, S_{42}, is the sum of the input flux, $S_{13} + S_{14}$, agreeing with conservation of volume.

In the next sections we explore the changes to the equilibrium values under perturbations, and the dynamic behaviour under different conditions.

3.5 Linear stability analysis

The steady state solution found in §3.4 will only be observed in reality if the system is stable, and so in this section we evaluate the effect of perturbations on the system.

Expanding Equations (3.17) and (3.18), we obtain

$$\frac{dp_3}{dt} = \frac{k_{13}(p_1^* - p_3) - k_{34}(p_3 - p_4)}{C_3} + \frac{-k_{13}(p_1^* - p_3) - k_{14}(p_1^* - p_4) + k_{42}I_{42}(p_4(1+H) - p_{20})}{\partial V_1/\partial p_4}, \tag{3.41}$$

$$\frac{dp_4}{dt} = \frac{-k_{13}(p_1^* - p_3) - k_{14}(p_1^* - p_4) + k_{42}I_{42}(p_4(1+H) - p_{20})}{\partial V_1/\partial p_4}, \tag{3.42}$$

which we rewrite in vector form[7] as

$$\frac{d\mathbf{p}}{dt} = \mathbf{M}\mathbf{p} + \mathbf{q}, \tag{3.43}$$

[7]Note the system is not truly linear since $\partial v_1/\partial p_4$ is in function of p_4.

where

$$\mathbf{p} = \begin{pmatrix} p_3 \\ p_4 \end{pmatrix}, \quad \mathbf{q} = \begin{pmatrix} \frac{k_{13}p_1^*}{C_3} - \frac{p_1^*(k_{13}+k_{14})+k_{42}I_{42}p_{20}}{\partial V_1/\partial p_4} \\ -\frac{p_1^*(k_{13}+k_{14})+k_{42}I_{42}p_{20}}{\partial V_1/\partial p_4} \end{pmatrix}, \tag{3.44}$$

and

$$\mathbf{M} = \begin{pmatrix} \frac{-k_{13}-k_{34}}{C_3} + \frac{k_{13}}{\partial V_1/\partial p_4} & \frac{k_{34}}{C_3} + \frac{k_{14}+k_{42}I_{42}(1+H)}{\partial V_1/\partial p_4} \\ \frac{k_{13}}{\partial V_1/\partial p_4} & \frac{k_{14}+k_{42}I_{42}(1+H)}{\partial V_1/\partial p_4} \end{pmatrix}. \tag{3.45}$$

The valve indicator function $I_{42} = 1$ if $p_{20} - Hp_4 \leqslant p4$, i.e. if $p_4 \geqslant p_{20}/(1+H) = 10.83$ mmHg.

We introduce a small perturbation $\delta\mathbf{p}$,

$$\mathbf{p} = \mathbf{p}_0 + \delta\mathbf{p}, \tag{3.46}$$

where $\mathbf{p}_0$ is the steady solution. Since $\mathbf{p}_0$ is at steady state, Equation (3.43) gives

$$\mathbf{0} = \mathbf{M}\mathbf{p}_0 + \mathbf{q}. \tag{3.47}$$

The time evolution of $\delta\mathbf{p}$ can then be found by

$$\frac{d\delta\mathbf{p}}{dt} = \mathbf{M}\delta\mathbf{p}. \tag{3.48}$$

To find the eigenvalues and eigenvectors of the system, we solve the characteristic equation,

$$\det(\mathbf{M} - \lambda\mathbf{I}) = \mathbf{0}, \tag{3.49}$$

where $\mathbf{I}$ is the identity matrix, and λ the eigenvalues. We obtain the following

$$\lambda = \frac{-(k_{13}+k_{34})\partial V_1/\partial p_4 + (k_{13}+k_{14}+k_{42}I_{42}(1+H))C_3}{2\ C_3\ \partial V_1/\partial p_4} \pm \frac{\Big[\Big(-\big(k_{13}+k_{34}\big)\partial V_1/\partial p_4 + \big(k_{13}+k_{14}+k_{42}I_{42}(1+H)\big)C_3\Big)^2 + 4\big(k_{13}+k_{34}\big)\big(k_{14}+k_{42}I_{42}(1+H)\big)C_3\ \partial V_1/\partial p_4\Big]^{1/2}}{2C_3\ \partial V_1/\partial p_4}. \tag{3.50}$$

Using the eigenvalues λ, we find the nonzero vectors, i.e. the eigenvectors, that satisfy

$$\mathbf{M}\mathbf{v} = \lambda\mathbf{v}. \tag{3.51}$$

In the case of the open valve, i.e. $I_{42} = 1$, we compute the eigenvalues and eigenvectors using the parameter values given in Table 3.1 and Table 3.2 for the appropriate pressure range (as mentioned in §3.3), we obtain the results shown in Table 3.6. We adopt the notation for eigenvectors as v_{ip} where i is the associated eigenvalue and p the pressure corresponding to the eigenvector component.

$\lambda_1 = -1.1 \times 10^{-3}$	$\lambda_2 = -2.2 \times 10^{-3}$
$v_{13} = -0.63$	$v_{23} = -0.99$
$v_{14} = -0.78$	$v_{24} = -0.01$

Table 3.6: Eigenvalues and eigenvectors for $I_{42} = 1$.

We find $\mathrm{tr}(\mathbf{M}) < 0$, $\det(\mathbf{M}) > 0$, and both eigenvalues to be real and negative, thus $\mathbf{p}$ converges to a stable solution. That is, the solution decays exponentially to a stable equilibrium. We also find $\mathrm{tr}^2(\mathbf{M}) - 4\ \det(\mathbf{M}) > 0$, with a value of 1.2×10^{-6} when the valve is open, meaning that the solution to the system is a stable node.

The general solution to equation (3.43), can be written in the form

$$\mathbf{p}(t) = c_1 e^{\lambda_1 t}\mathbf{v}_1 + c_2 e^{\lambda_2 t}\mathbf{v}_2, \tag{3.52}$$

where c_1 and c_2 are constant values which depend on the initial conditions, $\mathbf{v}_1$ the eigenvector corresponding to λ_1, and $\mathbf{v}_2$ the eigenvector corresponding to λ_2.

We observe that $|\lambda_2| > |\lambda_1|$, therefore $e^{\lambda_2 t} \to 0$ converges faster than $e^{\lambda_1 t} \to 0$. We thus refer to λ_2 and $\mathbf{v}_2$ as the *fast* eigenvalue and eigenvector, and to λ_1 and $\mathbf{v}_1$ as the *slow* eigenvalue and eigenvector.

Visualisation of the behaviour of the system when it is perturbed from the steady state is shown in the phase portrait Figure (3.5a), and trajectories in Figure (3.5b).

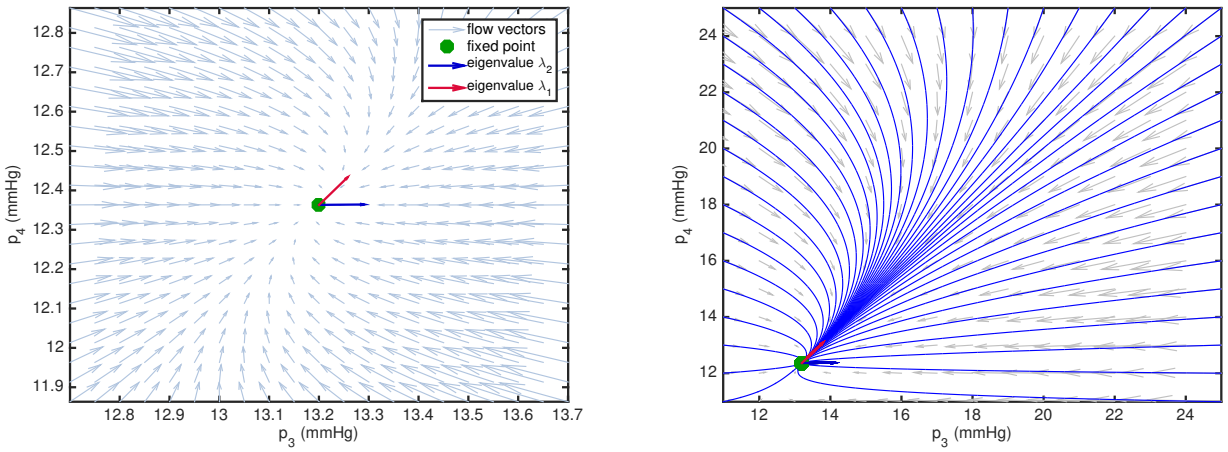

(a) **(b)**

Figure 3.5: Phase portrait when the valve is open showing the flow vectors near the steady state point (marked in green). (a) Eigenvectors (blue and red arrows) and flow vectors (light blue arrows) near the fixed point ($p_{3\text{eq}}$, $p_{4\text{eq}}$). (b) Trajectories (blue solid lines) in a pressure range of 11–25 mmHg.

We observe in Figure 3.5a the eigenvectors for each eigenvalues, centred at the fixed point, where p_3 and p_4 are in equilibrium, denoted as $p_{3\text{eq}}$ and $p_{4\text{eq}}$ respectively. From §3.4, we found the equilibrium for p_3 and p_4 at 13.2 mmHg and 12.4 mmHg, respectively, meaning the system will converge to (13.2, 12.4) in mmHg. In this figure we can observe the flow vectors are heavily influenced by the fast eigenvector. Once the pressures approach the slow eigenvector, they move more slowly towards the fixed point. This can be better visualised in Figure 3.5b, where we see the trajectories of solutions with different initial conditions.

For initial conditions where p_{40} is above the equilibrium, where p_{40} is the initial condition of p_4, we see there are mild overshoots and undershoots in p_3. For cases where $p_{40} \geq 20$ mmHg and $p_{30} \geq 18$ mmHg, where p_{30} is the initial condition of p_3, we can see a more linear descent to the fixed point, after an initial mild undershoot of p_3. This means the initial condition for p_4 is important for dictating the behaviour in the system when the valve is open. We see the

behaviour of the system for a wider range of initial conditions in Figure 3.7.

In the case of the valve closed, that is $I_{42} = 0$, the results are shown in Table 3.7.

$\lambda_1 = -7.5 \times 10^{-5}$	$\lambda_2 = -2.2 \times 10^{-3}$
$v_{13} = -0.67$	$v_{23} = -1.0$
$v_{14} = -0.74$	$v_{24} = -5.6 \times 10^{-3}$

Table 3.7: Eigenvalues and eigenvectors for $I_{42} = 0$.

We again find both eigenvalues to be real and negative, and $\mathrm{tr}^2(\mathbf{M}) - 4\det(\mathbf{M}) = 4.6 \times 10^{-5}$, meaning that for the valve closed, the solution to the system is also a stable node. We also find the second eigenvalue λ_2 to be the *fast* eigenvalue, and the first eigenvalue λ_1 to be the *slow* eigenvalue.

The fast eigenvalues are virtually identical for both cases (valve open and valve closed). This suggests that the rapid response of the system is determined by interactions between the compartments with little dependence on the rate of CSF out of the cranium.

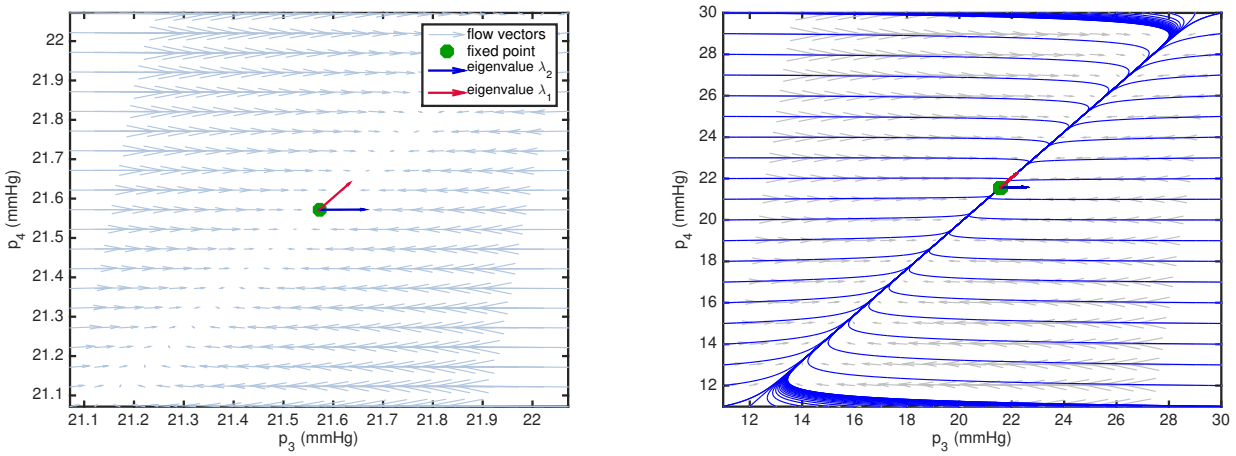

(a) **(b)**

Figure 3.6: Phase portrait when the valve is closed showing the flow vectors near the steady state point (marked in green). (a) Eigenvectors (blue and red arrows) and flow vectors (light blue arrows) near the fixed point ($p_{3\mathrm{eq}}$, $p_{4\mathrm{eq}}$). (b) Trajectories (blue solid lines) in a pressure range of 15–35 mmHg.

Figure 3.6a shows the phase portrait for the valve closed case, and Figure (3.6b) shows the trajectories for different initial conditions. We can observe on Figure 3.6a that most of the behaviour takes place along the fast eigenvector, that is, the flow vectors align in the direction

of the fast eigenvector (depicted by the blue vector) to quickly approach the slow eigenvector (depicted by the red vector), from which a significantly slower flow can be seen to reach the fixed point.

When the valve is closed, $p_{3\text{eq}} = p_{4\text{eq}} = p_1^*$, therefore in this case the system converges to the fixed point (21.6, 21.6) mmHg. In Figure 3.6b, trajectories are shown with different initial conditions, and we can appreciate the impact of the eigenvectors on the solutions. We see very fast overshoots and undershoots for p_3, specially as p_{30} is farther away from the slow eigenvector. In this case, whether p_{40} is above or below the equilibrium makes very little difference to the behaviour of p_3.

There are several differences between the open-valve and the closed-valve cases. Although we find a stable node in both cases, and the fast eigenvector is almost identical, the slow eigenvector of the closed-valve case is 15 times smaller in magnitude than the open-valve one, making the flow vectors significantly slower to reach the fixed point, and having a significant impact on the trajectories at different initial conditions, as can be appreciated in their phase portraits. In the open-valve case, we see some influence from the slow eigenvector, specially when the initial conditions are above the equilibrium. In the closed-valve case, however, the slow eigenvector has a very small influence, allowing for the majority of the behaviour to be guided by the fast eigenvector, until approaching the asymptote of the slow eigenvector. The overshoots and undershoots of p_3 can also be appreciated in the closed-valve case, though in a more pronounced manner than in the open-valve case.

Up to now, we have considered cases where the valve is always open or always closed. However, there are two fixed points, and a valve state associated with each fixed point. We now consider the valve changing from a closed position to an open one which is the solution that is found when the valves are free to open or close[8]. We do this by setting the initial conditions where $p_{40} \leq p_2$ (i.e. ≤ 10.9 mmHg) and observe its behaviour to reach equilibrium, where as we know from the steady-state results, the valve will have to be in an open position.

[8]In the next chapter we explore cases where a transition from open to closed is possible due to the influence of the spinal cavity.

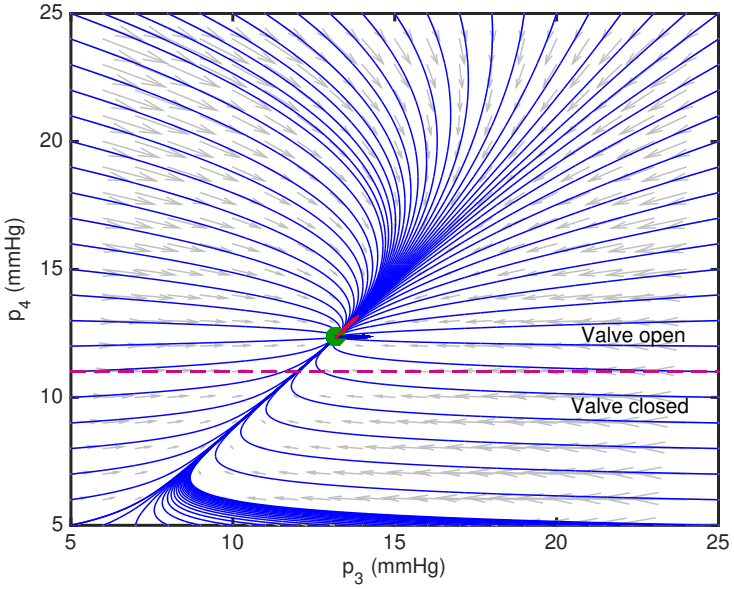

Figure 3.7: Phase portrait when the valve changes from closed to open showing the flow vectors near the steady state point (marked in green). (a) Eigenvectors (blue and red arrows) and flow vectors (light blue arrows) near the fixed point ($p_{3\text{eq}}$, $p_{4\text{eq}}$). (b) Trajectories (blue solid lines) in a pressure range of 5–25 mmHg, and regions where the valve is open and closed (magenta dash line).

In Figure 3.7, we observe solutions for cases where the initial conditions are below p_2, and can observe the transition from the valve closed to open. We observe that before the valve opens, the solutions follow the behaviour seen in Figure 3.6, they are heavily influenced by the first eigenvector and significantly less so by the slow eigenvector, there are fast overshoots and undershoots for p_3, followed by a slow linear ascent towards the fixed point. Immediately after the valve opens ($\geq p_2$), we observe a faster convergence to the fixed point due to a greater influence from the slow eigenvector, overshoots and undershoots are still visible for p_3 but less pronounced. Once the valve is open, we observe the same behaviour seen in Figure 3.5, where the trajectories for p_3 follow a milder overshoot or undershoot than for initial conditions below the equilibrium, and a significantly faster convergence of solutions. We see that as $t \to 0$, all trajectories become parallel to the fast eigenvector on both cases, as it is the one with a numerically bigger eigenvalue. This also means it will take longer for the valve to open the farther below the initial conditions are from the fixed point, this is because the steady state is reached shortly after the opening of the valve. For the case when the initial conditions are above the fixed point, we observe a faster convergence to the fixed point. In this case the valve remains open throughout the trajectory.

We can conclude that in the cases of $I_{42} = 1$ (valve open), and $I_{42} = 0$ (valve closed), the system of equations finds a stable equilibrium in the form of a stable node. This means that as the eigenvalues $\lambda_1 \neq \lambda_2$, there will be an eigenvector greater in magnitude (we denoted it here as the fast eigenvector) that will influence the initial behaviour of the system depending on the initial conditions. We identified that for initial conditions below the fixed point and $I_{42} = 1$, two behaviours can occur: (1) if $p_{30} > p_{40}$ an undershoot occurs in p_3 before following the behaviour of p_4 along the slow eigenvector to approach the fixed point; and (2) if $p_{30} \leq p_{40}$ an overshoot occurs in p_3 before following the behaviour of p_4. For initial conditions above the equilibrium and $I_{42} = 1$, we again observe the overshooting and undershooting of p_3 with respect to p_4 though milder, and we see the convergence to the fixed point is much quicker. For $I_{42} = 0$, the behaviour appears the same whether the initial conditions are above or below the equilibrium, here we can also see overshooting and undershooting of p_3 with respect to p_4 in a more pronounced manner due to a greater difference between the fast and the slow eigenvalue. For transitional cases, where the valve starts in a closed position and changes to open to reach the steady state, the system behaves as described in the closed-valve case for the region where the valve is closed, and as the open-valve case where the valve opens (i.e. $p_4 \geq p_2$).

We explore the behaviour of the system further by analysing the changes with respect to time in the next section.

3.6 The unsteady state solution

The phase plane analysis in the previous section reveals the nature of the dynamic behaviour of the system. To determine the true dynamics we must solve the ordinary differential equations (ODEs). For the unsteady state solution, we computed Equations (3.17) and (3.18) using Matlab ODE solver, ODE45. We use the parameter values in Table 3.1, Table 3.2 for the appropriate pressure range (as mentioned in §3.3), the baseline values of the vascular model, and boundary conditions $Q = 750$ ml/min (cerebral blood flow) and $p_{\text{root}} = 90$ mmHg (input vascular pressure). Here, we also find the value of $\partial V_1/\partial p_4$ by iteration, as detailed in §3.3. We

present four combinations of initial conditions for analysis:

- Case 1: $p_{30} = p_{40}$, and $(p_{30}, p_{40}) < (p_{3eq}, p_{4eq})$;
- Case 2: $p_{30} = p_{40}$, and $(p_{30}, p_{40}) > (p_{3eq}, p_{4eq})$;
- Case 3: $p_{30} \neq p_{40}$, $p_{30} < p_{3eq}$, and $p_{40} > p_{4eq}$;
- Case 4: $p_{30} \neq p_{40}$, $p_{30} > p_{3eq}$, and $p_{40} < p_{4eq}$;

where p_{30} is the pressure in compartment 3 at $t = 0$, p_{40} is the pressure in compartment 4 at $t = 0$, p_{3eq} is the pressure in compartment 3 at equilibrium, and p_{4eq} is the pressure in compartment 4 at equilibrium.

For each case, we highlight the time it takes for the valve to open (where applicable), the behaviour of the pressures and fluxes before and after the valve opens, the time at which they approach equilibrium within a given accuracy, and other behaviours observed on the time-dependent plots.

We define a pressure or flux has *reached*[9] equilibrium at the time when

$$\frac{x - x_{\text{abs}}}{x_{\text{abs}}} < \epsilon, \tag{3.53}$$

where x is the variable of interest ($p_2,\ p_3,\ p_4,\ S_{13},\ S_{14},\ S_{34}$, or S_{42}), x_{abs} its absolute steady-state value, and ϵ the accuracy limit, which we set as 0.01 mmHg for pressure and 0.001 ml/min for flux.

Case 1: $p_{30} = p_{40}$**,** $(p_{30}, p_{40}) < (p_{3eq}, p_{4eq})$

Figure 3.8a shows the pressures for case 1, where we set the initial condition $p_{30} = p_{40} =$ 5 mmHg, for a time span of 6 hours.

[9]N.B. We use the term *reach* to denote the variable is within a given accuracy of the steady-state value, however we acknowledge the term should be used with care as in reality the variable can only approach the asymptote, meaning $x(t) \to x_{\text{eq}}$ as $t \to \infty$.

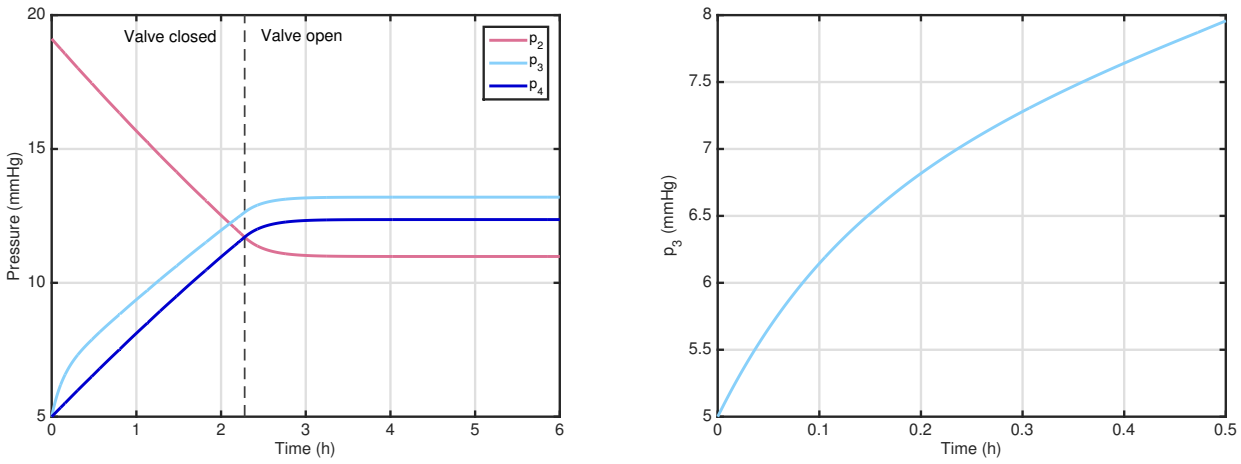

(a) **(b)**

Figure 3.8: Intracranial pressures for initial condition $p_{30} = p_{40} = 5$ mmHg, (a) pressure in the dural sinuses p_2, pressure in the ventricles p_3, and pressure in the SAS p_4 for $0 < t < 6$; (b) p_3 for $0 < t < 0.5$. The dashed line indicates the opening of the valve.

We observe that under these initial conditions, the valve changes from closed ($p_4 < p_2$) to open ($p_4 \geq p_2$) at $t = 2.3$ hours. Before the valve opens, pressure in the dural sinuses, p_2, decreases linearly from its initial value, and pressure in the SAS, p_4, increases linearly from its initial condition p_{40}, until $p_4 = p_2$.

Ventricular pressure p_3 can be seen to have two responses before the valve opens. First it has a steep rise from its initial condition p_{30} in the time interval $0 < t < 0.5$ hours (this is better visualised in Figure 3.8b), followed by a linear increase quasi-parallel to p_4. This behaviour can be explained by referring back to the linear stability analysis, where we see that whilst both p_3 and p_4 are heavily influenced by the fast eigenvector, the change in p_3 is more pronounced than in p_4, specially if p_{30} is far from the equilibrium.

When the valve opens, p_3 and p_4 continue to increase nonlinearly and monotonically, whilst p_2 decreases nonlinearly and monotonically. We find that it takes on average one hour for the pressures to reach equilibrium from the moment the valve opens. Pressure p_2 reaches equilibrium (10.9 mmHg) at $t = 3.3$ hours, p_3 reaches equilibrium (13.2 mmHg) at $t = 3.2$ hours, and p_4 reaches equilibrium (12.4 mmHg) at $t = 3.3$ hours. We find the time constant for p_3, $\tau_{p_3} = 1.3$ hours, and the time constant for p_4, $\tau_{p_4} = 1.5$ hours.

We assess the behaviour of the volumetric fluxes in Figure 3.9, where we see that flux from the vasculature to the ventricles, S_{13}, and flux from the ventricles to the SAS, S_{34}, behave nonlinearly when the valve is closed ($0 < t < 2.3$ hours). In the same time interval, flux from the vasculature to the SAS, S_{14}, decreases linearly, and flux from the SAS to the dural sinuses, S_{42} is zero (indicating a closed valve).

We can observe the effect of the initial response of p_3 on S_{13} and S_{34}, particularly in S_{34}, where an overshoot occurs from $t = 0.1$ hours onwards. Flux S_{34} becomes greater in magnitude than S_{13} from $t = 0.7$ hours until reaching equilibrium (Figure 3.9b shows a closer look at S_{13} and S_{34} as they approach equilibrium after the valve is opened). The compliance of the ventricles defines the curvature of S_{34}, however the overshoot can be seen even at higher values of compliance. This will be explored further in the sensitivity analysis section (§3.7).

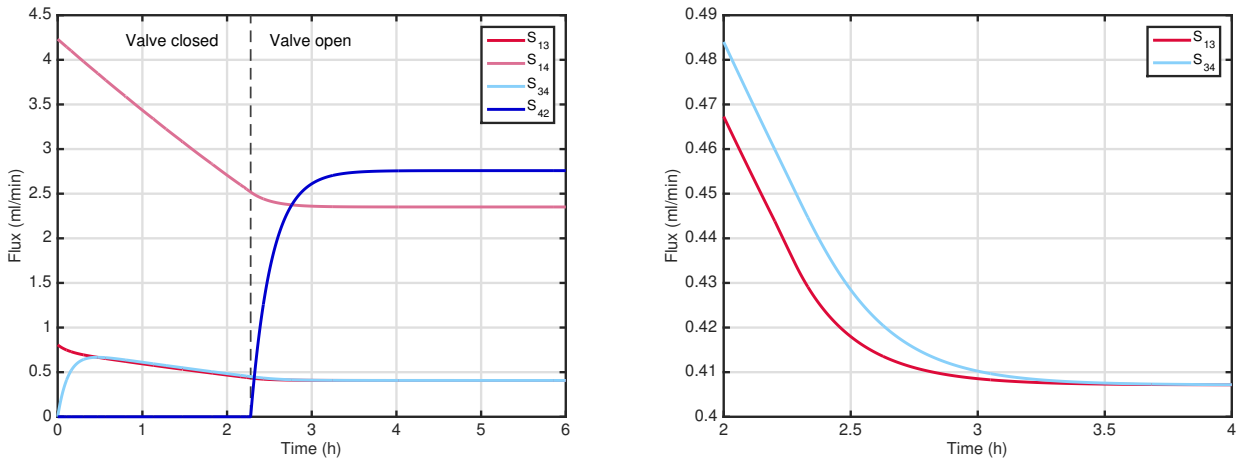

Figure 3.9: Intracranial fluxes for initial condition $p_{30} = p_{40} = 5$ mmHg, (a) flux from the vasculature to the ventricles S_{13}, flux from the vasculature to the SAS S_{14}, flux from the ventricles to the SAS S_{34}, flux from the SAS to the dural sinuses S_{42} (flux passing through the arachnoid villi valve); (b) detail of fluxes S_{13} and S_{34} for a time interval of $2 < t < 4$ hours. The dashed line indicates the opening of the valve.

At $t = 2.3$ hours, the valve opens and we observe in figure 3.9a the flux through the valve (S_{42}), has the most prominent change increasing rapidly for $2.3 < t < 3.4$ hours, before reaching equilibrium (2.8 ml/min) at $t = 4.6$ hours. S_{13} reaches equilibrium (0.41 ml/min) at $t = 3.9$ hours, S_{14} (2.4 ml/min) at $t = 3.9$ hours, and S_{34} (0.41 ml/min) at $t = 4.1$ hours. We know from the steady state analysis, that $S_{13} = S_{34}$ upon reaching equilibrium, thus when the valve

opens S_{42} reaches equilibrium when $S_{42} = S_{13} + S_{14}$, and by the timings above, this must be equal or greater than the last flux to reach equilibrium, in this case S_{34}, which is what we find.

Case 2: $p_{30} = p_{40}$**,** $(p_{30}, p_{40}) > (p_{3eq}, p_{4eq})$

For Case 2 we set $p_{30} = p_{40} = 15$ mmHg. In Figure 3.10a we observe that pressures reach the steady state much faster than in Case 1 where the initial conditions are below the equilibrium (faster on average by 2 hours), and at no time is the valve in a closed position. Pressures p_3 and p_4 decrease nonlinearly and monotonically until reaching equilibrium at 1.2 hours and 1.27 hours respectively. Pressure p_2 decreases nonlinearly until reaching equilibrium at 1.3 hours. We find the time constant for p_3, $\tau_{p_3} = 0.24$ hours, and the time constant for p_4, $\tau_{p_4} = 0.22$ hours.

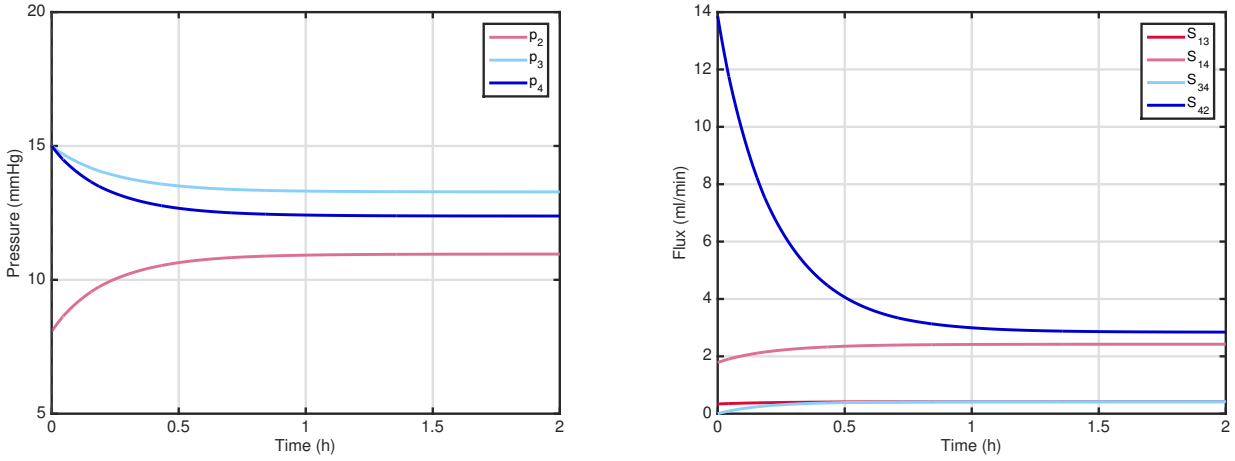

(a) **(b)**

Figure 3.10: Intracranial (a) pressures and (b) fluxes starting from initial pressure of 15 mmHg.

This rapid response in the system is due to the proximity to the steady state when the pressures are above the fixed point when the valve is open (as is the case since $p_{40} > p_2$). In the stability analysis we see that for initial conditions above the equilibrium, a faster convergence would indeed occur. We also observe that p_3 follows the behaviour of p_4, confirming what we find in the stability analysis.

In Figure 3.10b we observe the behaviour of the fluxes under these initial conditions. We see that they also reach the steady state much faster than in Case 1 (average 2 hours faster). Flux

S_{34} is zero at $t = 0$, it then follows a nonlinear increase at $0 < t < 0.5$ hours, and continues to increase at a slower rate to reach equilibrium at $t = 1.9$ hours. A very mild increase is seen in S_{13} and S_{14} (quantified as 0.05 ml/min and 0.5 ml/min respectively), before reaching equilibrium at $t = 1.8$ hours. Flux S_{42} can be seen with a rapid nonlinear decrease to reach equilibrium in exactly 2 hours.

There is a significant impact on S_{42} at $t = 0$ when the initial conditions are above the equilibrium. At high intracranial pressure (i.e. high p_4), flow from the vasculature to the ventricles and SAS must be very small, similarly, flow from the ventricles to the SAS, thus we see small changes in flux S_{13}, S_{14}, and S_{34}. Conversely, flux S_{42}, must allow flow to exit the cranial space to allow pressures to drop and reach equilibrium, which we can see is accomplished quickly.

Case 3: $p_{30} \neq p_{40}$, $p_{30} < p_{3eq}$, $p_{40} > p_{4eq}$

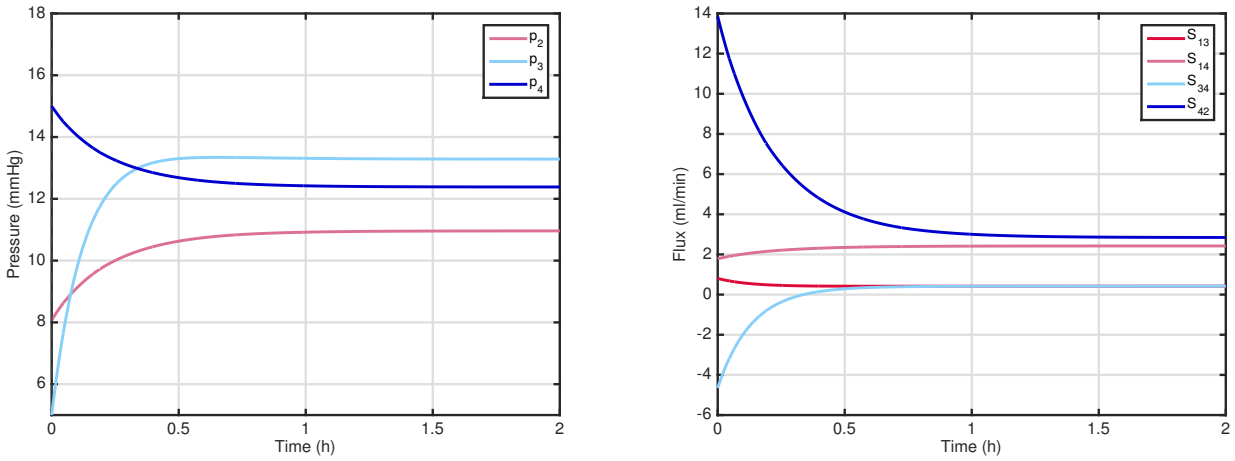

(a) **(b)**

Figure 3.11: Intracranial (a) pressures and (b) fluxes when $p_{30} = 5$ mmHg and $p_{40} = 15$ mmHg.

When setting $p_{30} = 5$ mmHg and $p_{40} = 15$ mmHg, we observe in Figure 3.11a a sharp increase followed by a subtle overshoot in p_3 between $0 < t < 1$ hours, before reaching equilibrium at $t = 1.2$ hours. Again in this case the valve remains open throughout. Pressures p_2 and p_4 behave similarly as in Case 2 (Figure 3.10a), reaching equilibrium at $t = 1.3$ hours, respectively.

In Figure 3.11b, we see flux S_{34} also behaves similarly to Case 2, but with a more pronounced increase from a significantly smaller value. We see that since pressure is much smaller in the

ventricles than in the SAS, flux from the SAS will go into the ventricles, rather than out of the ventricles to the SAS, thus S_{34} is negative until p_3 stabilises after the initial response. Flux S_{34} reaches equilibrium at 1.9 hours. Flux S_{13} decreases 0.20 ml/min nonlinearly between $0 < t \leq 0.30$ hours, and reaches equilibrium at $t = 1.8$ hours. Fluxes S_{14} and S_{42} behave as they do in Case 2, and reach equilibrium at $t = 1.8$ and $t = 1.9$ hours, respectively.

Case 4: $p_{30} \neq p_{40}$, $p_{30} > p_{3eq}$, $p_{40} < p_{4eq}$

For case 4, we set $p_{30} = 15$ mmHg and $p_{40} = 5$ mmHg. In figure 3.12a we observe the valve opens at $t = 2.3$ hours, as in Case 1. Pressure p_3 drops sharply at $0 < t \leq 0.30$ hours, before following the behaviour seen in Case 1. Equilibrium is reached at the same time as in Case 1 for all pressures. In Figure 3.12b, we see S_{34} decays rapidly between $0 < t \leq 0.30$ hours, and it

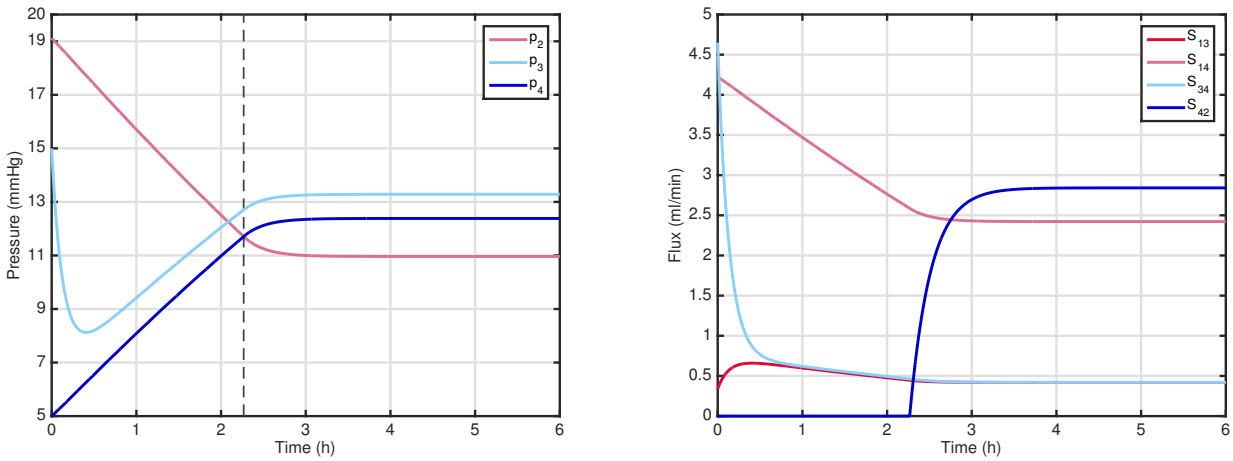

(a) **(b)**

Figure 3.12: Intracranial (a) pressures and (b) fluxes when $p_{30} = 15$ mmHg and $p_{40} = 5$ mmHg. The dashed line indicates the opening of the valve.

is kept again just above S_{13} before reaching equilibrium, thus behaving similar to Case 1 after $t = 0.30$ hours. Fluxes S_{14} and S_{42} also behave in a similar manner to Case 1. Equilibrium is reached at the same time as in Case 1 for all fluxes.

We see in the stability analysis that the initial condition for p_4 dictates the behaviour of the system to a great extent. In this case, we observe it more clearly since it is only when $p_{40} < p_{4\text{eq}}$

that the valve opens, and p_3 has a more pronounced undershoot since $p_{30} > p_{40}$. This is expected as both the valve and p_3 are in function of p_4.

3.6.1 Summary

We summarise the findings in three subsections: valve activation, pressure changes under different initial conditions, and flux changes with different initial conditions.

Valve activation

We notice the valve only opens when $p_{40} < p_{4\text{eq}}$. Since p_2 is a linear function of p_4 (see §3.3), we can expect that an initial higher p_4 will result in an initial lower p_2. Furthermore, the closer p_4 is to $p_{4\text{eq}}$ without surpassing it, the faster the valve opens. This can be observed in Figure 3.13, where we see the behaviour of S_{42} for different initial conditions below the equilibrium. For the cases where $p_{40} > p_{4\text{eq}}$, the valve is in an open position already, we observe this in Case 2 and 3 (Figures 3.10 and 3.11).

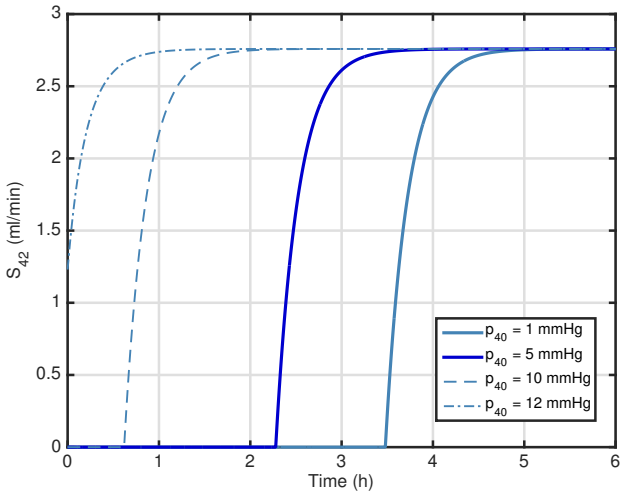

Figure 3.13: Valve opening under different initial conditions.

The valve can take more than 3 hours to open (Figure 3.13) when the initial condition is well below the equilibrium, and can open immediately if p_{40} is close to the equilibrium, as it is the case for $12 \leq p_{40} < 12.4$ mmHg.

Pressure behaviour

Pressure in the dural sinuses, p_2, has a rapid linear drop when $p_{40} < p_{4\text{eq}}$, which becomes nonlinear after the valve opens ($p_2 = p_4$). When $p_{40} > p_{4\text{eq}}$, p_2 increases nonlinearly until reaching equilibrium, here the valve remains open throughout. Pressure in the SAS, p_4, has a monotonic behaviour opposite to that of p_2, meaning it increases linearly as p_2 decreases linearly (although at different rates), and it has a nonlinear decrease when p_2 has a nonlinear increase. Pressure in the ventricles, p_3, has a similar behaviour to p_4, but only after its initial response at $t \geq 0.5$ hours.

For $0 < t < 0.5$ hours, p_3 has the following behaviour:

- steep increase when $p_{30} = p_{40}$, and $(p_{30}, p_{40}) < (p_{3eq}, p_{4eq})$;
- follows behaviour of p_4 when $p_{30} = p_{40}$, and $(p_{30}, p_{40}) > (p_{3eq}, p_{4eq})$;
- mild overshoot when $p_{30} \neq p_{40}$, $p_{30} < p_{3eq}$, and $p_{40} > p_{4eq}$;
- undershoot when $p_{30} \neq p_{40}$, $p_{30} > p_{3eq}$, and $p_{40} < p_{4eq}$.

The time at which the pressures reach equilibrium is greater when the initial conditions are far from the equilibrium. We show cases $p_{30} = p_{40} = 5$ mmHg vs $p_{30} = p_{40} = 15$, where the second case exhibits a faster response. We conducted more scenarios at different initial conditions (not shown) that further confirms this. This agrees with what we see in the linear stability analysis, where the flow vectors were greater the greater the initial conditions.

Flux behaviour

As with the pressures, the fluxes reach equilibrium faster when the initial conditions are close to the equilibrium. This is expected as flux depends on the pressure drop. We observe that for the given permeability k_{42} and initial conditions, flux through the valve, S_{42}, takes ≈ 2.30 hours to reach equilibrium (from the moment the valve opens) for initial conditions where $p_{40} < p_{4\text{eq}}$, and faster (≈ 0.3 hours) for initial conditions $p_{40} \geq p_{4\text{eq}}$ (Figure 3.13). Flux from the vasculature

to the SAS, S_{14}, decreases monotonically when $p_{40} < p_{4\text{eq}}$, and increases monotonically when $p_{40} > p_{4\text{eq}}$.

We observe flux from the vasculature to the ventricles, S_{13}, and from the ventricles to the SAS, S_{34}, have different behaviour depending on the time interval.

For $0 < t < 0.5$ hours:

- S_{13} decreases nonlinearly, and S_{34} overshoots, when $p_{30} = p_{40}$, and $(p_{30}, p_{40}) < (p_{3eq}, p_{4eq})$;
- S_{13} and S_{34} increase nonlinearly (S_{34} more pronounced than S_{13}) when $p_{30} = p_{40}$, and $(p_{30}, p_{40}) > (p_{3eq}, p_{4eq})$;
- S_{13} decreases nonlinearly, and S_{34} increases nonlinearly, when $p_{30} \neq p_{40}$, $p_{30} < p_{3eq}$, and $p_{40} > p_{4eq}$;
- S_{13} overshoots, and S_{34} decreases steeply nonlinearly, when $p_{30} \neq p_{40}$, $p_{30} > p_{3eq}$, and $p_{40} < p_{4eq}$.

For $t > 0.5$ hours:

- S_{13} and S_{34} decrease nonlinearly until reaching equilibrium when $p_{30} = p_{40}$, and $(p_{30}, p_{40}) < (p_{3eq}, p_{4eq})$, and when $p_{30} \neq p_{40}$, $p_{30} > p_{3eq}$, and $p_{40} < p_{4eq}$;
- S_{13} and S_{34} mildly increase nonlinearly when $p_{30} = p_{40}$, and $(p_{30}, p_{40}) > (p_{3eq}, p_{4eq})$, and when $p_{30} \neq p_{40}$, $p_{30} < p_{3eq}$, and $p_{40} > p_{4eq}$.

3.7 Parameter sensitivity analysis

We analyse the sensitivity of the model against all the parameters introduced in this chapter, the boundary conditions, and two key parameters from the vascular model.

The parameters introduced in this chapter are closely related to those introduced as part of the vascular model. The three parameters that are not derived from the vascular model are:

choroid plexuses constant of proportionality, α, ventricular compliance, C_3, and arachnoid villi permeability, k_{42}. Changing α results in complementary effects between flux S_{13} and S_{14} (as per Equations 3.23 and 3.24), but with no other effects on the rest of the system. We thus only focus on changes to C_3 and k_{42} in the rest of this section.

The parameters directly related to the vascular model are: permeability between the vasculature and ventricles k_{13}, permeability between the vasculature and SAS, k_{14}, permeability between the ventricles and SAS, k_{34}, effective vascular pressure, p_1^*, initial pressure at the dural sinuses, p_{20}, slope of pressure changes between dural sinuses and SAS, H, initial vascular flux, S_{10}, and local vascular permeability, k_1. We do not change these parameters directly but rather use the boundary conditions and parameters from the vascular model to change them according to their vascular relationship equations derived in §3.3. The boundary conditions are as defined in previous sections.

The parameters from the vascular model which are tested are: vascular permeability and vascular elastic modulus. We choose these parameters as they are highly sensitive to changes, as seen in Chapter 2.

We define the change in percentage from the baseline, and subscript b to denote the baseline parameter, for example 1.15 E_b denotes an increase of 15% change from the baseline vascular elastic modulus. In the case of the vascular parameters, the percentage change applies equally to both arteries and veins.

We use the initial conditions of Case 1 in §3.6, which we define as the baseline initial conditions. These are $p_{30} = p_{40} = 5$ mmHg, where p_{30} is the ventricular pressure p_3 at $t = 0$, and p_{40} is the pressure in the SAS p_4 at $t = 0$.

We present the variables most affected by each of these parameters[10]. We use a one-at-a-time sensitivity analysis method and analyse the effect each of the parameters has on the model whilst keeping the rest of the parameters fixed. We discuss here and in the next section the impact on the equilibrium points, what this means for the valve activation, and its physiological

[10]The plots on this section use red-based colours to denote vascular-related outputs and blue-based colours for CSF-related outputs.

relevancy.

The sensitivity analysis has a linearised behaviour around the equilibrium point so that responses are symmetrical about that point. It follows that if a positive change in a parameter causes a negative change in a variable, then a negative change will cause a positive change in that variable. This is implicit on the discussion about sensitivity.

Ventricular compliance

The variables most affected by a change in ventricular compliance, C_3, are those directly related to compartment 3: ventricular pressure, p_3, flux from the vasculature to the ventricles, S_{13}, and flux from the ventricles to the SAS, S_{34}. We set a variation range of $\pm$ 1 order of magnitude from the baseline value (3.1×10^{-8} m^3/Pa).

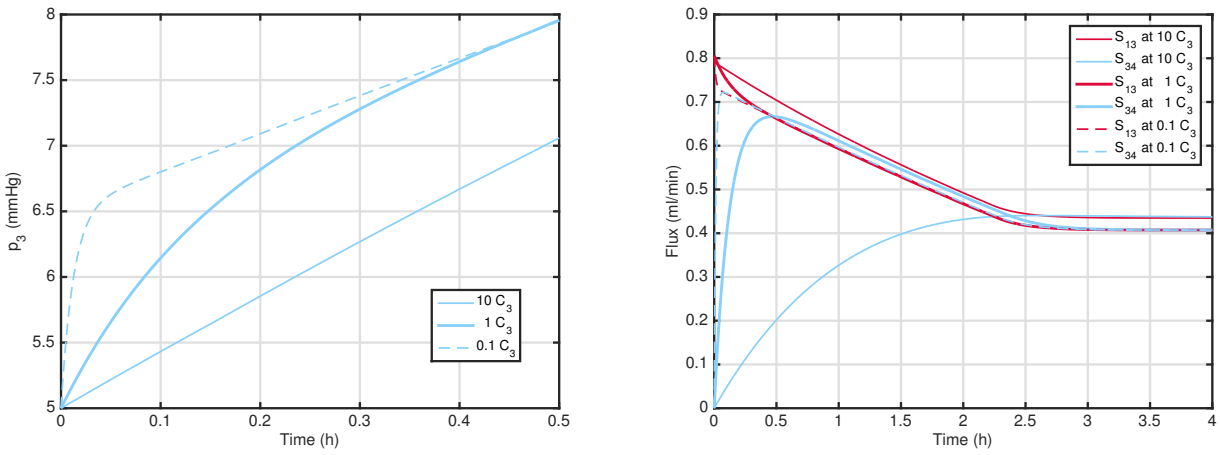

(a) **(b)**

Figure 3.14: Sensitivity to ventricular compliance, C_3, when $p_{30} = p_{40} = 5$ mmHg, (a) ventricular pressure, p_3; (b) flux from vasculature to the ventricles, S_{13}, and flux from ventricles to the subarachnoid space S_{34}.

Figure 3.14a shows the time frame where the change in ventricular compliance affects the ventricular pressure most significantly. We see that at the smaller compliance the initial response is steeper and at the bigger compliance the initial response is less steep, it meets the original p_3 curve at approximately 1.7 hours. This behaviour is reasonable since a less compliant compartment (i.e. stiffer), will lead to an increase in pressure.

The valve activation is not significantly affected, with changes of up to 3 minutes, and neither are the times at which the pressures p_2 and p_4 reach equilibrium, with changes between 1 to 2 minutes, or p_3 with changes on reaching equilibrium of up to 7 minutes from the baseline. There is an increase of 2 mmHg in p_1^* when increasing C_3 as we require a change in the range of p_4 region, as denoted in §3.3. This change however has a negligible impact on the equilibrium pressures and fluxes, with a variation of 0.19 mmHg and 0.10 ml/min, respectively.

In Figure 3.14b we observe the affected fluxes, where a more pronounced curvature of S_{34} and a smoother downwards curvature for S_{13} can be seen the larger the compliance. The overshooting of S_{34} with respect to S_{13} seen on the baseline case, takes longer to occur and it is more pronounced as the compliance increases. Equilibria for both fluxes are not significantly affected when the compliance is smaller, however, when the compliance is larger, S_{13} reaches equilibrium 30 minutes faster than the baseline, and S_{34} reaches equilibrium 1.85 hours slower than the baseline.

We can conclude that changes in ventricular compliance will not significantly affect the valve behaviour, pressure in the dural sinuses, pressure in the SAS, volumetric flux from the vasculature to the SAS or volumetric flux from the SAS to the dural sinuses. However, it will affect pressure in the ventricles, volumetric flux from the vasculature to the ventricles and flux from the ventricles to the SAS. The larger the compliance, the slower the response of pressure in the ventricles, it nevertheless reaches equilibrium at a similar time as the baseline. In the case of the fluxes, the larger the compliance the larger the flux from the vasculature to the ventricles and the small the flux from the ventricles to the SAS.

Arachnoid villi valve permeability

We assess the sensitivity of the model to the permeability of the valve (arachnoid villi), k_{42}. We set a variation range of $\pm$ 1 order of magnitude from the baseline value (2.5×10^{-10} m^3/Pa.s). We see in Figure 3.15 that the changes occur after the valve is opened, obviously. In Figure 3.15a we see a significant increase in pressure in the SAS, p_4, as we decrease k_{42}. This is reasonable since the smaller the permeability the longer the SAS will take to 'drain' CSF into

the dural sinuses. In consequence, pressure in the dural sinuses, p_2, decreases significantly as permeability k_{42} gets smaller and pressure in the SAS increases. We observed in the previous section that the rate at which p_2 drops is greater than the rate p_4 increases, therefore we observe a more pronounced nonlinear decrease in p_2 than the increase in p_4.

Figure 3.15b shows a similar behaviour for pressure in the ventricles, p_3, as that observed in p_4, however, as it is in the baseline case, pressure in the ventricles reaches equilibrium at a higher pressure than in the SAS. We can also appreciate from these figures that decreasing the permeability by a factor of 10, increases the time to reach equilibrium to over 13 hours for the fluxes, an increase of almost 9 hours from the baseline.

In Figure 3.15c we can observe flux through the valve, S_{42}, reaches equilibrium much faster the higher the permeability, resembling almost a step response from the moment the valve opens to the equilibrium. A faster behaviour for a higher permeability is also seen in the rest of the fluxes.

A higher permeability k_{42} will thus lead to faster equilibria for all pressures and fluxes, even though there is no change in the activation of the valve.

In Figure 3.15d we see minimal changes in S_{13} and S_{34} when permeability k_{42} is higher. When k_{42} is one order of magnitude smaller, a more noticeable effect can be seen in S_{13} and S_{34}.

We conclude that when decreasing the arachnoid villi permeability we can then expect an increase in pressure in the subarachnoid space and a decrease in pressure in the dural sinuses. This in turn will result in smaller flux through the valve, and a delayed equilibrium on all parameters. When increasing arachnoid villi permeability, pressures and fluxes reach equilibrium much faster from the moment the valve opens than in the baseline case (approximately 1 hour faster for pressures, and approximately 1.5 hours faster for fluxes).

Vascular permeability

We now assess the changes the vascular permeability has on the compartmental model. In Figure 3.16 we observe the changes when the vascular permeability is changed equally in arteries

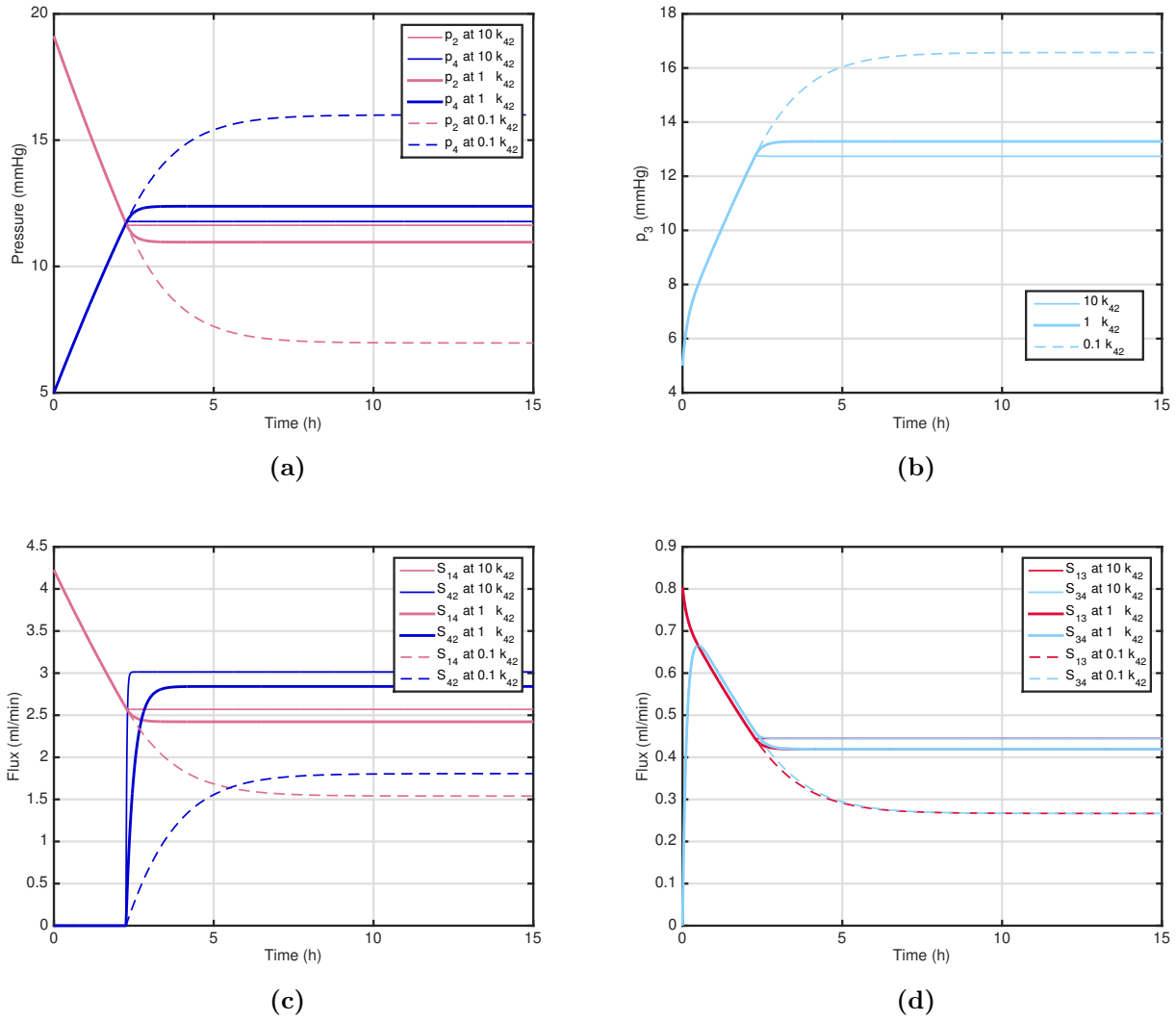

Figure 3.15: Sensitivity to arachnoid villi permeability, k_{42}, when $p_{30} = p_{40} = 5$ mmHg, (a) pressures p_2 and p_4, (b) pressure p_3, (c) fluxes S_{14} and S_{42}, and (d) fluxes S_{13} and S_{34}.

and veins by ± 50 % from their baseline value.

In Figure 3.16a we observe that the lower the vascular permeability the longer it takes for the valve to open ($p_4 \geq p_2$) and thus to reach equilibrium. We can also observe that at a lower permeability, the lower the equilibrium pressure for p_4 and the higher equilibrium pressure for p_2. Conversely, the higher the permeability the faster the valve opens, the higher the equilibrium pressure for p_4 and the lower equilibrium pressure for p_2. The rate at which they reach equilibrium after the valve opens remains similar (approximately 1 hour) for both cases.

In Figure 3.16b we observe that whilst p_3 is affected in a similar manner as p_4, its initial response (at $0 < t < 0.5$ hours) does not change significantly from the baseline.

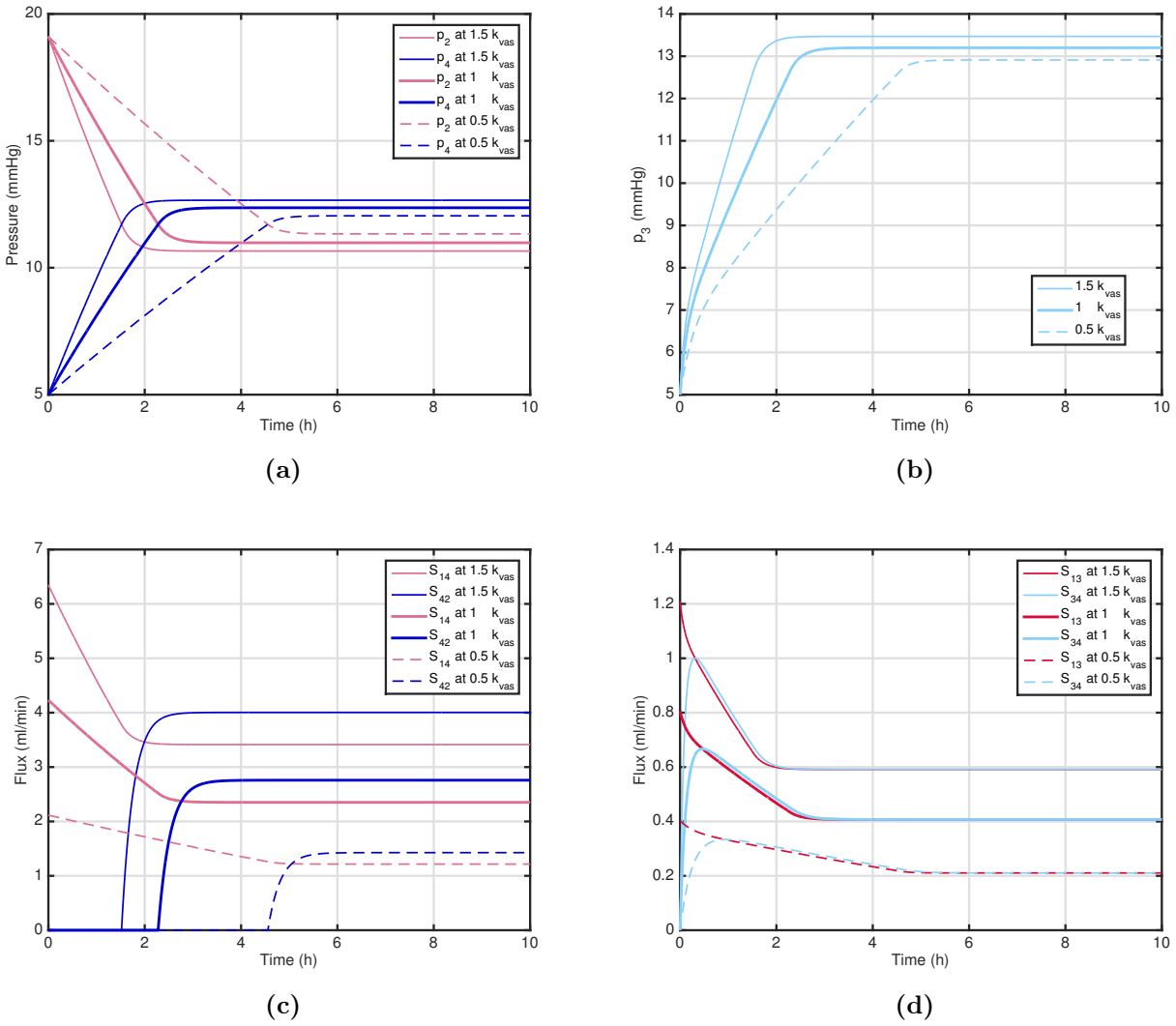

Figure 3.16: Sensitivity to vascular permeability, k_{42}, when $p_{30} = p_{40} = 5$ mmHg, (a) pressures p_2 and p_4; (b) pressure p_3; (c) fluxes S_{14} and S_{42}; (d) fluxes S_{13} and S_{34}.

In Figure 3.16c, we see the different times at which the valve opens (i.e. $S_{42} > 0$). The shape of the curves for S_{14} and S_{42}, as in the pressures, do not change significantly, though they do become steeper the higher the permeability, thus bringing the valve opening and equilibria forward. We can observe this behaviour as well for fluxes S_{13} and S_{34} in Figure 3.16d.

We can conclude that vascular permeability affects all parameters of the CSF compartments, especially pressures in the SAS and the dural sinuses, which in turn affects the opening of the valve and the equilibria time for both pressures and fluxes. At a smaller vascular permeability, the longer it takes for the valve to open and for the parameters to reach equilibrium. At a small permeability, pressure in the dural sinuses is slightly higher than the baseline, and

pressure in the SAS is slightly lower than the baseline. Fluxes decrease the smaller the vascular permeability. The opposite occurs when vascular permeability is high.

Vascular elasticity

We vary the elastic modulus of the vasculature by changing the elastic modulus of the arteries and veins equally by ±25 % from their baseline value[11]. The results are shown in Figure 3.17.

In Figure 3.17a we see that the larger the elastic modulus (i.e. the stiffer the vessels), the faster the valve opens and the faster the pressures reach equilibrium. The smaller the elastic modulus (i.e. the more compliant the vessels), the longer it takes for the valve to open, and the longer it takes the pressures to reach equilibrium.

The equilibrium pressures change in value with a change in elastic modulus. Equilibrium pressures for p_2 and p_4 have a small increase (approximately 1.5 mmHg) if the elastic modulus is larger and a small decrease (approximately 2.4 mmHg) if the elastic modulus is smaller. We notice that p_2 at $t = 0$, p_{20}, is higher the smaller the elastic modulus. The reason behind this initial behaviour is due to the effect the elastic modulus has on the vascular model. As seen in Chapter 2, the smaller the elastic modulus, the greater the pressure inside the vessel. This in turn gives a larger output pressure which becomes p_{20}. The pressure external to the vasculature in this intracranial model, i.e. p_4, now counteracts this effect in the vasculature to achieve equilibrium. This interaction can be seen by the pressure drop in p_2 as p_4 increases until the valve opens and equilibrium is reached. Equilibrium for pressures, as mentioned before, is farther from the reference case (rigid) the more compliant the vessels and closer to the reference the stiffer the vessels, as expected.

Figure 3.17b shows the changes in p_3, which again are similar to those in p_4 with the exception of the initial response where p_3 at $0 < t < 0.5$ hours remains close to that of the baseline. In other words, the initial response of p_3 remains unchanged irrespective of elasticity changes for the given initial conditions.

[11] We use the terms vessel stiffness and vessel compliance for simplicity.

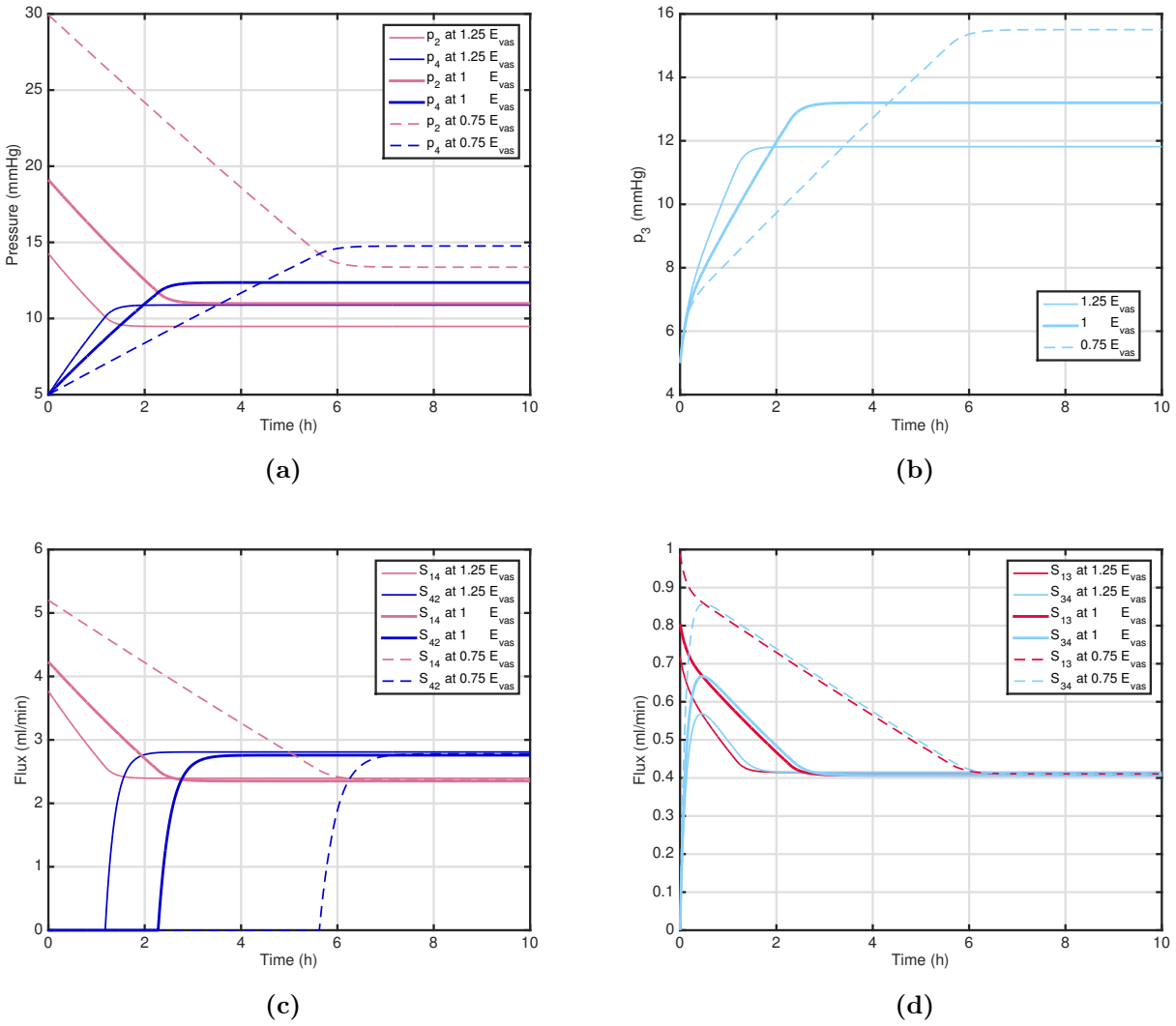

Figure 3.17: Sensitivity to vascular elastic modulus, E_{gen}, when $p_{30} = p_{40} = 5$ mmHg, (a) pressure in the dural sinuses p_2, and in the SAS, p_4 , and (b) ventricular pressure p_3.

The changes on the fluxes can be seen in Figures 3.17c and 3.17d, where we see the fluxes reach a similar equilibrium as the baseline despite their initial response to changes in elastic modulus. In Figure 3.17c we see a more pronounced effect on S_{14} and S_{42} the more compliant the vessels, as a consequence of the changes in pressures p_4 and p_2. We observe in Figure 3.17d, the fluxes dependent on p_3 are more mildly affected due to the initial response of p_3 being similar to the baseline.

We conclude that as the vessels get more compliant (smaller elastic modulus), the equilibrium pressures increase significantly, while the equilibrium fluxes remain similar to the baseline, and as the vessels get stiffer (larger elastic modulus), the equilibrium pressures decrease, while again

the fluxes remain close to the baseline. We also see the interaction between the elastic modulus and the input pressure to the dural sinuses dictates to a great extent the behaviour of the valve and this in turn affects the behaviour of the fluxes. The prolonged activation of the valve for a low elastic modulus allows for flux in the ventricles to increase to twice its equilibrium value while p_4 reaches p_2.

Input pressure

The input pressure, p_{root}, is the pressure to the vascular model which ultimately is the input to the intracranial model as well. It is varied within a range of ± 30 mmHg from the baseline (90 mmHg) to assess sensitivity on the intracranial parameters.

We observe in Figure 3.18a that the higher the input pressure, the pressure drop is more pronounced in p_2. Equilibrium pressures are relatively the same (up to 0.5 mmHg) for all when input pressure is high.

In Chapter 2 we introduced an autoregulation function where pressures in the microcirculation and subsequent venous tree remain unaffected for different input pressures. To test whether the autoregulation function has an effect on the intracranial model, we applied a fixed γ instead of a dynamic one and changed again p_{root}. This confirmed that the autoregulation function does have a strong effect on the intracranial model.

We observe that at higher input pressures, the equilibrium pressure is higher and *vice versa*. However, this does not explain why the autoregulation function, which is designed to work on the microcirculation, can be playing a role in the rest of the compartments. There are two behaviours taking place: (1) the autoregulation function allows the output pressure (i.e. p_{20}) to be dampened, e.g. an input pressure 30 mmHg higher than the baseline will result in only a subtle increase (approximately 5 mmHg increase); and (2) the linear relationship between p_2 and p_4 (as defined in §3.3), allows p_2 to change as its input is changed. When input pressure increases, the slope of p_2 is affected, as per Equation (3.28), the higher the input pressure, the steeper the slope of p_2. It is the combination of these two factors that allows for p_2 to have

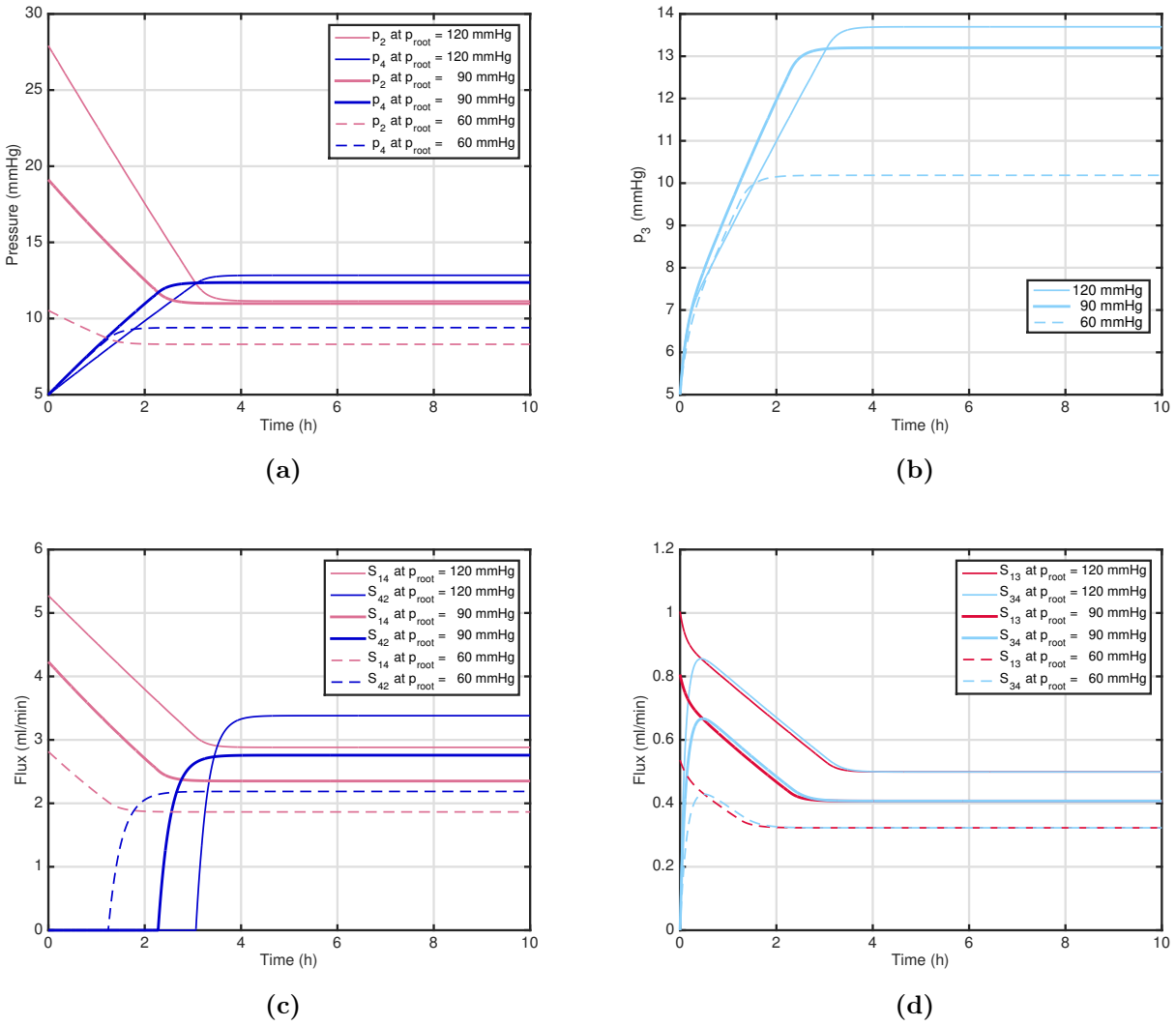

Figure 3.18: Sensitivity to vascular input pressure, p_{root}, when $p_{30} = p_{40} = 5$ mmHg, (a) pressure in the dural sinuses p_2, and in the SAS, p_4 , and (b) ventricular pressure p_3.

a higher pressure drop from an initial value that is higher than the baseline to an equilibrium value that is smaller than the baseline (by 3 mmHg). When input pressure is reduced, we see the opposite effect.

Figure 3.18b shows the changes in p_3, which as in p_4, are small in comparison to the change in input pressure. We again see very small variation at $0 < t < 0.5$ hours.

In Figures 3.18c and 3.18d we see the flux curves shift upwards as the input pressure increases. In Figure 3.18c we can see more clearly the opening of the valve which occurs between 1 and 4 hours. As with the pressures, the fluxes reach equilibrium shortly after the valve opens. This means as input pressure increases, fluxes will increase.

We conclude that a change in input pressure will have a more significant impact on the equilibrium fluxes (±1.5 ml/min), and not as significantly on the equilibrium pressures (±1 mmHg). The valve activation time is affected more noticeably when the input pressure is small, where we see a longer time for the valve to open and thus for parameters to reach equilibrium.

Cerebral blood flow

Cerebral blood flow, Q, is varied within a range of ±100 ml/min from the baseline of 750 ml/min. The changes in pressure and fluxes can be seen in Figure 3.19.

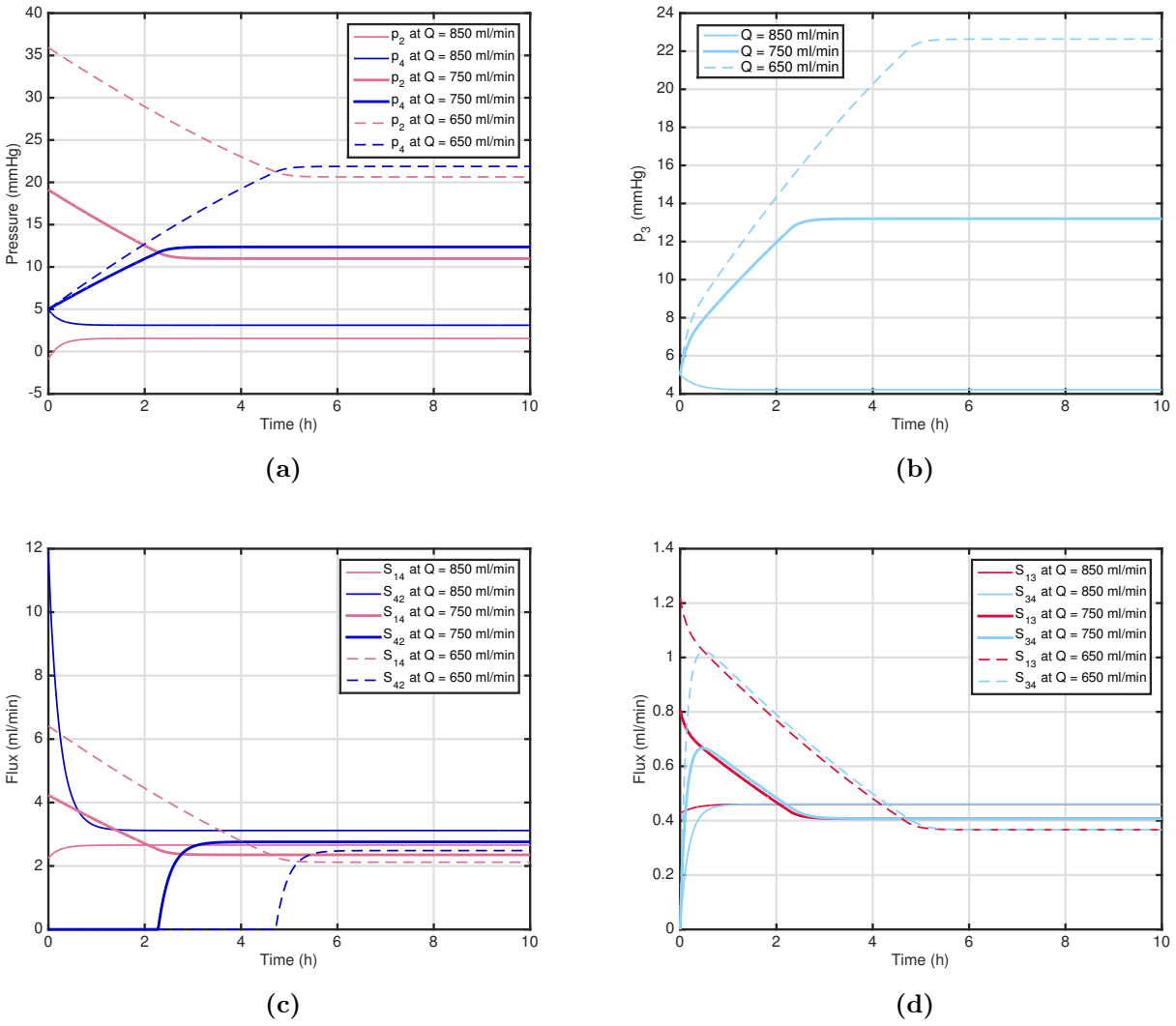

Figure 3.19: Sensitivity to cerebral blood flow, Q, when $p_{30} = p_{40} = 5$ mmHg, (a) pressure in the dural sinuses p_2, and in the SAS, p_4 , and (b) ventricular pressure p_3.

In Figure 3.19a we see that the valve is initially closed when Q is 750 ml/min or less. Further

scenarios explored (not shown), confirmed the limit for Q at which the valve changes from closed to open is 825 ml/min, above this value the valve remains open throughout. In this figure, we see that as Q decreases, the pressures increase, as expected since we have fixed compartmental permeabilities. This increase is approximately 10 mmHg for each 100 ml/min decrease in Q.

Figure 3.19b shows the behaviour of p_3 where we see that its initial response is in the form of an overshoot when Q is 750 ml/min or less, and no overshoot when Q is 850 ml/min. We also see a similar difference in pressure for every 100 ml/min.

In Figures 3.19c and 3.19d we see that as Q decreases, so do the fluxes, the equilibrium values however are not too dissimilar from the baseline. This means the interacting fluxes will accommodate for the changes in Q, while the pressures change significantly with Q. This is reasonable since we have fixed permeabilities, thus a change in Q will result in an inversely proportional change in pressure.

We conclude that a change in Q of 100 ml/min or more will have a significant impact on the intracranial pressures, with the activation of the valve taking almost twice as long when Q is 100 ml/min less than the baseline, and remaining open when $Q \geq 825$ ml/min.

3.8 Summary and discussion

In this chapter we present a compartmental model of the intracranial fluid spaces that interact with the vascular model from Chapter 2. The coupling takes place by means of an effective vascular pressure and its interconnectedness with the venous dural sinuses, cerebral ventricles, and SAS (§3.1), and their related fluxes. The interaction is described mathematically by a system of ordinary differential equations for the interacting compartmental fluxes and pressures. A novel feature of this model is the inclusion of a one-way valve to denote the action of the arachnoid villi, this allows us to analyse the role the arachnoid villi may play in intracranial dynamics. Another feature is the inter-compartmental arrangement where compartment 4 (subarachnoid space) surrounds and interacts with the rest of the compartments. We also

incorporate the Monro-Kellie hypothesis and assess the behaviour of the system accordingly (§3.2). A detailed review of the parameters chosen and their rationale is given (§3.3).

We find a steady state when the valve is open. At rest, in a supine position, and with the assumed parameter values, the open-valve steady state found the effective vascular pressure to be 21.6 mmHg, the dural sinuses pressure 10.9 mmHg, the ventricles 13.2 mmHg and the SAS 12.4 mmHg. All of these are consistent with clinical data as reported in the literature (Gupta et al., 2010; Brinker et al., 2014). The fluxes are in the range of 0.40–2.8 ml/min. The flux from the vasculature to the ventricles, which is analogous to that of the choroid plexus, is as reported in the literature (Czosnyka et al., 2004). As mentioned in §3.3, literature on the quantification of extrachoroidal CSF production is limited and a consensus is yet to be reached. Similarly, no data are available for flux from the ventricles to the SAS. In our model, we find extrachoroidal CSF production to be 2.4 ml/min and flux from the ventricles to the SAS to be 0.40 ml/min. Flux from the SAS to the dural sinuses has not, to our knowledge, been quantified. In our model, the flux through the valve is 2.8 ml/min, which is not insignificant.

When the valve is forced to be closed, we find that another steady state is reached, where the pressures equal the effective pressure of the vascular compartment, resulting in no net flux from the vasculature into the CSF compartments (§3.4). When the valve is free to open, this equilibrium is not a steady state solution because $p_4 > p_2$ causing the valve to open.

We find the solution to the system of equations to be a stable node, both when the valve is open and when it is closed. The eigenvector associated to the eigenvalue which is bigger in magnitude, which we identify as the fast eigenvector, dictates the majority of the behaviour in the open-valve case, with some influence of the slow eigenvector the higher the pressure in the SAS. Pressure in the ventricles overshoots when the pressure in the SAS is smaller than that of the ventricles, and undershoots when larger. The overshoots and undershoots are less pronounced when the initial conditions are above or closer to the fixed point. In the closed-valve case, the fast eigenvector is several orders of magnitude bigger than the slow eigenvector, thus the overshooting and undershooting of pressure in the ventricles is more noticeable, and the approach to the steady state is slower. In this case, the behaviour is the same irrespective

of whether the initial conditions are above or below the fixed point. The transitioning case, where the valve is initially closed and then opens to approach the fixed point, combines these two behaviours (open and closed valve), meaning the closer the initial conditions are to the opening of the valve or to the fixed point, the faster the convergence (§3.5), and the farther below the opening of the valve, the slower the convergence.

The dynamic behaviour of the system reveals that the valve will only open when the initial pressure in the SAS is below the equilibrium. When the initial pressure in the SAS is above the equilibrium, the system converges to the equilibrium without the need to activate the valve. The valve opening time changes depending on the initial conditions. In the baseline case, the valve opens at approximately 2 hours. However, the time extends if the initial conditions are very small and reduces if the initial conditions are large. For values close to the equilibrium, the valve opens immediately, and for values above the equilibrium, the valve remains open throughout. Behaviour of pressure in the ventricles and the SAS confirms what was seen in the stability analysis. Here, overshoots and undershoots for the pressure in the ventricles and related fluxes (flux from vasculature to ventricles, and from ventricles to SAS), are visible. There is limited literature on the functioning of the arachnoid villi, however, our results and analysis suggest the valve must be an integral part in keeping balanced pressures inside the cranium (§3.6). It was also observed that the time scales for changes in the compartmental model are consistently on the order of 1 hour or more. This justifies our use of a quasi-steady cardiovascular model that ignores the arterial pulsations with a time constant close to 1 second. The fast time constant is the same for both the open and closed valve cases implying that the fast adjustment of the model is determined by intra-compartmental exchanges whilst the slow adjustment is related to balancing the fluxes into and out of the model as a whole.

In the sensitivity analysis section (§3.7), we see the larger the ventricular compliance, the longer it takes for the ventricular pressure and related fluxes to reach equilibrium, even though the valve opening time remains similar to the baseline case. This is due to the ventricular compliance not significantly affecting the pressure in the dural sinuses and the SAS. This means that, as long as the arachnoid villi valve functions well, pressure in the SAS will not be affected since the change in ventricular pressure is relieved by the valve. To test this we ran the

compliance cases with a very small valve permeability (two orders of magnitude smaller), mimicking a partially blocked arachnoid villi, and we found that under these conditions both the ventricular pressure and pressure in the SAS find an equilibrium greater than 20 mmHg, and pressure in the dural sinuses becomes negative. Physiologically, this is important for the following reasons: (1) intracranial pressure of 20 mmHg or higher, is considered pathologically high and requires medical intervention; (2) enlargement of the ventricles is often seen in pathologies involving high intracranial pressure; (3) negative pressure in the dural sinuses is experienced in the standing position due to hydrostatic pressure, but rarely so in a supine position. This negative pressure can cause partial or total collapse of the jugular veins thus restricting blood flow back to the heart. Our model has the capability to explore similar vascular abnormalities and related pathologies, in order to investigate potential underlying causes.

The sensitivity to permeability of the arachnoid villi shows that increasing its value by one order of magnitude leads to a faster convergence to equilibrium, and when decreasing its value by the same magnitude, equilibrium is reached significantly later than the baseline value ($>$ 11 hours later). Further testing confirms that a 50% decrease in the permeability, results in $>$ 4 hours delay in reaching equilibrium. Interestingly, the valve opening time remains the same ($\pm$0.001 hours) irrespective of permeability variations. Blockage of the arachnoid villi has been researched extensively in traumatic brain injury (TBI) (Massicotte and Del Bigio, 1999; Ellington and Margolis, 1969), and more recently also in space travel (Roberts et al., 2017). It was observed that when astronauts experience microgravity, the brain and spinal cord is moved upwards blocking the superior sagittal sinus (SSS), which is the most prominent venous dural sinus. The effects of this is hypothesised to induce long-term visual impairment (Lawley et al., 2017). In the case of TBI, it depends on the specific lesion and the chain of events immediately after injury, however, it has been observed that a damaged pathway to the dural sinuses can contribute to swelling and mortality can be high as a result of the increased intracranial pressure (Parikh et al., 2007). As discussed in the ventricular compliance case, when analysed in combination with reduced permeability of the arachnoid villi, this can highlight the issues previously stated.

The vascular permeability has a significant impact on the intracranial model. The smaller the

vascular permeability, the longer it takes the valve to open (approximately twice the time for half the baseline permeability) and the longer the pressures and fluxes take to reach equilibrium. The larger the vascular permeability, the faster the valve opens (approximately 1 hour before the baseline) and the faster the convergence to equilibrium. The equilibrium pressures are similar to those of the baseline (± 1 mmHg in the SAS and ± 0.2 mmHg in the ventricles), however, change in the equilibrium fluxes was more noticeable with ± 1 ml/min difference depending on the smaller or larger vascular permeability, i.e. the larger vascular permeability the larger the flux. This is important since chronically increased vascular permeability could have implications for the intracranial fluxes. We again see that the valve helps regulating increases in permeability by allowing the increased flux to exit quickly. In the event of an acute increase in vascular permeability and a blocked or damaged arachnoid villi, the increased intracranial pressure could indeed be significant. We test this in the model and confirm that an increased vascular permeability of 50% combined with a decreased arachnoid villi permeability can result in intracranial pressure of ≥ 20 mmHg, again borderline critical.

The intracranial model is very sensitive to changes in vascular elastic modulus. Changes of 25% less than the baseline elastic modulus were shown to be enough to increase the pressure in the dural sinuses leading to a delay in the opening of the valve, and thus reaching equilibrium. The valve has a delay of over 2 hours when elastic modulus was smaller (i.e. more compliant vessels), the equilibrium pressures are closer to the reference case (rigid). The opposite was true for the larger elastic modulus, though in a more subtle manner. When combining the effects of elasticity with a reduced arachnoid villi permeability, not only were the pressures in the high intracranial pressure range, but it took over 10 hours to reach equilibrium. When the elastic modulus is larger (i.e. stiffer vessels), there is a decrease in intracranial pressure and the equilibrium pressures approach the reference. This effect is greater than with changes in permeability. An elastic modulus slightly different from the baseline, combined with a partly blocked arachnoid villi can quickly evolve into an undesired physiological range.

Sensitivity to input pressure is mild in comparison to cerebral blood flow (CBF). We found that this is in part due to the autoregulation function of the vascular model which helps to keep a smoother or more constant pressure in the microcirculation, and in part due to the

linear relationship between the pressure in the dural sinuses and the pressure in the SAS. This relationship dictates the valve opening which thus also helps to keep pressures and fluxes relatively constant. Extending the input pressure range further, we found that the average change in pressure was still ±1 mmHg, and in flux again approximately ±1.5 ml/min. An impaired autoregulation function would indeed affect both the pressure and flow. Our model is able to cope with both cases.

Lastly, the model is observed to be very sensitive to changes in CBF, with changes of ±100 ml/min being sufficient to delay the valve opening time by three hours when CBF was low, or remaining open throughout when high. Pressures have average changes of ±10 mmHg for each 100 ml/min, and the initial response of the ventricular pressure is only moderately disturbed. All fluxes, however, remain close to the baseline values. Further testing with a reduced arachnoid villi permeability reveals that with a smaller CBF, the intracranial pressure will increase further (to approximately 25 mmHg) and the intracranial fluxes will reduce slightly further. When CBF is larger, the pressure in the ventricles and SAS are on average 7 mmHg, however, the dural sinuses experience a negative pressure. This again highlights that the arachnoid villi valve may have a key role in balancing intracranial dynamics.

3.9 Concluding remarks

- We constructed a compartmental model of the main intracranial CSF spaces and coupled it with the vascular model from Chapter 2. The two models interact by means of the vascular volume, effective vascular pressure, pressure in the dural sinuses and transmural flux into the ventricles and subarachnoid space.
- Important parameters from the vascular model were able to be tested such as cerebral autoregulation. The model also integrates the Monro-Kellie hypothesis.
- The compartmental arrangement as well as the inclusion of a one-way valve to mimic the effect of the arachnoid villi proved to be key to the adequate functioning of the CSF distribution.

- The steady state results show the pressures, fluxes and volumes are as described in the literature.

- The stability analysis shows the system is a stable node with the fast eigenvalue having an eigenvector for the subarachnoid space that dictates the majority of the behaviour of the system, meaning the ventricular pressure is secondary to that of the subarachnoid space.

- Two steady states were shown to be possible, one with the valve open and one with the valve closed, though the latter resulted in all intracranial pressures balancing resulting in no net flux.

- The unsteady state results show the dynamics of the system confirming what was shown in the stability analysis. It is observed how the valve opens when the initial pressure in the subarachnoid space is less than that of the dural sinuses.

- The sensitivity results show the behaviour of the valve can be affected by changes in vascular permeability, vascular elastic modulus, cerebral blood flow and mildly by changes in input pressure. The latter minimised by the effects of autoregulation.

- The model captures the intricate behaviour between the cerebral circulation and the CSF compartments and the effects the arachnoid villi and autoregulation have on CSF distribution.

Chapter 4

Craniospinal model

In this chapter we augment the intracranial model developed in Chapter 3 by introducing the spinal fluid spaces and investigating their interaction with the intracranial fluids. We explore: (1) dynamics of pressures and fluxes of the craniospinal compartments for a range of parameters; (2) effects of opening and closing of the arachnoid villi valves; (3) stability of the solution to perturbations; and (4) effects of postural changes on the intracranial and spinal pressures and fluxes.

4.1 Introduction to the model

The bony structure of the spinal cavity[1] encases the spinal cord along the vertebral column. As in the cranium, the spinal nervous tissue, which extends from the intracranial nervous tissue via the medulla oblongata, has a set of protective layers or meninges. These meninges are the same as in the cranium (Figures 1.2 and 3.1), with the exception of the dural spaces[2] which now instead of forming dural sinuses with their two layers (meningeal and endosteal), they form small *sacs* encasing blood vessels, nerves, and drained CSF from spinal arachnoid villi as well

[1] As mentioned in Chapter 1, we use the term spinal cavity instead of spinal canal to avoid confusion with the central canal.

[2] The spine also has epidural spaces filled with CSF and lymphatic fluid in addition to the dural sacs. In this model we avoid the complexity of distinguishing these two spaces by assuming a single space outside the dura, which we will call the dural space.

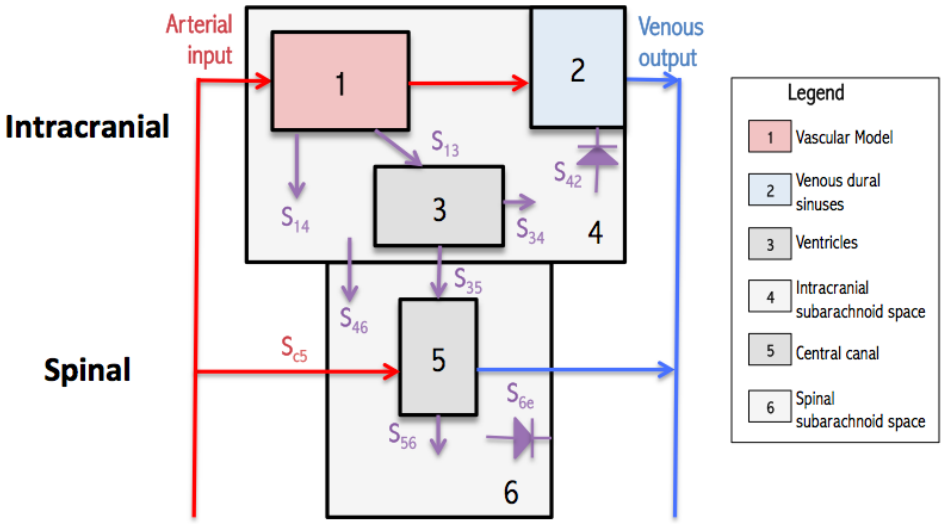

Figure 4.1: Coupled craninospinal compartmental model with CSF fluxes. Compartments (represented by black boxes): 1 represents the cerebral vasculature (i.e. generational model), 2 the venous dural sinuses, 3 the cerebral ventricles, 4 the intracranial SAS, 5 the central canal, and 6 the spinal SAS. Fluxes on figure: S_{13} flux from vasculature to the ventricles, S_{14} flux from vasculature to the intracranial SAS, S_{42} unidirectional flux to the venous dural sinuses, S_{35} flux from cerebral ventricles to central canal, S_{56} flux from central canal to spinal SAS, S_{46} flux from intracranial SAS to spinal SAS, S_{c5} net flux from the spinal vasculature to the central canal, S_{6e} unidirectional flux from spinal SAS to external spinal space (here, to spinal venous output).

as lymphatic fluid from outer dural spaces. These cranial and spinal structures were reviewed in detail in Chapter 1.

The spinal arachnoid villi are also present along the spinal arachnoid. These, as intracranially, allow CSF to exit the subarachnoid space[3] (SAS) into the dural sacs. Arachnoid villi can also drain into epidural spaces but for simplicity we assume a single outer dural space.

Another CSF space is that of the central canal which, in this model, we assume to be a very thin vessel filled with fluid extending along the spinal cord. The blood supply and drainage to the spinal cord is accounted for as a single input and output for simplicity.

In this model, we incorporate the vascular model developed in Chapter 2, the intracranial spaces developed in Chapter 3 and add two additional compartments of CSF space and an input and an output of blood to the spine. The model is represented schematically in Figure 4.1. We treat the spinal cavity as a cylinder concentric to the spinal cord and the central canal. Communication between intracranial and spinal spaces is as follows: the ventricles, in addition

[3]We distinguish SAS by denoting their location as spinal or intracranial, i.e. spinal SAS or intracranial SAS.

to communicating with the cerebral vasculature and the intracranial SAS, communicate directly with the central canal (compartment 5); and the intracranial SAS communicates directly with the spinal SAS (compartment 6). We represent the spinal arachnoid villi as a single one-way valve governed by the pressure difference between the spinal SAS and the spinal outer-dural space, denoted as spinal external pressure. As in the intracranial model, we delimit the spinal SAS by the dura mater.

In Figure 4.1 we observe the compartmental interaction between the two previous models (vascular generational model discussed in Chapter 2 and the intracranial model discussed in Chapter 3) and the spine. We note that whilst the intracranial fluxes S_{13}, S_{14}, and S_{34} are the same as in the intracranial model, the overall volume is affected by the fluxes between compartments 3 and 5 (S_{35}), compartments 4 and 6 (S_{46}), and compartments 5 and 6 (S_{56}).

We introduce a vascular component to the spinal compartments, S_{c5}, by means of a net flux source to compartment 5. This is analogous to the cerebral vascular compartment 1, with the exception that all of the vascular flux in this case is directed towards one CSF compartment (5) rather than two. Contributions of CSF flux from the vasculature to the spinal SAS are accounted by S_{56}. The unidirectional flux of the arachnoid villi is denoted by S_{6e}. We assume the spinal vasculature contributes to the production of CSF in the spine through the microcirculation in the spinal cord, thus adding to the CSF in the central canal. This is consistent with literature noting that CSF production in the spine is achieved through the ependyma of the central canal, which as in the intracranial ventricles, they are dense in capillaries (Gray, 1989).

We give special attention to the gravitational effects these spinal compartments provide to the intracranial ones. In this model we assume the zero reference pressure is at the heart level. We describe each of the fluxes, pressures and gravitational terms in the following section.

4.2 Governing equations

We build on the derived equations from Chapters 2–3 and apply the same principles to construct the spinal compartments. We adopt the same notation convention as in the intracranial model

where a variable X_{ij} denotes X between compartments i and j, e.g. S_{35} is the volumetrix flux between compartments 3 and 5. In addition to subscripts 5 and 6 to denote compartments 5 and 6, respectively, in this model we add the subscript c to denote circulation contributing to CSF production in the spine, subscript s to denote spinal, subscript b to denote brain, and subscript e to denote external to the arachnoid-dura meninges or, in other words, the outer-dural space. For the hydrostatic terms we also add a first subscript h before s, b or compartment numbers as second subscripts. As in the vascular model, we also use the subscript words csf to a variable pertaining to CSF spaces, *blood* to a variable pertaining to blood spaces, and *cord* to a variable pertaining to the spinal cord, e.g. p_{hcsf} is the hydrostatic pressure for CSF spaces.

Conservation of mass applies to compartments 5 and 6, thus changes in volume depends on the net sum of its fluxes. From Equations (3.1) and (3.3) we obtain,

$$\frac{dV_5}{dt} = S_{35} - S_{56} + S_{\mathrm{c5}}, \tag{4.1}$$

$$\frac{dV_6}{dt} = S_{46} + S_{56} - S_{\mathrm{6e}}, \tag{4.2}$$

$$V_5 = V_{50} + C_5\left(p_5 - p_6\right), \tag{4.3}$$

$$V_6 = V_{60} + C_6\left(p_6 - p_{\mathrm{e}}\right), \tag{4.4}$$

where the fluxes between compartments are proportional to the pressure difference between them. From Equation (3.2) we obtain

$$S_{\mathrm{c5}} = k_{\mathrm{c5}}(p_{\mathrm{c}} - p_5), \tag{4.5}$$

$$S_{56} = k_{56}(p_5 - p_6), \tag{4.6}$$

$$S_{35} = \frac{p_3 - p_5 + p_{\mathrm{h35}}}{R_{35}}, \tag{4.7}$$

$$S_{46} = \frac{p_4 - p_6 + p_{\mathrm{h46}}}{R_{46}}, \tag{4.8}$$

$$S_{6e} = k_{\mathrm{6e}} I_{\mathrm{6e}}(p_6 - p_{\mathrm{e}}), \tag{4.9}$$

where I_{6e} is the indicator function of the status of the spinal valve, defined as

$$I_{6e} = \begin{cases} 1 & \text{if} \quad p_6 \geq p_\text{e} \\ 0 & \text{if} \quad p_6 < p_\text{e}, \end{cases} \tag{4.10}$$

implying the valve is only open (and flux $S_{6\text{e}}$ is greater than zero) when the pressure in the spinal SAS, p_6, exceeds that of the external pressure, p_e.

4.2.1 Interconnectivity with cranial compartments

Adding the two spinal compartments has an impact on the volume conservation equations intracranially. Rewriting Equations (3.5) and (3.6) to include fluxes to the spinal compartment,

$$\frac{dV_3}{dt} = S_{13} - S_{34} - S_{35}, \tag{4.11}$$

$$\frac{dV_4}{dt} = S_{14} + S_{34} - S_{42} - S_{46}. \tag{4.12}$$

As mentioned previously, we assume the fluxes S_{13}, S_{14}, S_{34}, and S_{42} are as defined in the intracranial model. We assume compartment 5 is an extension of compartment 3, and compartment 6 is an extension of compartment 4, thus compartment 3 and 5 are directly connected, as are 4 and 6.

We modify the Monro–Kellie hypothesis to include the changes made from the inclusion of the spinal compartments to the intracranial compartments. We can thus obtain the intracranial pressure, p_4, by differentiating Equation (3.9),

$$\frac{dp_4}{dt} = \frac{-S_{13} + S_{35} - S_{14} + S_{42} + S_{46}}{\partial V_1 / \partial p_4}, \tag{4.13}$$

where $\partial V_1 / \partial p_4$ is found iteratively as done so for the intracranial model in Chapter 3.

4.2.2 Gravitational terms

In hydrostatic equilibrium, balance of forces in any fluid space requires

$$\partial p_{\mathrm{h}} = -\rho g \partial z, \tag{4.14}$$

where z is the vertical axis, p_{h} is the hydrostatic pressure, ρ the density of the fluid of interest (CSF or blood), and g the acceleration due to gravity. Hydrostatic pressure affects all compartments and vasculature in the model. Here we assume the distance between the ventricles and the heart is the same as that between the intracranial SAS and the heart, as we consider the same distance (Figure 4.2). Similarly, we assume the hydrostatic pressure between the central canal and the heart is the same as that between the spinal SAS and the heart.

Assuming that the axis of the body forms an angle θ with respect to a horizontal reference, and there is a linear distance h_{b} between the heart and the mid-brain and a distance h_{s} between the heart and the mid-spine, the hydrostatic pressure for the intracranial CSF compartments is

$$p_{\mathrm{h3}} = p_{\mathrm{h4}} = \rho_{\mathrm{csf}} g h_{\mathrm{b}} \sin\theta. \tag{4.15}$$

$$p_{\mathrm{h5}} = p_{\mathrm{h6}} = \rho_{\mathrm{csf}} g h_{\mathrm{s}} \sin\theta. \tag{4.16}$$

Then the hydrostatic pressure between intracranial and spinal CSF compartments is

$$p_{\mathrm{h35}} = p_{\mathrm{h46}} = \rho_{\mathrm{csf}} g (h_{\mathrm{b}} + h_{\mathrm{s}}) \sin\theta, \tag{4.17}$$

Figure 4.2: Hydrostatic reference in the vertical position ($\theta = \frac{\pi}{2}$).

The cerebral circulation is also affected by changes in posture, its hydrostatic pressure is

$$p_{\mathrm{hblood}} = \rho_{\mathrm{blood}} g h_{\mathrm{b}} \sin\theta. \tag{4.18}$$

To derive the resistances along the spinal cavity, we consider the geometry shown in Figure 4.3, where d_5 denotes the diameter of the central canal (compartment 5), d_{cord} the diameter of the spinal cord, and d_6 the diameter of the spinal cavity (compartment 6).

We assume Hagen–Pouiseuille flow in the central canal, and thus the resistance between compartments 3 and 5 is

$$R_{35} = \frac{8\pi\mu l_{35}}{(A_5)^2}, \tag{4.19}$$

where $l_{35} = h_b + h_s$ is the length between the central canal and the ventricles, and $A_5 = \pi(d_5)^2/4$ the cross-sectional area of the central canal.

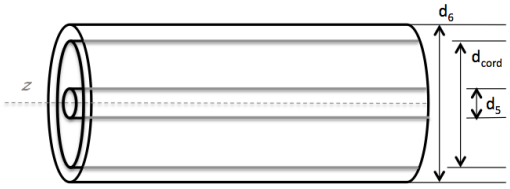

Figure 4.3: Concentric spinal cord schematic.

For flow in compartment 6 we use the Hagen–Poiseuille relationship for annular flow[4] between the spinal cord and the spinal cavity

$$Q = \frac{\pi G}{32\mu}\left((d_6)^2 - (d_{\text{cord}})^2\right)\left((d_6)^2 + (d_{\text{cord}})^2 - \frac{(d_6)^2 - (d_{\text{cord}})^2}{\ln(d_6/d_{\text{cord}})}\right). \tag{4.20}$$

Hence, we find that the resistance between compartment 4 and 6 is

$$R_{46} = \frac{32\mu_{\text{csf}} l_{46}}{\pi\left((d_6)^2 - (d_{\text{cord}})^2\right)\left((d_6)^2 + (d_{\text{cord}})^2 - ((d_6)^2 - (d_{\text{cord}})^2)\ln(d_6/d_{\text{cord}})\right)}, \tag{4.21}$$

which simplified further gives

$$R_{46} = \frac{32\mu_{\text{csf}} l_{46}}{\pi\Omega}, \tag{4.22}$$

where $\Omega = \left(((d_6)^2 - (d_{\text{cord}})^2)\left((d_6)^2 + (d_{\text{cord}})^2 - ((d_6)^2 - (d_{\text{cord}})^2)\ln(d_6/d_{\text{cord}})\right)\right)$.

[4]That can be derived from Equation (2.18) when the axial velocity $w = 0$ at $r = d_{\text{cord}}$, and $w = 0$ at $r = d_6$.

4.2.3 Summary of the governing equations

The equations governing the craniospinal model are

$$\frac{dV_3}{dt} = S_{13} - S_{34} - S_{35}, \tag{4.23}$$

$$\frac{dV_4}{dt} = S_{14} + S_{34} - S_{42} - S_{46}, \tag{4.24}$$

$$\frac{dV_5}{dt} = S_{35} - S_{56} + S_{c5}, \tag{4.25}$$

$$\frac{dV_6}{dt} = S_{46} + S_{56} - S_{6e}, \tag{4.26}$$

$$V_3 = V_{30} + C_3(p_3 - p_4), \tag{4.27}$$

$$V_4 = V_{40} + C_4\left(p_4 - p_{\text{skull}}\right), \tag{4.28}$$

$$V_5 = V_{50} + C_5\left(p_5 - p_6\right), \tag{4.29}$$

$$V_6 = V_{60} + C_6\left(p_6 - p_e\right), \tag{4.30}$$

$$V_1 + V_2 + V_3 + V_4 = \text{constant}. \tag{4.31}$$

The craniospinal fluxes are defined by,

$$S_{c5} = k_{c5}(p_c - p_5), \tag{4.32}$$

$$S_{56} = k_{56}(p_5 - p_6), \tag{4.33}$$

$$S_{35} = \frac{p_3 - p_5 + p_{\text{hbs}}}{R_{35}}, \tag{4.34}$$

$$S_{46} = \frac{p_4 - p_6 + p_{\text{hbs}}}{R_{46}}, \tag{4.35}$$

$$S_{6e} = k_{6e}I_{6e}(p_6 - p_e), \tag{4.36}$$

where

$$R_{35} = \frac{8\pi\mu l_{35}}{(A_{35})^2}, \tag{4.37}$$

$$R_{46} = \frac{32\mu_{\mathrm{csf}} l_{46}}{\pi\Omega}, \tag{4.38}$$

$$p_{\mathrm{h35}} = p_{\mathrm{h46}} = \rho_{\mathrm{csf}} g(h_b + h_s)\sin\theta, \tag{4.39}$$

$$p_{\mathrm{hblood}} = \rho_{\mathrm{blood}} g h_{\mathrm{b}} \sin\theta, \tag{4.40}$$

$$\Omega = \left(\left((d_6)^2 - (d_{\mathrm{cord}})^2\right)\left((d_6)^2 + (d_{\mathrm{cord}})^2 - \left((d_6)^2 - (d_{\mathrm{cord}})^2\right)\ln(d_6/d_{\mathrm{cord}})\right)\right). \tag{4.41}$$

and

$$I_{6e} = \begin{cases} 1 & \text{if} \quad p_6 \geq p_{\mathrm{e}} \\ 0 & \text{if} \quad p_6 < p_{\mathrm{e}}. \end{cases} \tag{4.42}$$

Substitution of the volume terms gives the following set of ordinary differential equations for the compartmental pressures which, assuming p_e is constant, gives

$$\frac{dp_3}{dt} = \frac{(S_{13} - S_{34} - S_{35})}{C_3} + \frac{(-S_{13} + S_{35} - S_{14} + S_{42} + S_{46})}{\partial V_1/\partial p_4}, \tag{4.43}$$

$$\frac{dp_4}{dt} = \frac{(-S_{13} + S_{35} - S_{14} + S_{42} + S_{46})}{\partial V_1/\partial p_4}, \tag{4.44}$$

$$\frac{dp_5}{dt} = \frac{(S_{35} - S_{56} + S_{\mathrm{c5}})}{C_5} + \frac{(S_{46} + S_{56} - S_{\mathrm{6e}})}{C_6}, \tag{4.45}$$

$$\frac{dp_6}{dt} = \frac{(S_{46} + S_{56} - S_{\mathrm{6e}})}{C_6}. \tag{4.46}$$

4.3 Estimation of model parameters

In this model we introduce the following additional parameters[5]: C_6, k_{56}, k_{6e}, k_{c5}, h_{b}, h_{s}, d_5, d_6, d_{cord}, p_{c}, and p_{e}. For simplicity, as a first approximation we assume the following relationships

[5]We also introduce the acceleration due to gravity $g = 9.81\mathrm{m/s}^2$.

exist between intracranial and spinal permeabilities

$$k_{56} \approx 20\ k_{34}, \tag{4.47}$$

$$k_{6e} \approx k_{42}, \tag{4.48}$$

$$k_{c5} \approx 3\ k_1, \tag{4.49}$$

$$C_5 \approx C_3. \tag{4.50}$$

The increase in permeability for k_{56} and k_{c5} is due to the assumption that spinal fluids span throughout the spinal cavity thus increasing their surface area. For the valves we assume they are both lumped into a single compartment and that they have the same permeability. We test the effects of differences from these baseline values as part of the sensitivity analysis (§4.7). For the compliance of the spinal cavity, we assume a value of 9×10^{-8} m^3/Pa, also similar to that of C_3 (3×10^{-8} m^3/Pa). Although the value of the spinal cavity, which relates to the spinal dura, is unlikely to be similar to that of the ventricles, we assume that to be the case in this first approximation. We discuss further the effects of different values of C_6 on the model in §4.8. The central canal varies in size along the spinal cord and it has been observed to be very small (Milhorat et al., 1994; Storer et al., 1998; Saker et al., 2016). In this model we assume it has a diameter of approximately 2×10^{-3} m. The resistance between compartment 4 and 6, R_{46}, in addition to the annular flow parameters, we assume it has a factor of two orders of magnitude higher than its calculated to account for the arachnoid trabeculae and the crossing of the spinal nerves.

For input and output vascular pressures, we make the following assumptions

$$p_c = p_1^* + p_{35}, \tag{4.51}$$

$$p_e = p_{60} - Hp_6, \tag{4.52}$$

where $p_{60} = p_{20} + p_{46}$.

It is important to note that values for p_1^*, k_{13}, k_{34}, k_{14}, S_{10}, H, and p_{20} will change due to the

introduction of p_{hblood} to the vascular model input pressure p_{root}, and the wider pressure range for finding the intracranial coefficients first described in §3.3. This will also be the case for the numerical iteration to find $\partial V_1/\partial p_4$.

The parameter values taken from literature are summarised in Table 4.1.

Parameter	Value (units)	Reference
h_{b}	0.35 (m)	(Blinkov, 1968)
h_{s}	0.15 (m)	(Watson et al., 2009)
d_{cord}	12×10^{-3} (m)	(Frostell et al., 2016)
d_6	34×10^{-3} (m)	(Kim et al., 2013)

Table 4.1: Parameter values for craniospinal model.

4.4 The steady state solution

In steady state, Equations (4.23)–(4.26) become

$$0 = S_{13} - S_{34} - S_{35}, \tag{4.53}$$

$$0 = S_{14} + S_{34} - S_{42} - S_{46}, \tag{4.54}$$

$$0 = S_{35} - S_{56} + S_{\text{c5}}, \tag{4.55}$$

$$0 = S_{46} + S_{56} - S_{\text{6e}}. \tag{4.56}$$

This in turn implies that $-S_{13} - S_{14} + S_{42} - S_{35} + S_{46} = 0$.

Expanding terms in Equations (4.53)–(4.56)

$$0 = k_{13}(p_1^* - p_3) - k_{34}(p_3 - p_4) - \frac{(p_3 - p_5 + p_{\text{h35}})}{R_{35}}, \tag{4.57}$$

$$0 = k_{14}(p_1^* - p_4) + k_{34}(p_3 - p_4) - k_{42}I_{42}(p_4(1 + H) - p_{20}) - \frac{(p_4 - p_6 + p_{\text{h46}})}{R_{46}}, \tag{4.58}$$

$$0 = \frac{(p_3 - p_5 + p_{\text{h35}})}{R_{35}} - k_{56}(p_5 - p_6) + k_{\text{c5}}(p_{\text{c}} - p_5), \tag{4.59}$$

$$0 = \frac{(p_4 - p_6 + p_{\text{h46}})}{R_{46}} + k_{56}(p_5 - p_6) - k_{\text{6e}}I_{\text{6e}}(p_6 - p_{\text{e}}). \tag{4.60}$$

There are two valves in the system, if we assume they are either open or closed at any one point in time (as in the intracranial model), we can linearise the system and find the pressures for each valve combination. We can then solve Equations (4.57)–(4.60) to find the pressures by

$$\mathbf{p} = \mathbf{A}^{-1}\mathbf{b}, \tag{4.61}$$

where,

$$\mathbf{p} = \begin{pmatrix} p_3 \\ p_4 \\ p_5 \\ p_6 \end{pmatrix}, \ \mathbf{b} = \begin{pmatrix} -k_{13}p_1^* + \frac{p_{\mathrm{h}35}}{R_{35}} \\ -k_{14}p_1^* - k_{42}I_{42}p_{20} + \frac{p_{\mathrm{h}46}}{R_{46}} \\ -\frac{p_{\mathrm{h}35}}{R_{35}} - k_{\mathrm{c}5}p_{\mathrm{c}} \\ -\frac{p_{\mathrm{h}46}}{R_{46}} - k_{6\mathrm{e}}I_{6\mathrm{e}}p_{20} \end{pmatrix}, \text{ and}$$

$$\mathbf{A} = \begin{pmatrix} -k_{13} - k_{34} - \frac{1}{R_{35}} & k_{34} & \frac{1}{R_{35}} & 0 \\ k_{34} & -k_{14} - k_{34} - k_{42}I_{42}(1+H) - \frac{1}{R_{46}} & 0 & \frac{1}{R_{46}} \\ \frac{1}{R_{35}} & 0 & -\frac{1}{R_{35}} - k_{56} - k_{\mathrm{c}5} & k_{56} \\ 0 & \frac{1}{R_{46}} & k_{56} & -\frac{1}{R_{46}} - k_{56} - k_{6\mathrm{e}}I_{6\mathrm{e}}(1+H) \end{pmatrix}$$

We observe that the permeability matrix $\mathbf{A}$ is symmetric, which simplifies analytical calculations.

Pressure in compartment 3 is[6]

$$\begin{aligned} p_3 = {} & p_1^*\left(-k_{13}\frac{A_{11}}{|\mathbf{A}|} - k_{14}\frac{A_{21}}{|\mathbf{A}|}\right) + \frac{p_{\mathrm{h}35}}{R_{35}}\left(\frac{A_{11} - A_{31}}{|\mathbf{A}|}\right) \\ & + \frac{p_{\mathrm{h}46}}{R_{46}}\left(\frac{A_{21} - A_{41}}{|\mathbf{A}|}\right) - k_{c5}p_c\frac{A_{31}}{|\mathbf{A}|} - k_{42}I_{42}p_{20}\frac{A_{21}}{|\mathbf{A}|} - k_{6\mathrm{e}}I_{6\mathrm{e}}p_{\mathrm{e}}\frac{A_{41}}{|\mathbf{A}|}, \end{aligned} \tag{4.62}$$

In the previous section we established $p_{\mathrm{h}35} = p_{\mathrm{h}46}$ and $k_{42} = k_{6\mathrm{e}}$, substituting these terms we

[6]Where we define A_{ij} as the cofactor of element a_{ij} in $\mathbf{A}$.

simplify Equation (4.62) and similarly find the rest of the pressures,

$$p_3 = p_1^* \left(-k_{13}\frac{A_{11}}{|\mathbf{A}|} - k_{14}\frac{A_{21}}{|\mathbf{A}|} \right) + p_{\mathrm{h35}} \left(\frac{A_{11} - A_{31}}{R_{35}|\mathbf{A}|} + \frac{A_{21} - A_{41}}{R_{46}|\mathbf{A}|} \right) - k_{\mathrm{c5}} p_{\mathrm{c}} \frac{A_{31}}{|\mathbf{A}|} - k_{42} \left(I_{42} p_{20} \frac{A_{21}}{|\mathbf{A}|} - I_{6\mathrm{e}} p_{\mathrm{e}} \frac{A_{41}}{|\mathbf{A}|} \right), \tag{4.63}$$

$$p_4 = p_1^* \left(-k_{13}\frac{A_{12}}{|\mathbf{A}|} - k_{14}\frac{A_{22}}{|\mathbf{A}|} \right) + p_{\mathrm{h35}} \left(\frac{A_{12} - A_{32}}{R_{35}|\mathbf{A}|} + \frac{A_{22} - A_{41}}{R_{46}|\mathbf{A}|} \right) - k_{\mathrm{c5}} p_{\mathrm{c}} \frac{A_{32}}{|\mathbf{A}|} - k_{42} \left(I_{42} p_{20} \frac{A_{22}}{|\mathbf{A}|} - I_{6\mathrm{e}} p_{\mathrm{e}} \frac{A_{42}}{|\mathbf{A}|} \right), \tag{4.64}$$

$$p_5 = p_1^* \left(-k_{13}\frac{A_{13}}{|\mathbf{A}|} - k_{14}\frac{A_{23}}{|\mathbf{A}|} \right) + p_{\mathrm{h35}} \left(\frac{A_{13} - A_{31}}{R_{35}|\mathbf{A}|} + \frac{A_{23} - A_{41}}{R_{46}|\mathbf{A}|} \right) - k_{\mathrm{c5}} p_{\mathrm{c}} \frac{A_{33}}{|\mathbf{A}|} - k_{42} \left(I_{42} p_{20} \frac{A_{23}}{|\mathbf{A}|} - I_{6\mathrm{e}} p_{\mathrm{e}} \frac{A_{43}}{|\mathbf{A}|} \right), \tag{4.65}$$

$$p_6 = p_1^* \left(-k_{13}\frac{A_{14}}{|\mathbf{A}|} - k_{14}\frac{A_{24}}{|\mathbf{A}|} \right) + p_{\mathrm{h35}} \left(\frac{A_{14} - A_{34}}{R_{35}|\mathbf{A}|} + \frac{A_{24} - A_{44}}{R_{46}|\mathbf{A}|} \right) - k_{\mathrm{c5}} p_{\mathrm{c}} \frac{A_{34}}{|\mathbf{A}|} - k_{42} \left(I_{42} p_{20} \frac{A_{24}}{|\mathbf{A}|} - I_{6\mathrm{e}} p_{\mathrm{e}} \frac{A_{44}}{|\mathbf{A}|} \right). \tag{4.66}$$

We see that the first term in each equation describes the dependency on p_1^* (i.e. intracranial vascular term), the second the gravitational terms, the third the spinal vascular term, and the last term depends on the behaviour of the valves.

When the valves are in a closed position ($I_{42} = I_{6e} = 0$) and the assumed posture is supine ($\theta = 0$), we see Equations (4.63)–(4.66) reduce to only two terms, the intracranial and spinal vascular terms. We can also observe that $p_3 = p_5$ when $A_{11} = A_{13}$, $A_{21} = A_{23}$, $A_{31} = A_{33}$ and $A_{41} = A_{43}$. Similarly, $p_4 = p_6$ when $A_{12} = A_{14}$, $A_{22} = A_{24}$, $A_{32} = A_{34}$ and $A_{42} = A_{44}$.

In the intracranial model we observed that when $I_{42} = 0$, $p_3 = p_4 = p_1^*$. In the craniospinal model, when either or both the valves are closed, the pressures may reach a different steady state for each valve condition and for each posture change. It can be seen that complexity has already escalated significantly from the intracranial model by the adding only two compartments and the gravitational terms.

To test each valve in their different states we adopt a binary notation 11, 10, 01, 00, where 1 denotes open, 0 closed, and the first digit corresponds to the intacranial valve I_{42} while the second corresponds to the spinal valve I_{6e}. Note that for each valve combination the

permeability matrix **A** changes. We test a range of postures, from supine to upright position ($\theta = 90°$) and upside down position ($\theta = -90°$), using the values[7] in Tables 2.6, 3.1, 3.2 for the appropriate pressure range, and Table 4.1. We solve numerically to keep the nonlinearity introduced by the valves and obtain the baseline condition from the solver, we do this by using the Matlab function *fsolve*. Results for steady state pressures and fluxes are given in Tables 4.2 and 4.3.

θ	-90°	-45°	0°	45°	90°
Valves	10	10	11	01	01
p_1^*	29.6	26.2	23.8	16.8	13.4
p_2	5.7	8.7	10.3	13.8	12.7
p_3	16.7	15.4	13.9	5.3	2.3
p_4	15.4	14.3	12.9	4.2	1.3
p_5	-20.2	-10.7	13.9	31.4	39.2
p_6	-21.4	-11.7	12.9	30.3	38.2

Table 4.2: Pressures (mmHg) for different postures where $\theta = -90°$ denotes upside down position, $\theta = 0$ supine position, and $\theta = 90°$ upright position. Valve status denotes 1 for open and 0 for closed, where the first digit corresponds to the intracranial valve and the second to the spinal valve.

θ	-90°	-45°	0°	45°	90°
Valves	10	10	11	01	01
S_{13}	0.75	0.44	0.42	0.60	0.60
S_{14}	4.4	2.6	2.4	3.4	3.5
S_{34}	0.74	0.43	0.39	0.56	0.56
S_{42}	19.4	11.4	5.3	0.00	0.00
S_{c5}	14.2	8.3	7.8	11.2	11.3
S_{56}	14.3	8.4	7.8	11.3	11.3
S_{6e}	0.00	0.00	5.3	15.3	15.4
S_{35}	0.02	0.02	0.02	0.04	0.04
S_{46}	-14.3	-8.4	-2.5	4.0	4.0

Table 4.3: Fluxes (ml/min) for different postures where $\theta = -90°$ denotes upside down position, $\theta = 0$ supine position, and $\theta = 90°$ upright position. Valve status denotes 1 for open and 0 for closed, where the first digit corresponds to the intracranial valve and the second to the spinal valve.

Comparing the results with the analytical solution we were able to confirm the values and the valve statuses. Solving analytically we can evaluate all valve cases for each of the postures. The analytical solution however, confirmed that only one steady state can be reached for a given posture and each has a specific valve combination as shown above.

[7]Baseline values for vascular model (Chapter 2) and intracranial model (Chapter 3).

There is an interesting pattern in the values as well as the valve statuses with respect to posture. In the supine position both valves are open, matching the intracranial model where the valve was in an open position. In the positive angles (towards upright position) the intracranial valve closes and the spinal valve opens, and in the negative angles (towards upside down position) the spinal valve closes and the intracranial valve opens. This is reasonable since in the upright position the cranium is above the heart level thus creating a negative hydrostatic pressure which can result in the closure of the intracranial valve. In the upside down position the opposite must occur. This implies the main CSF exit route in the standing position according to our model is through the spinal arachnoid villi. This coincides with the extracranial blood pathways in the standing position being that of the vertebral veins instead of the jugular veins due to hydrostatic pressure effects, as mentioned in Chapter 1, due to the partial collapse of the jugular veins.

In Table 4.2, we observe that in the supine position, steady state pressure between ventricles p_3, and the central canal p_5, is the same, as is the pressure in the intracranial SAS pressure p_4, and the spinal SAS pressure p_6. This makes sense since these compartments are in direct communication and in the supine position they are also at the heart level so their pressures balance.

In the upright position we see the intracranial pressures decrease whilst the spinal pressures increase, and in the upside down position ($-90°$) the opposite occurs. The intracranial vascular pressure p_1^* appears less affected than the pressures in the ventricles p_3 and intracranial SAS p_4. This is perhaps unsurprising given the larger pressure that the vasculature withstands, however, it is possible that autoregulation is aiding this compensation. The spinal pressures, p_5 and p_6, are the most sensitive to postural changes, reaching very high pressures in the upright position and negative pressures in the upside down position.

We notice the pressure in the dural sinuses p_2 increases slightly in the upright position. This is counter intuitive since the dural sinuses, specially the superior sagittal sinus, can become negative due to their location relative to the heart. We analyse this behaviour further. In the intracranial model we established that p_2 decreases linearly from an initial p_{20} with increasing

p_4 until reaching equilibrium. In this model the same occurs. In the upright position there is a decrease in p_{20}, however since p_4 also decreases, the overall p_2 increases slightly despite the positive angle.

There is another factor in this model that can also influence the dural sinuses, the interaction of the valves. We observe this in more detail in Table 4.3, where we see flux through S_{42} and S_{6e}. The increase in pressure in the dural sinuses in the upright position is small (+3 mmHg) compared to the rest of the pressure changes, it is possible that the closure of the intracranial valve prevents a rapid decline in pressure. From supine to a 45° angle we see the biggest change, at this point no flux goes into the intracranial SAS and the sinuses receive a reduced flux from the vasculature. From 45° to 90°, p_2 starts to decrease since p_1^* has decreased more significantly. This is reasonable since for blood and CSF to drain in the upright position a positive pressure gradient is required to allow for forward flow to extracranial pathways.

The results for fluxes, as those of the pressures, are physiologically realistic. Our results for ventricular pressure agree with those as measured by Lawley et al. (2017), where their findings (denoted in their study as intracranial pressure measured from the ventricles) are in the range of 2–6 mmHg in the upright position and 15–22 mmHg in the upside down position[8]. Similar detailed studies would be required to confirm the rest of the pressures in our model. We notice in the case of the fluxes, that there is a greater influx of CSF into the spine. Spinal flux in our model considers the entire spinal cavity which, as mentioned earlier, can account for up to 60% of the total CSF. Considering the input flux of the intracranial compartments, we see that it is less than half of the spinal influx which is reasonable.

We investigate further the dynamics of the system before reaching these steady states in §4.6. Before that however, we evaluate the stability of the system.

[8](Lawley et al., 2017) does not measure upside down position but rather a change from zero to 1G to simulate microgravity and a head down tilt of -6°, both of which give this range of intracranial pressure.

4.5 Linear stability analysis

We analyse the effects of perturbations on the system by first finding the eigenvalues and eigenvectors. Expanding Equations (4.43)–(4.46) and rewriting them in matrix form[9] we obtain

$$\frac{d\mathbf{p}}{dt} = \mathbf{M}\mathbf{p} + \mathbf{q}, \tag{4.67}$$

where

$$\mathbf{p} = \begin{pmatrix} p_3 \\ p_4 \\ p_5 \\ p_6 \end{pmatrix}, \quad \mathbf{q} = \begin{pmatrix} -p_1^* \left(\frac{k_{13}}{C_3} - \frac{k_{13}+k_{14}}{\partial V_1/\partial p_4} \right) + \frac{p_{\mathrm{h}35}}{R_{35}} + \frac{k_{\mathrm{c}5}p_{\mathrm{c}}+k_{42}I_{42}p_{20}+k_{6\mathrm{e}}I_{6\mathrm{e}}p_{20}}{\partial V_1/\partial p_4} \\ p_1^* \left(\frac{k_{13}+k_{14}}{\partial V_1/\partial p_4} \right) + \frac{k_{\mathrm{c}5}p_{\mathrm{c}}+k_{42}I_{42}p_{20}+k_{6\mathrm{e}}I_{6\mathrm{e}}p_{20}}{\partial V_1/\partial p_4} \\ -\frac{p_{\mathrm{h}35}}{C_5R_{35}} - \frac{k_{\mathrm{c}5}p_{\mathrm{c}}}{C_5} - \frac{p_{\mathrm{h}46}}{C_6R_{46}} - \frac{k_{6\mathrm{e}}I_{6\mathrm{e}}p_{20}}{C_6} \\ -\frac{p_{\mathrm{h}46}}{C_6R_{46}} - \frac{k_{6\mathrm{e}}I_{6\mathrm{e}}p_{20}}{C_6} \end{pmatrix},$$

and

$$\mathbf{M} = \begin{pmatrix} \frac{-k_{13}-k_{34}-1/R_{35}}{C_3} + \frac{k_{13}}{\partial V_1/\partial p_4} & \frac{k_{34}}{C_3} + \frac{k_{14}+k_{42}I_{42}(1+H)}{\partial V_1/\partial p_4} & \frac{1}{C_5R_{35}} + \frac{k_{\mathrm{c}5}}{\partial V_1/\partial p_4} & \frac{k_{6\mathrm{e}}I_{6\mathrm{e}}(1+H)}{\partial V_1/\partial p_4} \\ \frac{k_{13}}{\partial V_1/\partial p_4} & \frac{k_{14}+k_{42}I_{42}(1+H)}{\partial V_1/\partial p_4} & \frac{k_{\mathrm{c}5}}{\partial V_1/\partial p_4} & \frac{k_{6\mathrm{e}}I_{6\mathrm{e}}(1+H)}{\partial V_1/\partial p_4} \\ \frac{1}{C_5R_{35}} & \frac{1}{C_6R_{46}} & -\frac{(k_{\mathrm{c}5}+k_{56}+1/R_{35})}{C_5} + \frac{k_{56}}{C_6} & \frac{k_{56}}{C_5} - \frac{(k_{56}+k_{6\mathrm{e}}I_{6\mathrm{e}}(1+H)+1/R_{46})}{C_6} \\ 0 & \frac{1}{C_6R_{46}} & \frac{k_{56}}{C_6} & -\frac{(k_{56}+k_{6\mathrm{e}}I_{6\mathrm{e}}(1+H)+1/R_{46})}{C_6} \end{pmatrix}.$$

We solve the characteristic equation to find the eigenvalues, $\det(\mathbf{M} - \lambda\mathbf{I}) = \mathbf{0}$, where $\mathbf{I}$ is the identity matrix, and λ the eigenvalues, and use these to find the eigenvectors that satisfy $\mathbf{M}\mathbf{v} = \lambda\mathbf{v}$.

We compute the eigenvalues and eigenvectors using the same parameter values as in §4.4 and obtain the results in Table 4.4 for the supine position and its respective valve status. As in Chapter 3, we adopt the notation for eigenvectors as v_{ip} where i is the associated eigenvalue and p the pressure corresponding to the eigenvector component. The solution to the system is a stable node.

[9] N.B. As in the intracranial model, the system is not truly linear since $\partial v_1/\partial p_4$ is in function of p_4.

$\lambda_1 = -0.01$	$\lambda_2 = -0.02$	$\lambda_3 = -0.09$	$\lambda_4 = -3.12$
$v_{13} = 0.38$	$v_{23} = 0.67$	$v_{33} = -0.72$	$v_{43} = 0.69$
$v_{14} = 0.57$	$v_{24} = -0.51$	$v_{34} = -0.25$	$v_{44} = 0.69$
$v_{15} = 0.44$	$v_{25} = 0.16$	$v_{35} = 0.59$	$v_{45} = -0.13$
$v_{16} = 0.57$	$v_{26} = -0.50$	$v_{36} = -0.27$	$v_{46} = -0.13$

Table 4.4: Eigenvalues and eigenvectors for $\theta = 0$ and valve status 11.

We can observe that the magnitude of the last eigenvalue is significantly greater (by one order of magnitude) than the rest. This means the system will be influenced by this fast eigenvalue.

Eigenvector components v_{45} and v_{46} in this fast eigenvalue are much greater than eigenvector components v_{43} and v_{43}. This indicates the behaviour of p_3 and p_4 will be relatively unaffected by this fast eigenvalue, whereas p_5 and p_6 will be heavily influenced by it.

If we take a projection of p_3 and p_4 onto the $p_5 - p_6$ plane, we can see their convergence to a stable node. Figure 4.4 shows the 3D phase portrait in the $p_3,\ p_4,\ p_5$ space (Figure 4.4a), and a projection of the p_3–p_4 plane (Figure 4.4b). We choose p_5 for convenience as it appears to have the greatest eigenvector component between v_{45} and v_{46}.

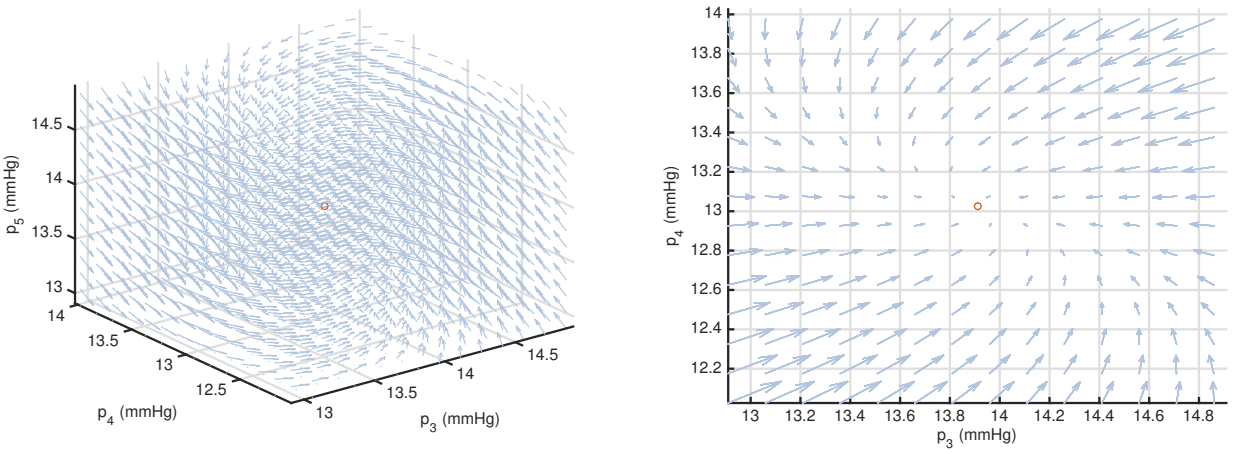

(a) **(b)**

Figure 4.4: Phase portrait in supine position ($\theta = 0$) when both valves are open ($I_{42} = I_{6e} = 1$). (a) 3D phase portrait of p_3, p_4 and p_5 with flow vectors (light blue arrows) near the fixed point (red circle). (b) Projection of the flow vectors on the p_3–p_4 plane about the stable point (red circle).

The system is not a star node since the eigenvalues are different, otherwise we would see perfectly aligned flow vectors, instead we see flow vectors rotating slightly meaning p_3 will experience

mild overshoots or undershoots. The behaviour is less pronounced than in the intracranial model indicating a subtle influence from the spinal pressures.

It is difficult to visualise solutions in three dimensions but we can assert from this analysis that the behaviour of the intracranial pressures will be influenced by the behaviour of the spinal pressures, and that p_3 can experience mild overshoots and undershoots with respect to p_4 as can p_5 with respect to p_6. Therefore, as we saw in Chapter 3, the solutions will converge to the fixed point following the flow vectors.

We found the eigenvalues for the other postures and valve statuses to be very similar to the one in Table 4.4, as will be seen in the next section on the dynamic solutions in different postures. We therefore conclude that the behaviour of the system at all postures will be similar to the one shown. That is, irrespective of posture and their corresponding valve status, the system will be influenced by the fast eigenvalue and in particular by the spinal pressures which account for the eigenvector components of these fast eigenvalue with greatest magnitude.

4.6 The unsteady state solution

We compute Equations (4.43)–(4.46) using Matlab ODE solver ODE15s. Using the same parameter values as in the previous sections we test three different cases:

- Case 1: supine position $\theta = 0$ with the initial condition of 5 mmHg for all pressures;
- Case 2: changing from the steady supine conditions to an upright position $\theta = 90°$;
- Case 3: changing from the steady supine conditions to an upside down position $\theta = -90°$.

Tolerances for reaching equilibrium values are the same as applied in Chapter 3. The colour code in the figures is the same for the intracranial pressures and fluxes in Chapter 3. For spinal pressures we introduce dark green for p_5, light green for p_6 and orange for external (epidural) spinal pressure p_e. For spinal fluxes S_{c5}, S_{56} and S_{6e} we use the same shades of green and orange, and for craniospinal fluxes S_{35} and S_{46} we use orchid and steel blue respectively.

Case 1: Supine position

In Figure 4.5a we observe the intracranial and spinal pressures for the supine position when the initial pressure is 5 mmHg. The first thing to notice is that the behaviour is very similar to that which we observed in the intracranial model (Case 1 §3.6). The one significant difference is the time scale. In the intracranial model we had a time scale of 6 hours, with the spinal compartments the time scale is reduced to half hour. This might be due in part to the difference in magnitude of the fast eigenvalues, in the intracranial model we have a fast eigenvalue of -0.002 for the equivalent valve case, whilst in the craniospinal model the fast eigenvalue is -0.45. Recalling Equation (3.52) we can see how the eigenvalue with largest magnitude will result in a fast convergence, and as we see in this case to a significant extent.

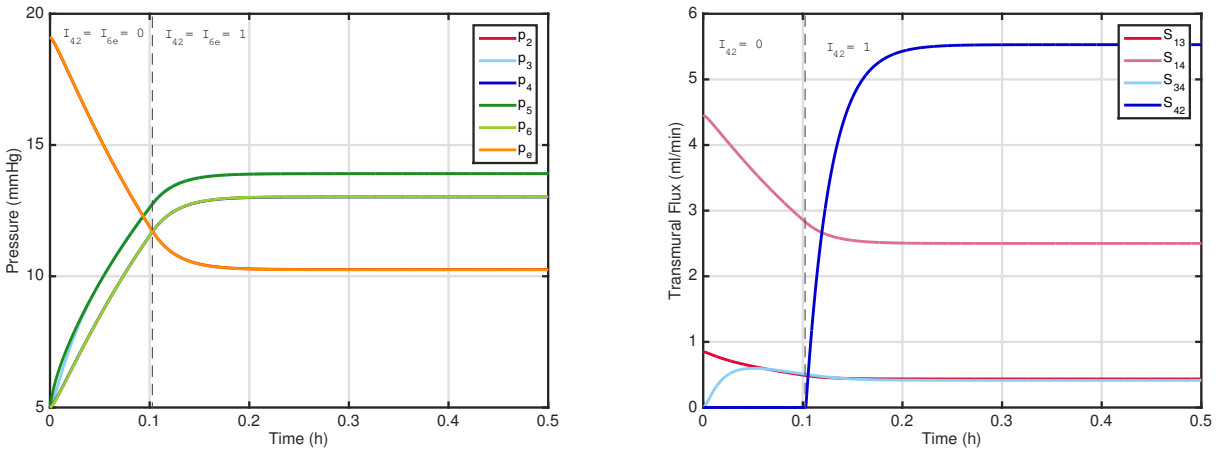

(a) **(b)**

Figure 4.5: Dynamic craniospinal pressures and intracranial fluxes in the supine position ($\theta = 0$) with an initial pressure of 5 mmHg in all compartments. (a) Intracranial pressures: pressure in the dural sinuses p_2, ventricular pressure p_3, intracranial SAS pressure p_4. (b) Intracranial fluxes: flux from the vasculature to the ventricles S_{13}, flux from the vasculature to the intracranial SAS S_{14}, flux from the ventricles to the intracranial SAS S_{34}, flux from the intracranial SAS to the dural sinuses S_{42}. The dashed line indicates the opening of the intracranial and spinal valves.

In the figure we see overlapping of pressures, external spinal pressure p_e overlaps with pressure in the dural sinuses p_2, pressure in the central canal p_5 overlaps with the ventricular pressure p_3, and the spinal SAS pressure p_6 overlaps with the intracranial SAS pressure p_4. This is due to the relationships established in §4.2 and §4.3. We also notice the opening of both valves at the same time ($\approx$ 6 min) and the pressures reaching equilibrium at approximately 15 min.

In Figure 4.5b we see the the intracranial fluxes have a similar behaviour to the intracranial model with the exception that the flux from the ventricles to the cranial SAS S_{34} the overshoot is not as pronounced. There is also slightly higher flux going through the intracranial valve, S_{42} which, as mentioned earlier, has to do with the larger influx through the spinal compartments.

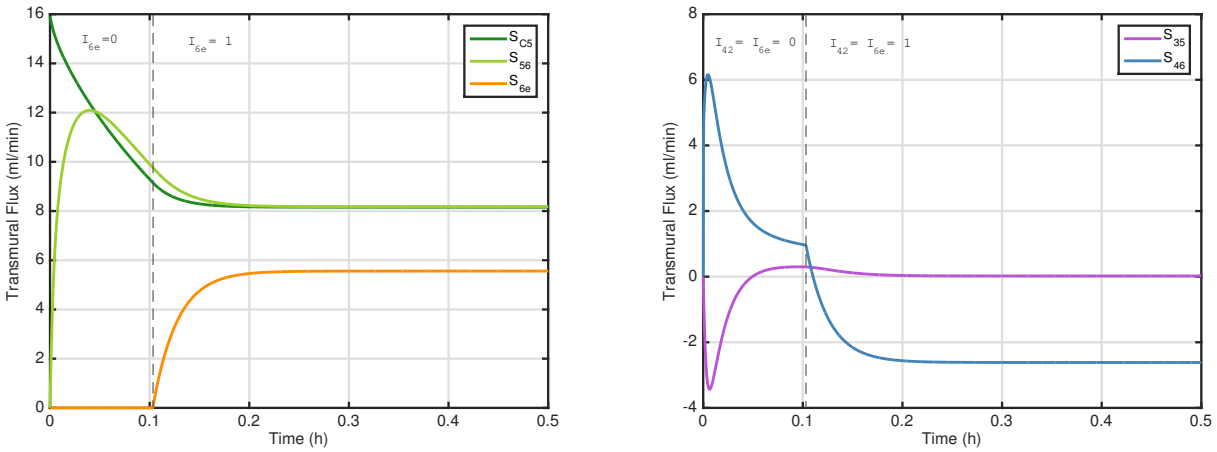

(a) **(b)**

Figure 4.6: Dynamic craniospinal fluxes in the supine position ($\theta = 0$) for the same initial conditions as Figure 4.5. (a) spinal fluxes: flux from the vasculature to the central canal S_{c5}, flux from the central canal to the spinal SAS S_{56}, flux from the spinal SAS S_{6e}. (b) Craniospinal fluxes: flux from the ventricles to the central canal S_{35}, flux from the intracranial SAS to the spinal SAS S_{46}. The dashed line indicates the opening of the intracranial and spinal valves.

In Figure 4.6a we see the behaviour of the flux from the spinal vasculature to the central canal S_{c5} and the flux from the central canal to the spinal SAS S_{56}, which is very similar to the behaviour seen in S_{13} and S_{34} of the intracranial model, though as mentioned with larger flux. This is reasonable since S_{13} and S_{34} are analogous to S_{c5} and S_{56}. Flux S_{56} has a significant overshoot when the spinal valve is closed and stabilises after it opens. The flux through the spinal valve S_{6e} is proportionally smaller to the other spinal fluxes in comparison to the intracranial valve S_{42}. This is likely due to the larger influx through the spinal vasculature in combination with the release of flux through the intracranial valve. We review this further in the following two cases.

We observe in Figure 4.6b that the craniospinal fluxes S_{35} and S_{46} have a fast overshoot and undershoot, respectively, before the valve opens. Since there is higher influx through the spinal vasculature, CSF initially flows from the central canal to the ventricles, thus creating negative

flux, before stabilising. It is possible that this flux then becomes part of compartment 4 creating a positive overshoot of flux before steadily decreasing. Flux S_{35} starts to increase around the time S_{56} and S_{c5} have reached approximately 60% of their total behaviour, as expected due to the influence of p_5. Flux S_{46} decreases significantly when the valve opens as expected.

We conclude that the supine case of the craniospinal model is substantially faster than the intracranial model. The time constants for pressures p_3 to p_6 are approximately 3 minutes. The intracranial pressures and fluxes behave qualitatively similar to the intracranial model, however the values for spinal fluxes are significantly higher than the intracranial ones. Spinal pressures p_5 and p_6 are analogous to intracranial pressures p_3 and p_4, respectively, thus behaving very similar in this supine case. The craniospinal fluxes S_{35} and S_{46} have a changing dynamic with respect to the input pressure and fluxes between the spinal and intracranial compartments, with both stabilising fully after the valves open. Equilibrium is reached at approximately 20 minutes for all pressures and fluxes.

Case 2: Supine to upright position

$\lambda_1 = -8 \times 10^{-4}$	$\lambda_2 = -0.02$	$\lambda_3 = -0.10$	$\lambda_4 = -0.57$
$v_{13} = 0.47$	$v_{23} = -0.90$	$v_{33} = 0.48$	$v_{43} = -0.16$
$v_{14} = 0.53$	$v_{24} = 0.02$	$v_{34} = 0.045$	$v_{44} = -0.11$
$v_{15} = 0.47$	$v_{25} = -0.43$	$v_{35} = -0.88$	$v_{45} = 0.72$
$v_{16} = 0.52$	$v_{26} = 0.003$	$v_{36} = 0.02$	$v_{46} = 0.66$

Table 4.5: Eigenvalues and eigenvectors for $\theta = 90$ and valve status 01.

We now set the initial conditions to the supine steady state and change to an upright position. We can see in Table 4.5 that the eigenvalues are almost identical to the supine case, with the exception that the eigenvalue with smallest magnitude (i.e slow eigenvalue) is one order of magnitude smaller than the slow eigenvalue of the supine case. We again see the eigenvector components for pressures p_5 and p_6 for the eigenvalue of largest magnitude (i.e. fast eigenvalue) are dominant over the eigenvector components for pressures p_3 and p_4, indicating the spinal pressures will have a very fast response in comparison to the intracranial pressures.

In Figure 4.7a we see this is the case as we observe the spinal pressures p_5 and p_6 have a

significant overshoot from the initial conditions whilst the spinal external pressure p_e also undershoots significantly. This is expected since p_e is a function of p_6 as per Equation (4.52). After this initial response pressures p_5 and p_6 decrease monotonically until reaching equilibrium at around 2 hours. The spinal external pressure p_e has the opposite behaviour increasing steadily to equilibrium after it undershoots.

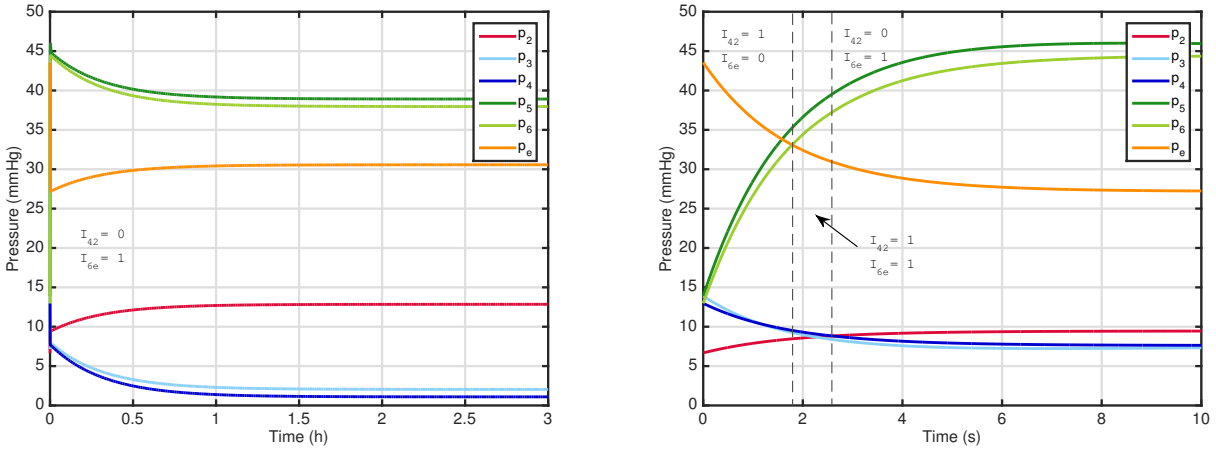

(a) **(b)**

Figure 4.7: Dynamic craniospinal pressures changing from the steady supine position to the upright position ($\theta = 90°$): pressure in the dural sinuses p_2 (red line), ventricular pressure p_3 (light blue line), intracranial SAS pressure p_4 (darker blue line), spinal external pressure p_e (orange line), pressure in the central canal p_5 (darker green line), spinal SAS pressure p_6 (light green line). (a) Time scale of 3 hours indicating valve status for intracranial valve I_{42} and spinal valve I_{6e}, where 1 denotes open and 0 denotes closed. (b) Time scale of 10 seconds with the time of changes in the status of the valves indicated by the dashed lines.

The intracranial pressures p_3 and p_4 have no overshoot or undershoot but rather start to decrease monotonically at the same time as p_2 increases. As we saw in the steady state, spinal pressures increase in the upright position, whilst the intracranial pressures decrease. We see the dural sinuses pressure increases slightly stabilising after the valve closes to an equilibrium value not far from its supine baseline value, thus confirming the analysis in §4.4.

It appears in Figure 4.7a that the spinal valve remains open and the intracranial valve remains closed throughout their time span, however, on closer inspection we can see this is not the case. In Figure 4.7b we see the behaviour of the pressures in the first 10 seconds of this change in posture and can distinguish three different valve states taking place. In the steady state supine position both valves are open. Upon changing to a positive θ the hydrostatic pressure changes

immediately, causing a change in the valves, in this case we see a valve status of 10 at $t = 0$, changing to 11 at $t = 1.8$ seconds, finally changing to 01 at $t = 2.5$ seconds. Since the response of the spinal pressures is fast, we see the spinal valve status change earlier than that of the intracranial valve.

Note that since the behaviour is fast, in Figure 4.7b it appears as if the pressures increase or decrease in an opposite manner as to Figure 4.7a, however, upon zooming out to a greater time scale, we start seeing the behaviour of Figure 4.7a.

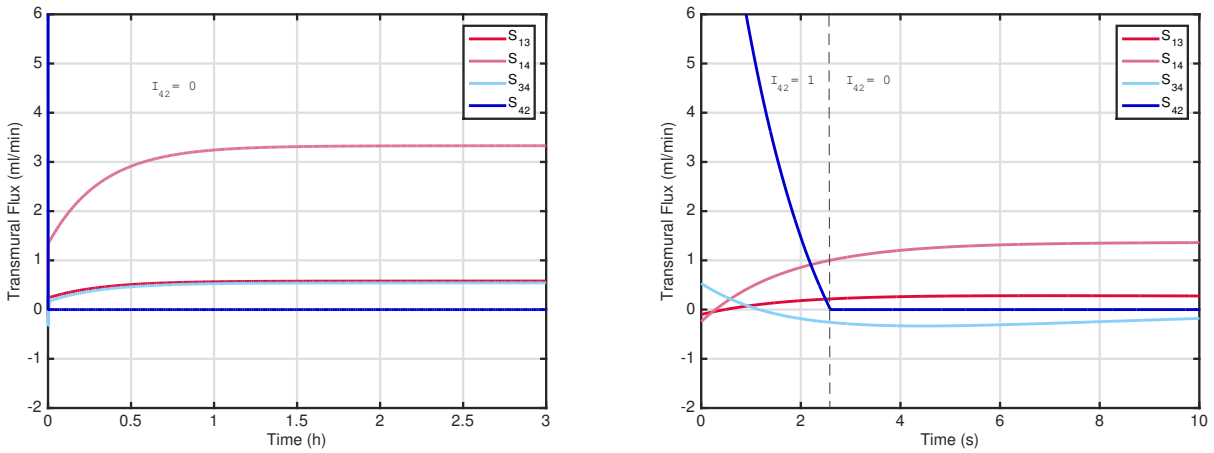

(a) **(b)**

Figure 4.8: Dynamic intracranial fluxes changing from the steady supine position to the upright position ($\theta = 90°$): flux from the cerebral vasculature to the ventricles S_{13} (red line), flux from the ventricles to the intracranial SAS S_{34} (light blue line), flux from the cerebral vasculature to the intracranial SAS S_{14} (pink line), flux through the intracranial valve S_{42} (darker blue line). (a) Time scale of 3 hours indicating valve status for the intracranial valve I_{42}, where 1 denotes open and 0 denotes closed. (b) Time scale of 10 seconds with the time of changes in the status of the valves indicated by the dashed lines.

The intracranial flux (Figure 4.8b) from the vasculature to the ventricles S_{13}, has negligible changes whilst flux from the ventricles to the intracranial SAS S_{34}, has a more pronounced change which is is driven by the very mild undershoot of p_3 in Figure 4.7b between 2 and 10 seconds. Flux from the vasculature to the intracranial SAS S_{14} increases steadily to reach equilibrium at around 2 hours, which is driven by the decrease in p_4. In the previous case we saw S_{14} decreasing until the valve opened, after which point it stabilised to equilibrium. In this case S_{14} continues to increase even after the valve closes, suggesting the influence of p_4 is greater than that of the valve. Pressure p_4 reaches equilibrium significantly faster when the

valve goes from open to closed, but from closed to open p_4 takes a longer time to reach the lower equilibrium thus S_{14} continues to increase. In other words, the change in the valve status has a faster response in p_4 when it goes from open to closed than going from closed to open, which in turn affects the related flux S_{14}.

The most prominent change is in the flux through the intracranial valve S_{42}, where a significant drop occurs between 0 and 2 seconds until it reaches 0 at the valve closure. Flux through S_{42} at $t = 0$ is very high (12 ml/min, shown only to 6 ml/min), this is due to the high spinal flux coming from the vasculature S_{c5}.

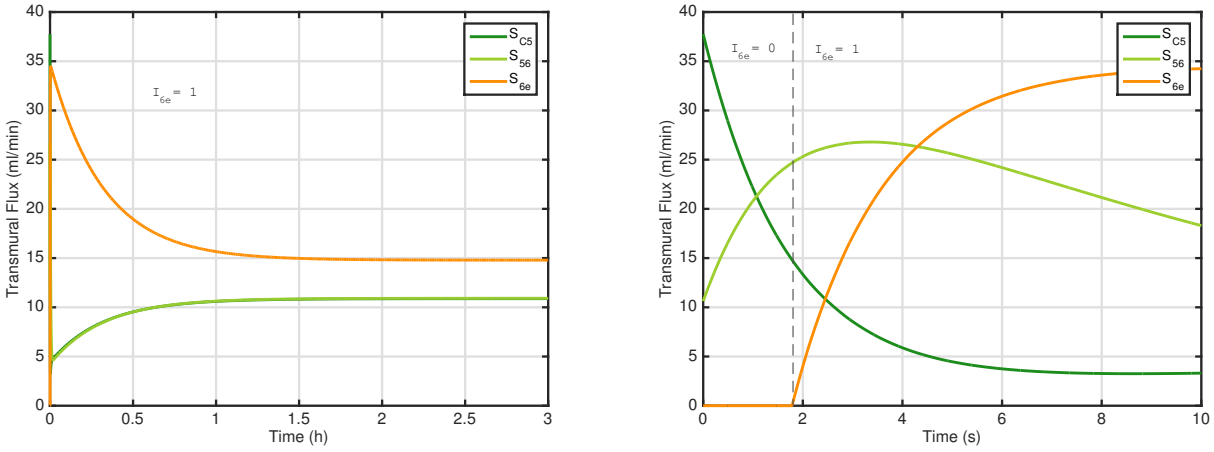

(a) (b)

Figure 4.9: Dynamic spinal fluxes changing from the steady supine position to the upright position ($\theta = 90°$): flux from the spinal vasculature to the central canal S_{c5} (light green line), flux from the central canal to the spinal SAS S_{56} (darker green line), flux through the spinal valve S_{6e} (orange). (a) Time scale of 3 hours indicating valve status for the spinal valve I_{6e}, where 1 denotes open and 0 denotes closed. (b) Time scale of 10 seconds indicating with the time of changes in the status of the valves indicated by the dashed lines.

In Figure 4.9 we see flux through the spinal valve S_{6e} overshooting significantly when changing from supine to upright position, this is expected as per the undershoot of p_e in Figure 4.7. Conversely, flux S_{56} undershoots before increasing monotonically to its equilibrium, this is due to the behaviour seen in pressures p_5 and p_6. Flux S_{c5} first overshoots followed by an undershoot and then a steady increase towards equilibrium, this is due to the undershoot of p_c (not shown) as it is dependent on hydrostatic pressure, hence the sudden change. It is then influenced by the overshoot of p_5 which causes the undershoot of S_{c5}. The value of the flux through the spinal valve S_{6e} is substantially large, however the change in spinal pressures is also very large which

accounts for the relatively large flux of CSF out of the system in the upright position.

We conclude that the initial response of the spinal pressures and intracranial pressures in the upright position allow the valves to change status from 10 to 11 and to 01 after which the variables reach equilibrium. The fast response of the spinal pressures is in agreement with the stability analysis and corresponding eigenvalues. The overshoot of the spinal pressures p_5 and p_6, and the undershoot of p_e due to the change in hydrostatic pressure, has a significant effect on the spinal fluxes, particularly that of the valve S_{6e}. The intracranial pressures and fluxes are only mildly affected, with p_3 having a very subtle undershoot around the time the intracranial valve closes. The slower response of the intracranial pressures allows for a longer time for the valve to close.

Case 3: Supine to upside down position

$\lambda_1 = -6.4 \times 10^{-4}$	$\lambda_2 = -0.02$	$\lambda_3 = -0.09$	$\lambda_4 = -0.46$
$v_{13} = -0.43$	$v_{23} = 0.88$	$v_{33} = -0.42$	$v_{43} = 0.02$
$v_{14} = -0.57$	$v_{24} = 0.005$	$v_{34} = 0.02$	$v_{44} = -0.03$
$v_{15} = -0.42$	$v_{25} = 0.46$	$v_{35} = 0.90$	$v_{45} = -0.74$
$v_{16} = -0.56$	$v_{26} = 0.02$	$v_{36} = 0.05$	$v_{46} = -0.67$

Table 4.6: Eigenvalues and eigenvectors for $\theta = -90$ and valve status 10.

We can see in Table 4.5 that in the upside position the eigenvalues are again almost identical to the previous cases, in particular to that of Case 2 where the slow eigenvalue has a difference of only 0.005. We can therefore expect similar response times and behaviour for the spinal and intracranial pressures.

As in the previous case, in Figure 4.10 we see a very fast response of the spinal pressures when compared to the intracranial pressures. This time it is the spinal valve that closes (as seen in the steady state solution), and it closes at a very fast rate, in approximately 1 second. We observe that the external pressure has the biggest change, going from a negative pressure to a steady state of 46 mmHg. This is the result of a hydrostatic pressure of -36.9 mmHg, which is increased by p_{20} as per Equation (4.52). After the spinal valve closes, all pressures stabilise to equilibrium in less than an hour.

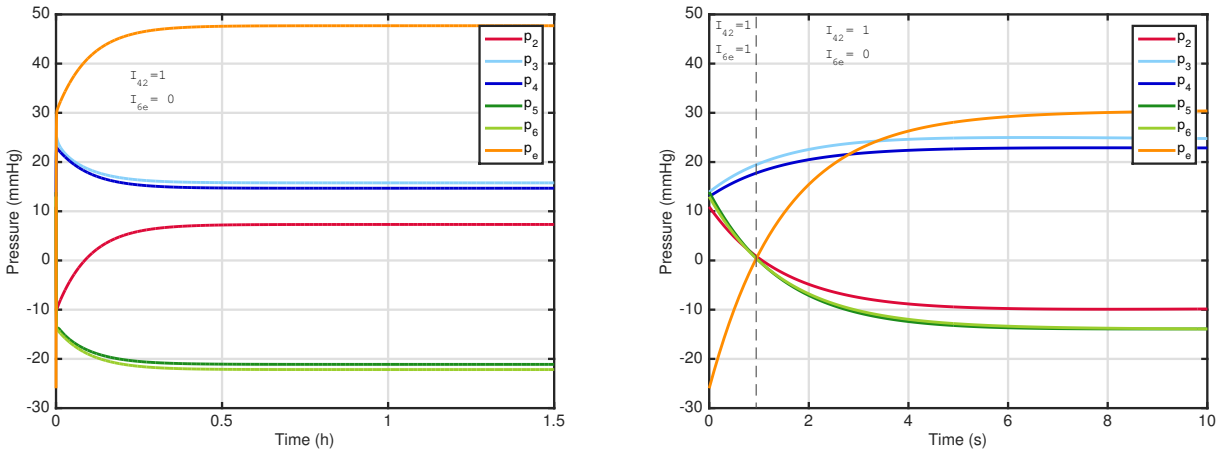

(a) (b)

Figure 4.10: Dynamic craniospinal pressures changing from the steady supine position to the upside down position ($\theta = -90°$): pressure in the dural sinuses p_2 (red line), ventricular pressure p_3 (light blue line), intracranial SAS pressure p_4 (darker blue line), spinal external pressure p_e (orange line), pressure in the central canal p_5 (darker green line), spinal SAS pressure p_6 (light green line). (a) Time scale of 1.5 hours indicating valve status for intracranial valve I_{42} and spinal valve I_{6e}, where 1 denotes open and 0 denotes closed. (b) Time scale of 10 seconds with the time of changes in the status of the valves indicated by the dashed lines.

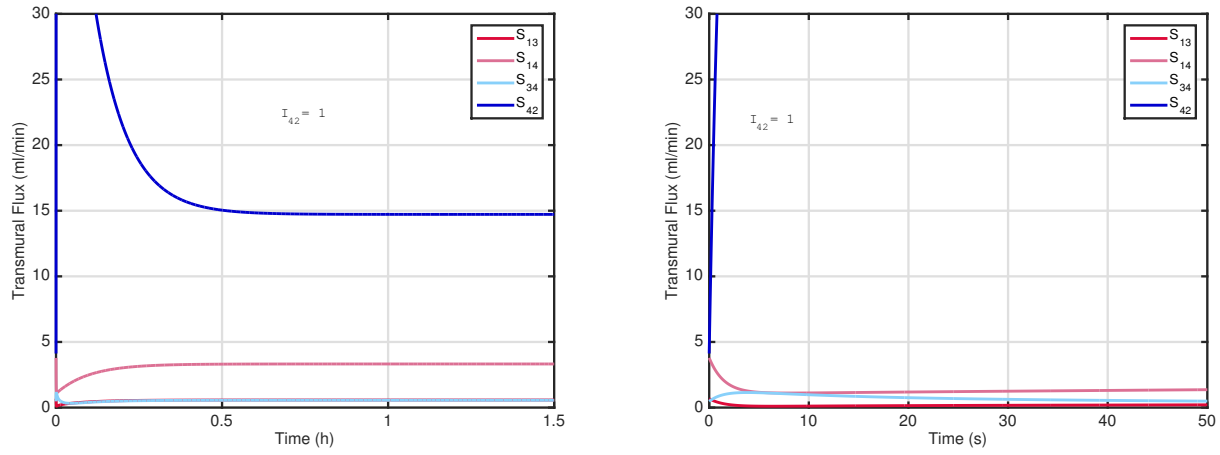

(a) (b)

Figure 4.11: Dynamic intracranial fluxes changing from the steady supine position to the upside down position ($\theta = -90°$): flux from the cerebral vasculature to the ventricles S_{13} (red line), flux from the ventricles to the intracranial SAS S_{34} (light blue line), flux from the cerebral vasculature to the intracranial SAS S_{14} (pink line), flux through the intracranial valve S_{42} (darker blue line). (a) Time scale of 1.5 hours indicating valve status for the intracranial valve I_{42}, where 1 denotes open and 0 denotes closed. (b) Time scale of 10 seconds with the time of changes in the status of the valves indicated by the dotted lines.

In Figure 4.11 we see a substantial overshoot in flux through the intracranial valve, this is again due to the uptake of spinal flux as the spinal valve closes and until the pressures reach

equilibrium. Changes in the rest of the intracranial fluxes are negligible in comparison.

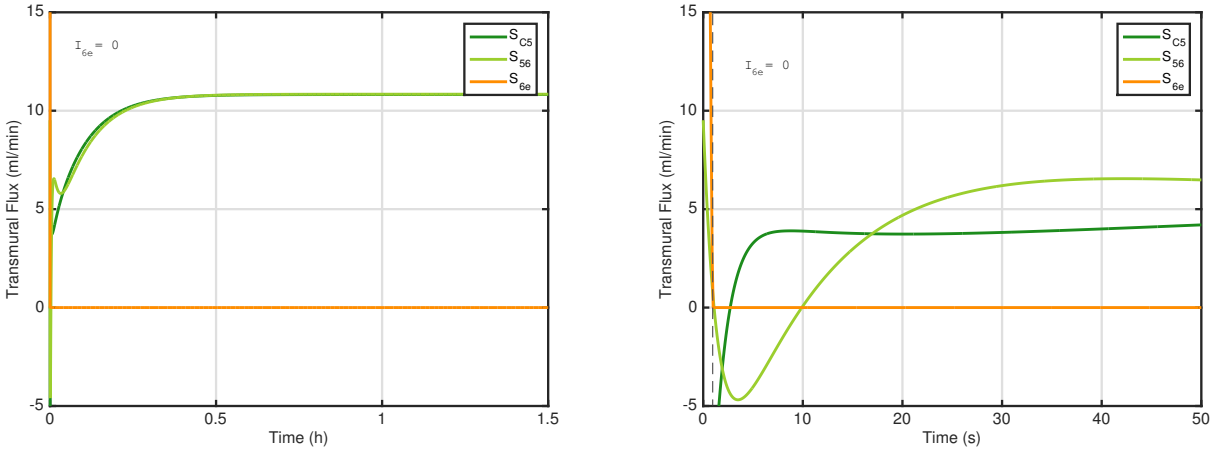

Figure 4.12: Dyanmic spinal fluxes changing from the steady supine position to the upside down position ($\theta = -90°$): flux from the spinal vasculature to the central canal S_{c5} (light green line), flux from the central canal to the spinal SAS S_{56} (darker green line), flux through the spinal valve S_{6e} (orange). (a) Time scale of 1.5 hours indicating valve status for the spinal valve I_{6e}, where 1 denotes open and 0 denotes closed. (b) Time scale of 10 seconds with the time of changes in the status of the valves indicated by the dashed lines.

The spinal fluxes have a changing dynamic in their initial response. We see in Figure 4.12 that flux through the spinal valve S_{6e} drops rapidly, in agreement with the rapid increase in p_e seen in Figure 4.10. We observe S_{56} undershoots before and after the valve closes (Figure 4.12b), before steadily increasing with a small overshoot before stabilising to equilibrium. S_{c5} is influenced by pressures p_c and p_5, as in the previous case since p_c has a fast response with respect to hydrostatic pressure, and p_5 has also a fast response but in the opposite direction, the result is an undershoot (from the change in hydrostatic pressure) followed by a nonlinear increase towards equilibrium as influenced by the nonlinear decay in p_5.

We conclude that in the upside down position the changes in the spinal pressures are again very fast and very significant. In particular that of the spinal external pressure where it goes from a negative pressure to a very large positive pressure. This causes the spinal valve to close at around 1 second. The high hydrostatic pressure and the larger spinal flux causes the intracranial flux through the valve to overshoot significantly, but it is later accommodated in less than one hour, which is the approximate equilibrium time for pressures and fluxes.

4.7 Parameter sensitivity analysis

In the previous two chapters, we saw the effects of varying the model parameters on the vascular and intracranial models. As we have seen similarities in this model in the supine position, we focus instead on the two new postures, upright and upside down, and analyse the effects on pressures when their main exit route (i.e. intracranial and spinal valves), according to the valve statuses seen in §4.4, is either reduced or increased. From the previous sections we have seen that the effect the pressures have on the fluxes and can therefore deduce the behaviour of the fluxes from analysing the pressures.

We assess the sensitivity to the permeability of the spinal valve (k_{6e}) in the standing position, and the permeability of the intracranial valve (k_{42}) in the upside down position.

Supine to upright position with modified k_{6e}

In upright position, starting from supine steady state conditions, we vary the permeability of the spinal valve k_{6e} by one order of magnitude from its baseline. As established in §4.3, the baseline value of this permeability is that of permeability k_{42}. The behaviour for the initial response (< 50 seconds), was the same as the baseline, therefore it is only shown the longer time response.

We observe in Figure 4.13 that as we increase this permeability the intracranial pressures p_3 and p_4 decrease further, resulting in negative pressure, while the pressure in the dural sinuses p_2 increases slightly. The spinal pressures p_5 and p_6 decrease more significantly than the intracranial pressures but at no point do they reach the spinal external pressure p_e which increases slightly. We know from the steady state that in the upright position intracranial pressures decrease from the supine values and spinal pressures increase. A higher permeability therefore makes this effect more pronounced.

When the permeability of the spinal valve is reduced, the intracranial pressures do not decrease as significantly from their baseline (≈ 13 mmHg), and the pressure in the dural sinuses does not

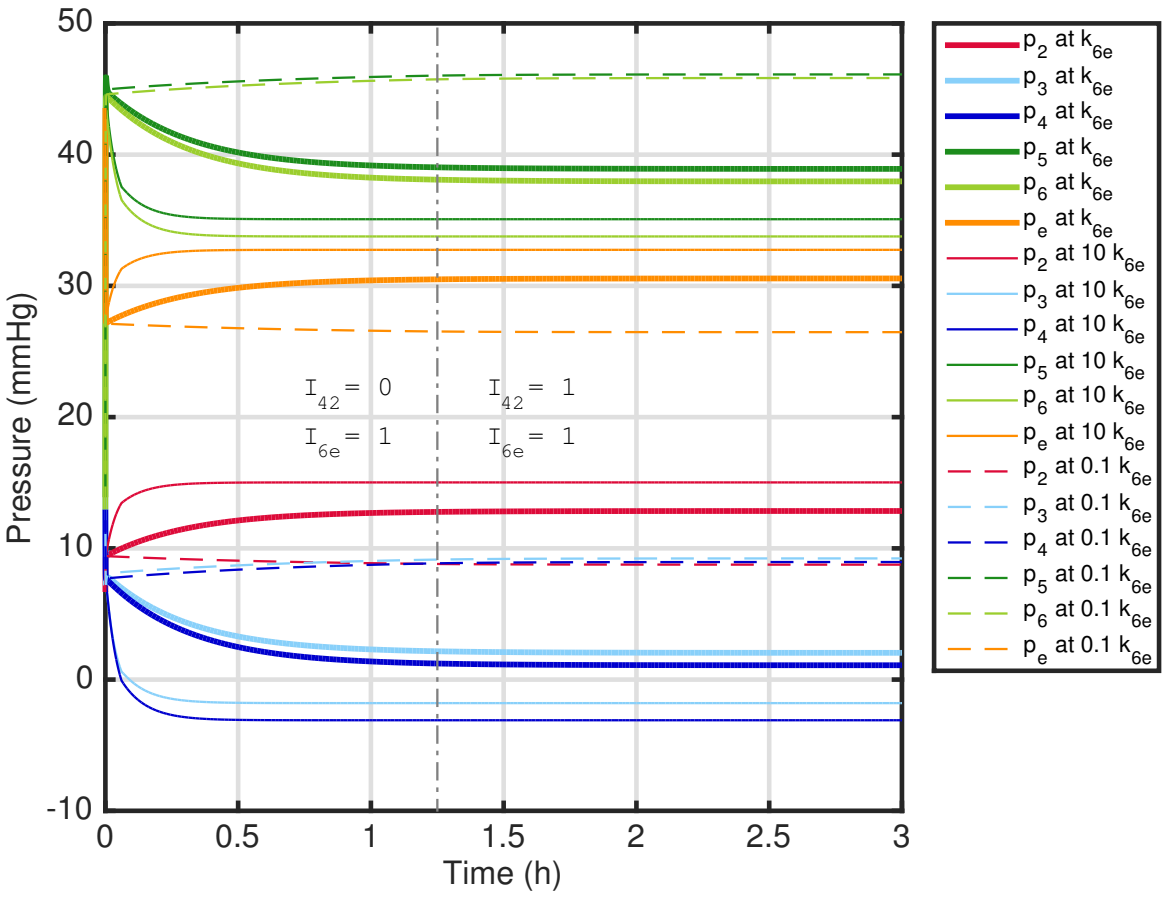

Figure 4.13: Craniospinal pressures changing from the steady supine position to the upright position position ($\theta = 90°$) when the spinal valve permeability k_{6e} is changed: pressure in the dural sinuses p_2 (red line), ventricular pressure p_3 (light blue line), intracranial SAS pressure p_4 (darker blue line), spinal external pressure p_e (orange line), pressure in the central canal p_5 (darker green line), spinal SAS pressure p_6 (light green line). Thick solid line denotes the baseline value, think solid line the value when permeability is increased, and the dotted line when permeability is decreased. The vertical dot-dash line indicates a change of valve status, where I_{42} denotes the intracranial valve, I_{6e} the spinal valve, and where 1 denotes open and 0 denotes closed.

increase from its baseline (10 mmHg) but rather slightly decreases. After the initial response the intracranial pressures start to slowly increase until reaching the pressure in the dural sinuses at which point (1.25 hours) the intracranial valve opens to relieve the pressure. Equilibrium is reached at approximately 2.5 hours.

The spinal pressures p_5 and p_6 have the same fast response seen in Case 2 of §4.6, with the difference that the pressures do not decay to equilibrium but rather increase slightly until reaching equilibrium at the same time as the rest of the pressures. The opposite effect occurs

for spinal external pressure p_e as expected. Since the pressures are kept relatively constant after their initial response, we can deduce the fluxes will be minimal after the initial overshoots and undershoots.

It is interesting to see that the intracranial valve is sensitive to changes in the permeability of the spinal valve. Physiologically this could mean that in the absence of a functional spinal valve, the intracranial arachnoid villi would indeed have to do most of the CSF drainage in order to prevent high intracranial pressure in the upright posture.

We conclude that the permeability of the spinal valve k_{6e} is similarly important to intracranial pressures, a reduction of its value by one order of magnitude results in p_3 and p_4 reaching the value of the dural sinuses p_2, thus opening the intracranial valve to relieve the pressure. An increase in the spinal valve permeability from its baseline value accentuates the behaviour seen in Case 2 of §4.6 but no valve status change is observed.

Supine to upside down with modified k_{42}

In the case of supine to upside down with a change of one order of magnitude in k_{42}, we see the effects in Figure 4.14. The behaviour for the initial response (< 50 seconds), was again the same as the baseline, therefore only the longer time response is shown. In Figure 4.14 we can see that again as we increased the permeability a more pronounced effect on pressures can be seen; that is, the pressures that increase have a higher equilibrium value when the permeability is higher, and those that decrease have a lower equilibrium value.

We observe that when the permeability is higher, intracranial pressures p_3 and p_4 decrease to a value very close to that of the dural sinuses pressure p_2, although they do not cross to activate the valve. Further testing revealed that irrespective of the increase in permeability these pressures continued to approach but never reach each other in order to change the intracranial valve status.

The spinal pressures p_5 and p_6 have a similar behaviour to that of p_3 and p_4, as they decrease further with a higher permeability and are higher when the permeability is reduced. For the

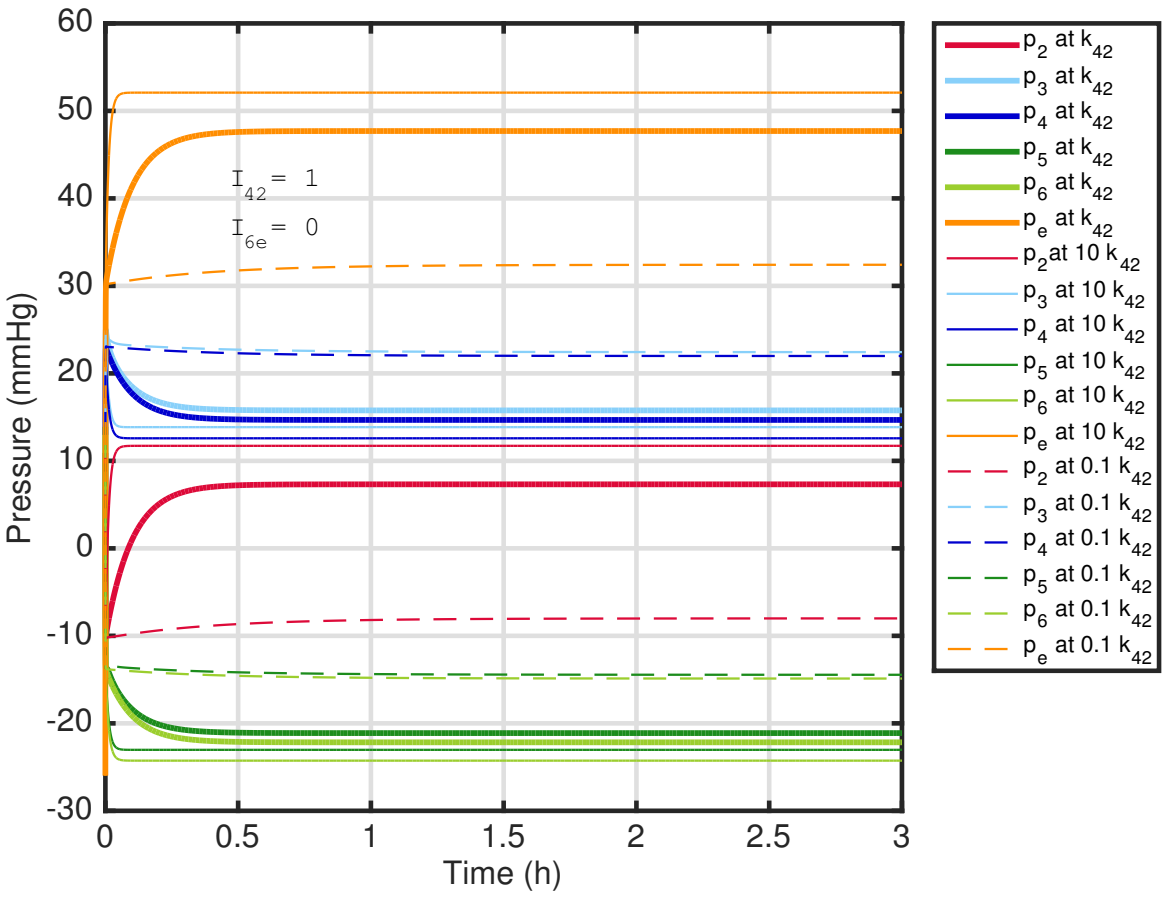

Figure 4.14: Craniospinal pressures changing from the steady supine position to the upside down position position ($\theta = -90°$) when the intracranial valve permeability k_{42} is changed: pressure in the dural sinuses p_2 (red line), ventricular pressure p_3 (light blue line), intracranial SAS pressure p_4 (darker blue line), spinal external pressure p_e (orange line), pressure in the central canal p_5 (darker green line), spinal SAS pressure p_6 (light green line). Thick solid line denotes the baseline value, think solid line the value when permeability is increased and the dotted line when permeability is decreased. The intracranial and spinal valve status, I_{42} and I_{6e} respectively, shown where 1 denotes open and 0 denotes closed.

higher permeability the pressures are close to their baseline values. The spinal external pressure p_e sees the biggest effect (as p_2 does intracranially). At no point is the spinal valve status changed. For I_{6e} to change to 1, a significant pressure difference would have to be overcome for p_e to reach p_6. In our testing no value was found to reach this valve status.

This testing suggests that in the upside down position a reduced intracranial valve permeability can be physiologically damaging for intracranial pressures since we see both p_3 and p_4 with sustained pressure values above 20 mmHg. The pressure in the dural sinuses p_2 would then be

reduced to negative pressure thus preventing the direct return of cranial blood to the heart.

We conclude that in the upside down position a larger permeability of the intracranial arachnoid villi mildly accentuates the behaviour seen in Case 3 §4.6, whilst a smaller permeability can be physiologically detrimental since the effects cannot be compensated by the other valve as is seen in the upright position sensitivity case.

4.8 Summary and discussion

In this chapter we introduced two spinal cerebrospinal fluid (CSF) compartments to the intracranial model, the spinal cavity and central canal, along with a spinal vascular input and output. The spinal cavity, which we delimit by the spinal dura mater, contains a lumped parameter arachnoid villi valve, which we denote as the spinal valve. The constructed craniospinal model effectively integrates the vascular model introduced in Chapter 2 and the intracranial model introduced in Chapter 3 (§4.1).

The craniospinal model is governed by the equations introduced in the intracranial model which are now modified to account for the additional compartments and the introduction of gravitational terms to account for postural changes (§4.2).

The choice of parameter values for permeabilities and compliances is based on similitude with the intracranial parameters and approximate relationships to the extension of the spinal compartments. The model was tested under different sets of values and through different combinations, and concluded that the parameters selected were a sound first approximation, one that would allow for reasonable results in light of new values becoming available. Similar sensitivity tests were carried out on the new compliances and although we do not show the results in detail we can conclude that for a stiffer spinal cavity (i.e. smaller compliance), the fast eigenvalue was found to be four orders of magnitude greater, resulting in a significantly faster convergence, qualitatively however, the results were not affected. The model proved to be flexible enough to allow for parameters to be introduced without a compromise on its qualitative behaviour and neither modifying its quantitative behaviour substantially other than with respect

to convergence times to equilibrium (§4.3).

The steady state shows that only one valve status (i.e. combination of intracranial and spinal valves state) can be reached for a given posture. We tested five different postures accounting for each 45° in angle referenced to the horizontal, the summarised combinations are: in the supine position both valves are open (agreeing with what we saw in the intracranial model), in both upright positions the intracranial valve closes and the spinal valve opens, and in both upside down positions the intracranial valve opens and the spinal valve closes. This is reasonable since in the upright position the intracranial compartments experience negative hydrostatic pressure thus allowing for a closure of the intracranial valve, and in the upside down position the opossite occurs and the spinal valve closes as a result of the negative hydrostatic pressure acting on the spinal compartments (§4.4). This suggests that the presence and adequate function of the spinal arachnoid villi must be crucial in ensuring intracranial pressures are kept relatively constant in the upright position. The spinal arachnoid villi despite its role in CSF drainage has been given little attention.

The stability analysis shows that with the choice of parameters selected, the system converges rapidly into a stable node, with eigenvector components for the spinal pressures having a more pronounced effect. The overshoots and undershoots of the pressure in the ventricles was seen to be more subtle than in the intracranial model. Pressure in the central canal has more pronounced overshoots and undershoots given the greater magnitude of its eigenvector component in relation to that of the pressure in the spinal subarachnoid space (SAS), both of which are analogous to the pressures in the ventricles and intracranial SAS. Different postures had a negligible change regarding stability. The craniospinal model showed a faster convergence than the intracranial model due to the fast eigenvalue being two orders of magnitude greater than that of the intracranial fast eigenvalue (§4.5).

The unsteady state solution shows the fast convergence seen in §4.5 with the supine case reaching equilibrium in less than 30 minutes, and the upright and upside down position in less than 3 hours. The initial response taking place in the first minute of the upright and upside down positions shows a changing dynamic, specially in the upright position where the valves

can be seen to change their state twice respectively, resulting in three different valve statuses before reaching equilibrium. In the upside down position one valve change was seen. The steady state and stability behaviour was confirmed (§4.6). The change from supine to upright position was selected as it may be more relevant to physiology since this change is encountered regularly on a daily basis. The change from supine to upside down can also be encountered although with less frequency, although it may be important when studying the effects of of microgravity on cerebral fluids.

The sensitivity analysis focused on the effect of permeability of the spinal and intracranial valves under postural changes. An increased spinal valve permeability in the upright position causes more pronounced effects on the pressures, causing the intracranial pressures to become negative and the spinal pressures to be reduced as well, while the pressure in the dural sinuses and the spinal external pressure increase. A reduced spinal valve permeability causes the spinal and intracarnial pressures to increase whilst the opposite occurs in the dural sinuses and spinal external pressure. This increase in intracranial pressure continues to rise slowly until meeting with the pressure of the dural sinuses opening the intracranial valve. This is interesting physiologically since a change in the funcitonality of the spinal valve activates the intracranial valve thus relieving the increase in intracranial pressure. In the case of the permeability of the intracranial valve increasing when in an upside down position, we saw a moderate effect on the intracranial and spinal pressures, all with more pronounced effects from its baseline but remaining relatively close to the baseline values. When the spinal valve permeability was reduced, the intracranial and spinal pressures increased while the pressure in the dural sinuses and spinal external pressure decreased. None of these changes in permeability of the intracranial valve caused a change in valve status. Further testing revealed that at no point did the intracranial valve close or the spinal valve open for this case. This suggests that in the case of an upside down position, good permeability of the intracranial arachnoid villi valve is crucial to maintain pressures within a physiologically healthy range. A reduced intracranial valve permeability in the upside down position sees intracranial pressures above 20 mmHg which can become detrimental if sustained for prolonged periods (§4.7).

If we translate this into space travel we can see how a reduced permeability in the intracranial

arachnoid villi could have a long term detrimental effect. Recent evidence suggests the shift of fluids in microgravity pushes the nervous tissue upwards blocking the arachnoid villi of the superior sagittal sinus which in turn can accentuate the high intracranial pressure experienced leading to permanent visual impairment if prolonged (Roberts et al., 2017). Whilst we cannot claim that our model predicts this, we can certainly see that given a reduced intracranial valve permeability, a sustained high intracranial pressure follows.

4.9 Concluding remarks

- We built on the intracranial model Chapter 3 to incorporate the spinal subarachnoid space, central canal and spinal vasculature. The model connects with the intracranial compartments through shared fluxes and the hydrostatic pressures between them relative to the heart.

- Important parameters from the vascular and intracranial models were tested though only showed those of major interest due to gravitational effects. The model also integrates the Monro-Kellie hypothesis.

- The compartmental arrangement as well as the inclusion of a one-way valve to mimic the effect of the spinal arachnoid villi are novel and have not been seen in modelling efforts before.

- The steady state results show there is only one steady state for each posture (supine, standing and upside down).

- The steady state for each posture is also linked to a specific valve combination: in the supine position both the intracranial and spinal valve are open, in the standing position the intracranial valve is closed and the spinal valve open, and in the upside down position the spinal valve is closed and the intracranial valve is open.

- The stability analysis shows the four-dimensional system is a stable node with the fast eigenvalue having an eigenvector for the spinal subarachnoid space that dictates the ma-

jority of the behaviour of the spinal system, meaning the central canal pressure is secondary to that of the spinal subarachnoid space, much like the ventricular pressure is to the intracranial subarachnoid space.

- The unsteady state results show the dynamics of the system confirming what was shown in the stability analysis. It is observed how the valves open at different times, in particular in the standing position.

- The sensitivity results show the behaviour of the valve can be affected by changes in the valves permeability. This was noticeable in the upside down position (potential to mimic microgravity environment) where a decreased intracranial permeability led intracranial pressures to increase to pathological levels.

- The model captures an interesting behaviour between the intracranial and spinal arachnoid villi for accomodating CSF during changes in posture. It also highlights the importance of these exit routes for CSF clearance.

Chapter 5

Conclusions and future work

5.1 Summary

In this work we present three complementary mathematical models concerning cerebral blood flow and cerebrospinal fluid (CSF) distribution in the cranial and spinal cavities.

In Chapter 2 we introduced a model of the cerebral vasculature as a one-dimensional distributed model consisting of two symmetrical bifurcating trees, one for the arteries and one for the veins. These trees were joined together by a lumped parameter compartment of the capillaries. The model focused on details of the smaller vasculature which is often neglected in cerebrovascular models. The bifurcations follow a set of scaling relationships related to cross-sectional area (CSA) and length of the cylindrical vessels with Hagen–Poiseuille flow, which results in a fairly tight set of inequalities for finding the appropriate range of values. The rest of the variables were derived from these scaling relationships. We created a reference case which we then used to account for distensibility of the vasculature. We introduced a pressure-area relationship for relating the reference CSA to the compliant CSA, and constructed the bifurcating trees accordingly. The model also incorporates a novel autoregulation function based on the scaling factor of CSA. The results are physiologically realistic and predict reasonable values for CSA, volume, surface area, pressure, and transmural flux.

We used the results of the vascular model as input to the intracranial model introduced in Chapter 3. The intracranial model incorporates the vascular compartment (vascular model), CSF spaces, ventricles and subarachnoid space (SAS), and the venous dural sinuses where blood and CSF exit the cranium. All compartments were assumed as averaged over a time which is long compared to the cardiac period. The Monro-Kellie hypothesis was enforced, and a one-way valve to describe the behaviour of the intracranial arachnoid villi was introduced. Two steady states can be reached, one for each valve state, with only the open valve state resulting in flux interaction. The system was found to be a stable node with a faster response from the ventricular pressure than the SAS pressure. Results were physiologically realistic and the unsteady solution shows a compensating dynamics of pressure in the dural sinuses and ventricles to accommodate for the SAS pressure.

The intracranial model provided the foundation of the craniospinal model introduced in Chapter 4, where we added two spinal compartments and an input and output of spinal vascular flux. One steady state with a specific valve status was found for each posture. In the supine position the status of the valves was open for both, in the upright position the intracranial valve closed, and in the upside down position the spinal valve closed. The four-dimensional solution converges to a stable node, with subtle changes in the intracranial pressures and more pronounced changes in the spinal pressures. The stability analysis showed a much faster convergence than the intracranial model, which was also confirmed in the unsteady solution. The initial response showed a different dynamic for each posture, with the upright position undergoing three changes in valve status before entering the monotonic behaviour to equilibrium. Results were physiologically feasible and the behaviour of the intracranial and spinal pressures in different postures was seen to be influenced by the interaction of the two valves.

5.2 Limitations and future work

As with any model, there are limitations to this work. We discuss some of these limitations in this section and suggest improvements as part of future work.

Vascular model

In the vascular model we work with steady state flow rather than dynamic. Blood flow is pulsatile due to the contractions of the heart with every cardiac cycle. This dynamic nature affects the behaviour of pressure and related variables. The study of wave propagation is complex, and that in the brain is further complicated by the effect the arterial pulsatility has on the CSF in the subarachnoid space (SAS). With every cardiac cycle, the arterial pulse causes intracarnial CSF to shift outwardly and towards the spinal cavity (Wagshul et al., 2011; Madsen et al., 2006; Alperin et al., 2006; Linninger et al., 2005). Inevitably, the reflection of these waves, both inside the vasculature and in the SAS, will have an effect on the cerebrovasculature and CSF spaces. We acknowledge the importance of considering this as the next step in the presented model.

Anatomically, the arterial and venous branching is not exactly symmetrical, especially if extended to the bigger arteries (i.e. Circle of Willis). However assuming the given symmetry can provide good functional models as shown in chapter 2-4 and extensively in literature (Olufsen, 1999; Gabryś et al., 2005). Further anatomical accuracy can be accommodated by adding segment models of the bigger vessels as highlighted in §2.1, or by the introduction of asymmetry. Although the latter would have to be assessed on whether the extra anatomical accuracy provides any further functionality accuracy to justify the increase in complexity.

The cerebral capillaries are modelled as a lumped parameter compartment. This is far from the complex nature of capillaries, however, as discussed in detail in §2.2.2, we embarked on first analysing the global behaviour of the capillaries on the rest of the vasculature. Flow in the capillary bed is difficult to reproduce, the non-Newtonian behaviour combined with the asymmetries and other forces (e.g. osmotic pressure gradients) can escalate the complexity of the model significantly. This aspect of the model would therefore require significant future work if more detail is included for the cerebral capillaries.

In the model we assume the brain to be incompressible. We know this is not entirely the case, however, assuming negligible compressibility has led to important findings in CSF dynamics

before (Marmarou et al., 1994, 1978), so although we acknowledge a better approximation is needed to account for small but finite compliance; the current method is accurate enough to enhance our understanding of cerebral fluids physiology.

The intracranial volumes being constant is also not necessarily true since the cranial cavity has an opening through the foramen magnun, and multiple smaller pathways within a non-rigid dura mater. However, when analysing intracranial volumes it is often convenient to assume constant volume is the case as it facilitates the analysis, while agreeing with the Monro-Kellie hypothesis. The Monro-Kellie hypothesis however, is conflicting when adding the spinal compartments since the cranial space is not fully closed, thus the restriction set by the rigidity of the skull cannot be sustained for the compliant spinal compartments, it is therefore important this part of the blood-CSF dynamics is revisited in future work to improve the good but limited hypothesis of Monro and Kellie.

Intracranial model

The intracranial model was approached as a zero-dimensional model. The spaces within the cranium other than the vasculature are not in a specific geometry which makes the analysis and approximations difficult to justify. Modelling the different interconnected CSF compartments in an anatomically more realistic way would add complexity without necessarily achieving better understanding. It is possible that the coupling of several smaller models each representing a specific spatially dimensioned region of the CSF spaces can accommodate for this, however this requires a greater computational demand conflicting with the simplicity aim we had set on this model.

In this model, we adopt a piecewise linear calculation of the vascular transmural flux with respect to an external pressure, i.e. the SAS pressure. This can be improved in the next iteration of the model with a nonlinear numerical approximation to avoid assuming linearity. As it stands, the model gives very good approximations, and the linear behaviour of each segment is reasonable. However, it is an improvement that can be adapted in future work.

Craniospinal model

We model the spinal compartments without accounting for the different regions of the spine: cervical, thoracic and lumbo-sacral. Each of these regions can change the ability to deal with changes in hydrostatic pressure (e.g. curvature, disc elongation). Similarly, these regions have a different composition when it comes to the dura mater (and hence its elasticity), as well as different cross sections and number of arachnoid villi. Given the complexity of adding only two compartments to the intracranial model, the inclusion of further compartments to distinguish regions would undoubtedly escalate the complexity faster. As our initial aim was to make a connection between the brain and spinal cavity to enable their interaction, we achieved this with two compartments. However, future iterations of this model would require the inclusion of different spinal regions but it would be important to decide if the extra detail offered by the model is worth the increased complexity of the model.

The craniospinal model assumes perfect concentricity of the spinal cord and the central canal. The spinal cord has different diameters at different regions of the spine and so does the central canal. For simplicity we assume this symmetry which as it was seen, gives reasonable results. Lack of concentricity is another line of research that can be explored as has been incorporated by other research teams (Sánchez et al., 2018). This could be considered as part of future work, specially if increasing the dimensionality of the model was considered to be desirable.

As mentioned before, the Monro-Kellie hypothesis is not fully compatible with the spinal compartments. Further review of the hypothesis is required either to improve this hypothesis and its use in cerebral modelling or to create a new one based on the craniospinal interaction and not just on the cranial volumes.

The choice of parameters for this model are largely based on the intracranial model. Whilst this is a reasonable first approach, we acknowledge the properties of the spinal meninges and permeabilities differ and should be adjusted to experimental values whenever available. The results of our modelling however, are physiologically reasonable. On the emergence of future experimental studies, it should be easy to incorporate their results into the model. Similarly,

future experiments may provide results that can be used to test the model. An aim would be that the current results of the model may stimulate future experimental work.

The model makes assumptions about the spinal vasculature for simplicity, however, it is possible to construct a model of the spinal vasculature in a similar manner as we constructed the one for the cerebral vasculature. Future work may require this consideration.

5.3 Conclusions

The work presented here gives a physiologically reasonable model of the cerebral circulation and CSF distribution in the cranial and spinal spaces, composed of three individual but linked mathematical models.

The vascular model (Chapter 2) was able to predict realistic intracranial pressures, fluxes, volumes and related parameters for a distensible cerebral vasculature. The model incorporates an autoregulation function based on the CSA scaling factor which ensures that changes in arterial pressure are compensated for in the small arterial vessels by the increase in resistance as a result of a reduced CSA from this scaling factor.

Sensitivity analysis revealed that an increased elastic modulus results in an increased venous pressure drop which can in turn contribute to a higher pressure in the dural sinuses thus restricting the passage of CSF into the dural sinuses. If prolonged, this could result in high intracranial pressure according to the intracranial model (Chapter 3).

The intracranial model highlights the importance of the arachnoid villi as an exit route and the behaviour of the intracranial system when their properties are reduced or increased. We assessed the effects of changes in parameters the vasculature had on the intracranial model and found that CSF spaces are sensitive to cerebral blood flow changes, external pressure and elastic modulus. We see the effects of autoregulation in the intracranial dynamics which were found to be more pronounced when the autoregulation function was absent.

The craniospinal model gives an overview of the behaviour of intracranial and spinal pressures

and fluxes when subjected to different postures. We were able to show the importance of additional CSF pathways to the intracranial, i.e. spinal arachnoid villi, and the effects a reduced permeability would have in the intracranial and spinal compartments. From the data we can assess the vasculature, the intracranial and the spinal parameters in combination and independently, giving us a good range of information to enhance our understanding of cerebrovascular and CSF physiology.

We conclude that by combining simple 1D and 0D models of cerebral vasculature and CSF spaces it is possible to analyse in-depth behaviour of the fluid shifts and spaces inside the cranial and spinal cavity. In each of the models we learned the importance of certain parameters in the models and their relevance in physiology, particularly in pathology. We also analysed in detail their interconnectivity and their interactions, which were frequently non-intuitive. Previous modelling approaches focus on specific features often with higher dimensionality increasing the difficulty of the analysis, while others focus on globalised parameters with lack of detail of the vasculature. We reach a suitable compromise by finding a good model at a low computational expense with sufficient level of detail to model different cases that can be further explored in pathology.

Furthermore, our models involve novel features that make them stand out from other models. In the vascular model, we achieve an accurate model from first principles with simplicity by including scaling laws without the need to specify values other than those of the root vessel. In this model we also incorporate the effects of autoregulation of the cerebral vasculature, a mechanism crucially important in cerebrovascular dynamics, by means of the scaling law of vessel CSA. In the intracranial model, the combination of having a distributed model coupled with the compartmental model and their interaction with the arachnoid villi gives a set of features with which it is possible to test physiologically realistic scenarios, for example by changing the vessels elastic modulus and assessing the effects on the CSF spaces. Lastly, the craniospinal model introduces two novel features: the central canal which is often neglected despite anatomical evidence of its patency and potential role in syriongemella, and the inclusion of the spinal arachnoid villi which has, to our knowledge, not been modelled before as a potential drainage route of CSF. The existence of these spinal pathways suggests they should play a role

in regulating CSF spinally and by extension intracranially. In our model we account for all of these and achieve physiologically realistic results that can be further explored for different values and postures.

Our model can serve as a tool in new areas of research and help in several aspects of cerebral hydrodynamics including:

Arachnoid villi and CSF clearance. Quantification and behaviour of CSF flow through intracranial and spinal arachnoid villi under different pathological conditions (i.e. hydrocephalus, Alzheimer's disesase).

Blood-brain barrier. Potential disruption of the blood-brain barrier by one or several of the following parameters in combination: permeability changes, defective autoregulation response, or chronic changes (e.g. mimic hypertension or local trauma by inducing a change of parameters and analysing the effects).

Ageing blood vessels. Further analysis on the effects stiffer vessels have on the dynamics when in combination with defective arachnoid villi or an absence of the autoregulation response.

Microgravity. Cerebral fluid shifts during space travel can be studied with this model by inducing postural changes to mimic upward flow and analyse the effects different parameters have under this condition.

Dura mater. Distensibility of the cranial and spinal dura mater and its effects on fluids in the subdural and epidural spaces, changes in distensibility with age and potential role in cerebral dynamics.

Central canal. Assessment of the role of the central canal in the flow and distribution of CSF, particularly the link between obliteration of the central canal in older age or pathologies associated with the formation of syrinxes.

In conjunction with clinical experiments these and further aspects of the cerebral fluids dynamics can be explored with the model presented in this thesis in order to advance our understanding of the cerebral circulation and distribution of cerebrospinal fluid within the cranial and spinal

cavities.

Bibliography

Aaslid, R., K.-F. Lindegaard, W. Sorteberg, and H. Nornes

1989. Cerebral autoregulation dynamics in humans. *Stroke*, 20(1):45–52.

Abbott, N. J.

2013. Blood–brain barrier structure and function and the challenges for cns drug delivery. *Journal of Inherited Metabolic Disease*, 36(3):437–449.

Abbott, N. J., M. E. Pizzo, J. E. Preston, D. Janigro, and R. G. Thorne

2018. The role of brain barriers in fluid movement in the cns: is there a 'glymphatic'system? *Acta Neuropathologica*, Pp. 1–21.

Adar, E. and S. Sorek

1989. Multi-compartmental modelling for aquifer parameter estimation using natural tracers in non-steady flow. *Advances in Water Resources*, 12(2):84–89.

Adeeb, N., M. M. Mortazavi, A. Deep, C. J. Griessenauer, K. Watanabe, M. M. Shoja, M. Loukas, and R. S. Tubbs

2013. The pia mater: a comprehensive review of literature. *Child's Nervous System*, 29(10):1803–1810.

Alastruey, J., A. W. Khir, K. S. Matthys, P. Segers, S. J. Sherwin, P. R. Verdonck, K. H. Parker, and J. Peiró

2011. Pulse wave propagation in a model human arterial network: assessment of 1-d visco-elastic simulations against in vitro measurements. *Journal of Biomechanics*, 44(12):2250–2258.

Alastruey, J., K. Parker, J. Peiró, S. Byrd, and S. Sherwin

2007. Modelling the circle of willis to assess the effects of anatomical variations and occlusions on cerebral flows. *Journal of Biomechanics*, 40(8):1794–1805.

Albeck, M. J., S. E. Børgesen, F. Gjerris, J. F. Schmidt, and P. S. Sørensen

1991. Intracranial pressure and cerebrospinal fluid outflow conductance in healthy subjects. *Journal of Neurosurgery*, 74(4):597–600.

Aldea, R.

2017. *Modelling cerebral interstitial flows and their failure in Alzheimer's disease*. PhD thesis, University of Southampton.

Alperin, N., M. Mazda, T. Lichtor, and S. H. Lee

2006. From cerebrospinal fluid pulsation to noninvasive intracranial compliance and pressure measured by mri flow studies. *Current Medical Imaging Reviews*, 2(1):117–129.

Alsop, D. C., J. A. Detre, and M. Grossman

2000. Assessment of cerebral blood flow in alzheimer's disease by spin-labeled magnetic resonance imaging. *Annals of Neurology*, 47(1):93–100.

Ambarki, K., O. Baledent, G. Kongolo, R. Bouzerar, S. Fall, and M.-E. Meyer

2007. A new lumped-parameter model of cerebrospinal hydrodynamics during the cardiac cycle in healthy volunteers. *IEEE transactions on Biomedical Engineering*, 54(3):483–491.

Barbee, J. H. and G. R. Cokelet

1971. The fahraeus effect. *Microvascular Research*, 3(1):6–16.

Barson, A. and J. Sands

1977. Regional and segmental characteristics of the human adult spinal cord. *Journal of Anatomy*, 123(Pt 3):797.

Bateman, G.

2008. The pathophysiology of idiopathic normal pressure hydrocephalus: cerebral ischemia or altered venous hemodynamics? *American Journal of Neuroradiology*, 29(1):198–203.

Beggs, C. B.

2013. Venous hemodynamics in neurological disorders: an analytical review with hydrodynamic analysis. *BMC Medicine*, 11(1):142.

Bennett, J., J. Basivireddy, A. Kollar, K. E. Biron, P. Reickmann, W. A. Jefferies, and S. McQuaid

2010. Blood–brain barrier disruption and enhanced vascular permeability in the multiple sclerosis model eae. *Journal of Neuroimmunology*, 229(1-2):180–191.

Bering, E.

1952. Water exchange of central nervous system and cerebrospinal fluid. *Journal of Neurosurgery*, 9(3):275–287.

Bering Jr, E. A. and O. Sato

1963. Hydrocephalus: changes in formation and absorption of cerebrospinal fluid within the cerebral ventricles. *Journal of Neurosurgery*, 20(12):1050–1063.

Berkovitz, B, M. B.

1988. *Head and Neck Anatomy*. London, England: Wolfe Publishing Ltd.

Bertram, C.

2009. A numerical investigation of waves propagating in the spinal cord and subarachnoid space in the presence of a syrinx. *Journal of Fluids and Structures*, 25(7):1189–1205.

Bertram, C., L. Bilston, and M. Stoodley

2008. Tensile radial stress in the spinal cord related to arachnoiditis or tethering: a numerical model. *Medical & Biological Engineering & Computing*, 46(7):701–707.

Bertram, C., A. Brodbelt, and M. Stoodley

2005. The origins of syringomyelia: numerical models of fluid/structure interactions in the spinal cord. *Journal of Biomechanical Engineering*, 127(7):1099–1109.

Blanco, P., L. M. Alvarez, and R. Feijo

2015. Hybrid element-based approximation for the navier–stokes equations in pipe-like domains. *Computer Methods in Applied Mechanics and Engineering*, 283:971–993.

Blanco, P. and R. Feijóo

2013. A dimensionally-heterogeneous closed-loop model for the cardiovascular system and its applications. *Medical Engineering & Physics*, 35(5):652–667.

Blanco, P. J., S. M. Watanabe, E. A. Dari, M. A. R. Passos, and R. A. Feijóo

2014. Blood flow distribution in an anatomically detailed arterial network model: criteria and algorithms. *Biomechanics and Modeling in Mechanobiology*, 13(6):1303–1330.

Blinkov, S., M. L. G. I.

1968. *The human brain in figures and tables: a quantitative handbook*. Basic Books.

Blomqvist, C. G. and H. L. Stone

2011. Cardiovascular adjustments to gravitational stress. *Comprehensive Physiology*, Pp. 1025–1063.

Børgesen, S. E. and F. Gjerris

1987. Relationships between intracranial pressure, ventricular size, and resistance to csf outflow. *Journal of Neurosurgery*, 67(4):535–539.

Boron, W. and E. Boulpaep

2016. *Medical Physiology: A Cellular and Molecular Approach*. Philadelphia, Pensylvannia: Elsevier Health Sciences.

Boulton, M., M. Flessner, D. Armstrong, R. Mohamed, J. Hay, and M. Johnston

1999. Contribution of extracranial lymphatics and arachnoid villi to the clearance of a csf tracer in the rat. *American Journal of Physiology-Regulatory, Integrative and Comparative Physiology*, 276(3):R818–R823.

Bradley, K.

1970. Cerebrospinal fluid pressure. *Journal of Neurology, Neurosurgery & Psychiatry*, 33(3):387–397.

Brinker, T., E. Stopa, J. Morrison, and P. Klinge

2014. A new look at cerebrospinal fluid circulation. *Fluids and Barriers of the CNS*, 11(1):10.

Campos, A., N. A.

2015. Anatomy of spinal blood supply.

Caplan, L., A. Norohna, and L. Amico

1990. Syringomyelia and arachnoiditis. *Journal of Neurology, Neurosurgery & Psychiatry*, 53(2):106–113.

Caro, C. G., T. Pedley, and R. Schroter

2012. *The mechanics of the circulation*. Cambridge University Press.

Cassot, F., M. Zagzoule, and J.-P. Marc-Vergnes

2000. Hemodynamic role of the circle of willis in stenoses of internal carotid arteries. an analytical solution of a linear model. *Journal of Biomechanics*, 33(4):395–405.

Cathalifaud, P., M. Zagzoule, and M. Maher

2016. Wave propagation into the spinal cavity: a 1d model with coaxial compliant tubes.

Cavaglia, M., S. M. Dombrowski, J. Drazba, A. Vasanji, P. M. Bokesch, and D. Janigro

2001. Regional variation in brain capillary density and vascular response to ischemia. *Brain Research*, 910(1-2):81–93.

Cebral, J. R., M. A. Castro, O. Soto, R. Löhner, and N. Alperin

2003. Blood-flow models of the circle of willis from magnetic resonance data. *Journal of Engineering Mathematics*, 47(3-4):369–386.

Cheng, S., D. Fletcher, S. Hemley, M. Stoodley, and L. Bilston

2014. Effects of fluid structure interaction in a three dimensional model of the spinal subarachnoid space. *Journal of Biomechanics*, 47(11):2826–2830.

Cipolla, M.

2009. *The Cerebral Circulation*. San Rafael, California: Morgan & Claypool Life Sciences.

Cohn, D. L.

1954. Optimal systems: I. the vascular system. *The Bulletin of Mathematical Biophysics*, 16(1):59–74.

Cserr, H. F.

1971. Physiology of the choroid plexus. *Physiological Reviews*, 51(2):273–311.

Czosnyka, M., Z. Czosnyka, K. J. Agarwal-Harding, and J. D. Pickard

2012. Modeling of csf dynamics: legacy of professor anthony marmarou. In *Hydrocephalus*, Pp. 9–14. Springer.

Czosnyka, M., Z. Czosnyka, S. Momjian, and J. D. Pickard

2004. Cerebrospinal fluid dynamics. *Physiological Measurement*, 25(5):R51.

Czosnyka, M. and J. D. Pickard

2004. Monitoring and interpretation of intracranial pressure. *Journal of Neurology, Neurosurgery & Psychiatry*, 75(6):813–821.

Damadian, R., L. Minkoff, M. Goldsmith, M. Stanford, and J. Koutcher

1976. Field focusing nuclear magnetic resonance (fonar): visualization of a tumor in a live animal. *Science*, 194(4272):1430–1432.

Damkier, H. H., P. D. Brown, and J. Praetorius

2013. Cerebrospinal fluid secretion by the choroid plexus. *Physiological Reviews*, 93(4):1847–1892.

Dandy, W. E.

1918. Extirpation of the choroid plexus of the lateral ventricles in communicating hydrocephalus. *Annals of Surgery*, 68(6):569.

Davis, T.

2014. *Pharmacology of the Blood Brain Barrier: Targeting CNS Disorders*. Elsevier Advances in Pharmacology.

Davson, H., G. Hollingsworth, and M. Segal

1970. The mechanism of drainage of the cerebrospinal fluid. *Brain*, 93(4):665–678.

DeVault, K., P. A. Gremaud, V. Novak, M. S. Olufsen, G. Vernieres, and P. Zhao

2008. Blood flow in the circle of willis: modeling and calibration. *Multiscale Modeling & Simulation*, 7(2):888–909.

Di Terlizzi, R. and S. Platt

2006. The function, composition and analysis of cerebrospinal fluid in companion animals: Part i–function and composition. *The Veterinary Journal*, 172(3):422–431.

Drake, R., A. W. Vogl, and A. W. Mitchell

2009. *Gray's Anatomy for Students E-Book*. Elsevier Health Sciences.

Duvernoy, H. M., S. Delon, and J. Vannson

1981. Cortical blood vessels of the human brain. *Brain Research Bulletin*, 7(5):519–579.

Edsbagge, M., G. Starck, H. Zetterberg, D. Ziegelitz, and C. Wikkelso

2011. Spinal cerebrospinal fluid volume in healthy elderly individuals. *Clinical Anatomy*, 24(6):733–740.

Ekstedt, J.

1978. Csf hydrodynamic studies in man. 2. normal hydrodynamic variables related to csf pressure and flow. *Journal of Neurology, Neurosurgery & Psychiatry*, 41(4):345–353.

El Sankari, S., C. Gondry-Jouet, A. Fichten, O. Godefroy, J. M. Serot, H. Deramond, M. E. Meyer, and O. Balédent

2011. Cerebrospinal fluid and blood flow in mild cognitive impairment and alzheimer's disease: a differential diagnosis from idiopathic normal pressure hydrocephalus. *Fluids and Barriers of the CNS*, 8(1):12.

Ellington, E. and G. Margolis

1969. Block of arachnoid villus by subarachnoid hemorrhage. *Journal of Neurosurgery*, 30(6):651–657.

Elliott, N., C. Bertram, B. A. Martin, and A. Brodbelt

2013. Syringomyelia: a review of the biomechanics. *Journal of Fluids and Structures*, 40:1–24.

Eriksson, P. S., E. Perfilieva, T. Björk-Eriksson, A.-M. Alborn, C. Nordborg, D. A. Peterson, and F. H. Gage

1998. Neurogenesis in the adult human hippocampus. *Nature Medicine*, 4(11):1313.

Fitzgerald, M.

1998. *Neuroanatomy: basic and clinical*. London, England: W B Saunders Company Ltd.

Fog, M.

1938. The relationship between the blood pressure and the tonic regulation of the pial arteries. *Journal of Neurology and Psychiatry*, 1(3):187.

Frostell, A., R. Hakim, E. P. Thelin, P. Mattsson, and M. Svensson

2016. A review of the segmental diameter of the healthy human spinal cord. *Frontiers in Neurology*, 7:238.

Fung, Y. and B. Zweifach

1971. Microcirculation: mechanics of blood flow in capillaries. *Annual Review of Fluid Mechanics*, 3(1):189–210.

Fung, Y.-c.

2013. *Biomechanics: mechanical properties of living tissues*. Springer Science & Business Media.

Gabryś, E., M. Rybaczuk, and A. Kędzia

2005. Fractal models of circulatory system. symmetrical and asymmetrical approach comparison. *Chaos, Solitons & Fractals*, 24(3):707–715.

Gertz, D, T. R.

2007. *Lievman's Neuroanatomy*. Austin, Texas: PRO-ED Inc.

Gisolf, J., J. Van Lieshout, K. Van Heusden, F. Pott, W. Stok, and J. Karemaker

2004. Human cerebral venous outflow pathway depends on posture and central venous pressure. *The Journal of Physiology*, 560(1):317–327.

Gould, I. G., P. Tsai, D. Kleinfeld, and A. Linninger

2017. The capillary bed offers the largest hemodynamic resistance to the cortical blood supply. *Journal of Cerebral Blood Flow & Metabolism*, 37(1):52–68.

Gray, H.

1921. History of lumbar puncture (rachicentesis): The operation and the idea. *Archives of Neurology & Psychiatry*, 6(1):61–69.

Gray, H, W. P. R. W. D. M. B. L.

1989. *Gray's Anatomy*. London, England: Churchil Livingstone.

Greenberg, D. A. and K. Jin

2005. From angiogenesis to neuropathology. *Nature*, 438(7070):954.

Greenwald, S.

2007. Ageing of the conduit arteries. *The Journal of Pathology*, 211(2):157–172.

Gupta, S., M. Soellinger, P. Boesiger, D. Poulikakos, and V. Kurtcuoglu

2009. Three-dimensional computational modeling of subject-specific cerebrospinal fluid flow in the subarachnoid space. *Journal of Biomechanical Engineering*, 131(2):021010.

Gupta, S., M. Soellinger, D. M. Grzybowski, P. Boesiger, J. Biddiscombe, D. Poulikakos, and V. Kurtcuoglu

2010. Cerebrospinal fluid dynamics in the human cranial subarachnoid space: an overlooked mediator of cerebral disease. i. computational model. *Journal of the Royal Society Interface*, 7(49):1195–1204.

Guyton, Arthur C, H. J. E.

2006. *Textbook of medical physiology*. Philadelphia, Pensylvannia: Elsevier Health Sciences.

Hacking, C., G. F.

2018a. Cerebral blood volume.

Hacking, C., G. F.

2018b. Dura mater.

Hakim, S. and R. Adams

1965. The special clinical problem of symptomatic hydrocephalus with normal cerebrospinal fluid pressure: observations on cerebrospinal fluid hydrodynamics. *Journal of the Neurological Sciences*, 2(4):307–327.

Hammock, M. K. and T. H. Milhorat

1976. The cerebrospinal fluid: current concepts of its formation. *Annals of Clinical & Laboratory Science*, 6(1):22–26.

Han, P. Y., J. H. Kim, H. I. Kang, and J. S. Kim

2008. " syndrome of the sinking skin-flap" secondary to the ventriculoperitoneal shunt after craniectomy. *Journal of Korean Neurosurgical Society*, 43(1):51.

Hartmann, P., A. Ramseier, F. Gudat, M. Mihatsch, and W. Polasek

1994. Normal weight of the brain in adults in relation to age, sex, body height and weight. *Der Pathologe*, 15(3):165–170.

Hillen, B., H. W. Hoogstraten, and L. Post

1986. A mathematical model of the flow in the circle of willis. *Journal of Biomechanics*, 19(3):187–194.

Hladky, S. B. and M. A. Barrand

2014. Mechanisms of fluid movement into, through and out of the brain: evaluation of the evidence. *Fluids and Barriers of the CNS*, 11(1):26.

Iliff, J. J., M. Wang, Y. Liao, B. A. Plogg, W. Peng, G. A. Gundersen, H. Benveniste, G. E. Vates, R. Deane, S. A. Goldman, et al.

2012. A paravascular pathway facilitates csf flow through the brain parenchyma and the clearance of interstitial solutes, including amyloid β. *Science Translational Medicine*, 4(147):147ra111–147ra111.

Iwabuchi, T., E. Sobata, M. Suzuki, S. Suzuki, and M. Yamashita

1983. Dural sinus pressure as related to neurosurgical positions. *Neurosurgery*, 12(2):203–207.

Johansson, B. B.

2000. Brain plasticity and stroke rehabilitation: the willis lecture. *Stroke*, 31(1):223–230.

Kamiya, A. and T. Togawa

1972. Optimal branching structure of the vascular tree. *The Bulletin of Mathematical Biophysics*, 34(4):431–438.

Kim, K. H., J. Y. Park, S. U. Kuh, D. K. Chin, K. S. Kim, and Y. E. Cho

2013. Changes in spinal canal diameter and vertebral body height with age. *Yonsei Medical Journal*, 54(6):1498–1504.

Klarica, M., D. Orešković, B. Božić, M. Vukić, V. Butković, and M. Bulat

2009. New experimental model of acute aqueductal blockage in cats: effects on cerebrospinal fluid pressure and the size of brain ventricles. *Neuroscience*, 158(4):1397–1405.

Koh, L., A. Zakharov, and M. Johnston

2005. Integration of the subarachnoid space and lymphatics: is it time to embrace a new concept of cerebrospinal fluid absorption? *Cerebrospinal Fluid Research*, 2(1):6.

Krieger, S. N., M. N. Streicher, R. Trampel, and R. Turner

2012. Cerebral blood volume changes during brain activation. *Journal of Cerebral Blood Flow & Metabolism*, 32(8):1618–1631.

Kuschinsky, W. and O. Paulson

1992. Capillary circulation in the brain. *Cerebrovascular and Brain Metabolism Reviews*, 4(3):261–286.

Lakin, W. D., S. A. Stevens, and P. L. Penar

2007. Modeling intracranial pressures in microgravity: the influence of the blood-brain barrier. *Aviation, space, and environmental medicine*, 78(10):932–936.

Lakin, W. D., S. A. Stevens, B. I. Tranmer, and P. L. Penar

2003. A whole-body mathematical model for intracranial pressure dynamics. *Journal of Mathematical Biology*, 46(4):347–383.

Lassen, N.

1964. Autoregulation of cerebral blood flow. *Circulation Research*, 15:SUPPL–201.

Lassen, N. A.

1959. Cerebral blood flow and oxygen consumption in man. *Physiological Reviews*, 39(2):183–238.

Lawley, J. S., L. G. Petersen, E. J. Howden, S. Sarma, W. K. Cornwell, R. Zhang, L. A. Whitworth, M. A. Williams, and B. D. Levine

2017. Effect of gravity and microgravity on intracranial pressure. *The Journal of Physiology*, 595(6):2115–2127.

Levick, J.

2010. *An introduction to cardiovascular physiology*. London, England: Hodder Arnold.

Lew, H. and Y. Fung

1969. On the low-reynolds-number entry flow into a circular cylindrical tube. *Journal of Biomechanics*, 2(1):105–119.

Linninger, A. A., K. Tangen, C.-Y. Hsu, and D. Frim

2016. Cerebrospinal fluid mechanics and its coupling to cerebrovascular dynamics. *Annual Review of Fluid Mechanics*, 48:219–257.

Linninger, A. A., C. Tsakiris, D. C. Zhu, M. Xenos, P. Roycewicz, Z. Danziger, and R. Penn

2005. Pulsatile cerebrospinal fluid dynamics in the human brain. *IEEE Transactions on Biomedical Engineering*, 52(4):557–565.

Linninger, A. A., M. Xenos, B. Sweetman, S. Ponkshe, X. Guo, and R. Penn

2009. A mathematical model of blood, cerebrospinal fluid and brain dynamics. *Journal of Mathematical Biology*, 59(6):729–759.

Linninger, A. A., M. Xenos, D. C. Zhu, M. R. Somayaji, S. Kondapalli, and R. D. Penn

2007. Cerebrospinal fluid flow in the normal and hydrocephalic human brain. *IEEE Transactions on Biomedical Engineering*, 54(2):291–302.

Loth, F., M. A. Yardimci, and N. Alperin

2001. Hydrodynamic modeling of cerebrospinal fluid motion within the spinal cavity. *Journal of Biomechanical Engineering*, 123(1):71–79.

Madsen, J. R., M. Egnor, and R. Zou

2006. Cerebrospinal fluid pulsatility and hydrocephalus: the fourth circulation. *Clinical Neurosurgery*, 53:48.

Magendie, F.

1842. Recherches anatomique et physiologique sur le liquide céphalo-rachidien ou cérebro-spinal. *Paris, France*.

Maguire, E. A., K. Woollett, and H. J. Spiers

2006. London taxi drivers and bus drivers: a structural mri and neuropsychological analysis. *Hippocampus*, 16(12):1091–1101.

Marieb, E, H. K.

2010. *Human Anatomy and Physiology*. San Francisco, CA: Pearson Education, Inc.

Marmarou, A., G. Hochwald, T. Nakamura, K. Tanaka, J. Weaver, and J. Dunbar

1994. Brain edema resolution by csf pathways and brain vasculature in cats. *American Journal of Physiology-Heart and Circulatory Physiology*, 267(2):H514–H520.

Marmarou, A., A. L. Maset, J. D. Ward, S. Choi, D. Brooks, H. A. Lutz, R. J. Moulton, J. P. Muizelaar, A. DeSalles, and H. F. Young

1987. Contribution of csf and vascular factors to elevation of icp in severely head-injured patients. *Journal of Neurosurgery*, 66(6):883–890.

Marmarou, A., K. Shulman, and J. LaMorgese

1975. Compartmental analysis of compliance and outflow resistance of the cerebrospinal fluid system. *Journal of Neurosurgery*, 43(5):523–534.

Marmarou, A., K. Shulman, and R. M. Rosende

1978. A nonlinear analysis of the cerebrospinal fluid system and intracranial pressure dynamics. *Journal of Neurosurgery*, 48(3):332–344.

Massicotte, E. M. and M. R. Del Bigio

1999. Human arachnoid villi response to subarachnoid hemorrhage: possible relationship to chronic hydrocephalus. *Journal of Neurosurgery*, 91(1):80–84.

Matsumoto, T. and K. Nagayama

2012. Tensile properties of vascular smooth muscle cells: bridging vascular and cellular biomechanics. *Journal of Biomechanics*, 45(5):745–755.

Michael, A. P. and K. Marshall-Bowman

2015. Spaceflight-induced intracranial hypertension. *Aerospace Medicine and Human Performance*, 86(6):557–562.

Milhorat, T. H., M. W. Chou, E. M. Trinidad, R. W. Kula, M. Mandell, C. Wolpert, and M. C. Speer

1999. Chiari i malformation redefined: clinical and radiographic findings for 364 symptomatic patients. *Neurosurgery*, 44(5):1005–1017.

Milhorat, T. H., R. M. Kotzen, and A. P. Anzil

1994. Stenosis of central canal of spinal cord in man: incidence and pathological findings in 232 autopsy cases. *Journal of Neurosurgery*, 80(4):716–722.

Miller, K., K. Chinzei, G. Orssengo, and P. Bednarz

2000. Mechanical properties of brain tissue in-vivo: experiment and computer simulation. *Journal of Biomechanics*, 33(11):1369–1376.

Mokri, B.

2013. Spontaneous low pressure, low csf volume headaches: spontaneous csf leaks. *Headache: The Journal of Head and Face Pain*, 53(7):1034–1053.

Müller, L. O., C. Parés, and E. F. Toro

2013. Well-balanced high-order numerical schemes for one-dimensional blood flow in vessels with varying mechanical properties. *Journal of Computational Physics*, 242:53–85.

Müller, L. O. and E. F. Toro

2014. Enhanced global mathematical model for studying cerebral venous blood flow. *Journal of Biomechanics*, 47(13):3361–3372.

Murray, C. D.

1926. The physiological principle of minimum work: I. the vascular system and the cost of blood volume. *Proceedings of the National Academy of Sciences*, 12(3):207–214.

Najeme, A., M. Zagzoule, and J. Mauss

1992. Numerical analysis of flow in arterial stenoses. *Mechanics Research Communications*, 19(5):379–384.

Nedergaard, M.

2013. Garbage truck of the brain. *Science*, 340(6140):1529–1530.

Norman, D., C. M. Mills, M. Brant-Zawadzki, A. Yeates, L. E. Crooks, and L. Kaufman

1983. Magnetic resonance imaging of the spinal cord and canal: potentials and limitations. *American Journal of Roentgenology*, 141(6):1147–1152.

Obermeier, B., R. Daneman, and R. M. Ransohoff

2013. Development, maintenance and disruption of the blood-brain barrier. *Nature Medicine*, 19(12):1584.

Olufsen, M., H. Tran, and J. Ottesen

2004. Modeling cerebral blood flow control during posture change from sitting to standing. *Cardiovascular Engineering: an International Journal*, 4(1):47–58.

Olufsen, M. S.

1999. Structured tree outflow condition for blood flow in larger systemic arteries. *American Journal of Physiology-Heart and Circulatory Physiology*, 276(1):H257–H268.

Olufsen, M. S., J. T. Ottesen, H. T. Tran, L. M. Ellwein, L. A. Lipsitz, and V. Novak

2005. Blood pressure and blood flow variation during postural change from sitting to standing: model development and validation. *Journal of Applied Physiology*, 99(4):1523–1537.

Olufsen, M. S., C. S. Peskin, W. Y. Kim, E. M. Pedersen, A. Nadim, and J. Larsen

2000. Numerical simulation and experimental validation of blood flow in arteries with structured-tree outflow conditions. *Annals of Biomedical Engineering*, 28(11):1281–1299.

OpenStax

2016. Textbook openstax anatomy and physiology.

Orešković, D. and M. Klarica

2014. Measurement of cerebrospinal fluid formation and absorption by ventriculo-cisternal perfusion: what is really measured? *Croatian Medical Journal*, 55(4):317–327.

Panerai, R. B.

2008. Cerebral autoregulation: from models to clinical applications. *Cardiovascular Engineering*, 8(1):42–59.

Papadopoulos, M. C., G. T. Manley, S. Krishna, and A. Verkman

2004. Aquaporin-4 facilitates reabsorption of excess fluid in vasogenic brain edema. *The FASEB Journal*, 18(11):1291–1293.

Pardridge, W. M.

2012. Drug transport across the blood–brain barrier. *Journal of Cerebral Blood Flow & Metabolism*, 32(11):1959–1972.

Parikh, S., M. Koch, and R. K. Narayan

2007. Traumatic brain injury. *International Anesthesiology Clinics*, 45(3):119–135.

Patronis, A., R. A. Richardson, S. Schmieschek, B. J. Wylie, R. W. Nash, and P. V. Coveney

2018. Modelling patient-specific magnetic drug targeting within the intracranial vasculature. *Frontiers in Physiology*, 9:331.

Petit-Lacour, M., P. Lasjaunias, C. Iffenecker, F. Benoudiba, M. H. Rabia, M. Hurth, and D. Doyon

2000. Visibility of the central canal on mri. *Neuroradiology*, 42(10):756–761.

Peyrounette, M., Y. Davit, M. Quintard, and S. Lorthois

2018. Multiscale modelling of blood flow in cerebral microcirculation: Details at capillary scale control accuracy at the level of the cortex. *PloS One*, 13(1):e0189474.

Piechnik, S. K., M. Czosnyka, H. K. Richards, P. C. Whitfield, and J. D. Pickard

2001. Cerebral venous blood outflow: a theoretical model based on laboratory simulation. *Neurosurgery*, 49(5):1214–1223.

Pollay, M.

2010. The function and structure of the cerebrospinal fluid outflow system. *Cerebrospinal Fluid Research*, 7(1):9.

Queens University at Kingston

2005. Physiological status of the pre-term infant: Part ii - perfusion of the brain.

Radaelli, A., L. Augsburger, J. Cebral, M. Ohta, D. R fenacht, R. Balossino, G. Benndorf, D. Hose, A. Marzo, R. Metcalfe, et al.

2008. Reproducibility of haemodynamical simulations in a subject-specific stented aneurysm model—a report on the virtual intracranial stenting challenge 2007. *Journal of Biomechanics*, 41(10):2069–2081.

Radojicic, M., G. Nistor, and H. S. Keirstead

2007. Ascending central canal dilation and progressive ependymal disruption in a contusion model of rodent chronic spinal cord injury. *BMC Neurology*, 7(1):30.

Reina, M. A., O. D. L. Casasola, A. López, J. A. De Andrés, M. Mora, and A. Fernández

2002. The origin of the spinal subdural space: ultrastructure findings. *Anesthesia & Analgesia*, 94(4):991–995.

Relkin, N., A. Marmarou, P. Klinge, M. Bergsneider, and P. M. Black

2005. Diagnosing idiopathic normal-pressure hydrocephalus. *Neurosurgery*, 57(suppl_3):S2–4.

Rengachary, S. S., A. Xavier, S. Manjila, U. Smerdon, B. Parker, S. Hadwan, and

M. Guthikonda

2008. The legendary contributions of thomas willis (1621–1675): the arterial circle and beyond.

Roberts, D. R., M. H. Albrecht, H. R. Collins, D. Asemani, A. R. Chatterjee, M. V. Spampinato, X. Zhu, M. I. Chimowitz, and M. U. Antonucci

2017. Effects of spaceflight on astronaut brain structure as indicated on mri. *New England Journal of Medicine*, 377(18):1746–1753.

Rosen, B. R., J. W. Belliveau, B. R. Buchbinder, R. C. McKinstry, L. M. Porkka, D. N. Kennedy, M. S. Neuder, C. R. Fisel, H. J. Aronen, K. K. Kwong, et al.

1991. Contrast agents and cerebral hemodynamics. *Magnetic Resonance in Medicine*, 19(2):285–292.

Saker, E., B. M. Henry, K. A. Tomaszewski, M. Loukas, J. Iwanaga, R. J. Oskouian, and R. S. Tubbs

2016. The human central canal of the spinal cord: a comprehensive review of its anatomy, embryology, molecular development, variants, and pathology. *Cureus*, 8(12).

Sakka, L., G. Coll, and J. Chazal

2011. Anatomy and physiology of cerebrospinal fluid. *European Annals of Otorhinolaryngology, Head and Neck Diseases*, 128(6):309–316.

Sánchez, A., C. Martínez-Bazán, C. Gutiérrez-Montes, E. Criado-Hidalgo, G. Pawlak, W. Bradley, V. Haughton, and J. Lasheras

2018. On the bulk motion of the cerebrospinal fluid in the spinal canal. *Journal of Fluid Mechanics*, 841:203–227.

Schachenmayr, W. and R. Friede

1978. The origin of subdural neomembranes. i. fine structure of the dura-arachnoid interface in man. *The American Journal of Pathology*, 92(1):53.

Schwirtz, M.

2009. Staying put on earth, taking a step to mars.

Shapiro, K., A. Marmarou, and K. Shulman

1980. Characterization of clinical csf dynamics and neural axis compliance using the pressure-volume index: I. the normal pressure-volume index. *Annals of Neurology: Official Journal of the American Neurological Association and the Child Neurology Society*, 7(6):508–514.

Sorek, S., J. Bear, and Z. Karni

1988. A non-steady compartmental flow model of the cerebrovascular system. *Journal of Biomechanics*, 21(9):695–704.

Steiner, L. and P. Andrews

2006. Monitoring the injured brain: Icp and cbf. *BJA: British Journal of Anaesthesia*, 97(1):26–38.

Storer, K., J. Toh, M. A. Stoodley, and N. R. Jones

1998. The central canal of the human spinal cord: a computerised 3-d study. *The Journal of Anatomy*, 192(4):565–572.

Støverud, K.-H., H. P. Langtangen, G. A. Ringstad, P. K. Eide, and K.-A. Mardal

2016. Computational investigation of cerebrospinal fluid dynamics in the posterior cranial fossa and cervical subarachnoid space in patients with chiari i malformation. *PloS One*, 11(10):e0162938.

Strandgaard, S. and O. B. Paulson

1984. Cerebral autoregulation. *Stroke*, 15(3):413–416.

Sweeney, M. D., A. P. Sagare, and B. V. Zlokovic

2018. Blood–brain barrier breakdown in alzheimer disease and other neurodegenerative disorders. *Nature Reviews Neurology*, 14(3):133.

Taoka, T., G. Jost, T. Frenzel, S. Naganawa, and H. Pietsch

2018. Impact of the glymphatic system on the kinetic and distribution of gadodiamide in the rat brain: observations by dynamic mri and effect of circadian rhythm on tissue gadolinium concentrations. *Investigative Radiology*, 53(9):529–534.

Tardy, Y., J. Meister, F. Perret, H. Brunner, and M. Arditi

1991. Non-invasive estimate of the mechanical properties of peripheral arteries from ultrasonic and photoplethysmographic measurements. *Clinical Physics and Physiological Measurement*, 12(1):39.

Terem, I., W. W. Ni, M. Goubran, M. S. Rahimi, G. Zaharchuk, K. W. Yeom, M. E. Moseley, M. Kurt, and S. J. Holdsworth

2018. Revealing sub-voxel motions of brain tissue using phase-based amplified mri (amri). *Magnetic Resonance in Medicine*.

Toro, E. F.

2016. Brain venous haemodynamics, neurological diseases and mathematical modelling. a review. *Applied Mathematics and Computation*, 272:542–579.

Toro, E. F., B. Thornber, Q. Zhang, A. Scoz, and C. Contarino

2019. A computational model for the dynamics of cerebrospinal fluid in the spinal subarachnoid space. *Journal of Biomechanical Engineering*, 141(1):011004.

Tubbs, R. S., A. Hansasuta, W. Stetler, D. R. Kelly, D. Blevins, R. Humphrey, G. D. Chua, M. M. Shoja, M. Loukas, and W. J. Oakes

2007. Human spinal arachnoid villi revisited: immunohistological study and review of the literature.

Tully, B. and Y. Ventikos

2011. Cerebral water transport using multiple-network poroelastic theory: application to normal pressure hydrocephalus. *Journal of Fluid Mechanics*, 667:188–215.

Ursino, M.

1988a. A mathematical study of human intracranial hydrodynamics part 1—the cerebrospinal fluid pulse pressure. *Annals of Biomedical Engineering*, 16(4):379–401.

Ursino, M.

1988b. A mathematical study of human intracranial hydrodynamics part 2—simulation of clinical tests. *Annals of Biomedical Engineering*, 16(4):403–416.

Ursino, M. and P. Di Giammarco

1991. A mathematical model of the relationship between cerebral blood volume and intracranial pressure changes: the generation of plateau waves. *Annals of Biomedical Engineering*, 19(1):15–42.

Ursino, M. and C. A. Lodi

1997. A simple mathematical model of the interaction between intracranial pressure and cerebral hemodynamics. *Journal of Applied Physiology*, 82(4):1256–1269.

Ursino, M. and C. A. Lodi

1998. Interaction among autoregulation, co2 reactivity, and intracranial pressure: a mathematical model. *American Journal of Physiology-Heart and Circulatory Physiology*, 274(5):H1715–H1728.

Ursino, M., A. Ter Minassian, C. Lodi, and L. Beydon

2000. Cerebral hemodynamics during arterial and co2 pressure changes: in vivo prediction by a mathematical model. *American Journal of Physiology-Heart and Circulatory Physiology*, 279(5):H2439–H2455.

Vandenabeele, F., J. Creemers, and I. Lambrichts

1996. Ultrastructure of the human spinal arachnoid mater and dura mater. *Journal of Anatomy*, 189(Pt 2):417.

Venton, J., P. Harris, and G. Phillips

2017. Development of a poroelastic model of spinal cord cavities. In *Integral Methods in Science and Engineering, Volume 2*, Pp. 275–283. Springer.

Wagshul, M. E., P. K. Eide, and J. R. Madsen

2011. The pulsating brain: a review of experimental and clinical studies of intracranial pulsatility. *Fluids and Barriers of the CNS*, 8(1):5.

Wakeland, W. and B. Goldstein

2008. A review of physiological simulation models of intracranial pressure dynamics. *Computers in Biology and Medicine*, 38(9):1024–1041.

Watson, C., G. Paxinos, and G. Kayalioglu

2009. *The spinal cord: a Christopher and Dana Reeve Foundation text and atlas*. Academic press.

Weed, L. H.

1914. Studies on cerebro-spinal fluid. no. iii: The pathways of escape from the subarachnoid spaces with particular reference to the arachnoid villi. *The Journal of Medical Research*, 31(1):51.

Welch, K. and V. Friedman

1960. The cerebrospinal fluid valves. *Brain*, 83(3):454–469.

Welch, K. and M. Pollay

1961. Perfusion of particles through arachnoid villi of the monkey. *American Journal of Physiology-Legacy Content*, 201(4):651–654.

Weller, R. O. and R. O. Carare

2018. Lymphatic drainage of the cns and its role in neuroinflammation and neurodegenerative disease. In *Neuroinflammation*, Pp. 601–617. Elsevier.

Weller, R. O. and J. A. Nicoll

2003. Cerebral amyloid angiopathy: pathogenesis and effects on the ageing and alzheimer brain. *Neurological research*, 25(6):611–616.

Wijdicks, E. F.

2018. The first ct scan of the brain: entering the neurologic information age. *Neurocritical Care*, 28(3):273–275.

Wilson, M. H.

2016. Monro-kellie 2.0: The dynamic vascular and venous pathophysiological components of intracranial pressure. *Journal of Cerebral Blood Flow & Metabolism*, 36(8):1338–1350.

Woo, J.

2002. A short history of the development of ultrasound in obstetrics and gynecology.

Xie, L., H. Kang, Q. Xu, M. J. Chen, Y. Liao, M. Thiyagarajan, J. O'Donnell, D. J. Christensen, C. Nicholson, J. J. Iliff, et al.

2013. Sleep drives metabolite clearance from the adult brain. *Science*, 342(6156):373–377.

Yan, T. D., P. G. Bannon, J. Bavaria, J. S. Coselli, J. A. Elefteriades, R. B. Griepp, G. C. Hughes, S. A. LeMaire, T. Kazui, N. T. Kouchoukos, et al.

2013. Consensus on hypothermia in aortic arch surgery. *Annals of Cardiothoracic Surgery*, 2(2):163.

Yau, Y., I. Piper, C. Contant, G. Citerio, K. Kiening, P. Enblad, P. Nilsson, S. Ng, J. Wasserberg, M. Kiefer, et al.

2002. Multi-centre assessment of the spiegelberg compliance monitor: interim results. In *Intracranial Pressure and Brain Biochemical Monitoring*, Pp. 167–170. Springer.

Yau, Y.-H., I. R. Piper, R. E. Clutton, and I. R. Whittle

2000. An experimental evaluation of the spiegelberg intracranial pressure and intracranial compliance monitor. *Journal of Neurosurgery*, 93(6):1072–1077.

Zagzoule, M. and J.-P. Marc-Vergnes

1986. A global mathematical model of the cerebral circulation in man. *Journal of Biomechanics*, 19(12):1015–1022.

Zamboni, P., R. Galeotti, E. Menegatti, A. M. Malagoni, G. Tacconi, S. Dall'Ara, I. Bartolomei, and F. Salvi

2009. Chronic cerebrospinal venous insufficiency in patients with multiple sclerosis. *Journal of Neurology, Neurosurgery & Psychiatry*, 80(4):392–399.

Zatorre, R. J., R. D. Fields, and H. Johansen-Berg

2012. Plasticity in gray and white: neuroimaging changes in brain structure during learning. *Nature Neuroscience*, 15(4):528.

Appendix A

Vascular model

A.1 Detail of arterial and venous trees

This appendix provides further detail into the construction of the venous tree by expanding on the pressures in series as seen in §2.2.

In the generational arrangement, we assume $p^{\text{out}}_{\text{a}N-1} = p^{\text{in}}_{\text{c}}$, and, $p^{\text{out}}_{\text{c}} = p^{\text{in}}_{\text{v}N-1}$, then,

$$
\begin{aligned}
p^{\text{in}}_{\text{v}n} - p^{\text{out}}_{\text{v}n} &= \widehat{R}_{\text{v}n} Q, \\
p^{\text{out}}_{\text{v}N-1} &= p^{\text{out}}_{\text{c}} - \widehat{R}_{\text{v}N-1} Q = p^{\text{out}}_{\text{c}} - R_{\text{v}0} Q \xi^{N-1}, \\
\text{and since} \quad p^{\text{out}}_{\text{v}N-1} &= p^{\text{in}}_{\text{v}N-2} \quad \text{then,} \\
p^{\text{out}}_{\text{v}N-2} &= p^{\text{in}}_{\text{v}N-2} - \widehat{R}_{\text{v}N-2} Q, \\
&= \left(p^{\text{out}}_{\text{c}} - R_{\text{v}0} Q \xi^{N-1}\right) - R_{\text{v}0} Q \xi^{N-2}, \\
&= p^{\text{out}}_{\text{c}} - R_{\text{v}0} Q \left(\xi^{N-1} + \xi^{N-2}\right), \\
&\vdots \\
p^{\text{out}}_{\text{v}n} &= p^{\text{out}}_{\text{c}} - R_{\text{v}0} Q (\xi^{N-1} + \xi^{N-2} + \xi^{N-3} + \cdots + \xi^{n}) \\
&= p^{\text{out}}_{\text{c}} - R_{\text{v}0} Q \xi^{N-1} (1 + \xi^{-1} + \xi^{-2} + \cdots + \xi^{n-(N-1)}) \\
&= p^{\text{out}}_{\text{c}} - R_{\text{v}0} Q \xi^{N-1} \sum_{i=0}^{-(n-(N-1))} \xi^{-i} \\
&= p^{\text{out}}_{\text{c}} - R_{\text{v}0} Q \xi^{N-1} \sum_{i=0}^{N-1-n} \xi^{-i} \\
&= p^{\text{out}}_{\text{c}} - R_{\text{v}0} Q \xi^{N-1} \left(\frac{1 - \xi^{-(N-n)}}{1 - \xi^{-1}}\right).
\end{aligned} \tag{A.1}
$$

A.2 Arterial compliant matrix

This appendix provides detail of the compliant matrix for the arterial and vascular tree as per section §2.4.

From Equation (2.104) we have

$$
\mathscr{P}^{\text{in}}_{an} - \mathscr{P}^{\text{out}}_{an} + \psi_{\text{a}n} \mathscr{P}^{\text{ave}}_{an} = \widehat{R}_{an} Q \left(1 - 15 \mathscr{P}_e\right). \tag{A.2}
$$

For $n = 0, 1, 2, \cdots, N-1$ we can solve by

$$
\mathbf{A}\mathbf{p}_{\text{a}} = \mathbf{a}, \tag{A.3}
$$

where

$$\mathbf{p} = \begin{pmatrix} \mathscr{P}^{\text{in}}_{\text{a1}} \\ \mathscr{P}^{\text{in}}_{\text{a2}} \\ \vdots \\ \mathscr{P}^{\text{in}}_{\text{a}N} \\ \mathscr{P}^{\text{ave}}_{\text{a0}} \\ \mathscr{P}^{\text{ave}}_{\text{a1}} \\ \vdots \\ \mathscr{P}^{\text{ave}}_{\text{a}N-1} \end{pmatrix}, \quad \mathbf{a} = \begin{pmatrix} -p_{\text{root}} + \widehat{R}_{\text{a0}} Q \left(1 - 15\mathscr{P}_e\right) \\ \widehat{R}_{\text{a1}} Q \left(1 - 15\mathscr{P}_e\right) \\ \vdots \\ \widehat{R}_{\text{a}N-1} Q \left(1 - 15\mathscr{P}_e\right) \\ -p_{\text{root}}/2 \\ 0 \\ \vdots \\ 0 \end{pmatrix}, \tag{A.4}$$

and

$$\mathbf{A} = \begin{pmatrix} -1 & 0 & 0 & \cdots & 0 & \psi_{\text{a0}} & 0 & 0 & \cdots & 0 \\ 1 & -1 & 0 & \cdots & 0 & 0 & \psi_{\text{a1}} & 0 & \cdots & 0 \\ 0 & 1 & -1 & \cdots & 0 & 0 & 0 & \psi_{\text{a2}} & \cdots & 0 \\ \vdots & \vdots & \ddots & \vdots & \vdots & \vdots & \vdots & \ddots & \vdots & \vdots \\ 0 & 0 & 0 & \cdots & -1 & 0 & 0 & 0 & \cdots & \psi_{\text{a}N-1} \\ -1/2 & 0 & 0 & \cdots & 0 & 1 & 0 & 0 & \cdots & 0 \\ -1/2 & -1/2 & 0 & \cdots & 0 & 0 & 1 & 0 & \cdots & 0 \\ 0 & -1/2 & -1/2 & \cdots & 0 & 0 & 0 & 1 & \cdots & 0 \\ \vdots & \vdots & \ddots & \vdots & \vdots & \vdots & \vdots & \ddots & \vdots & \vdots \\ 0 & 0 & 0 & \cdots & -1/2 & 0 & 0 & 0 & \cdots & 1 \end{pmatrix}. \tag{A.5}$$

A.3 Venous compliant matrix

Similarly for the veins we have from Equation (2.105)

$$\mathscr{P}^{\text{in}}_{\text{v}n} - \mathscr{P}^{\text{out}}_{\text{v}n} + \psi_{\text{v}n} \mathscr{P}^{\text{ave}}_{\text{v}n} = \widehat{R}_{\text{v}n} Q \left(1 - 15\mathscr{P}_e\right). \tag{A.6}$$

For $n = N-1, N-2, \cdots, 0$ we can solve by

$$\mathbf{V}\mathbf{p}_{\mathrm{v}} = \mathbf{v}, \tag{A.7}$$

where

$$\mathbf{p} = \begin{pmatrix} \mathscr{P}^{\mathrm{in}}_{\mathrm{v}N-2} \\ \mathscr{P}^{\mathrm{in}}_{\mathrm{v}N-3} \\ \vdots \\ \mathscr{P}^{\mathrm{in}}_{\mathrm{v}0} \\ \mathscr{P}^{\mathrm{ave}}_{\mathrm{v}N-1} \\ \mathscr{P}^{\mathrm{ave}}_{\mathrm{v}N-2} \\ \vdots \\ \mathscr{P}^{\mathrm{ave}}_{\mathrm{v}1} \end{pmatrix}, \quad \mathbf{v} = \begin{pmatrix} -\mathscr{P}^{\mathrm{out}}_{\mathrm{c}} + \widehat{R}_{\mathrm{v}N-1} Q \left(1 - 15\mathscr{P}_e\right) \\ \widehat{R}_{\mathrm{v}N-2} Q \left(1 - 15\mathscr{P}_e\right) \\ \vdots \\ \widehat{R}_{\mathrm{v}0} Q \left(1 - 15\mathscr{P}_e\right) \\ -\mathscr{P}^{\mathrm{out}}_{\mathrm{c}}/2 \\ 0 \\ \vdots \\ 0 \end{pmatrix}, \tag{A.8}$$

and

$$\mathbf{V} = \begin{pmatrix} -1 & 0 & 0 & \cdots & 0 & \psi_{\mathrm{v}N-1} & 0 & 0 & \cdots & 0 \\ 1 & -1 & 0 & \cdots & 0 & 0 & \psi_{\mathrm{v}N-2} & 0 & \cdots & 0 \\ 0 & 1 & -1 & \cdots & 0 & 0 & 0 & \psi_{\mathrm{v}N-3} & \cdots & 0 \\ \vdots & \vdots & \ddots & \vdots & \vdots & \vdots & \vdots & \ddots & \vdots & \vdots \\ 0 & 0 & 0 & \cdots & -1 & 0 & 0 & 0 & \cdots & \psi_{\mathrm{v}0} \\ -1/2 & 0 & 0 & \cdots & 0 & 1 & 0 & 0 & \cdots & 0 \\ -1/2 & -1/2 & 0 & \cdots & 0 & 0 & 1 & 0 & \cdots & 0 \\ 0 & -1/2 & -1/2 & \cdots & 0 & 0 & 0 & 1 & \cdots & 0 \\ \vdots & \vdots & \ddots & \vdots & \vdots & \vdots & \vdots & \ddots & \vdots & \vdots \\ 0 & 0 & 0 & \cdots & -1/2 & 0 & 0 & 0 & \cdots & 1 \end{pmatrix}. \tag{A.9}$$